

Southern Radio Gravitational Lens Survey and Observations

by

James Edward John Lovell, B.Sc.(Hons.)

Submitted in fulfilment of the requirements
for the Degree of
Doctor of Philosophy

UNIVERSITY OF TASMANIA
HOBART

January 1997

Declaration

This thesis contains no material which has been accepted for the award of any other higher degree or graduate diploma in any tertiary institution. To the best of my knowledge and belief, this thesis contains no material previously published or written by another person, except where due reference has been made in the text of the thesis.

James Edward John Lovell

This thesis may be made available for loan and limited copying in accordance
with the Copyright Act 1968.

James Edward John Lovell

Thesis Summary

This thesis presents two related investigations, the first is a systematic radio survey in search of strong ($S_{2.7} > 0.34$ Jy) gravitational lenses in a complete sample of flat-spectrum radio sources, the second is a detailed study of the known, southern gravitational lens/Einstein ring radio source PKS 1830–211.

The motivation for these investigations was the discovery in 1991 that PKS 1830–211 is a strong gravitational lens. Because of its intensity, very detailed and sensitive observations can be made, and some of them form the second part of this thesis. The discovery of such a strong gravitational lens immediately raises the question of whether there are other strong lenses to be found.

Gravitational lenses provide a powerful astrophysical tool for measuring the properties of our universe. To date the majority of the known gravitational lenses have been found in the northern sky due to the concentration of surveys in that hemisphere. This thesis describes a search of the southern part of the sky for strong gravitational lenses and involved a study of a complete sample of the 461 strongest southern flat-spectrum radio sources in the Parkes Catalogue.

Flat-spectrum sources were chosen because they typically possess a single high brightness temperature nucleus of milliarcsecond size. Such sources, if lensed, will show multiply imaged nuclei with separations that are large compared to their sizes. All objects in the sample were observed with the Australia Telescope Compact Array (ATCA) by making at least six short observations (or “cuts”) at 4.8 and 8.6 GHz, separated by approximately two hours. In this way, all objects were imaged over ~ 8 days of telescope time, the dual wavelength observations allowing spectral index information to be determined for any structural components of the sources. Data simulations showed that the survey was capable of resolving any compact double source with component separations and flux densities greater than 1.5 arcsec and 6 mJy respectively.

The data were edited and calibrated within **AIPS** and imaged using **Difmap**. All correlated visibilities were examined and those that revealed signs of structure were imaged to search for signs of gravitational lensing. The only previously known lens in the sample, PKS 1830–211, was successfully re-discovered and the survey was demonstrated to be sensitive to extended ring-like structure by the detection of the planetary nebula PKS 1350–662. Two new gravitational lens candidates were found within the sensitivity of the survey, they are PKS 0252–549 and PKS 2321–375. As a check that no lens candidates had been overlooked and in order to obtain statistical information on the survey, a data processing script was written for **Difmap** to image the entire survey dataset. The data analysis revealed that over 60% of the sources contained at least 95% of their total flux

density in an unresolved core. All survey sources were classified (many for the first time) according to their structural and spectral characteristics, the point source component of this catalogue being especially useful in establishing a grid of potential reference sources for future ATCA calibration observations.

Many of the sources in the sample had catalogued radio positions with large errors (up to 30 arcsec). The ATCA survey provided positions with accuracy better than 1 arcsec for all objects with compact structure and allowed optical identifications to be made from the COSMOS/UKST Southern Sky Catalogue. This observational database is a significant contribution to the completion of radio identifications in the Parkes 1/2 Jy Complete Sample (Drinkwater *et al.*, 1996).

The second part of this thesis describes a detailed study of the properties of PKS 1830–211, the only known southern radio lens. This source is the strongest by almost an order of magnitude (Rao and Subrahmanyan, 1988; Jauncey *et al.*, 1991) and lies in a crowded and heavily obscured field close to the Galactic Centre. So far all efforts to identify optical or infra-red counterparts either for the lensing galaxy or the lensed source have been unsuccessful (Djorgovski *et al.*, 1992; Jauncey *et al.*, 1993). In particular, the failure of optical measurements to furnish any redshifts has driven the search for these critical parameters into the radio spectrum. This thesis describes the detection of a new absorption feature towards the lens, due to H I at a redshift of 0.19. This discovery, together with that of a second absorption system at $z = 0.89$ (Wiklind and Combes, 1996a) indicates that PKS 1830–211 may be a compound gravitational lens.

Total flux density measurements of PKS 1830–211 have been made with the University of Tasmania’s 26 m radiotelescope at 2.3 and 8.4 GHz since 1990. These observations have revealed dramatic variations in flux density on timescales of months. More recently, the ATCA has been used to monitor the total flux density at four wavelengths as well as the flux densities of the two individual compact components at 8.6 GHz. Large flux density variations in the two components were detected and analysed, leading to new constraints on the lensing time delay and the relative magnification ratio of the two compact components.

Acknowledgements

I wish to express my sincere thanks to the people who have helped me in the course of my studies. In particular, my supervisors Prof. Peter McCulloch and Dr. Dave Jauncey. This thesis would not have been possible without Dave's encouragement and sound advice throughout the last four and a half years. His boundless enthusiasm has provided inspiration on many occasions. I would like to thank Peter for his support during this project. His efforts (in conjunction with Prof. Pip Hamilton) in establishing the Mt Pleasant observatory, and providing the computing equipment needed for this work have been invaluable.

I would especially like to thank Edward King for his advice, support and, above all, friendship over the past 6 years. I am also grateful to Edward for collecting a large amount of the early PKS 1830–211 flux monitoring data at Mt. Pleasant.

A big thankyou also goes to John Reynolds, the man for whom too much VLBI is barely enough. John has been a great source of wisdom on all things related to radio interferometry. He has also helped with observations at the ATCA on several occasions and provided valued friendship and patient advice. Thanks to John, Dayton Jones and Tas van Ommen for several useful discussions on PKS 1830–211. Tas also made available his VLA snapshot data on PKS 1830–211 for which I am grateful. I would also like to thank Tasso Tzioumis, Warwick Wilson, Mal Sinclair and Russel Gough for assisting in the VLBI observations and data processing.

Thanks to the Project Phoenix team, in particular Peter Backus and Jill Tartar, for supporting observations at Parkes during the search for absorption towards PKS 1830–211 (Chapter 6).

I would like to thank the staff of the Physics Department and fellow postgraduate students, Simon, Edward and Chris for their support and friendship over the past five and a half years. For most of that time I have shared an office with Simon Ellingsen. This experience has left a lasting impression on me. I have always been amazed at Simon's complete lack of ability to retain useless trivia and only remember the important things. I think he might find the phrase "*Kino o nomisugimashita*" non-trivial and perhaps quite useful if he should find himself in Japan. I would also like to thank Chris for keeping his desk messier than mine and for his company, along with Edward on many expeditions into our beautiful wilderness. I am indebted to the staff of the Mt. Pleasant observatory, Gordon Gowland, Phil Jenkins, John Smith and Marco Costa for their assistance and technical support in getting observations up and running.

Edward King and Phil Edwards have both selflessly volunteered to proof-read this thesis. *Doomo aríгато gozaimásu!*

I am grateful to the Australian Government for a Postgraduate Award, which

provided me with the financial support necessary to undertake the work presented in this thesis. The ATNF also provided financial support for travel to and accommodation at their observatories for which I am thankful. This work has used data from the COSMOS/UKST Southern Sky Catalogue as provided by the Anglo-Australian Observatory, has made use of the NASA/IPAC Extragalactic Database (NED) which is operated by the Jet Propulsion Laboratory, Caltech, under contract with the National Aeronautics and Space Administration. The Digitized Sky Surveys have also been used and. They were produced at the Space Telescope Science Institute under U.S. Government grant NAG W-2166. The images of these surveys are based on photographic data obtained using the Oschin Schmidt Telescope on Palomar Mountain and the UK Schmidt Telescope.

Thankyou to my parents for their continuing love and support. They have provided the encouragement and opportunity to pursue a career in astronomy for which I will always be grateful.

Finally, thankyou to my wife, Jenny, for her love and encouragement and for putting up with me when I was preoccupied with work. Thanks for all those cups of tea too!

Contents

Thesis Summary	iv
Acknowledgements	vi
1 Introduction	1
1.1 Previous Gravitational Lens Surveys	1
1.2 A Southern Hemisphere Survey	3
1.3 Outline of the Thesis	6
2 Understanding the Survey	7
2.1 Planning the Observations	7
2.2 Simulations	7
2.2.1 Survey Limitations	8
2.2.2 Conclusions	18
3 Gravitational Lens Candidates	19
3.1 ATCA Observations and Imaging	19
3.2 Identification of Gravitational Lens Candidates	20
3.3 Candidate Selection	21
3.4 The Gravitational Lens Candidates	24
3.4.1 Detected Lensed Cores	24
3.4.2 Detected Lensed Jets	27
3.4.3 Marginally Detected Lensed Cores	30
3.4.4 Marginally Detected Lensed Jets	33
3.5 Lensing Frequency	33
3.6 Summary	36
4 Properties and Statistics	38
4.1 Introduction	38
4.2 The Automatic Imaging Process	38
4.3 Automatic Processing: Results	41
4.4 Survey Source Properties	45
4.4.1 Structural Classifications	45
4.4.2 Large Separation Double Sources	46
4.4.3 Intra-day Variable Sources	48
4.4.4 A Comparison of ATCA and Parkes Flux Densities	49

4.4.5	Optical Identifications	53
4.4.6	Overlap with Other Catalogues	56
4.5	Summary	56
5	PKS 1830–211: Radio Structure	86
5.1	Introduction	86
5.2	Low Resolution Radio Structure	87
5.2.1	Modelling the Lens	88
5.3	High Resolution Radio Structure	91
5.3.1	Brightness Temperature Estimates	92
5.3.2	Spectral Index Analysis	93
5.3.3	Conclusion	96
5.4	Continuum Spectra of the Components of PKS 1830–211	96
5.4.1	Measuring the Compact Component Flux Densities	97
5.4.2	Results	99
5.5	Summary	100
6	PKS 1830–211: A Search for Absorption	103
6.1	Introduction	103
6.2	Single Dish Observations	103
6.3	VLBI Observations	104
6.4	A Compound Gravitational Lens?	107
6.5	Summary	108
7	Flux Density Monitoring of PKS 1830–211	109
7.1	Total Flux Density Measurements	109
7.2	ATCA Flux Density Monitoring Observations	114
7.2.1	Simulations	115
7.2.2	The Observations	116
7.2.3	Analysis	116
7.3	Implications on Source Redshift and H_0	123
7.4	Summary	124
8	Conclusions	128
8.1	The Gravitational Lens Survey	128
8.2	PKS 1830–211	129
	References	131

List of Tables

2.1	Estimated ATCA detection efficiency for compact double sources. . .	12
2.2	Minimum detectable flux density in mJy for a weak compact core. .	14
3.1	A summary of the ATCA cuts observations.	20
4.1	RMS differences between observed and model visibilities	43
4.2	The point to total flux density ratio distribution.	46
4.3	Mean offset between radio and optical positions (radio – optical) for the 339 radio sources with COSMOS identifications.	53
4.4	Mean offset between radio and optical positions (radio – optical) for the 339 radio sources with COSMOS identifications after an estim- ated correction for the systematic position errors in the COSMOS database as derived by Drinkwater <i>et al.</i> (1995).	55
4.5	Flux density and structural information obtained from the ATCA survey and optical identifications from the COSMOS/UKST South- ern Sky Catalogue.	57
4.6	Additional notes on selected survey sources.	71
5.1	Elliptical Gaussian sub-components fitted to the NE and SW images in the 5 GHz VLBI image of PKS 1830–211 and their associated brightness temperatures.	93
5.2	Position angle and separation estimates for sub-components of the NE VLBI image of PKS 1830–211 at three frequencies.	96
5.3	Estimated compact component flux densities and flux density ratios.	98
7.1	Predicted peak outburst times and flux densities for various reas- onable values of γ	113
7.2	The template model derived from a cuts observation at 8.6 GHz of PKS 1830–211.	115
7.3	Estimated values for time delay and component magnification from a correlation of the 8.6 GHz light curves.	121

List of Figures

2.1	Simulated response of a 6 km ATCA baseline to a compact double source.	8
2.2	Determined values for D_m based on simulations of double point sources.	11
2.3	Estimated ATCA detection efficiency for compact double sources at 4.8 and 8.6 GHz.	12
2.4	Images from simulated observations of a 5 arcsec ring.	15
3.1	Examples of ATCA survey data	22
3.2	Visibility amplitudes for PKS 1830–211.	24
3.3	ATCA images of PKS 1830–211.	25
3.4	The ATCA cuts images of PKS 0252–549 at 4.8 GHz and 8.6 GHz.	26
3.5	The 8.6 GHz ATCA image of PKS 0252–549 with optical counter-parts.	26
3.6	Visibility amplitudes for PKS 1350–662.	28
3.7	ATCA images of PKS 1350–662.	28
3.8	4.8 GHz ATCA image of PKS 2321–375.	29
3.9	ATCA images of PKS 0253–754.	30
3.10	ATCA images of PKS 0451–282.	31
3.11	ATCA images of PKS 2210–257.	32
3.12	ATCA images of PKS 1236–684.	33
3.13	ATCA images of PKS 1800–660.	34
3.14	ATCA images of PKS 1833–772.	34
3.15	Separation of observed lenses and limitations of the present survey.	35
3.16	Separation of observed lenses in the survey.	36
4.1	Visibility amplitudes for PKS 0521–365.	42
4.2	ATCA images of PKS 0521–365.	42
4.3	PKS 2303–656, PKS 0113–285 and PKS 2138–377 at 4.8 GHz imaged with the three automatic processing methods.	44
4.4	The confirmed intra-day variable source PKS 1144–379 and the candidate intra-day variable PKS 1415–349.	48
4.5	Spectral index distribution of the ATCA survey sources.	50
4.6	Two examples of contaminating sources in the flat-spectrum sample	51
4.7	Parkes flux densities as a function of ATCA flux densities.	52
4.8	Offsets between ATCA and COSMOS catalogue positions.	54
4.9	Histograms of offsets between ATCA and COSMOS catalogue positions.	54
4.10	Images of selected ATCA survey sources.	73

5.1	A 14.94 GHz VLA snapshot image of PKS 1830–211 at 0.1 arcsec resolution.	87
5.2	PKS 1830–211 at 4.993 GHz, imaged with the MERLIN array in September 1991.	88
5.3	The NE and SW compact components of PKS 1830–211 at 5.0 GHz.	92
5.4	Superimposed images of the NE component of PKS 1830–211.	94
5.5	Quiescent flux density continuum spectra of PKS 1830–211 and its compact components.	100
5.6	Quiescent flux density continuum spectra of PKS 1830–211 and its variable and non-variable components.	101
5.7	Quiescent compact component flux density ratios of PKS 1830–211.	101
6.1	Absorption spectra towards PKS 1830–211.	105
6.2	1.19 GHz VLBI continuum map of PKS 1830–211. Also shown are the spectra of the two continuum components.	106
7.1	Total flux density light curve for PKS 1830–211. The vertical dashed lines indicate the time of the outburst peak for $\gamma = 2$ as shown in Table 7.1	111
7.2	The time at which flux density reached a maximum as a function of wavelength.	113
7.3	Total flux density light curve for PKS 1830–211 from ATCA service and gravitational lens survey observations. Also shown are 8.4 GHz data from Mt. Pleasant.	117
7.4	The 8.6 GHz light curve data for both components PKS 1830–211 from the ATCA.	118
7.5	Contours of D^2 and combined light-curves for PKS 1830–211 when $\delta = 15$ and $\delta = 20$	122
7.6	H_0 plotted against source redshift for several time delay values for a $z = 0.19$ lens.	125
7.7	H_0 plotted against source redshift for several time delay values for a $z = 0.89$ lens.	126

Chapter 1

Introduction

Measurements of the properties of gravitational lenses have the power to tell us what sort of universe we live in. The close study of an individual lens can provide an estimate of the Hubble constant, H_0 whilst the statistical properties of the gravitational lens population provides valuable information on the amount of matter in the universe and has implications for the existence of a cosmological constant. Therefore finding gravitational lenses has a great potential return.

Strong gravitational lenses in particular are of great importance as they allow a detailed investigation of properties that are difficult to measure in weaker lenses. PKS 1830–211 is the strongest known radio gravitational lens, being ~ 10 Jy at 2.3 GHz. PKS 1830–211 is suitable for VLBI investigations of its compact structure, single-dish monitoring of its total flux density and monitoring of the flux densities of its two compact cores, with VLBI and connected element arrays, to measure a lensing time delay. These observations would be more difficult in a weaker gravitational lens, requiring longer integrations to achieve the same sensitivity. PKS 1830–211 is obscured by our Galaxy at optical wavelengths and so far a redshift measurement by conventional (optical) means has proved impossible. However, because it is strong, it provides the opportunity to search for weak molecular absorption that might be undetectable in fainter sources.

If one assumes that the number of gravitational lenses increases as their flux densities decrease in a similar manner to all extragalactic radio sources then given the presence of one ~ 10 Jy gravitational lens it is not unreasonable to expect others stronger than 1 Jy. This thesis describes a survey of strong southern hemisphere flat-spectrum radio sources to search for new, strong gravitational lenses, and includes a study of the known strong gravitational lens PKS 1830–211.

1.1 Previous Gravitational Lens Surveys

At the time that work on this survey started the results from two major surveys were published and at least one other survey was underway. The first was a VLA imaging survey from the MIT/Greenbank (MG) catalogue (Burke, 1989) and the second was an HST snapshot survey of high luminosity quasars (Maoz *et al.*, 1992). The third survey was a radio imaging survey of a large number of flat-spectrum sources (Patnaik *et al.*, 1992). The survey of Burke *et al.* made VLA

images of a large number of objects in the MG 4.8 GHz survey with a flux density greater than 100 mJy. The sources covered a range of declinations between -0.5° and 19.5° with $|b| > 10^\circ$. No spectral index selection criteria were applied to the survey sources and this meant that the sample contained a large number of steep-spectrum objects which often have extended radio structure.

The MG VLA imaging survey discovered at least four and possibly eight examples of gravitational lensing from the 1786 sources imaged (Burke, 1989). From this statistic, the author predicted a lensing frequency of one in every 100 to 200 quasars, after accounting for the expected number of undetected gravitational lenses. In an analysis of the results from the MG VLA survey, Kochanek (1993a) estimated that 50% of gravitational lenses contained in the sample were not detected, thus verifying the lensing frequency predicted by Burke.

The HST survey was of a sample of all quasars in the catalogue of Véron-Cetty and Véron (1987) with $z > 1$, $|b| > 10^\circ$ and absolute magnitude brighter than $M_V = -25.5$. The sample was not complete as the catalogue from which it was drawn is a collection of quasars drawn from many surveys with different selection criteria. Also, quasars with bright, nearby foreground stars or in other HST programs were excluded from the Maoz *et al.* survey. There were 354 quasars in the sample and each one was observed to search for evidence of multiply imaged point sources. Maoz *et al.* (1992) had found 3 lenses in the 184 quasars observed at that stage and so predicted a lensing frequency of approximately one in 60 bright quasars.

The primary aim of the survey of Patnaik *et al.* (1992) was to search for compact radio sources suitable for phase calibration of the MERLIN array. Approximately 900 flat-spectrum sources were selected with flux densities greater than 200 mJy at 5 GHz, declinations in the range $+35^\circ$ to $+75^\circ$ and galactic latitudes greater than 2.5° . The sources were imaged with the VLA in snapshot mode at 8.4 GHz and the vast majority were found to be point-like with over 85% of sources possessing at least 80% of their total flux density in a compact component.

When observations were being planned for the present thesis, 14 sources from the VLA survey of Patnaik *et al.*, later known as the Jodrell Bank-VLA Astrometric Survey (JVAS), were identified to possess multiple compact nuclei and were thus potential gravitational lenses, although only 0218+357 had been confirmed as a gravitational lens.

The JVAS gravitational lens survey has since been concluded for a complete sample of approximately 2200 flat-spectrum northern hemisphere sources with $S_{5\text{ GHz}} \geq 200$ mJy. Four confirmed and two probable lensing systems were found in the survey, all but one possessing component separations of at least 1.0 arc-sec. Of particular note is that the survey detected an equal number of three and five-image systems which is surprising given the greater predicted likelihood of a three-image system. A newer survey still in progress is the Cosmic Lens All Sky Survey, or CLASS (Myers *et al.*, 1995) which has similar spectral index selection criteria and observing strategy to JVAS but aims to survey $\sim 10^4$ flat-spectrum radio sources. Preliminary results indicate at least two lens candidates in ~ 3000 sources.

Shortly after this gravitational lens search had started, the HST snapshot survey was completed (Maoz *et al.*, 1993) for all sources in the original sample as well as an additional 163 high luminosity quasars. The total number of objects successfully observed was 498. After including previously known gravitational lenses that satisfied the sample criteria but were not observed, the lensing frequency was 4 to 6 out of 502 quasars, the uncertainty due to two candidates that were unconfirmed. In an analysis of these results, Kochanek (1993a) concluded that all gravitational lenses in the sample for the HST survey were detected within statistical errors. Therefore, the HST snapshot survey predicts a lensing frequency of one in every 80 to 130 quasars.

1.2 A Southern Hemisphere Survey

In planning the observations for the present thesis, a sample size was chosen based on two considerations. First, the observing constraints for a southern hemisphere radio gravitational lens survey and second, the observational evidence available at the time from surveys with comparable properties:

Observing Constraints. Unlike VLA snapshot observations which provide structural information in two dimensions from a single snapshot, ATCA observations require several snapshots over a wide range of hour angles. This significantly increases the observing time needed for each source in the sample and so reduces the number of objects that can be observed over a reasonable period of time. As will be described later, a sample was chosen that could be fully observed within 8 days at the ATCA.

The ATCA allows for observations to be made simultaneously at two wavelengths. Therefore, gravitational lens candidates may be selected based on spectral properties as well as morphology. This is a significant advantage over previous VLA gravitational lens surveys.

Observational Evidence. The only large scale radio gravitational lens survey at the time was from the MG survey (Burke, 1989) which had comparable flux density limits to those chosen for the present survey and had estimated a lensing frequency of 0.5 to 1% of quasars. The completed HST survey was also used to provide an estimate of the frequency of gravitational lensing as it was sensitive to lensed point sources only, the kind of source that dominates a flat-spectrum radio sample. The results from the two completed surveys suggested that a radio survey of ~ 500 southern hemisphere quasars might contain 2 to 8 candidate gravitational lenses.

A recent summary of the advantages of radio over optically selected gravitational lens surveys has been presented by Kochanek (1996). Optically, gravitational lens images may suffer extinction if their light passes through the dust of the lensing galaxy. Therefore using optically selected quasars for a gravitational lens search may actively de-select lenses. Radio selected samples on the other hand do

not suffer this problem as dust does not markedly affect the transmission of radio waves.

Because the main aim of the present survey was to detect gravitational lenses, the sample was selected to maximise the chance of unambiguous lens detection. Therefore, starting selection criteria were required that would produce a sample dominated by extragalactic sources. Over 80% of flat-spectrum radio sources are identified with quasars on the basis of accurate radio-optical position coincidence (see for example Jauncey *et al.*, 1982). The presence of a flat spectrum in an extragalactic radio source is usually indicative of synchrotron self-absorption. These sources typically possess a single high brightness temperature nucleus. Such a source, if lensed, will show multiply imaged nuclei with a separation that is large compared to their milliarcsecond sizes. Therefore any source in this sample with 2 or more flat-spectrum components must immediately be considered as a gravitational lens candidate. Most flat spectrum sources also have a coincident optical counterpart which is important for confirmation of lensing and permitting redshifts to be measured.

A radio selected sample that is not restricted to flat-spectrum sources only, will include a large number of objects dominated by extended, steep-spectrum components. The probability of such an object being lensed by a foreground mass is significantly greater than that for a point source simply because of the larger lensing cross-section for an extended source. It might therefore be considered worthwhile to broaden the sample to include steep-spectrum sources and thus increase the likelihood of a new lens detection, *i.e.* a survey similar to that of Burke *et al.* (1989). The main problem with such a strategy comes in identifying the object as a lens. For example if the background object is a core-jet source and the lensing mass lies in front of, or perpendicular to the jet, and a significantly large distance from the core, the resulting image will appear with a “broken” or “tangentially stretched” jet (Kochanek, 1993b). Such scenarios, whilst much more likely than a lensed core, produce an image that looks not too different from that found in many un-lensed sources. Furthermore, because extended radio emission is rarely seen at optical wavelengths, it is difficult to confirm optically if the source is lensed unless the core itself is multiply imaged. A survey that includes steep-spectrum sources is therefore not likely to be complete (the MG VLA survey is only 50% according to Kochanek (1993a)) and the lens detection efficiency is poorly defined. Understanding the detection efficiency of a survey is very important for cosmological studies based on gravitational lensing statistics.

When this survey was started, the most complete catalogue of southern radio sources from which a sample could be drawn was the Parkes 2.7 GHz Catalogue which also has the advantage of being available in a computer readable format. This catalogue, collated over 20 years, contains sources that were in the original Parkes survey (Bolton *et al.*, 1979 and references therein) which claims 95% completeness to a flux density level of 0.25 Jy at the epoch of observation except for the region $|b| < 10^\circ$. The sources in the catalogue also have 5.0 GHz flux densities, measured with the same instrument allowing construction of a flat-spectrum sample.

The 2.7 and 5 GHz measurements were not made at the same epoch. As a consequence of this time difference, a flat spectrum sample of Parkes sources made using spectral indices calculated from the 2.7 and 5.0 GHz flux densities is not statistically complete at a single epoch. Sources that might be selected while quiescent may not be selected if the 2.7 GHz flux density was unusually high and/or the 5.0 GHz flux density was unusually low at the epoch of observation or vice versa. Therefore it is likely that a small number of steep spectrum sources will be selected and one might expect a similar small number of flat spectrum sources not to be selected.

For the present gravitational lens survey, the sources were not selected based on optical identifications for two reasons. First, many objects in the Parkes 2.7 GHz Catalogue (Bolton *et al.*, 1979) have large uncertainties in their radio positions and so optical identifications are far from complete at present. Second, it is known that a small number of the optical identifications within the catalogue are erroneous and, although the number is small (probably less than a few percent are incorrectly identified), it is similar in magnitude or greater than the abundance of gravitational lenses amongst extragalactic radio sources.

No galactic latitude cut-off was imposed in the selection criteria for the present survey. This has the advantage of not excluding any gravitational lens systems that may be obscured optically by our galaxy. However, if a low galactic latitude source is identified as a gravitational lens candidate in the sample it may be difficult to confirm based on redshift measurements, although it should be noted that PKS 1830–211 is a confirmed gravitational lens with a low galactic latitude and no known optical counterpart. Therefore, the survey is only complete for $|b| > 10^\circ$.

An additional aim of the present gravitational lens survey was to provide accurate radio positions, and then optical identifications based on radio-optical position coincidence alone. This in turn will give (when redshifts are completed) a much better luminosity function for flat-spectrum radio sources found at 2.7 GHz (see, for example Drinkwater *et al.*, 1996).

The Flat Spectrum Sample

The sample was selected from the Parkes Catalogue (Bolton *et al.*, 1979) computer database (Wright and Otrupcek, 1990) using the following criteria:

1. 2.7 to 5.0 GHz spectral index ≥ -0.5 ($S \propto \nu^\alpha$).
2. B1950 declination south of -20 degrees.
3. 2.7 GHz flux density $> 0.34\text{Jy}$.

This yielded a sample of 461 radio sources for the gravitational lens survey, a number that was observable with the Australia Telescope Compact Array (ATCA) in a reasonable time. These criteria are discussed in more detail in the following chapter.

1.3 Outline of the Thesis

This project has involved the collection, processing and analysis of single dish, connected element interferometry and very long baseline interferometry data. The following chapters describe aspects of this work and present the results. A brief outline of the thesis is given below.

Chapter 2. Simulated ATCA observations are described. They were carried out to understand the gravitational lens detection efficiency of the survey. Attention is given to sources with multiple compact components to determine the minimum detectable flux density and component separation as well as the maximum detectable component separation. The sensitivity of the survey to extended structure is also discussed.

Chapter 3. The ATCA observations are described and the data processing and analysis techniques outlined with particular reference to identifying gravitational lens candidates from the data. Candidates arising from the survey are presented and discussed.

Chapter 4. Results and discoveries arising from the survey that are not directly related to gravitational lensing are presented. An automatic process used to image all of the sources is described as well as the procedure used for identifying optical counterparts. Source flux densities, spectral indices, ratios of point to total flux density, radio morphology classifications, radio positions and optical identifications are all tabulated. Images of sources of particular interest are shown.

Chapter 5. This chapter and the two that follow it present a detailed investigation into the Einstein ring/gravitational lens PKS 1830–211. Following an introduction, the radio structure of PKS 1830–211 is described with special reference to the unusual milliarcsecond-scale morphology of this source. Attempts to model the lensing system are described.

Chapter 6. Radio spectral-line observations that revealed an HI absorption system toward PKS 1830–211 at $z = 0.19$ are described. The implications of this discovery are discussed.

Chapter 7. Total flux density monitoring observations of PKS 1830–211 at several frequencies are presented and analysed. The ATCA has been used to monitor the flux densities of the two lensed compact components of PKS 1830–211 at 8.6 GHz to determine a relative component magnification ratio and a time delay. The results of a correlation analysis of the two light curves are presented and discussed.

Chapter 8. The investigations presented in this thesis and their results are summarised and briefly discussed.

Chapter 2

Understanding the Survey

2.1 Planning the Observations

It was necessary to image all of the sources in the sample to determine if they were lensing candidates. The ATCA was chosen for this task as it is the only imaging radio telescope available for sources south of $\delta \approx -45^\circ$. It provides an arcsecond resolution imaging capability at 8.6 GHz which is similar to that available from existing ground-based optical observations. The ATCA also allows for simultaneous observations at 4.8 and 8.6 GHz so the resulting images provide spectral index information essential in identifying the flat-spectrum components.

The ATCA is an east-west linear array, so its u - v coverage becomes one-dimensional for equatorial sources. It was for this reason that the equatorial zone was avoided and a northern declination limit of -20° imposed. The flux density limit was chosen to keep the sample to a manageable size based on observing time constraints for this thesis, whilst maintaining a reasonable probability of detecting any new gravitational lenses.

A complete 12 hour synthesis of each source at the compact array would require 230 days of observing time which is impractical. All of the sources in the sample are bright enough not to require long integrations to achieve a detection, so total integrations of the order of one minute are sufficient for detection (a one minute observation with the ATCA at 4.8 or 8.6 GHz yields a (theoretical) flux density sensitivity of ~ 0.7 mJy rms). In order to determine structure, several observations are required at different hour angles – the so-called “cuts mode” of observing. To quantify the sensitivity of this observing mode to arcsecond scale structure, it is necessary to understand the response of the ATCA to such structure when the u - v plane is under-sampled.

2.2 Simulations

The response of the ATCA to arcsecond-scale structure was examined by carrying out simulated observations of various source structures. The first aim was to determine the minimum number of cuts needed and, once that had been decided, to establish the sensitivity and resolution limits of the survey.

All of the simulated ATCA data described hereafter were created using the Caltech VLBI Software package (Pearson, 1991). The program *Fake* was used to simulate data from a typical ATCA configuration (6C) with baselines of up to 6 km in length. Expected antenna system temperatures and efficiencies were used to create the simulated data, thus providing the expected amplitude noise levels. Zero phase noise was applied in each case thus simulating the excellent phase calibration that is typically achieved during observations. All simulations were carried out at 8.6 GHz.

Sampling of the u - v Plane

Shown in Figure 2.1 is the response of the ATCA to a one arcsecond compact double source where both components have a flux density of 1.0 Jy. Only the visibility amplitudes on the longest baseline are shown and they reveal the expected response of an interferometer that has clearly resolved the two components (*e.g.* Fomalont and Wright, 1974). The amplitudes are seen to “beat” at a rate of once every ~ 4.7 hr and therefore the minimum sampling rate for such an object is one observation every ~ 2.4 hr (*i.e.* the Nyquist rate). A minimum sampling rate of one observation, or cut, every 2 hr was chosen for the survey so that slightly larger separation components would not be under-sampled on the longest baseline. This also introduces a degree of redundancy in the event of the loss of data or data quality due to problems encountered during the observations such as wind stows, external radio interference or poor atmospheric conditions.

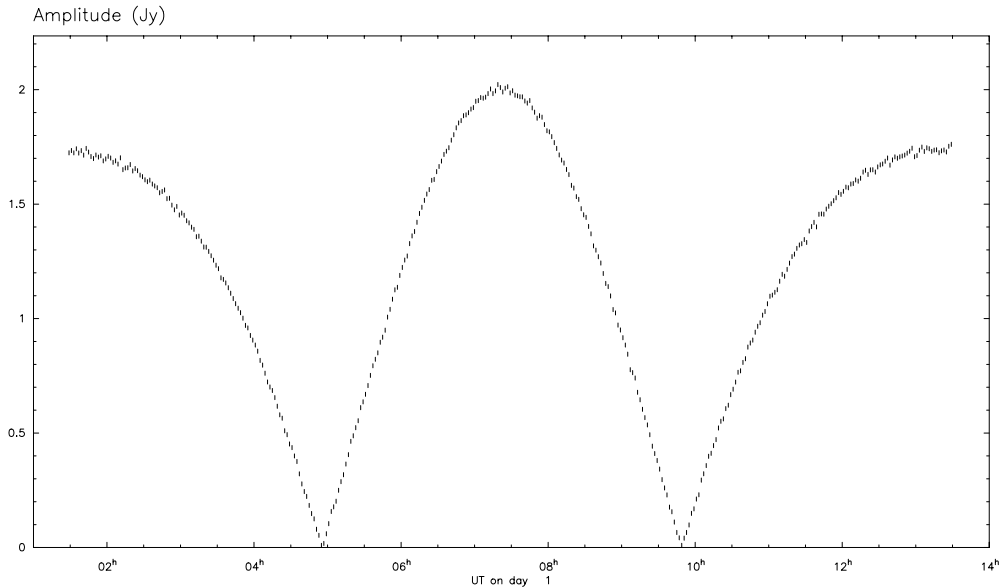


Figure 2.1: Simulated response of a 6 km ATCA baseline to a compact double source.

2.2.1 Survey Limitations

An important part of any survey of this type is to define its limitations so that the sensitivity of the survey to various source component separations and flux densities

can be stated. This information is important in determining the proportion of gravitational lenses amongst flat-spectrum radio sources. While this survey is primarily aimed at detecting multiple compact flat spectrum nuclei, its sensitivity to ring- and arc-like structure should also be considered. Therefore, the survey characteristics and limitations that must be determined are:

- The ability of the ATCA cuts survey to resolve two or more compact components with various flux density ratios, separations, position angles and declinations.
- The ability of the ATCA cuts survey to detect extended structure, such as Einstein rings, with the limited u - v coverage provided by cuts observations.

Compact Component Separation

The resolving power of an east-west linear interferometer array such as the ATCA is affected by the declination of the source and is determined by the degree of rotation of the array with respect to the source during the time the source is above the horizon. Any source at $\delta = 0^\circ$ will not be seen to rotate with respect to the array, resulting in no spatial information in the north-south direction. For sources further south from the celestial equator this effect becomes less apparent and the synthesised beam of the array becomes more circular.

Consider first the ability of the ATCA to resolve compact components, assuming that they are strong compared to the noise. The ability of the ATCA to resolve these components then depends on their separation (D), declination (δ) and position angle (θ), which is defined as the angle subtended by weakest of the two components with respect to the strongest measured north through east. D_m is defined as the minimum separation for the two compact components to be unambiguously resolved and depends on δ and θ . It is helpful to divide the separation parameter into three groups:

- **Group 1:** If $D > D_1$ then any source will be resolved no matter what its declination or the component position angles. *i.e.* $D_1 = \max(D_m)$.
- **Group 2:** If $D < D_2$ then it is not possible to resolve the components no matter what the position angle or declination. *i.e.* $D_2 = \min(D_m)$.
- **Group 3:** If $D_2 \leq D \leq D_1$ then the ability of the ATCA to resolve the components depends on both position angle and declination.

The situation defined as Group 3 is discussed first as this leads to a definition of D_1 and D_2 . Only position angles in the range 0 to 90° are discussed due to the symmetry of a simple two point source scenario. If the position angle is at 90° then D_m is independent of declination because the ATCA beam FWHM remains constant in the east-west direction as declination changes. For position angles closer to 0° a higher dependence on declination results.

It is necessary to determine when a two-component source is resolved. This was done by generating simulated 8.6 GHz ATCA observations of compact double

sources with a range of separations, position angles and declinations. The components were each given a flux density of 1.0 Jy, well within the sensitivity limits of the ATCA, thus rendering negligible any effects due to noise. The response of the survey to binary sources with weaker and unequal flux densities will be discussed later in this chapter. Initially, source models were used with a constant position angle of 0° and only separation and declination values were changed. This position angle was chosen because the ATCA beam changes most in the north-south direction so the array sensitivity is best examined in this direction as declination changes.

For each simulated dataset, the Caltech VLBI Software package program **Modelfit** was used to fit three different source models; a point, a line and a double point source. In each case, the model parameters were allowed to vary until convergence was achieved between the “observed” and model visibilities and the resulting “agreement factor”¹ noted. A point source model was classified as inadequate once a significant difference between the agreement factors for that model and the line model was observed. Similarly, the line model was determined to be no longer sufficient once a significant difference between its agreement factor and that for a double point source model was detected. The point source model only provided an acceptable fit for small component separations ($\lesssim 100$ mas) and for near-equatorial declinations ($\gtrsim -40^\circ$). The agreement factor difference between the line and double point models remained small no matter what the declination for separations $\lesssim 300$ mas but became significantly different at a separation of 500 mas for declinations south of $\sim -40^\circ$. More datasets were simulated for the regions where the agreement factors determined for the linear and double point source models began to differ so that the relationship between the declination and the component separation at which this divergence occurred could be established.

The component separation, D_m , at which one can distinguish between an extended source (modelled by a line) and two distinct sources (modelled by a double point source) is directly related to the resolution of the array. In the case of these simulated data the array resolution is proportional to the FWHM of the synthesised beam which, in the north-south direction is $\lambda/(d \sin \delta)$ at wavelength λ where d is the length of the longest baseline. Figure 2.2 shows the values determined for D_m from the simulations plotted against FWHM. As expected, there is a linear relationship between these values with a slope of $245 \text{ mas arcsec}^{-1}$.

This information can be used to determine the expected efficiency of detecting compact doubles of a given separation for the entire survey. The expected detection efficiency is then a function of declination and component position angle. For a source with position angle θ and declination δ , the ability of the ATCA to resolve this source depends on the projected FWHM of the synthesised beam, B_{proj} , which is elliptical and given by:

$$B_{\text{proj}}(\theta, \delta) = \frac{\lambda}{d} [1 - \cos \theta (1 - \sin^2 \delta)]^{-1/2} \quad (2.1)$$

¹**Modelfit** defines the “agreement factor”, AF , as the square root of the reduced χ^2 of the fit between the source model and the data, *i.e.* $AF = \sqrt{\chi^2/\nu}$ where ν is the number of degrees of freedom. For a good fit, AF approaches unity.

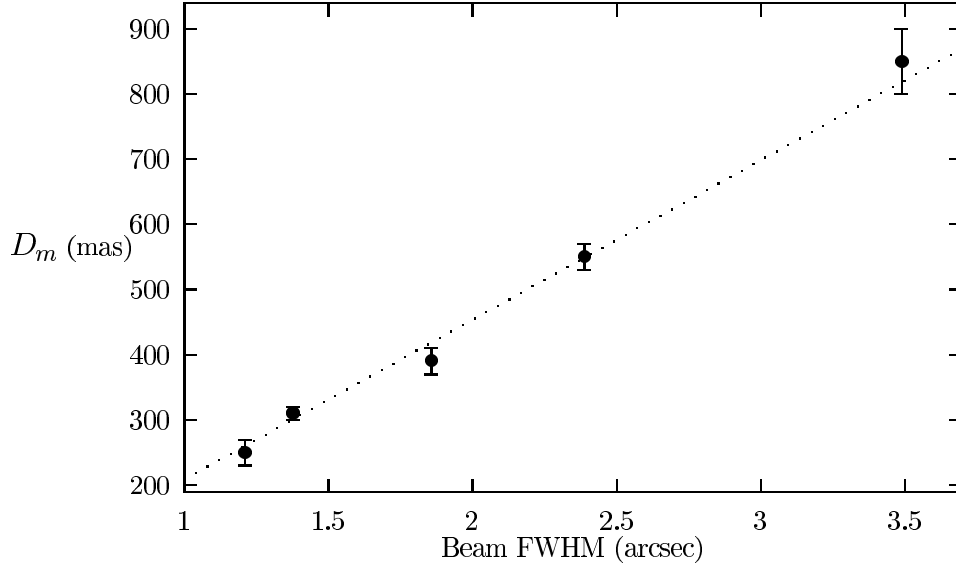


Figure 2.2: Determined values for D_m based on simulations of double point sources with position angle 0° and varying separations and declinations. The horizontal axis is the synthesised beam FWHM. The line of best fit is also shown.

Analysis of the simulated data shows that a double point source is uniquely identifiable when the projected FWHM of the beam, $B_I = (1/245 \text{ mas arcsec}^{-1}) D_m$. These values, when applied to Equation 2.1 provide the minimum position angle, θ_I , for a unique double source detection at a given δ . Therefore, the fraction of all resolvable double sources may be written as

$$F(\delta, D_m) = \frac{90 - \theta_I}{90} \quad (2.2)$$

Integrating this function over all declinations in the survey for a given component separation thus provides an indication of the efficiency of detecting such a source in the survey. A similar estimate for a large component separation, D_{max} (where all sources are guaranteed to be resolvable), provides the total number of sources in this simulated survey and this allows for an estimate for the percentage of sources detectable as doubles at a given separation, $P(D)$, for the entire survey:

$$P(D) = \frac{\int_{-90}^{-20} F(\delta, D) \cos \delta d\delta}{\int_{-90}^{-20} F(\delta, D_{\text{max}}) \cos \delta d\delta} \times 100 \quad (2.3)$$

A scale factor of $\cos \delta$ was applied because the number of sources decreases by this factor as $|\delta|$ increases for a uniform density of sources in the sky.

Figure 2.3 shows $P(D)$ for the simulated 8.6 GHz observations as well as $P(D)$ at 4.8 GHz, derived by re-scaling the 8.6 GHz simulations (since antenna resolution is proportional to wavelength). Table 2.1 presents the same results and also provides values for D_1 and D_2 at both wavelengths.

A strong, 2.0 Jy, radio source was considered in the above simulations. However the majority of the survey sources are weaker than this and so it is important to

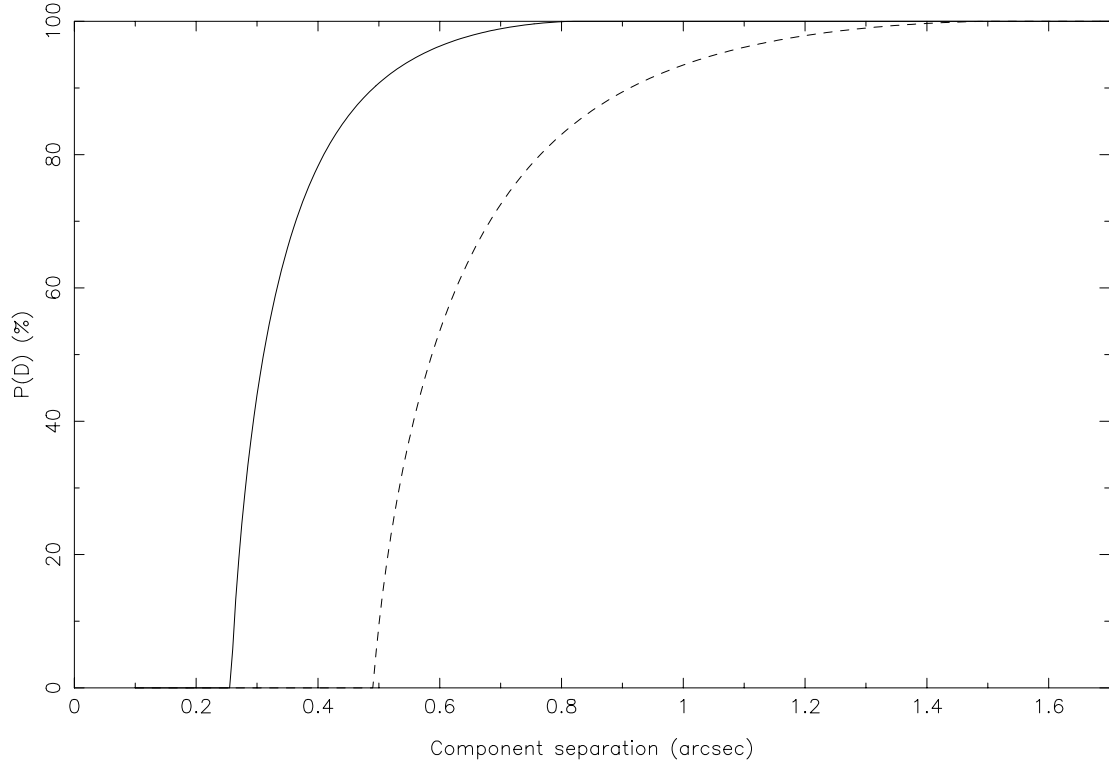


Figure 2.3: Estimated ATCA detection efficiency for compact double sources at 8.6 GHz (solid line) and 4.8 GHz (dashed line).

Table 2.1: Estimated ATCA detection efficiency for compact double sources for various values of $P(D)$.

$P(D)$ (%)		$D_{8.6 \text{ GHz}}$ (arcsec)	$D_{4.8 \text{ GHz}}$ (arcsec)
0	$P(D_2)$	0.25	0.50
40		0.30	0.56
80		0.41	0.76
90		0.49	0.91
99		0.71	1.30
100	$P(D_1)$	0.82	1.50

determine if the efficiency of the survey is in anyway changed for fainter sources. This was done by simulating a portion of data identical to that used above except with much weaker flux densities and then carrying out the model fitting procedure to determine D_m . A 0.1 Jy source was simulated consisting of two compact components of equal flux density with position angle 0° at a declination of -40° . The value determined for D_m in this case was entirely consistent with the value obtained for a 2.0 Jy source. This suggests that the compact component separation limitations are applicable over the entire flux density range of the survey.

Spectral Index

An important parameter that must be determined when classifying an object as a gravitational lens candidate is the spectral index of each image sub-component. Such a measurement is not possible unless the sub-component in question is resolved by the ATCA at both frequencies. Therefore the limiting resolution for a compact double gravitational lens candidate identification is defined by the angular resolution at 4.8 GHz, rather than at 8.6 GHz.

Compact Component Flux Densities

Similar simulations to those described above were made for a source with two compact components, one with a flux density of 1.0 Jy and the other with a weaker flux density at a position angle of 0° . The response of the ATCA to such a source with various declinations and component separations was investigated to determine the minimum flux density the secondary component could possess and still be reliably detected.

The results from these simulations for fifteen combinations of component separation and declination are given in Table 2.2. For each simulated dataset, the Difmap imaging software (Shepherd, 1994) was used to fit a point source to the brightest point in the dirty map. Once this had been done, the residual map (*i.e.* the dirty map with the 1 Jy point source removed) was examined for evidence of the weaker secondary. The secondary was considered detected when it appeared brighter than the noise in the residual map. Once again, this table shows that the sensitivity of the survey is dependant on source declination. For large component separations (~ 2 arcsec or greater) the minimum detectable flux density is 2.6 to 5.8 mJy, but as separations decrease, the ATCA no longer clearly separates the components and the flux density detection limit increases. It is also apparent that this increased detection limit remains significant for larger separations as declinations become more equatorial. This behaviour is consistent with that seen above for equal compact doubles.

Further simulations at $\delta = -25^\circ$ were made to estimate the separation at which the minimum detectable secondary flux began to increase. The separation was found to be 1.5 arcsec. It is important to note that the selection process that lead to Table 2.2 assumed some *a priori* knowledge about the source structure so the minimum detectable flux estimates shown here are possibly optimistic. The off-source noise in a typical clean map was 0.85 mJy per beam rms. In order then

Table 2.2: Minimum detectable flux density in mJy for a weak compact core near a 1.0 Jy compact core, position angle is 0° .

Separation (arcsec)	Declination (degrees)		
	−25	−50	−75
0.5	51	15	11
1.0	13	6.0	5.0
2.0	5.8	4.0	3.6
4.0	3.6	4.4	5.8
8.0	5.2	3.8	2.6

for a compact component of unknown position to be unambiguously detected, a minimum flux density of 6 mJy, or 7σ , was imposed.

Low Declination, North-south Compact Doubles

The most difficult type of compact double to detect in this survey is one that lies close to all the detection limits. Such a source would possess a small component separation (~ 1 arcsec), a weak secondary component flux density (~ 10 mJy), a relative component position angle near 0° and a declination close to -20° . For this case, there may be only one or two cuts, near source rise and set, that clearly resolves the two components so a successful detection relies on, at most, two one-minute observations. If these vital cuts are not made close enough to source rise or set, or if the data is of poor quality (as can be the case at low elevations) then it is possible that the survey detection limits will be worse for such a source.

Sources of this type were indeed detected in the sample and they are described in Chapter 3, Section 3.4.3.

Multiple Compact Components

The simulations described above have investigated the response of the survey to compact double sources only. However the results can be used to draw some conclusions regarding the effectiveness of the survey in detecting three (or more) compact components, as might be expected in close-alignment gravitational lenses. Clearly, if at least two components are separated from the others by more than D_m then it will be possible to measure the spectral indices of those components and the object will be classified as a candidate gravitational lens. Furthermore, an object may also be considered as a candidate in the case where all components are too closely spaced to be unambiguously resolved but the source is nevertheless extended and flat-spectrum.

Extended Structure

The simulations described above have determined survey limitations for isolated compact structures only. It is likely that in many cases, sources with compact

structure will also possess a certain amount of extended, steep spectrum structure. If this extended structure is close to a compact component then it may appear to be part of that component or add confusion to the image. This is likely to raise the minimum detectable flux density limit.

Considered here is the response of the ATCA to an Einstein ring. A simulated dataset was created using a model consisting of a circular 0.35 Jy ring of diameter 5 arcsec, well within the sensitivity limits of the survey. This hypothetical source has been placed at a declination of -45° and four 8.6 GHz datasets created: the first represents a continuous 12 hr synthesis whilst the other three simulate the effect of sampling the $u-v$ plane for one minute every 2, 3 and 4 hr respectively.

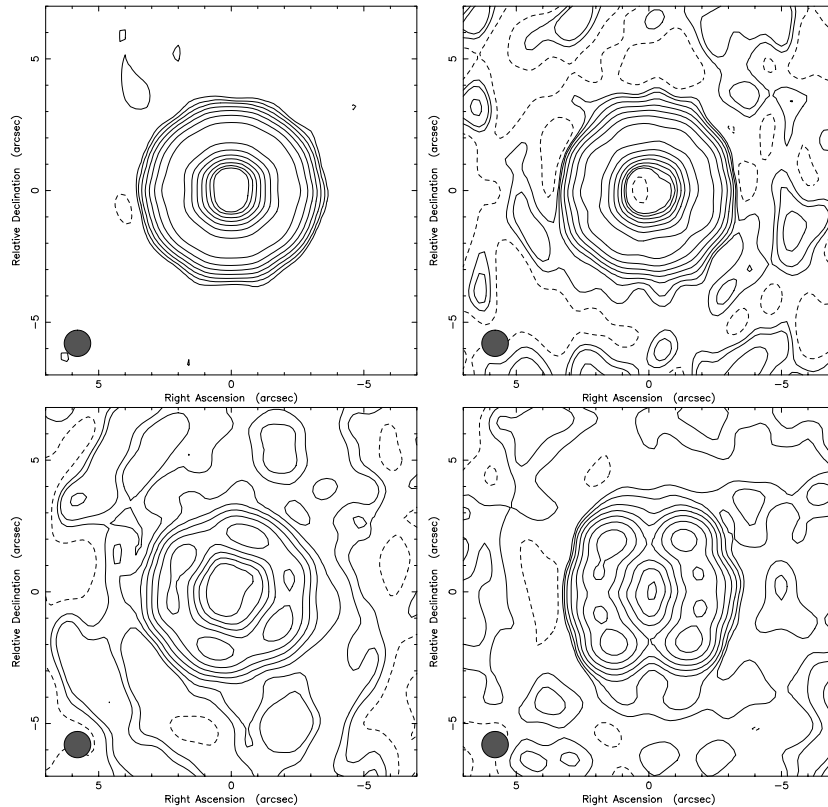


Figure 2.4: Images from simulated observations of a 5 arcsec ring. The top left panel shows a map made from a full synthesis, the top right, lower left and lower right panels show maps made from cuts observations where the $u-v$ plane has been sampled once every 2, 3 and 4 hr respectively. In all cases, the contours are $-1, 1, 2, 4, 8, 16, 32$ and 64% of the peak flux density which is 29 mJy. The restoring beam is circular with a FWHM of 1.0 arcsec.

Figure 2.4 shows the images produced from these datasets. The top left hand panel shows the image from a complete synthesis and clearly demonstrates the ability of the ATCA to faithfully reproduce the source structure. The top right hand panel in this figure shows a map made from the simulated cuts data with one cut every two hours, the chosen sample rate for the survey. Once again, a ring is clearly detected with no significant structural differences to the complete synthesis image that might be expected from a sparse sampling of the $u-v$ plane. The main difference between the two maps is the poorer signal to noise ratio in

the two hour cuts map, which is expected from a much shorter total integration time (7 min compared with ~ 700 min).

The lower left and lower right panels clearly demonstrate the effects of observing this type of structure at larger sample intervals. By increasing the sample rate to one every three hours the ring structure appears to break up and one can begin to see the effects of individual cuts. When the sample interval is increased to four hours, a lot of the structural information is lost and the image becomes difficult to recognise as a ring. Furthermore, such under-sampling would make spectral-index measurements less reliable.

Coincidental Associations

The number of radio sources in the sky increases sharply as flux density decreases. The relationship is approximately $N(S)ds \propto S^{-\alpha}$ where α is between 2.0 and 2.5 (Wall, 1994). Therefore, as the flux density cutoff of a survey decreases, the radio source surface-density count increases and the chance of finding two nearby but unrelated sources also increases. It is important to understand the implications of this to gravitational lens surveys which are searching for nearby but related sources.

The density of radio sources at 5 GHz with flux densities stronger than 6 mJy (the minimum detectable component flux density in this survey for well separated compact sources) is 4×10^4 sterad $^{-1}$ (Wall, 1994). The area of sky within r rad of a radio source is πr^2 for small r . Therefore the predicted number of sources in this sample of 461 with an unrelated source stronger than 6 mJy within r rad of it is

$$N = 461 \times (4 \times 10^4) \times (\pi r^2) \quad (2.4)$$

Except for cluster lenses, all known gravitational lenses have component separations of less than 10 arcsec (Keeton and Kochanek, 1996). The predicted number of sources in this sample with an unrelated source within 10 arcsec of it is 0.1. Moreover, the proportion of flat-spectrum sources in the radio source population is less than ~ 0.35 (Wall and Peacock, 1985) and decreases with flux density. Therefore the predicted number of unrelated flat-spectrum sources with separations of less than 10 arcsec in the sample is less than 0.035 so it can be stated with confidence that any gravitational lens candidates found in the survey are likely to be real and not chance associations.

An estimate is now made on the upper limit on the separation of multiply imaged components that can be detected in the present survey. This is done by considering the chance of detecting an unrelated flat-spectrum source in the field of only one of the sources in the sample at the 5σ level. The number of chance coincidences in the survey would then be $N = 5\sigma = 1$, therefore $\sigma = 0.2$. Applying equation 2.4 gives a component separation of 12 arcsec for all sources regardless of spectral index and 20 arcsec for flat-spectrum sources if they constitute 35% of the extragalactic radio source population. Therefore, based on coincidental association arguments and within other limitations stated in this chapter, the survey is complete for all gravitationally lensed flat-spectrum sources with image separations of less than 20 arcsec.

Maximum Detectable Compact Component Separations

The ATCA observations were made at the widest possible bandwidth, 128 MHz, to provide maximum sensitivity. All the channels in the band were averaged together to reduce the size of the dataset and speed the processing stage. This means that a single (u, v) coordinate and a single frequency is assigned to each visibility, resulting in a loss in information (as u and v change across the band). This averaging results in a radial smearing of the source brightness distribution which worsens with source distance from the phase centre - an effect known as “Bandwidth Smearing” (Walsh and McKay, 1996). This smearing will reduce the peak amplitude of a source as well as elongating its morphology. This means that secondary compact objects, especially weak ones on the limits of detectability, may not be detected if they are well removed from the phase centre. Another consequence of bandwidth smearing is that the two observing frequencies are affected differently: as distance from the phase centre increases, the measured peak amplitude decreases more rapidly at 8.6 GHz than at 4.8 GHz. This means that spectral index measurements become less accurate as separation increases. A maximum source separation was chosen so that the measured peak flux density in a component was at least 90% of its true flux density. This corresponds to a maximum separation of 50 arcsec at 4.8 GHz and 45 arcsec at 8.6 GHz.

Although flat-spectrum components can be detected for all fields out to 45 arcsec, they can only be confidently assumed to be lensed images of the same background source if their separation is less than 20 arcsec. This argument is based on the previous discussion on coincidental associations.

Compact Component Flux Density Ratio Limits

An important quantity to understand in any lensing survey is the range of compact component flux density ratios to which it is sensitive. This is estimated by assuming a simple compact double source in which the components are well separated (*i.e.* separation is greater than 1.5 arcsec) and there is no extended structure. The flux densities of the two components are defined to be S_1 and S_2 where $S_1 \geq S_2$, the flux density ratio is $R = S_1/S_2$ and the total flux density of the source is $S_T = S_1 + S_2$. Now R will be at a maximum when S_2 is the smallest detectable flux density, *i.e.* $R_{\max} = S_1/(6 \text{ mJy})$. The largest flux density ratio for which all compact doubles are detectable in the survey is therefore defined as the *minimum* value of R_{\max} and it occurs when S_T is at a minimum.

The minimum value of S_T may be estimated from the lower flux density limit of the survey. A general expression for R_{\max} when S_T is at a minimum, given a sample of radio sources with a lower flux density limit of S_L Jy at ν_L GHz is

$$R_{\max} = \frac{\min(S_T) - S_{\min}}{S_{\min}} = \frac{S_L \left(\frac{\nu_o}{\nu_L} \right)^\alpha - S_{\min}}{S_{\min}}$$

where ν_o is the ATCA observing frequency in GHz, α is spectral index and S_{\min} is the minimum detectable flux density at ν_o . For the present survey, $S_L = 0.34$ Jy at $\nu_L = 2.7$ GHz, $S_{\min} = 6 \times 10^{-3}$ Jy (as derived previously). A flat-spectrum

source with $\alpha = -0.5$ is considered as it defines the lower limit for $\min(S_T)$ as objects with flatter spectra will have larger flux densities. Applying these assumptions to the above equation provides $R_{\max} = 43$ at $\nu_o = 4.8$ GHz and $R_{\max} = 32$ at $\nu_o = 8.6$ GHz. In the case of a gravitational lens where the background source is an isolated compact core, R is expected to be the same at both frequencies and so it must be measurable at both frequencies. Therefore the survey is complete for flux density ratios in the range 1 to 32 for flat-spectrum compact double sources within the other sensitivity limits of the survey.

2.2.2 Conclusions

The simulations have shown the sensitivity of the ATCA survey to compact structure and to extended structure that might be expected in a gravitationally lensed radio source. *In particular, the survey is capable of resolving and determining spectral indices of all compact doubles with separations greater than 1.5 arcsec and less than 45 arcsec and with individual flux densities greater than 6 mJy. The survey is complete for flux density ratios of less than ~ 30 for these sources but only for compact flat-spectrum components with separations of less than 20 arcsec.* The flux density limit may be greater in the presence of broad, weak, extended structure. Moreover, the survey is sensitive to compact structure at 8.6 GHz for all compact sources with separations greater than 0.82 arcsec. Therefore sources with compact components between 0.82 and 1.5 arcsec in separation may be identified as marginal gravitational lens candidates. The simulations have also shown the survey to be capable of reliably detecting large Einstein ring-like morphology provided a sample rate of one cut every two hours is achieved. Arguments based on radio source population statistics have shown that the probability of a chance coincidence of two unrelated sources (that might be interpreted as a gravitational lens) is suitably low.

Chapter 3

Gravitational Lens Candidates from the ATCA Imaging Survey

3.1 ATCA Observations and Imaging

The ATCA observations were made at 4.80 and 8.64 GHz ($\lambda = 6$ and 3 cm respectively) with a bandwidth of 128 MHz and the four linear polarisation products XX, YY, XY and YX. Each observing session was conducted with the array in a 6 km configuration; either 6A, 6B, 6C or 6D, thus providing consistent resolution at each epoch. During each observing session, scheduling was carried out so that all observations for each chosen source were completed in one observing session. This was done to avoid problems that might arise due to changes in the flux density of a particular source or changes in the configuration or response of the ATCA between observing sessions (typically several months). This method also simplified the data processing stage as all observations for a given program source were contained within a single dataset. Each observing session at the ATCA was divided up into one or more 12 hour blocks within which a group of sources was to be fully observed with at least one 60 sec cut per source every two hours. Each group was selected so that all the sources within it lay within ~ 30 degrees on the sky and all passed north or south of zenith at the ATCA at transit, thus avoiding the need for long azimuth slew times.

PKS 1934–638 was chosen as the primary flux density calibrator for all of the observations. All data were calibrated on the assumption that the primary calibrator, PKS 1934–638 has a flux density of 5.83 Jy at 4.8 GHz and 2.84 Jy at 8.64 GHz (Reynolds, 1990). Position calibrators were chosen so that they were in the same part of the sky as the group of program sources being observed. It was especially important that they were point sources at the arcsecond resolution achieved by the ATCA and that their positions were well known so that accurate measurements could be made of the program source positions. Wherever possible, they were drawn from a list of sources that had positions derived from VLBI astrometry observations (Reynolds *et al.*, 1994; Johnston *et al.*, 1995).

The program and position calibrator sources within each group were scheduled such that the antenna slew times were kept to a minimum thus maximising the

number of observable program sources in the group. This observing method allowed for ~ 30 program sources to be observed with a single cut within two hours with a secondary calibrator observed for 180 sec every ~ 20 min. Such a method allowed the entire sample to be observed in approximately eight full days. It also allowed accurate positions to be measured.

Table 3.1 displays the dates that survey observations were made and the number of sources observed. A hardware problem at the ATCA irretrievably corrupted the data that were collected in February 1994, however the affected sources were successfully re-observed in the observing session held in September of that year. Analysis of the data between observing sessions showed that some objects required re-observation due to poor data quality. Those objects were re-scheduled in following sessions. Four of these sources remained outstanding after the September 1994 observations and they were re-observed in November 1995 as part of other non-survey observations.

Table 3.1: A summary of the ATCA cuts observations.

Date	Allocated time (hr)	Number of Program Sources Observed
March 1993 [†]	48	86
July 1993	24	74
November 1993	60	145
February 1994	55	0 [‡]
July 1994	12	33
September 1994	65	128
November 1995	39	4 [*]

[†]This session was shared with two other proposals.

[‡]An ATCA hardware problem corrupted the data. Observations were repeated in September 1994.

^{*} Repeat observations of these sources, see text.

All the data were edited and calibrated using the AT AIPS (Astronomical Image Processing Software), a version of the NRAO software package AIPS modified to handle ATCA data. Imaging of the data was done with the difference mapping program Difmap (Shepherd, 1994), part of the Caltech VLBI package (Pearson, 1991) which uses the CLEAN deconvolution procedure (Högbom, 1974).

3.2 Identification of Gravitational Lens Candidates

Once the program source observations are completed, the data must be analysed so that all possible gravitational lens candidates are recognised. It is important

that such “filtering” is efficient so that no candidates are missed within the limits of the survey, though it does not matter if non-lenses are also selected. Any prospective candidate must possess more than one compact flat-spectrum component and/or a feature resembling an Einstein ring. Although this sample was specifically selected as a flat-spectrum subset of the Parkes Catalogue, many of the objects are likely to possess a steep-spectrum component of the type often associated with extended structure. Such components, if lensed, may form an Einstein ring (*e.g.* PKS 1830–211 (Rao and Subrahmanyan, 1988; Subrahmanyan *et al.*, 1990; Jauncey *et al.*, 1991) and MG 1654+1346 (Langston *et al.*, 1989)), so it is important to identify them.

3.3 Candidate Selection

This selection process was carried out by examining both the visibility data and the deconvolved image for each object in the flat-spectrum sample.

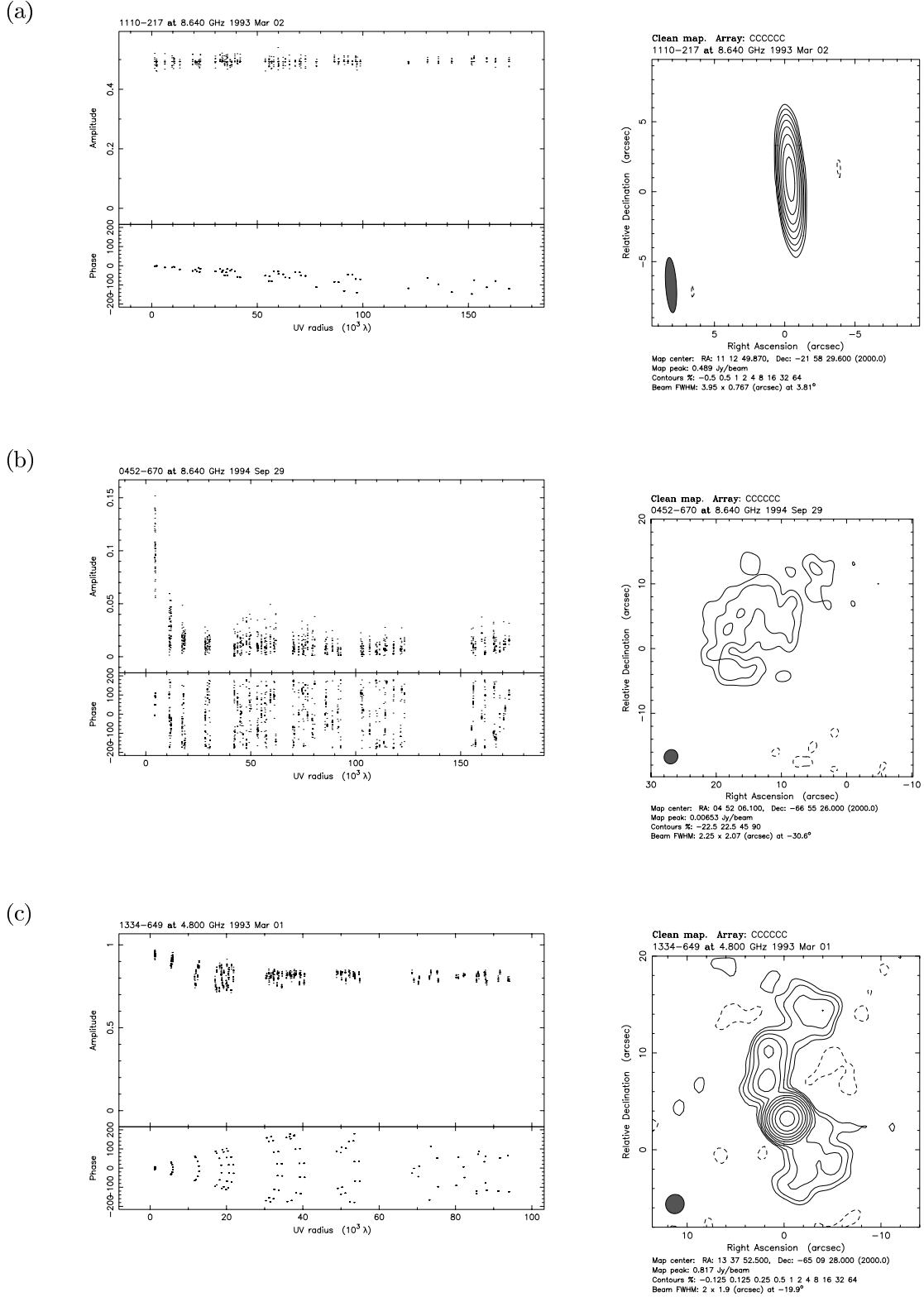
Much information on the structure of a radio source can be obtained from a visual examination of the correlated interferometer visibilities (*e.g.* Fomalont and Wright, 1974). Not only is such an inspection important as a check that the deconvolved image is a good representation of the data but the visibilities can also reveal the presence of structure that is not immediately evident from the image. The visibility data were available on-line during the ATCA observations. Shown in Figure 3.1 are examples of the visibility data collected during the ATCA observations. They represent the four broad classifications of source structure seen in the survey sources. Also shown are deconvolved images of each source.

Figure 3.1a shows the data for PKS 1110–217. The visibility amplitudes for this object are constant for all baseline lengths, indicating that the object is unresolved, whilst the visibility phase changes linearly with baseline length, showing that the object is displaced from the assumed phase centre for this object. The image of this object illustrates these inferences, where the source is displaced 0.97 arcsec from the phase centre at a position angle of -24° (measured north through east).

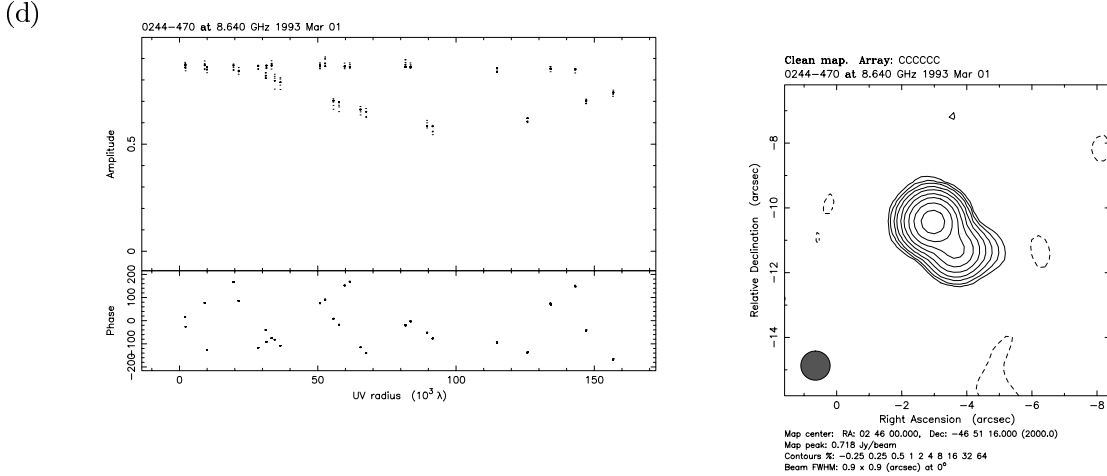
Figure 3.1b shows a very different visibility plot. The visibility amplitudes decrease quickly to the noise level as baseline length increases. This absence of any detectable flux density on the longest baselines and the accompanying random visibility phase indicates the absence of any unresolved components and hence no compact core, as can be seen in the accompanying image. PKS 0452–670 was included in the survey because of its flat-spectrum, but it is clearly a thermal source and is associated with the Magellanic Clouds.

An object that is essentially a combination of the above two examples is shown in Figure 3.1c. The visibilities show amplitudes dropping from ~ 0.95 Jy to a level of ~ 0.8 Jy as baseline length increases. This indicates the presence of some resolved extended structure and an unresolved compact core. The 4.8 and 8.6 GHz images reveal a central 0.8 Jy flat-spectrum core and two weak steep-spectrum regions extended towards the north and south showing S-shaped symmetry. The optical counterpart for this source is coincident with the flat-spectrum core.

Figure 3.1: Examples of visibility data collected during the gravitational lens survey observations (left) and images made with these data (right). The visibility amplitudes and phases are plotted separately against u - v radius.



Examples of ATCA survey data continued...



The visibility plot in Figure 3.1d shows data for just two cuts of a six cut observation to more clearly demonstrate the hour-angle dependant response for a compact double source. The first cut was made when the orientation of the ATCA was approximately perpendicular to the position angle of one compact component with respect to the other. This means that the ATCA is insensitive to double structure and, as there is little other flux density in the field apart from that in the two components, a constant visibility amplitude is seen. However, at a later time the orientation of the ATCA was approximately parallel to the position angle of the two compact components and they are clearly resolved as such in the visibility measurements, the amplitudes of which are seen to “beat”, the minimum amplitude giving the difference in flux density between the two components and the maximum corresponding to the sum. The position of the first null also allows for the separation of the two components to be estimated. The visibilities thus predict a separation of ~ 1 arcsec and fluxes for the two components of ~ 0.72 and ~ 0.16 Jy with a position angle of $\sim 45^\circ$. The accompanying image shows a compact double with position angle of 42° , separation of 1.1 arcsec and component fluxes 0.72 and 0.14 Jy, very close to the parameters inferred from the visibility data. A third, weak component is also detected in the image that was not easily detected in the visibilities. The optical counterpart to this object is a single “stellar” object, probably a QSO coincident with the flat-spectrum component.

All of the survey visibility data were examined for signs of structure containing multiple compact components or extended emission. The selected data were then imaged and inspected for multiple flat-spectrum components, ring-like structure or any other unusual extended structure that suggested gravitational lensing. To check that no lens candidates were missed in this analysis, all sources were imaged using the automatic processing method described in Chapter 4 (Section 4.2). The resulting images were inspected for multiple flat-spectrum components or evidence of gravitationally lensed extended structure. This analysis was especially efficient at revealing weak secondary components that are not readily apparent from an inspection of the visibility data.

3.4 The Gravitational Lens Candidates

As discussed earlier, any radio gravitational lens candidates to be uncovered in this survey can be roughly divided into two categories; multiply imaged compact flat-spectrum sources and lensed steep-spectrum extended structure. For the purposes of this discussion, they will be referred to as “lensed cores” and “lensed jets”. It is useful to further classify the candidates as those that have component flux densities and separations within the detection limits of the survey and those that do not but still possess the characteristics of a gravitational lens. These categories will be referred to as “detected” and “marginally detected” lens candidates respectively.

When candidate lenses lay within the region of sky covered by the COSMOS/UKST Southern Sky Catalogue (Yentis *et al.*, 1992), the catalogue was used to attempt to identify optical counterparts. The STScI Digitised Sky Survey (DSS) (WWW, 1996) was also used, both to confirm the COSMOS identifications, and to provide identification for sources outside the region covered by the COSMOS catalogue.

3.4.1 Detected Lensed Cores

There were several sources in the sample that were found to possess two or more compact components. However, only two, PKS 1830–211 and PKS 0252–549, showed two clearly separated flat-spectrum components. In every other case only one component (usually the brightest) possessed a flat-spectrum and the other component(s) a steep spectral index. For example, in the case of PKS 0244–470 (Figure 3.1d), the NE compact component has a spectral index of 0.20 and the SW component has a spectral index of -0.94 .

PKS 1830–211

Although PKS 1830–211 is already a confirmed gravitational lens, its presence in the survey acts as a test to make sure that no strong, small separation lenses are missed.

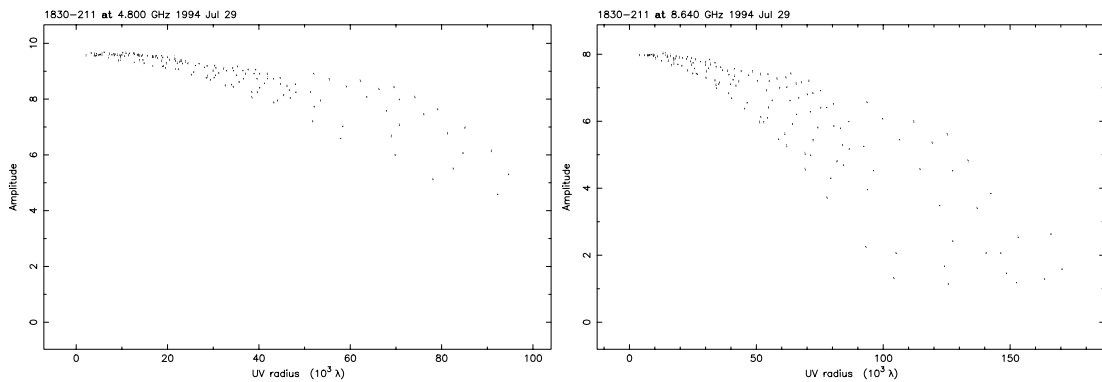


Figure 3.2: Visibility amplitudes (in Jy) for PKS 1830–211 plotted as a function of baseline length at 4.8 GHz (left) and 8.6 GHz (right).

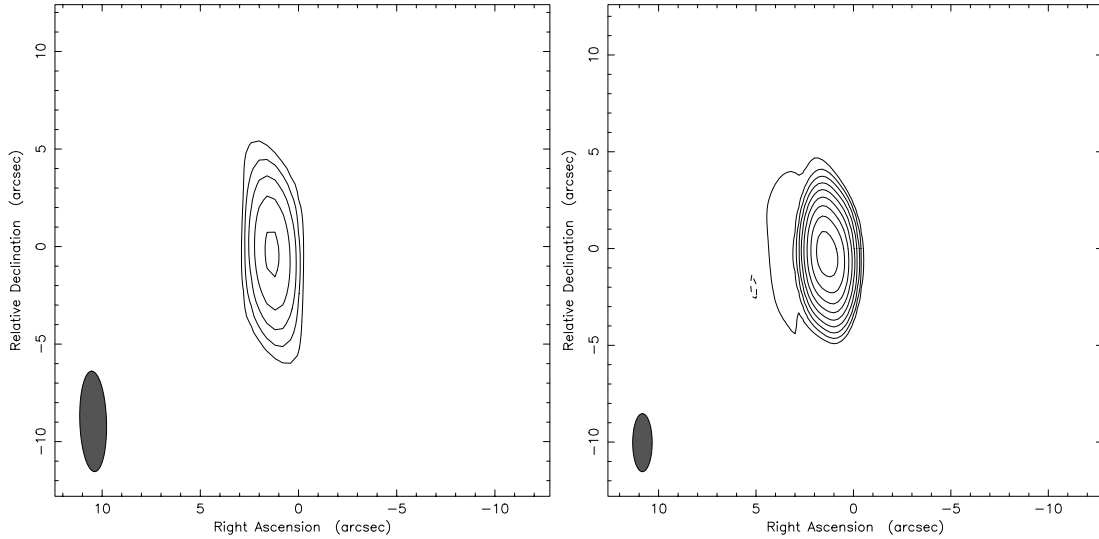


Figure 3.3: 4.8 GHz (left) and 8.6 GHz ATCA images of PKS 1830–211. All contours are multiples (–1, 1, 2, 4, 8, 16, 32, 64, 128, 256, 512) of the bottom contour level which is three times the rms noise level in the map.

PKS 1830–211 is just resolved into a two component source at 8.6 GHz but is only partially resolved at 4.8 GHz as can be seen from the visibility amplitudes in Figure 3.2 and the images presented in Figure 3.3. Despite this, a simple two component model was fitted to the data at 8.6 GHz using the `modelfit` function in `Difmap`. To provide an estimate of spectral index, this model was used to estimate component flux densities at 4.8 GHz by holding the positions and sizes of the model components constant and allowing only the flux densities to change. The spectral indices thus derived were -0.27 ± 0.02 for the NE component and -0.33 ± 0.03 for the SW, making this object a strong candidate gravitational lens, and confirming that it would have been found easily in the survey.

Other properties of this source were studied in detail and are described in Chapters 5, 6 and 7.

PKS 0252–549

PKS 0252–549 is dominated by a compact ~ 750 mJy core with two weaker components, one 8 arcsec to the south (the position angle is 160°) with a peak flux density of ~ 12 mJy and another 7 arcsec to the north (position angle -4°) which is extended and detected only at 4.8 GHz (Figure 3.4). The bright central component has a spectral index of 0.06 ± 0.02 and the southern component has a spectral index of 0.03 ± 0.15 . This object thus has two flat-spectrum components, the spectral indices of which are not significantly different – properties that are consistent with a gravitationally lensed core.

The COSMOS/UKST Southern Sky Catalogue was used to identify the optical counterpart for this source (Figure 3.5). The bright central radio component is coincident, within position error estimates, with an object classified as stellar by the COSMOS catalogue with $M_J = 17.3$. There is a second stellar object in the field approximately 9 arcsec to the south-west of the first with $M_J = 22.0$.

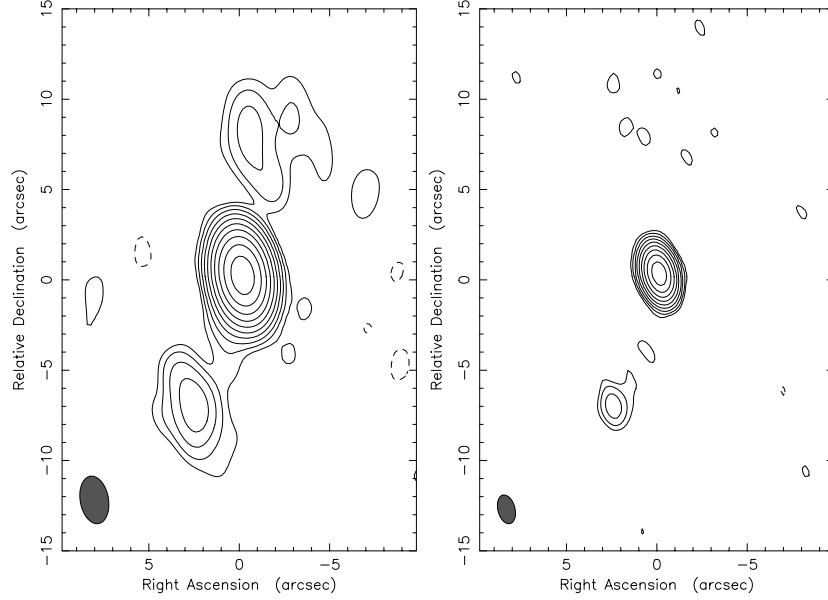


Figure 3.4: The ATCA cuts images of PKS 0252–549 at 4.8 GHz (left) and 8.6 GHz (right). The contours in the 4.8 GHz image are at $-0.125, 0.125, 0.25, 0.5, 1, 2, 4, 8, 16, 32$ and 64% of the peak which is 0.720 Jy and the restoring beam FWHM is 1.6 by 2.7 arcsec at a position angle of 10.0° . The contours in the 8.6 GHz image are at $-0.25, 0.25, 0.5, 1, 2, 4, 8, 16, 32$ and 64% of the peak which is 0.758 Jy and the restoring beam FWHM is 0.9 by 1.6 arcsec at a position angle of 14.5° .

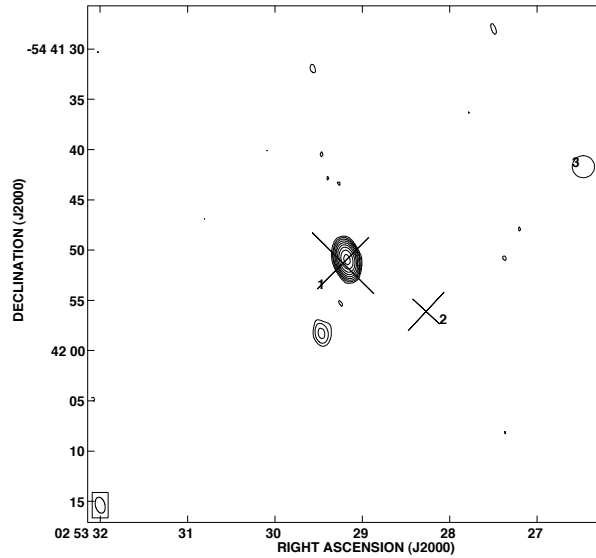


Figure 3.5: The 8.6 GHz ATCA image of PKS 0252–549 with optical counterparts derived from the COSMOS database superimposed. Contour levels are $-0.3, 0.3, 0.6, 1.2, 2.4, 4.8, 9.6, 19.2, 38.4, 76.8$ percent of the peak flux density which is 0.758 Jy. The restoring beam is 0.9 by 1.6 arcsec with position angle 14.5° . Optical counterparts from the COSMOS database are shown as crosses for stellar objects and ellipses for galaxies, their sizes increased by a factor of two to aid the eye. M_J magnitudes for optical components 1, 2 and 3 are $17.3, 22.0$ and 23.5 respectively.

A comparison between the COSMOS catalogue and the corresponding DSS field shows no discrepancies in this case. Therefore, there would appear to be no optical counterpart to the ~ 12 mJy component. The object coincident with the bright central component has been identified as a quasar with a redshift of 0.537 (Jauncey *et al.*, 1978). Gravitational lensing is achromatic and so the optical brightness ratio of the two components must be identical to the radio flux density ratio of $\sim 63 : 1$ *provided the source is non-variable*. If the bright optical component has a visual magnitude of 17.3 then the southern component must be 4.5 magnitudes weaker, *i.e.* $M_J = 21.8$. Such an object, if it exists, may be present in the COSMOS database as is demonstrated by the apparently unrelated 22nd magnitude object also seen in the optical field (labelled as object number 2). However, the presence of an optical counterpart to the 12 mJy compact component can not be ruled out for two reasons. First, if PKS 0252–549 is a variable source (which is likely, given its flat-spectrum) and if it is a gravitational lens, then there will be a time delay between a change in one component and the other which will result in a change in flux density ratio with time. Therefore, it is possible that the optical counterpart to the 12 mJy component was too faint to be detected when the UKST plates were made. Second, the predicted optical magnitude of the weak component is very close to the detection limits of the COSMOS database which is estimated to be complete only to 20th or 21st magnitude (Unwin *et al.*, 1993), so it is possible that the object is missing from the COSMOS database. Clearly there is a need for a deep CCD image of the field to search for the optical counterpart of the weaker of the two flat-spectrum components.

3.4.2 Detected Lensed Jets

As discussed in Section 1.2, the probability that an extended radio feature will be lensed is greater than that for a single compact core. Problems arise however in identifying such lens candidates as there are many more likely and well understood processes that produce similar structure. Although the source selection criteria were deliberately targeted away from objects where steep-spectrum extended structure dominates there are nevertheless many survey objects that possess extended structure (approximately 30% of sources have non-compact structure that contributes more than 5% to the total flux density (Table 4.2), *e.g.* Figures 3.1b, c and e). As a consequence of the problems inherent in identifying such candidates, not all lenses of this type will be identified. Two candidate lensed jets emerged from the survey: PKS 1350–662 and PKS 2321–375.

PKS 1350–662

Figure 3.6 shows the visibility amplitudes for PKS 1350–662, an object that shows the characteristics of a resolved double source (*e.g.* Figure 3.1d) at all position angles. The drop in peak amplitude with increasing baseline also implies a dominance of extended, resolved structure. This indicates rotational symmetry in the source, presumably a ring-like structure, and a separation of ~ 3 arcsec. The accompanying image (Figure 3.7) reveals the ring-like structure and demonstrates

the ability of cuts observations to detect such structure.

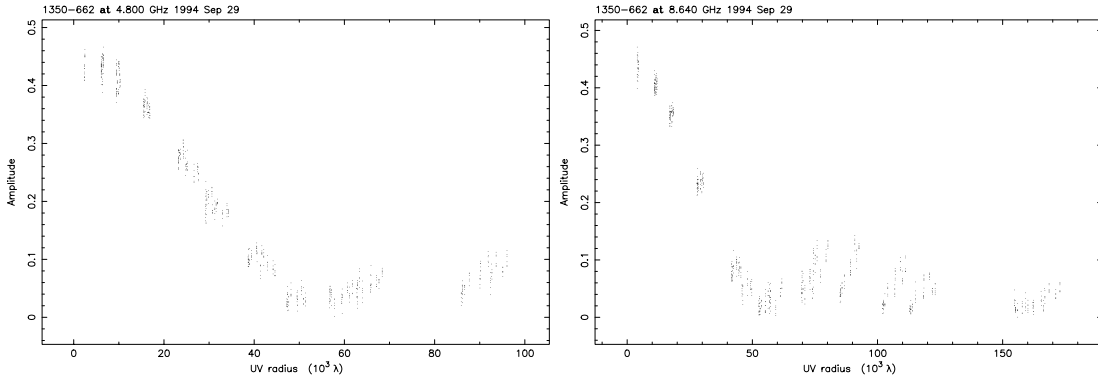


Figure 3.6: Visibility amplitudes (in Jy) for PKS 1350–662 plotted as a function of baseline length at 4.8 GHz (left) and 8.6 GHz (right).

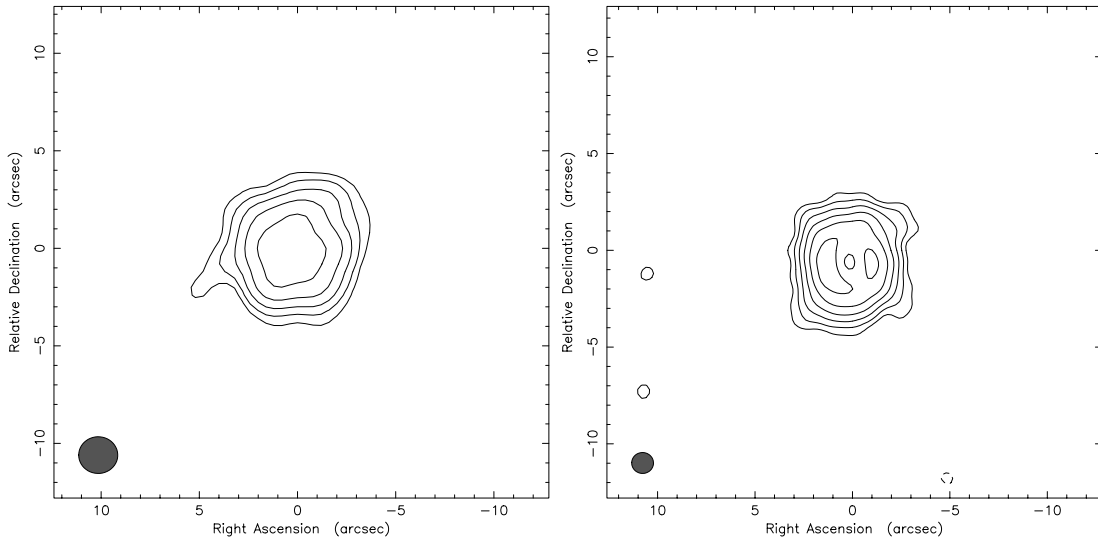


Figure 3.7: 4.8 GHz (left) and 8.6 GHz ATCA images of PKS 1350–662. All contours are multiples (–1, 1, 2, 4, 8, 16, 32, 64, 128, 256, 512) of the bottom contour level which is three times the rms noise level in the map.

Based on the radio observations, this source is a strong Einstein ring/gravitational lens candidate. Despite the excitement of finding this source, the ring-like structure which was apparent whilst examining the visibility data during the observations, the position of this object was found to be coincident with a Planetary Nebula. The object is, unfortunately, not an Einstein ring. Its discovery does however make clear the survey’s ability to find and recognise ring-like structures.

PKS 2321–375

An ATCA image of PKS 2321–375 is shown in Figure 3.8. It consists of a bright, ~ 0.5 Jy core with an inverted spectrum (spectral index is 0.2) and an easterly steep-spectrum jet (spectral index ~ -1.5) at a position angle of 70° that has a peak flux density of ~ 9.4 mJy at 4.8 GHz. Also visible in the 4.8 GHz image is a

slightly extended ~ 4 mJy steep-spectrum component 10 arcsec from the core at a position angle of 108° . This object has the appearance of a lensed jet where the lens lies somewhere between the jet and the weak component 10 arcsec from the core. Optically, this object has been identified as an 18th magnitude quasar with a redshift of 0.37 (Osmer and Smith, 1980). This identification was confirmed based on the coincidence of the accurate sub-arcsecond positions derived from the ATCA observations and the COSMOS database.

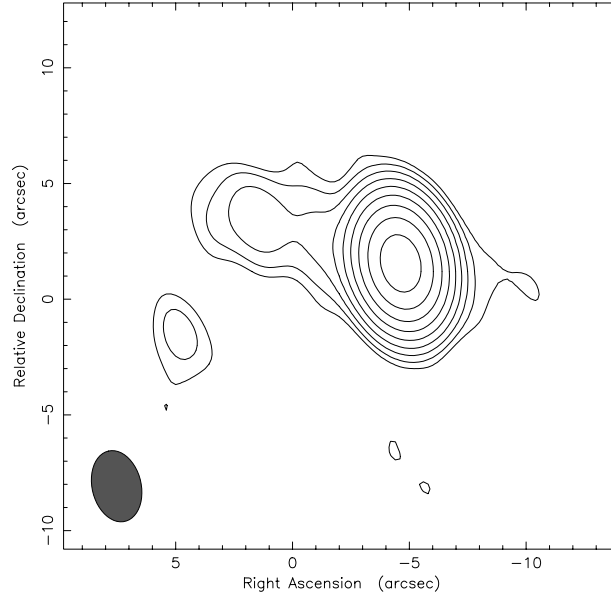


Figure 3.8: 4.8 GHz ATCA image of PKS 2321–375. Contour levels are $-0.25, 0.25, 0.5, 1, 2, 4, 8, 16, 32$ and 64 percent of the peak flux density which is 0.521 Jy. The restoring beam is 2.1 by 3.1 arcsec with position angle 13.0° .

The radio image suggests gravitational lensing as a possible cause of the second steep-spectrum component. If this were the case, one would expect to detect a foreground lensing object with a redshift of less than 0.37. The absence of a potential lensing object in the COSMOS database suggests that the extra feature may be an unrelated background (or foreground) object, or that the lensing mass is dark. The probability of detecting an unrelated source within a certain angular separation of another in this survey has already been discussed in Section 2.2.1. This analysis predicts that the number of sources in the sample with unrelated components within a 10 arcsec radius stronger than 5 mJy at 5 GHz is 0.1. The predicted number of chance coincidences within 10 arcsec is an order of magnitude less than the number found making this object a good gravitational lens candidate providing the extra component is not in some way related to the jet seen in the image. Long integration radio imaging is required to search for any association between the extra component and the jet, which would rule out the lensing hypothesis. If no association is detected then a deep CCD image of the field is required to search for signs of a lensing galaxy.

3.4.3 Marginally Detected Lensed Cores

Several sources in the sample possess small-separation components that are resolved at 8.6 GHz but not at 4.8 GHz. In such cases, simple point source model components were fitted to the data and the spectral indices of the components calculated from the flux densities of the model components. A number of other sources showed a dominant compact flat-spectrum core and a very weak secondary that is close to but below the detection limits of the survey. These sources are gravitational lens candidates but because they fall outside the nominal detection limits they are not included in the statistics.

PKS 0253–754

This object would appear to be a ~ 1.0 arcsec double (Figure 3.9). The brightest component has a flux density of 0.2 Jy and a spectral index of -0.25 ± 0.01 whilst the secondary component is below the flux density detection limits of the survey, being 4.9 mJy at 4.8 GHz and 3.8 mJy at 8.6 GHz, giving a spectral index of -0.4 ± 0.3 . The position angle of the secondary is 164° at 8.6 GHz and -180° at 4.8 GHz. The optical identification for PKS 0253–754, as derived from the COSMOS database, has a magnitude of $M_J = 23.0$ and is classified as “too faint” to be identified as a stellar or galaxy-like object. If this optical counterpart corresponds to the lensed image as seen in the radio, the secondary would be very faint ($B_J = 27$), making an optical verification difficult.

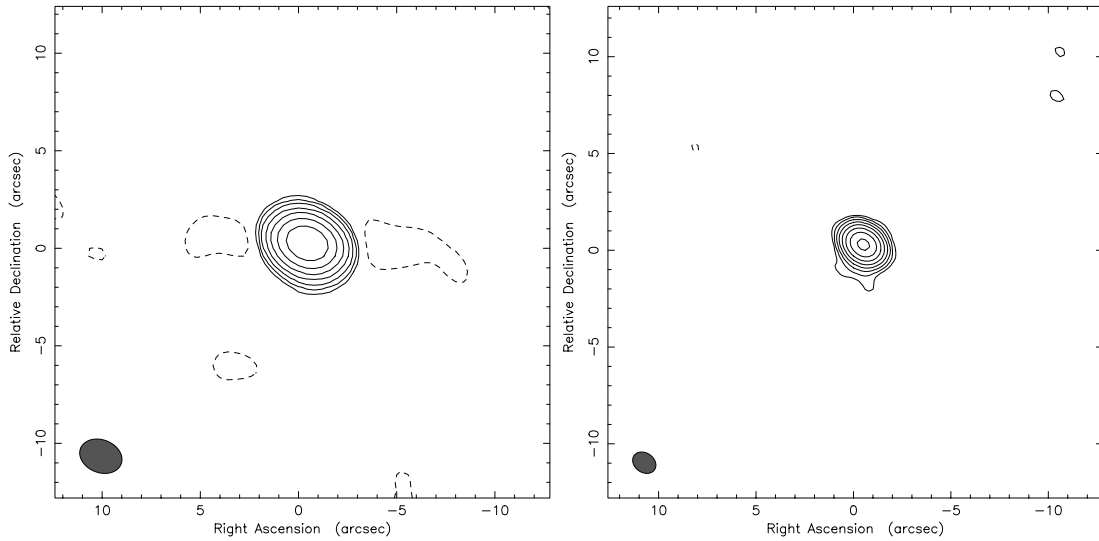


Figure 3.9: 4.8 GHz (left) and 8.6 GHz ATCA images of PKS 0253–754. All contours are multiples (–1, 1, 2, 4, 8, 16, 32, 64, 128, 256, 512) of the lowest contour level which is three times the rms noise level in the map.

Although a full synthesis imaging observation with the ATCA would help to verify the existence of this secondary component, higher resolution radio observations are needed to clearly separate the components and measure their spectral indices. The secondary is weak but it may be possible to detect it using a VLBI array containing two large antennas (*e.g.* the Parkes 64 m and Tidbinbilla 70 m

antennas) at 2.3 GHz with the new S2 recording system (Wietfeldt *et al.*, 1991) now available in Australia. Also, the ATCA is soon to be fitted with 22 GHz receivers and an image at this frequency would clearly separate the two components and therefore help in verifying the candidacy of this object.

PKS 0451–282

PKS 0451–282 appears as a ~ 3.5 arcsec double with the two components having a flux density ratio of approximately 80:1, the weaker component being ~ 20 mJy at a position angle of -12° at 8.6 GHz (Figure 3.10). Whilst the separation and flux density of the weaker component put this source within the detection limits of the survey, this source is relatively close to the equator, has a north-south orientation and the secondary is very weak compared to the bright component making it especially difficult to detect at 4.8 GHz; consequently it can only be classified as a marginal candidate. Model-fitting two point sources to the visibilities at both wavelengths reveals the strongest to have a spectral index of -0.26 ± 0.01 and the weaker component a spectral index of -0.4 ± 0.3 .

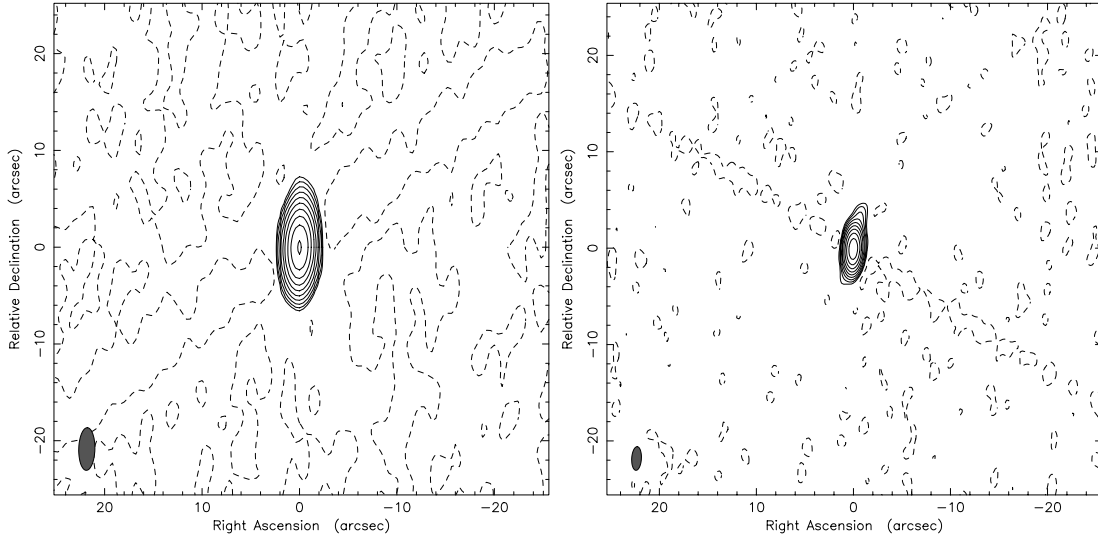


Figure 3.10: 4.8 GHz (left) and 8.6 GHz ATCA images of PKS 0451–282. All contours are multiples (–1, 1, 2, 4, 8, 16, 32, 64, 128, 256, 512) of the bottom contour level which is three times the rms noise level in the map.

PKS 0451–282 was more clearly resolved at 3 and 20 cm with the VLA by Perley (1981) who detected a similar weak component 3.7 arcsec away from a bright flat-spectrum core at a position angle of -10° . The spectral index of the weak component in this case was < -1.0 . In light of this evidence it seems unlikely that this weak secondary is a lensed image and is more likely to be a steep-spectrum jet.

The measurements made at the VLA are not in contradiction with those made in the present survey, however. The difference in identification of the weaker component simply stems from the poorer flux density sensitivity in the ATCA data which results in a large uncertainty in the spectral index measurement of the weaker component.

PKS 2210–257

In common with PKS 0451–282, PKS 2210–257 appears to possess a weak, flat-spectrum secondary component which is determined to have a steep-spectrum in slightly higher resolution images (Figure 3.11). At 4.8 GHz, the brightest component has a flux density of 0.7 Jy and the weaker component is 10 mJy. Both components are slightly weaker at 8.6 GHz, in fact the 8.6 GHz flux density of the weaker component is at the flux density sensitivity limit of the survey, and the derived spectral indices are -0.20 ± 0.02 and -0.3 ± 0.3 for the bright and weak components respectively. At 8.6 GHz the weak secondary is 2.3 arcsec from the bright component at a position angle of 12.2° whilst the separation and position angle at 4.8 GHz is 2.9 arcsec and 18.7° respectively. VLA observations by Perley (1981) at 3 and 20 cm show a 2.3 arcsec separation double with a 10° position angle. The spectral index of the weak secondary as calculated from the VLA data was -1.6 .

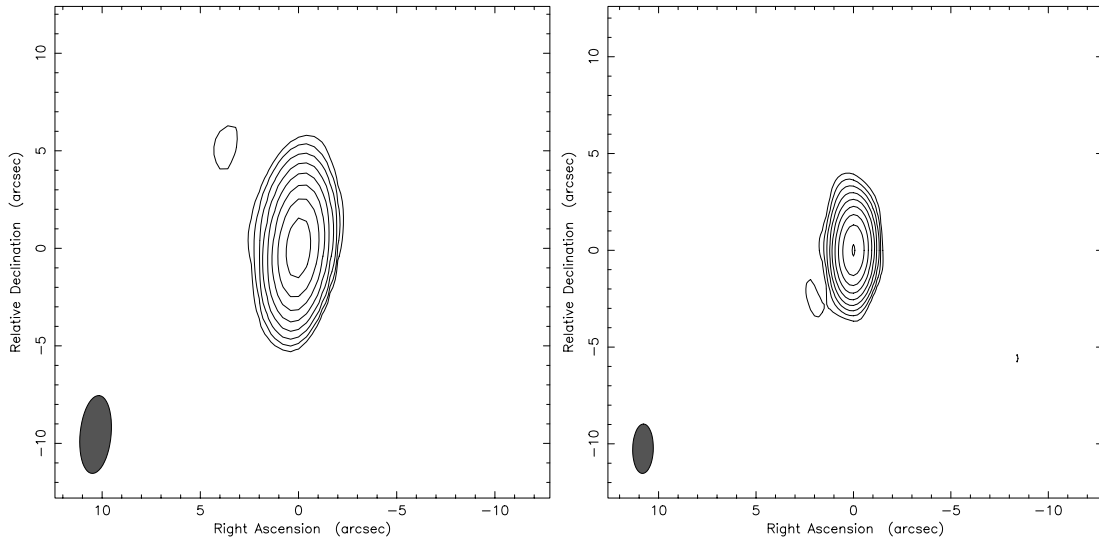


Figure 3.11: 4.8 GHz (left) and 8.6 GHz ATCA images of PKS 2210–257. All contours are multiples ($-1, 1, 2, 4, 8, 16, 32, 64, 128, 256, 512$) of the bottom contour level which is three times the rms noise level in the map.

It is apparent that spectral index estimates from these close separation \sim north-south doubles with one weak component are difficult to determine reliably as was demonstrated in Chapter 2, Section 2.2.

It may not be a coincidence that both PKS 0451–282 and PKS 2210–257 are \sim north-south doubles. In Chapter 2 (Section 2.2.1) it was noted that compact doubles on the limits of detection for this survey may prove difficult to separate, especially if the relative component position angles lie near 0° and the source declination is close to -20° . PKS 0451–282 and PKS 2210–257 lie near the northerly declination limit and as such rely critically on a cut at low elevation to resolve the two components (Section 2.2). In both cases, higher resolution imaging has shown the weaker component to possess a steep-spectrum and this indicates either a small error introduced in the phase calibration of the ATCA data for these sources or an influence from the sidelobes of the strong, nearby companion. A full

12 hr synthesis observation with the ATCA is required to confirm the presence of the weak secondary component.

3.4.4 Marginally Detected Lensed Jets

Some objects on the sample showed weak extended structure very close to a strong, flat-spectrum core. Consequently the extended component is difficult to see in the cleaned image. These sources have been termed “core-halo” as the steep-spectrum extension tends to at least partially surround the flat-spectrum core. Two examples of this type of source are PKS 1236–684 and PKS 1800–660 (Figures 3.12 and 3.13 respectively), both have stellar optical counterparts. The extended structure for these sources might be the result of a gravitationally lensed jet. However, a lensing model that results in an Einstein ring with a flat-spectrum component at its centre is not possible without the flat-spectrum component being multiply imaged.

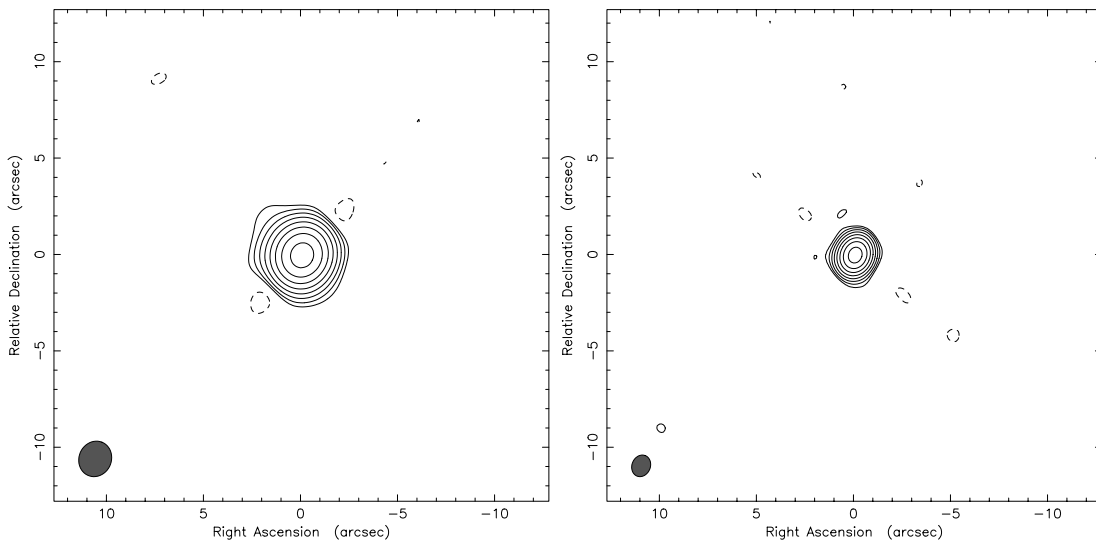


Figure 3.12: 4.8 GHz (left) and 8.6 GHz ATCA images of PKS 1236–684. All contours are multiples (–1, 1, 2, 4, 8, 16, 32, 64, 128, 256, 512) of the bottom contour level which is three times the rms noise level in the map.

These extended regions are more likely to be weaker and more compact versions of the extension seen in the galaxy PKS 1833–772 (Figure 3.14) where there is presumably a small, weak outflow from the flat-spectrum core.

3.5 Lensing Frequency

In Chapter 2 the limitations of the survey for detecting radio gravitational lens candidates were defined. Within these limits, four gravitational lens candidates were detected; PKS 1830–211, PKS 0252–549, PKS 1350–662 and PKS 2321–375. Of these, PKS 1830–211 is already a confirmed gravitational lens and PKS 1350–662 is certainly a planetary nebula and therefore definitely not a gravitational lens. These gravitational lens detections (three with a minimum of one) are shown in

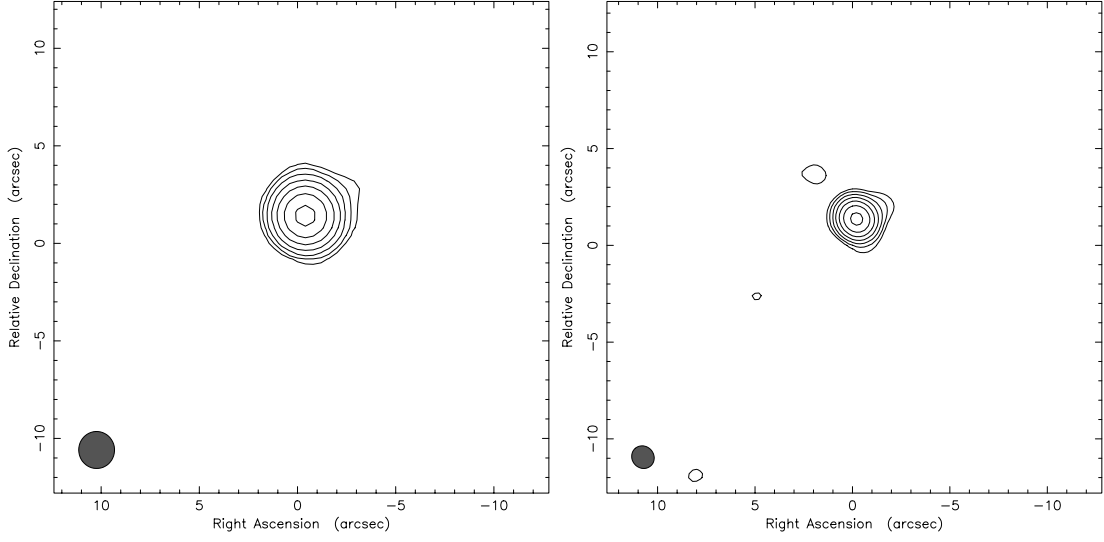


Figure 3.13: 4.8 GHz (left) and 8.6 GHz ATCA images of PKS 1800–660. All contours are multiples (–1, 1, 2, 4, 8, 16, 32, 64, 128, 256, 512) of the bottom contour level which is three times the rms noise level in the map.

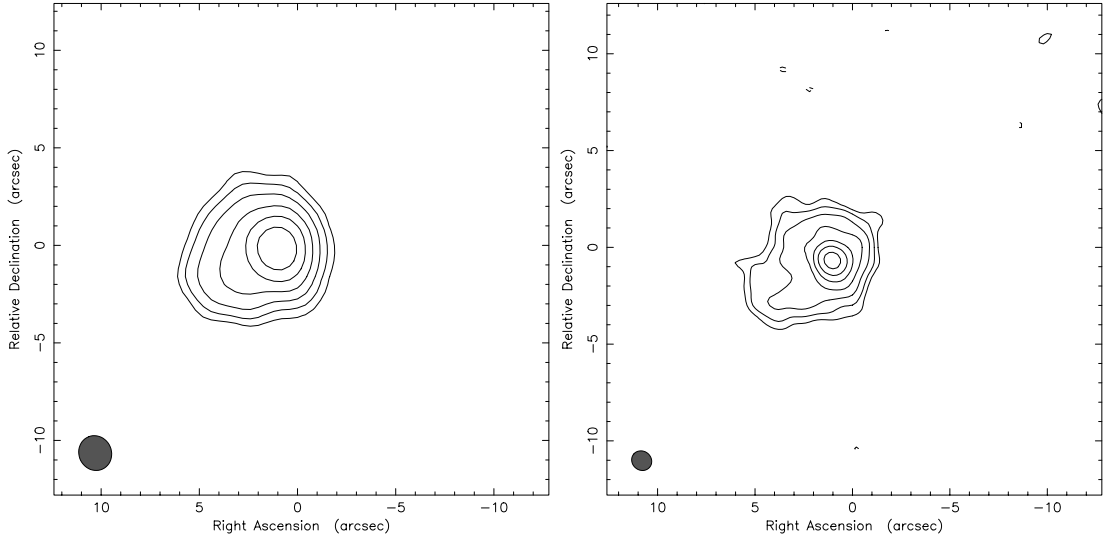


Figure 3.14: 4.8 GHz (left) and 8.6 GHz ATCA images of PKS 1833–772. All contours are multiples (–1, 1, 2, 4, 8, 16, 32, 64, 128, 256, 512) of the bottom contour level which is three times the rms noise level in the map.

Figure 3.15 as a cumulative probability distribution as a function of component separation, assuming PKS 0252–549 and PKS 2321–375 are gravitational lenses. The figure also displays the spatial resolution limits of the survey as well as the lower limit on probability which is 1 gravitational lens in 461 sources or 0.002.

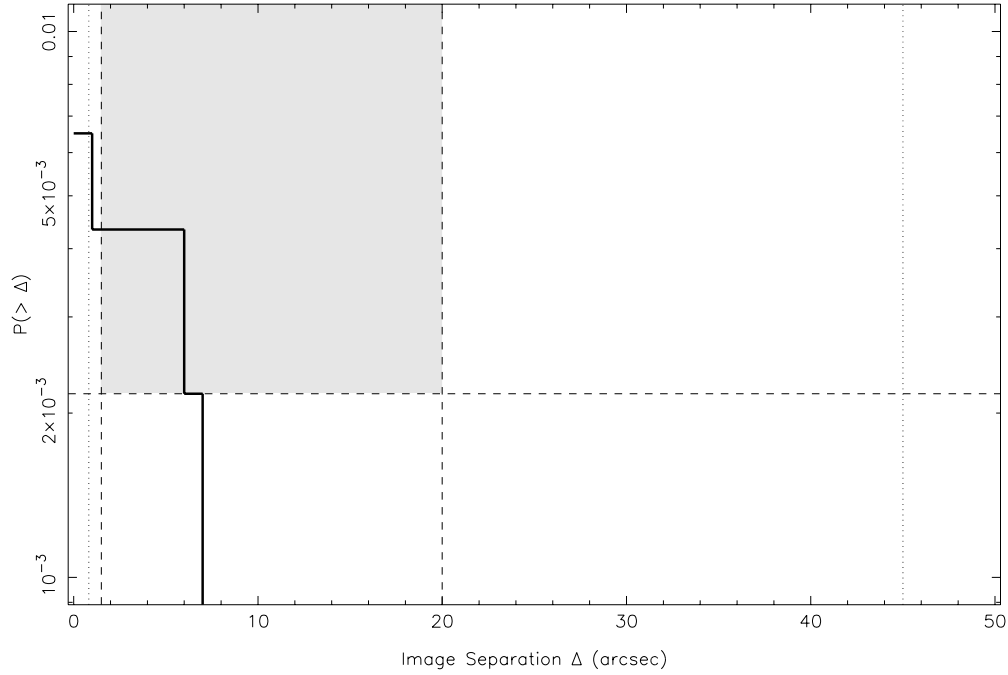


Figure 3.15: The observed gravitational lens cumulative probability distribution for this survey (solid line) assuming the candidates PKS 0252–549 and PKS 2321–375 are indeed gravitationally lensed. Also shown are the detection limits of the survey for component separation. The region of parameter space where the survey is complete (*i.e.* spectral index measurements can be made for compact flat-spectrum components within the survey flux density limits) is displayed as a shaded region bounded by the dashed lines. The vertical dashed lines are the survey completeness limits as discussed in Chapter 2 and the horizontal dashed line indicates a probability of one lens in the sample of 461. The vertical dotted line at a separation of 0.82 arcsec indicates the component separation above which all compact double sources can be resolved at 8.6 GHz. The vertical dotted line at a separation of 45 arcsec indicates the maximum component separation below which objects with multiple compact components can be detected within the flux density limits of the survey but not necessarily determined to be lensed images of the same object.

For comparison, the gravitational lens detections are shown on a plot of the predicted cumulative lensing probability distribution as a function of component separation (Wambsganss *et al.*, 1996) in Figure 3.16. Wambsganss *et al.* investigated the propagation of light rays through a standard cold dark matter universe ($q_0 = 0.5$ and $H_0 = 50 \text{ km s}^{-1} \text{ Mpc}^{-1}$) model with multiple lensing planes. Their predictions are shown for image separations larger than 5 arcsec and magnification ratios of less than 1.5 magnitudes. Also shown in the figure are the cumulative component separation distributions of confirmed or possible multiply imaged quasars from a compilation of all known gravitational lenses up until 1993 (Surdej and Soucail, 1993) and from the present survey, assuming the candidates PKS 0252–549 and PKS 2321–375 are indeed gravitationally lensed. There would

appear to be good agreement between the two observed distributions. The lensing rate of a few tenths to one percent as predicted by the model of Wambsganss *et al.* is consistent with the observations, however the distribution of image separations is in contradiction with the model.

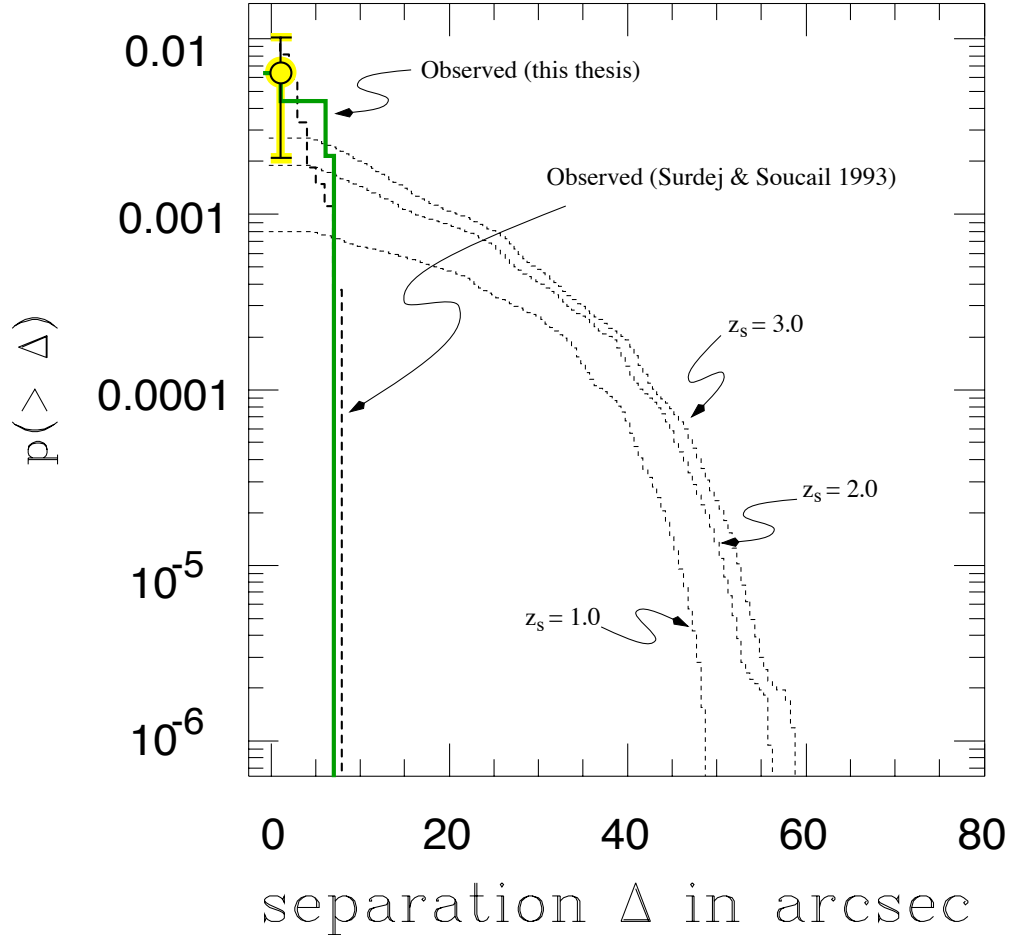


Figure 3.16: Separation of observed lenses in the present survey (circle with error-bars) plotted on the predicted multiple lensing probability distribution as a function of separation of Wambsganss *et al.* (1996) for background sources at $z = 1, 2$ and 3 . The predicted distributions are for images with less than 1.5 magnitudes difference and separations greater than 5 arcsec. The observed gravitational lens cumulative distribution is also shown for this survey (solid line) assuming the candidates PKS 0252–549 and PKS 2321–375 are indeed gravitationally lensed and for all other gravitational lens systems (dashed line) according to Surdej and Soucail (1993).

3.6 Summary

PKS 0252–549 is a very interesting object. From a morphological point of view it would appear to be a double-lobed radio galaxy. However the spectral index of the southern “lobe” is flat and it is difficult to interpret this feature as anything but a gravitational lensed compact core based on the available evidence. A more sensitive ATCA synthesis image is required to confirm the detection of the second

flat-spectrum component and to search for other low-level structure that might reveal evidence of a lensing object. A contemporary, deep CCD image of the field is also needed to search for the optical counterpart to the weak flat-spectrum radio component.

PKS 2321–375 shows evidence of a lensed jet. If there is any physical connection between the jet and the displaced steep-spectrum component, then this object simply displays a “bent” jet and is therefore not a gravitational lens. A synthesis image made using the ATCA will aid in determining this. If the jet and the displaced component appear to be separated then a deep optical CCD image of the field may prove useful in detecting a lensing object.

As well as the gravitational lens candidates found within the limitations of the survey, there were three sources with compact, weak, close separation secondary components that appeared to possess flat spectra. These are the objects that are resolved at 8.6 GHz but not at 4.8 GHz and are therefore below the nominal limits as described in Chapter 2, Section 2.2.2. While they can not be ruled out as gravitational lenses based on the survey data, two of the objects have been imaged with the VLA and they display steep-spectrum secondaries. This indicates the difficulty in imaging and measuring accurate flux densities of very close weak companions, especially for those sources with declinations close to the celestial equator and \sim north-south component position angles.

Several sources were also found to possess a flat-spectrum core surrounded by a steep-spectrum halo. These halos are unlikely to be the result of a gravitationally lensed extended object because they do not have multiply imaged compact cores.

The predicted lensing frequency in radio-selected flat-spectrum source gravitational lens surveys based on these observations (three detections with a minimum of one) is between 0.2 and 0.7%, or one gravitational lens for every 150 to 461 sources. The lensing frequency of the larger and higher spatial resolution JVAS survey (King and Browne, 1996) is close to the lower limit of the present survey, being 0.2%, or one multiply-imaged core-dominated flat-spectrum source in every 440 sources. These results show that a larger sample of flat-spectrum sources is required to detect new examples of gravitational lensing in the southern hemisphere.

Any new southern hemisphere radio gravitational lens search will continue to rely on the ATCA for observations in the foreseeable future. To maintain completeness over a similar dynamic range will require longer integration times on program sources as the flux density limit must be reduced. For example, increasing the flat-spectrum sample to 2000 sources would require a flux density cutoff of $S_{5.0} \approx 100$ mJy for similar declination limits but would require an increase in integration time to approximately 4 min per cut. Such a survey would require ~ 40 days of ATCA observing time.

As well as providing new gravitational lens candidates, this survey has the potential to provide valuable information on the properties of southern flat-spectrum radio sources. This is presented in the following chapter.

Chapter 4

The ATCA Survey: Properties and Statistics

4.1 Introduction

A large complete sample of imaged radio sources such as this can provide valuable statistical information on the properties of flat-spectrum radio sources.

Presented in this chapter are the results of imaging of all of the 461 sources in the sample, together with a review of the types of structures and morphology. The determination of the morphology of all the sources in the sample permits an investigation of the existence of possible correlations between the types of structures seen and the other properties that the sources have in common.

The observations for each source were, in general, made over 12 hours and the survey is sensitive therefore to source variability on this timescale. One new intra-day variable source has been discovered and another that was previously detected (Kedziora-Chudczer *et al.*, 1996) has been verified.

A comparison is made with existing Parkes Catalogue flux density measurements at 5.0 and 8.4 GHz. Such a comparison provides an indication of source flux density variability and structure. It also provides information on any systematic differences between Parkes and ATCA flux density measurements.

Finally, accurate measurement of source positions has allowed optical identifications to be made. In many cases, the initial Parkes Catalogue position uncertainties for these sources were too large to identify a unique optical counterpart, however the ATCA data enable positions to be estimated with sub-arcsecond precision, making possible reliable optical identifications based on radio/optical positional coincidence alone.

4.2 The Automatic Imaging Process

In order for these aims to be realised, it is necessary for a consistent and robust imaging method to be implemented and applied to all sources at both of the observed frequencies. The Difmap software was chosen for this task as it is well suited to imaging this type of data and allows for processing scripts to be written

easily. Such scripts provide an efficient hands-off processing environment where strict rules can be applied to the data in a consistent manner. A **Difmap** script was written to satisfy the following criteria:

- Must attempt to image all emission in the field.
- Must provide a total flux density estimate as well as an estimate of any unresolved ATCA flux density.
- Must report the position of the brightest point of emission in the image.

After calibration within AIPS the data for each source were exported as FITS files, one for each observing frequency. Initially a large 8.5 arcmin field (\sim the primary HPBW) was imaged and then after the extent of the emission had been established, was reduced to the smallest size that still encompassed all the emission. The minimum size allowed was 51 arcsec across. Three imaging methods within **Difmap** were then used; *modelfit*, *clean* and *hybrid*. The *modelfit* method was written with compact sources in mind and attempts to approximate a given brightness distribution by a series of unresolved sources. The *clean* method is designed for any source that consists mainly of extended structure and the *hybrid* method was written to deal with a combination of the above and might be suitable for a source that is dominated by an unresolved core but also possesses extended structure.

Each method was applied in turn to every dataset as described below and the method that resulted in the smallest root-mean-square difference between observed and model visibilities was chosen as the most suitable for the data in question.

1. Method 1: *Modelfit*

This method was designed to image fields containing unresolved point sources only. The position and flux density of the brightest pixel in the dirty map were chosen and a point source fitted using the **Difmap** *modelfit* command (allowing position and flux density of the model to vary). Once the model had converged, phase self-calibration was applied and the *modelfit* command was re-run followed by another phase self-calibration. New point source models were added and fitted as described above until the maximum flux density in the residual map had a smaller amplitude than the most negative flux density, or the residual peak flux density was less than 5 mJy (slightly less than the predicted flux density detection limit for compact doubles (see Chapter 2, Section 2.2.1)), or the number of clean components exceeded 10. These criteria were set so that this method did not attempt to fit extended components that would be better fitted by the other two methods described below.

Once this model fitting sequence had been completed, the map size was reduced to the minimum possible to contain all clean components (but no less than 51 arcsec across), thus reducing the amount of computer memory required and decreasing the processing time. All clean components were removed but the effects of phase self-calibration maintained and the above

model fitting method repeated. This was done because during the first pass through the data there may have been peaks in the map caused by phase calibration errors that the self-calibration removed.

2. Method 2: *Clean*

This method was designed to image sources that contain a large amount of extended structure. All effects of phase calibration from Method 1 were first removed although the previous reduced map size was retained. A “clean box” was placed around and centred on the brightest pixel in the dirty map. This box, which has dimensions chosen equal to that of the clean beam, was used so that clean components were selected only from within it. The dirty map was then cleaned until the first negative component is reached, then phase self-calibration was applied. The clean loop gain was chosen to be 0.02 on the assumption that the source contained very little compact structure. Another clean box of identical dimensions was then chosen in the same way as before and the clean/self-calibration loop was repeated on the residual map. More clean windows were chosen and the flux density within them cleaned and self-calibrated until the maximum flux density in the residual map had a smaller amplitude than the most negative flux density.

All clean components were then deleted but the phase calibrations kept and the above method repeated with a smaller clean loop gain of 0.01.

3. Method 3: *Hybrid*

This part of the processing script was written to image objects that contain a compact core as well as an extended component (a core-jet source for example). The brightest point in the dirty map was chosen to provide the parameters for a point source model which was then fit using `modelfit` as described for Method 1. The remaining data were then imaged using the *clean* method as described above.

The method which resulted in the smallest root-mean-square difference between observed and model visibilities was taken as the final image for each particular source. In the case where the final rms was identical in two or more methods, *modelfit* was chosen in preference to *hybrid* which in turn was selected over *clean* as this order ensures that the simplest method is chosen.

The calibration from the most successful method was re-applied and a single point source was fitted to the dirty map with the starting parameters being obtained from the brightest pixel. This was done in order to estimate the flux density in the source that constitutes an unresolved point source. It should be stressed that this method does not necessarily provide the flux density of the compact, flat-spectrum core, though for the present sample this was mostly the case. For extragalactic sources ($|b| > 10^\circ$) the flux density of the flat-spectrum core was always obtained except for contaminating sources (see Section 4.4.4). If the brightest pixel in the map was associated with an extended steep spectrum component, then that is the component whose flux density was measured. However, this measurement is still useful in distinguishing compact from non-compact sources in the survey. The position of the brightest pixel in the clean map was also determined

with a typical positional precision of ~ 0.04 mas. This was measured from a clean map where the effects of phase self-calibration (which can move the phase centre of an image) had been accounted for.

The uncertainty in source positions measured from these ATCA images comprises a component due to thermal noise, which is proportional to $\sim \text{beamwidth}/(\text{S/N})$ and a component due to systematic effects arising from the phase-referencing. The latter term dominates for strong sources and scales linearly with angular distance between the source and the phase-reference used to calibrate its position. The error is approximately 0.1 arcsec for an angular separation of 5 degrees (Reynolds *et al.*, 1995). For all sources in the sample, the systematic position error never exceeds ~ 0.5 arcsec, the rms adopted for all of the sources. This is based on the maximum separation of a source from its phase calibrator. The source positions were measured so that optical identifications could be made from the COSMOS database which has typical position errors of ~ 1 arcsec. Therefore the optical position errors dominate when making an identification.

In the few cases where the brightest point in the radio map was a steep-spectrum component (*e.g.* one lobe of a classical double or a bright jet in a core-jet), the maps were re-examined at both 4.8 and 8.6 GHz to locate the flat-spectrum component. In cases where there was a classical double and no flat-spectrum core was evident, the likely position of the optical component was estimated to be the midpoint between the two lobes.

The flux densities and positions of all the sample sources, together with other parameters that will be discussed in Section 4.4, are presented in Table 4.5.

4.3 Automatic Processing: Results

Every image produced by the automatic procedure was inspected to search for data that had not been correctly processed. The procedure performed very well for almost every source, failing only when there was little or no correlated flux density in the full 8.5 arcmin field or when the source was highly extended with no compact structure (*i.e.* flux density on the shortest baselines only). Data were re-imaged using Difmap interactively if the procedure produced an un-satisfactory result. For example, the $z = 0.055$ galaxy PKS 0521–365 was selected for the sample because of its overall flat-spectrum. However it also possesses much extended, steep-spectrum material.

The visibility amplitudes at both observed frequencies, shown in Figure 4.1, demonstrate the presence of a large amount of flux density on the shortest baselines. Figure 4.2 presents 4.8 GHz images produced by the automatic processing procedure and interactively by the author. Of the three automatic processing methods, *clean* was the most successful. However, the clean boxes used in the *clean* method would appear to have been too restrictive, whereas the use of large clean boxes in the interactive method has resulted in a better quality image. This object is not a gravitational lens candidate because there is only one flat-spectrum component in the image and it is coincident with the nucleus of the optical galaxy.

Figure 4.3 illustrates the effects of the automatic fitting procedure on three

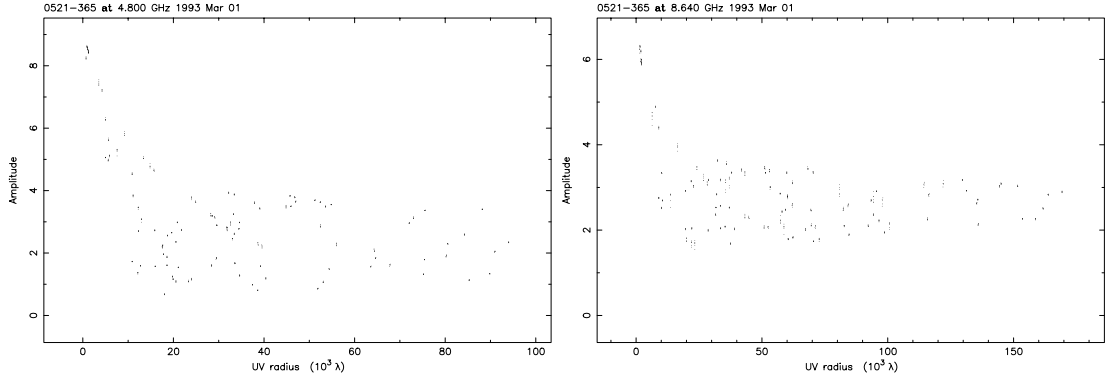


Figure 4.1: Visibility amplitudes (in Jy) for PKS 0521–365 plotted as a function of baseline length at 4.8 GHz (left) and 8.6 GHz (right).

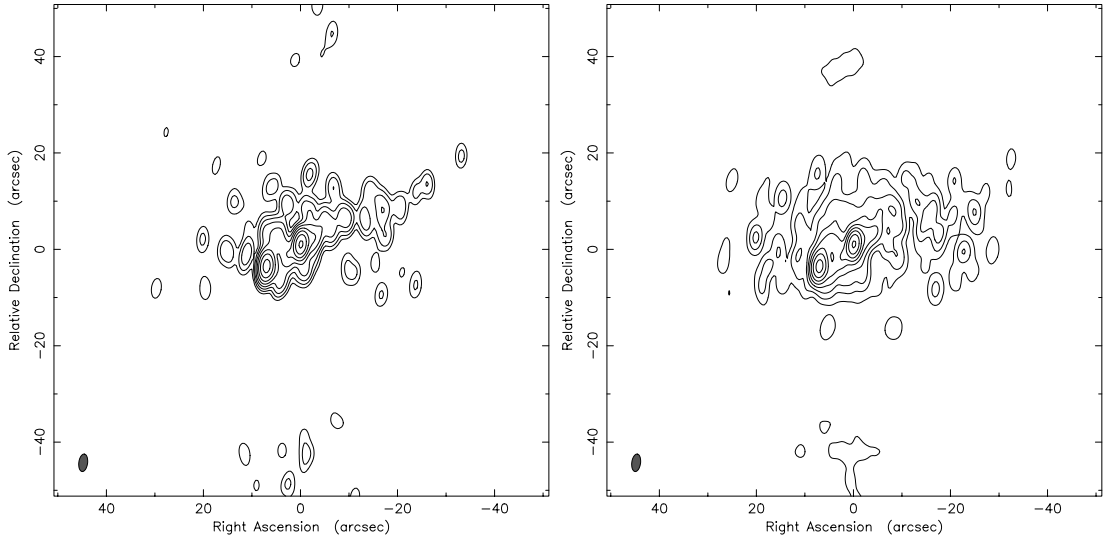


Figure 4.2: 4.8 GHz ATCA images of PKS 0521–365 using the automatic processing procedure (left) and using *Difmap* interactively (right). All contours are multiples (–1, 1, 2, 4, 8, 16, 32, 64, 128, 256) of the bottom contour level which is 8.8 mJy.

different objects whilst Table 4.1 shows the rms error between observed and model visibilities in each case. The final images that were produced by each of the three methods for any given source showed essentially the same brightness distribution, although the low-level extended structure was much better accounted for by the methods employing the CLEAN algorithm.

Figure 4.3a shows the resulting images produced by the procedure where the *modelfit* method was the most suitable. The resulting image appears to be point-like after applying all three methods however the rms error after using the *clean* method is significantly worse than the other two methods. A more careful inspection of the final model used in the *clean* method shows two spatially separated clean components where clearly only one is justified. Presumably this is because of the relatively small loop gain which was chosen with cleaning extended structure in mind. The *hybrid* method produced a clean map with an identical rms to that produced by *modelfit* which is not surprising when one considers that a single point source, once it has been removed by model fitting a single unresolved component should leave a residual map containing only noise. This is confirmed by the equality of the images for both techniques in Figure 4.3.

Table 4.1: rms differences between observed and model visibilities (Jy) at 4.8 GHz for the three examples described, and shown in Figure 4.3.

Source		PKS 2303–656	PKS 0113–285	PKS 2138–377
rms	<i>modelfit</i>	0.0125	0.0194	0.0134
	<i>clean</i>	0.0145	0.0156	0.0142
	<i>hybrid</i>	0.0125	0.0193	0.0120

The result of a successful *clean* method at 4.8 GHz is shown in Figure 4.3b. The object would appear to be a “classical double” source consisting of two steep-spectrum lobes and possibly a weak flat-spectrum core between them. The extended components dominate in this object and so applying the *modelfit* method does not produce a component model that agrees well with the data. This problem persists for the *hybrid* since the brightest region of emission is clearly extended.

Finally, Figure 4.3c demonstrates the situation where the *hybrid* method was the most successful. The object consists of some weak extended structure with a strong flat-spectrum core. The *modelfit* method performed better than the *clean* method, probably because the bright point-like core dominates in this source and is much better modelled by fitting a single point than by cleaning with a relatively small loop gain. The *hybrid* method clearly provides the best results in this case as it immediately removes the bright point and leaves the extended structure to be correctly removed by CLEAN.

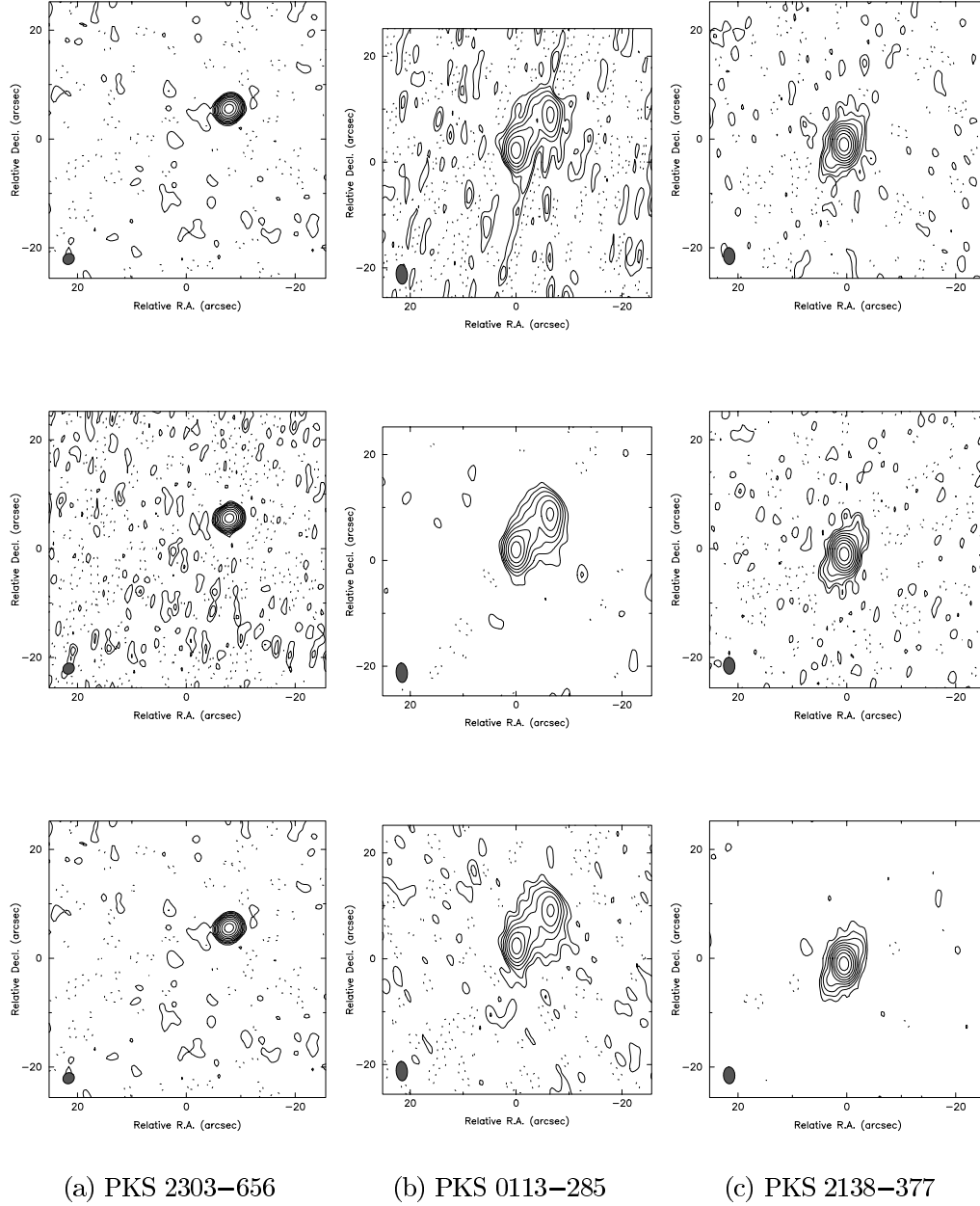


Figure 4.3: PKS 2303–656, PKS 0113–285 and PKS 2138–377 at 4.8 GHz imaged with the three automatic processing methods: *modelfit* (top), *clean* (centre) and *hybrid* (bottom). Contours for PKS 2303–656 are all set at $-0.25, 0.25, 0.5, 1, 2, 4, 8, 16, 32$ and 64% of the peak flux density which is 0.319 Jy/beam. Contours for PKS 0113–285 are all set at $-1, 1, 2, 4, 8, 16, 32$ and 64% of the peak flux density which is 0.114 Jy/beam. Contours for PKS 2138–377 are all set at $-0.25, 0.25, 0.5, 1, 2, 4, 8, 16, 32$ and 64% of the peak flux density which is 0.396 Jy/beam.

4.4 Survey Source Properties

4.4.1 Structural Classifications

Most extragalactic radio sources can be classified into one of three morphological categories: points, core-jets or classical doubles. Point sources, as the name suggests consist of a single, isolated and unresolved core which, typically for this flat-spectrum sample, possesses a flat-spectrum. Core-jet sources typically consist of a point source and a resolved steep-spectrum component which is usually linear and appears to originate at the core. Classical double sources, usually associated with radio galaxies, show the steep-spectrum components usually found in two bright lobes. At the centre of this emission there is usually a flat-spectrum core coincident with the optical identification.

In Table 4.5, the structures of all of the sample sources have been described using the above classifications where possible. However, during this process a number of other classifications were defined which were essentially sub-categories of the above. For example, there were a number of objects that were point sources but also possessed nearby weak secondary components that were too weak for a spectral index classification to be made. There were also some objects with structure that was too extended or compact components that were too close to be properly imaged by the survey and therefore were given a tentative classification. For those objects that were difficult to classify or were of particular interest, a more detailed description is given in Table 4.6.

New ATCA Position Calibration Sources

Position calibration sources are objects for which the interferometer response is well known *a priori*, and hence they permit measurement (and correction) of the relative individual antenna gains. The simplest structure is that of a point source which the interferometer should detect as possessing a constant visibility amplitude and phase throughout the observation and on all baselines. Hence point sources are the optimal calibrators.

Point sources found in this survey may, in the future, prove useful in supplementing the current catalogue position calibration sources for the ATCA. Furthermore, if any of these sources (especially the strong ones) are shown to have a flux density that remains constant over a long time period, they may prove to be useful for amplitude calibration. A method of determining suitable sources for ATCA calibration is to measure the ratio of core flux density to total flux density. Sources with a core to total flux density ratio close to 1.0 will most likely be point sources and objects with a ratio sufficiently less than 1.0 will possess multiple components and/or extended structure. This classification provides a “rating” on how good a calibrator the source might be. The measurement described in Section 4.2, where a single point source model was fit to the map at a position coincident with the brightest pixel, provides an estimate of the core flux density if the core is the brightest feature in the map. If this bright feature is not compact then the ratio of point flux density to total flux density is unlikely to be close to 1.0.

It should also be noted that an object that is a good calibrator at one frequency is not necessarily so at another. For example, PKS 0135–247 which has been classified as a core-dominated classical double, has a core to total flux density ratio of 0.97 at 8.6 GHz and so might be considered a suitable 8.6 GHz calibrator, however the ratio has a value of 0.86 at 4.8 GHz, indicating a significant amount of extended structure, thus making it an unsuitable 4.8 GHz calibrator. For this reason, the core to total flux density ratio classification has been tabulated at both observation frequency in Table 4.5. The distribution of this ratio at both wavelengths is shown in Table 4.2 and demonstrates that most objects are dominated by a single bright compact component. The table also shows that there is generally more extended structure in the 4.8 GHz data than the 8.6 GHz data as is expected given the steep-spectra characteristic of extended structure. Over 140 sources have been measured to possess a point to total flux density ratio ≥ 0.99 and may prove to be excellent position calibrators.

Table 4.2: The point to total flux density ratio (F) distribution. The number, N , and percentage, P , of sources with a core to total flux density ratio greater than or equal to F are shown for selected ratios.

F	$N_{4.8}$	$N_{8.6}$	$P_{4.8}$	$P_{8.6}$
0.25	443	449	96	97
0.50	423	422	92	92
0.75	389	398	84	86
0.90	338	361	73	78
0.95	297	325	64	71
0.99	142	158	31	34
1.00	71	75	15	16

Another important consideration when selecting calibration sources is the presence of confusing sources in the field. A strong confusing source will contribute both to the amplitude and the phase of the measured visibilities, thus making an accurate calibration difficult. Also, a confusing source may be a problem during long wavelength observations but not at short wavelength observations. This is because the beam of the individual antennas, and thus the field-of-view of the observation, increases with wavelength. The presence of confusing sources near program sources has been catalogued in Table 4.5.

4.4.2 Large Separation Double Sources

Ten of the sources presented in Figure 4.10 are accompanied by a secondary component at a separation greater than 45 arcsec and up to 366 arcsec. Based on the discussion in Section 2.2.1, the predicted number of sources in this sample with an unrelated source stronger than 10 mJy (the weakest flux density detected in any secondary component of these sources) at 5 GHz within the 8.5 arcmin region imaged is 56, so it is perhaps surprising that more objects of this type were not

found. However, for large separations bandwidth smearing effects will decrease the peak flux density of a source, making it more difficult to detect.

In all of these sources, the weaker component is always further from the phase centre than the strong one. The weak sources also possess a steep-spectrum in every case. In four of the sources (PKS 0055–328, PKS 1034–374, PKS 1117–270 and PKS 2352–342) the weaker secondary has an optical COSMOS counterpart. In the remaining six sources (PKS 0130–447, PKS 0619–468, PKS 0726–476, PKS 1404–342, PKS 1922–341 and PKS 2314–340) there is no optical counterpart to the secondary component. Every field has been re-imaged to search for further weak secondary components, especially at a position angle $\sim 180^\circ$ removed from that of the weak secondary with respect to the bright core. Such a component might be expected in a double lobed radio galaxy. None were found.

All of the bright flat-spectrum components in these sources have “stellar” COSMOS Catalogue optical counterparts except for PKS 0726–476 which has an optical counterpart classified as “too faint”, and PKS 0130–447 which has no COSMOS identification but is identified with an infra-red (*Kn*-band) object too faint to classify (Drinkwater *et al.*, 1996). Further, redshifts are available for PKS 1034–374, PKS 1404–342, PKS 2314–340 and PKS 2352–342 which are all classified as quasars.

Because the chances of finding a second source in the field are high, There is little justification for the suggestion that the two objects in a given image are somehow related. However, in two cases there is good evidence for a relationship between the bright core and the steep-spectrum secondary. In both PKS 0130–447 and PKS 0619–468 (Figure 4.10) the weak steep-spectrum secondary component is extended and points toward the flat-spectrum core. This would be highly unlikely if the two sources were unrelated. Also, in both cases the degree of extension is much greater than one would expect from bandwidth smearing effects.

If the secondary components in PKS 0130–447 and PKS 0619–468 are related to the core components then these two objects must be very large indeed and may be large radio galaxies where one of the lobes is too weak to detect in these observations. PKS 0130–447, as mentioned above, is only detected in the infra-red and is too faint to identify as a stellar object or a galaxy. PKS 0619–468 is identified with a stellar object with magnitude $M_J = 19.3$ and is therefore likely to be a quasar. No redshift measurements are available for either source, but if one assumes they lie in the range $z = 0.5$ to 1.0 (which is typical for a radio galaxy) and $H_0 = 75 \text{ km s}^{-1} \text{ Mpc}^{-1}$ then PKS 0130–447 and PKS 0619–468 must be 0.9 to 1.8 Mpc and 3.2 to 6.3 Mpc in extent respectively. By comparison, the large radio galaxy Centaurus A is ~ 1 Mpc in extent. It would therefore seem that these two objects are either unusually large or much closer than expected. Radio imaging of these two sources at a lower frequency (such as 1.4 or 2.3 GHz), would reveal more of the steep-spectrum structure and therefore help in understanding their structure.

4.4.3 Intra-day Variable Sources

One of the most interesting discoveries in recent times has been the detection of intra-day variable radio sources (Heeschen *et al.*, 1987). These are extragalactic sources that show changes in flux density over a period of days. If such variability is intrinsic to the source then it implies brightness temperatures well in excess of the 10^{12} K inverse Compton limit. The rate of variability of these sources would also appear to be related to wavelength. Sources with relatively long variability timescales show greater flux density changes at ~ 2 GHz than at 4.8 and 8.6 GHz (Qian *et al.*, 1996).

PKS 1415–379 has shown short timescale flux density changes (Figure 4.4), varying by approximately 10% of its total flux density over ~ 21 hr. This object appears to be unresolved and extragalactic based on its stellar COSMOS identification although a redshift measurement has not yet been made.

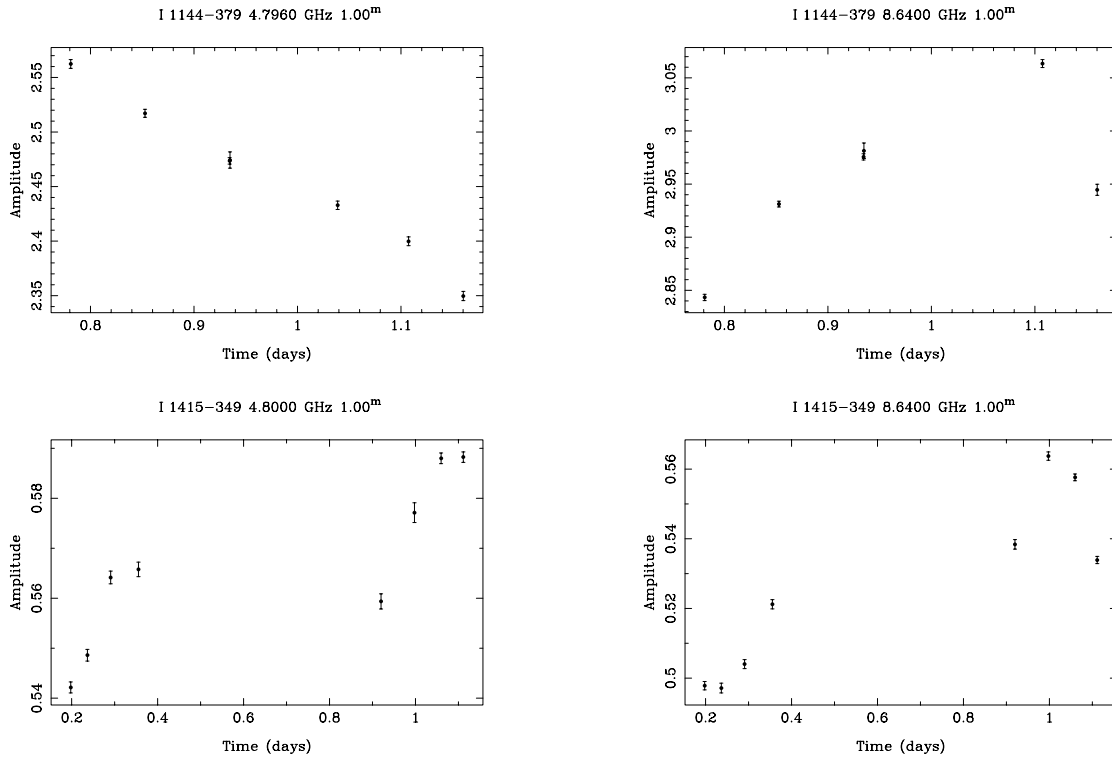


Figure 4.4: The confirmed intra-day variable source PKS 1144–379 (top) and the candidate intra-day variable PKS 1415–349 (bottom). Total flux density in Jy is plotted against UT at 4.8 GHz (left) and 8.6GHz (right). PKS 1144–379 was observed during survey observations in November 1993 while PKS 1415–349 was observed in September 1994.

The variability behaviour of PKS 1415–379 would therefore seem to be similar to that of the extraordinary intra-day variable PKS 0405–385 (Kedziora-Chudczer *et al.*, 1996), in that the variations at 4.8 and 8.6 GHz appear to be strongly correlated. The variability of PKS 1415–379 is episodic as was shown during ATCA observations in August 1996 at 4.8 and 8.6 GHz, where several cuts were

made over a 24 hr period and no significant change in flux density was seen. Further ATCA observations of PKS 1415–379 are required to verify that this source is an intra-day variable and to better sample the light curve.

Four strong intra-day variable sources have been found in the ATCA survey of Kedziora-Chudczer *et al.* (1996). They are: PKS 0405–385, PKS 1034–293, PKS 1144–379 and PKS 1519–273, all of which have been observed during the present cuts survey. Kedziora-Chudczer *et al.* monitored a large sample of flat-spectrum sources over several days and at four frequencies (1.2, 2.3, 4.8 and 8.6 GHz) and was therefore more sensitive to the longer period intra-day variable sources than the gravitational lens survey observations which typically lasted for 12 hours per source.

The present survey detected significant flux density variations in PKS 1144–379 (Figure 4.4) but not in the other three intra-day variables. PKS 1144–379 varied by approximately 8% of its total flux density over ~ 9 hr. It is interesting to note that no flux density variability was detected in PKS 0405–385 which has shown large flux density variations at 4.8 and 8.6 GHz (Kedziora-Chudczer *et al.*, 1996) thereby confirming the episodic nature of the dramatic variability of this source.

Although the present survey was not aimed at finding intra-day variable sources, it has proved particularly valuable at providing verification of a known source in this class as well as detecting a new one. The data currently available on PKS 1415–379 shows it to possess similar properties to PKS 0405–385, making it an exciting new intra-day variable.

4.4.4 A Comparison of ATCA and Parkes Flux Densities

Sample “Contamination”

All sources in this sample were selected from the Parkes Catalogue to possess a spectral index based on the 2.7 and 5.0 GHz flux densities given in PKSCAT90 (Wright and Otrupcek, 1990) larger than -0.5 ($S \propto \nu^\alpha$). The flux densities in PKSCAT90 were not all measured at the same epoch so the potential exists for “contamination” from steep-spectrum sources with a variable component (as discussed in Section 1.2). The spectral index distribution for this sample derived from the total cleaned ATCA flux densities given in Table 4.5 is shown in Figure 4.5. These spectral index measurements have the advantage that both flux density measurements for each source were made at the same epoch but have the disadvantage that the measured total flux density may be depressed for sources with very extended structure. The figure shows that the sample is dominated by flat-spectrum sources as expected but there is also a small number of steep-spectrum sources.

A possible cause for this shift toward steep spectra in the sample is a population of steep-spectrum sources contaminating the sample. Figure 4.6 presents two examples of steep-spectrum source contamination in the sample. With the exception of the 2.7 GHz Parkes flux density the spectrum of PKS 0241–513 is steep. The radio morphology of this source is typical of a steep-spectrum source, consisting of two bright lobes and a weak flat-spectrum core, the optical counterpart being identified with the core. This object was selected for the sample because of

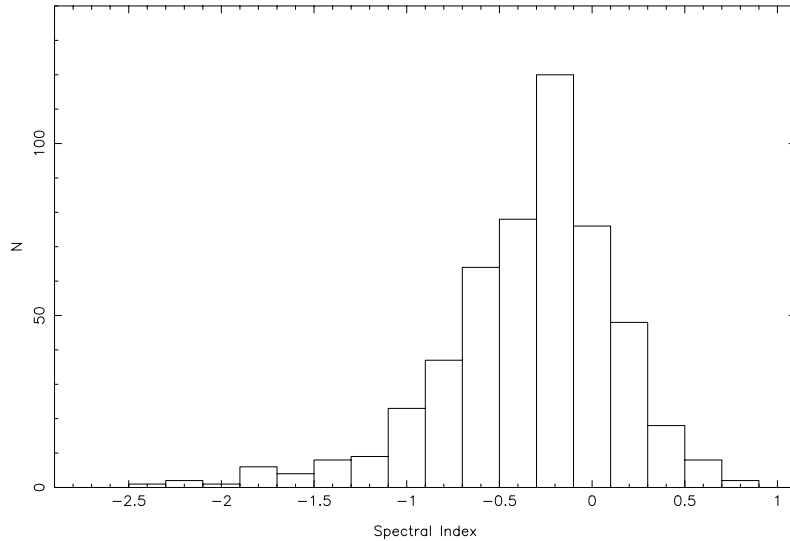


Figure 4.5: Spectral index distribution of the ATCA survey sources.

its depressed 2.7 GHz Parkes Catalogue flux density which is most likely a large error in the 2.7 GHz flux density measured at Parkes.

The spectrum of PKS 1254–333 (Figure 4.6, right-hand side) also appears steep and the ATCA images verify this, once again showing two bright steep-spectrum lobes and a weak flat-spectrum core coincident with the optical counterpart. The 8.4 GHz Parkes flux density is slightly larger than the ATCA 8.6 GHz flux density and this may indicate that the flat-spectrum core was brighter at the epoch of the Parkes measurement.

Accuracy of the Parkes Flux Densities

A simple method of comparing the ATCA and Parkes Catalogue flux density measurements is to plot the Parkes flux densities against the ATCA flux densities at both 4.8 and 8.6 GHz (Figure 4.7). In the following discussion, point sources are defined as having $\geq 95\%$ of their total flux density contained in an unresolved component. Both point and non-point sources are plotted in Figure 4.7.

In general, the source flux densities are clustered along a line of equal intensity (the dashed lines in the figure) which is as one would expect for non-variable sources. However, there are several sources that have significantly weaker flux densities at the ATCA than at Parkes and the great majority of such sources possess extended structure. Furthermore, this effect is more pronounced at 4.8 GHz than at 8.6 GHz. Non-point sources, especially those with very extended structure, will not be well imaged with the ATCA as a lot of the flux density will not be present on all but the shortest baselines. The ATCA is thus likely to underestimate the total flux density of these sources. This effect is more pronounced at 4.8 GHz because of the steep-spectrum nature of extended emission.

Point sources, however should possess the same flux density at both Parkes and the ATCA as they are unresolved with both instruments and there should

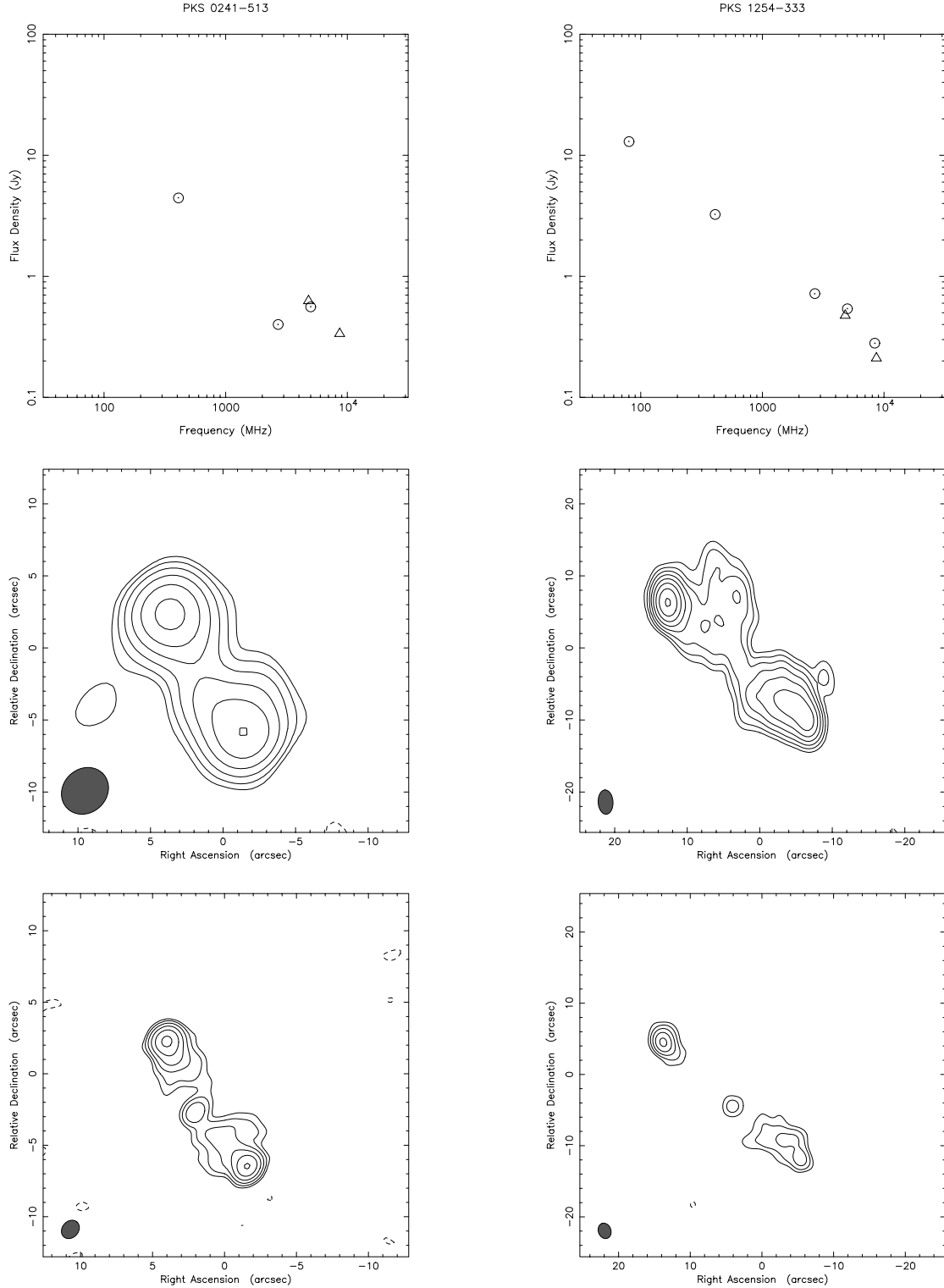


Figure 4.6: Two examples of contaminating sources in the flat-spectrum sample: PKS 0241-513 (left) and PKS 1254-333 (right). The top panels show continuum spectra, the circles represent Parkes Catalogue flux densities while the triangles represent total flux densities measured during the ATCA survey. The central panels are the 4.8 GHz images and the bottom panels are the 8.6 GHz images. Contours are multiples ($-1, 1, 2, 4, 8, 16, 32, 64, 128, 256, 512$) of the bottom contour level which is three times the rms noise level in the map.

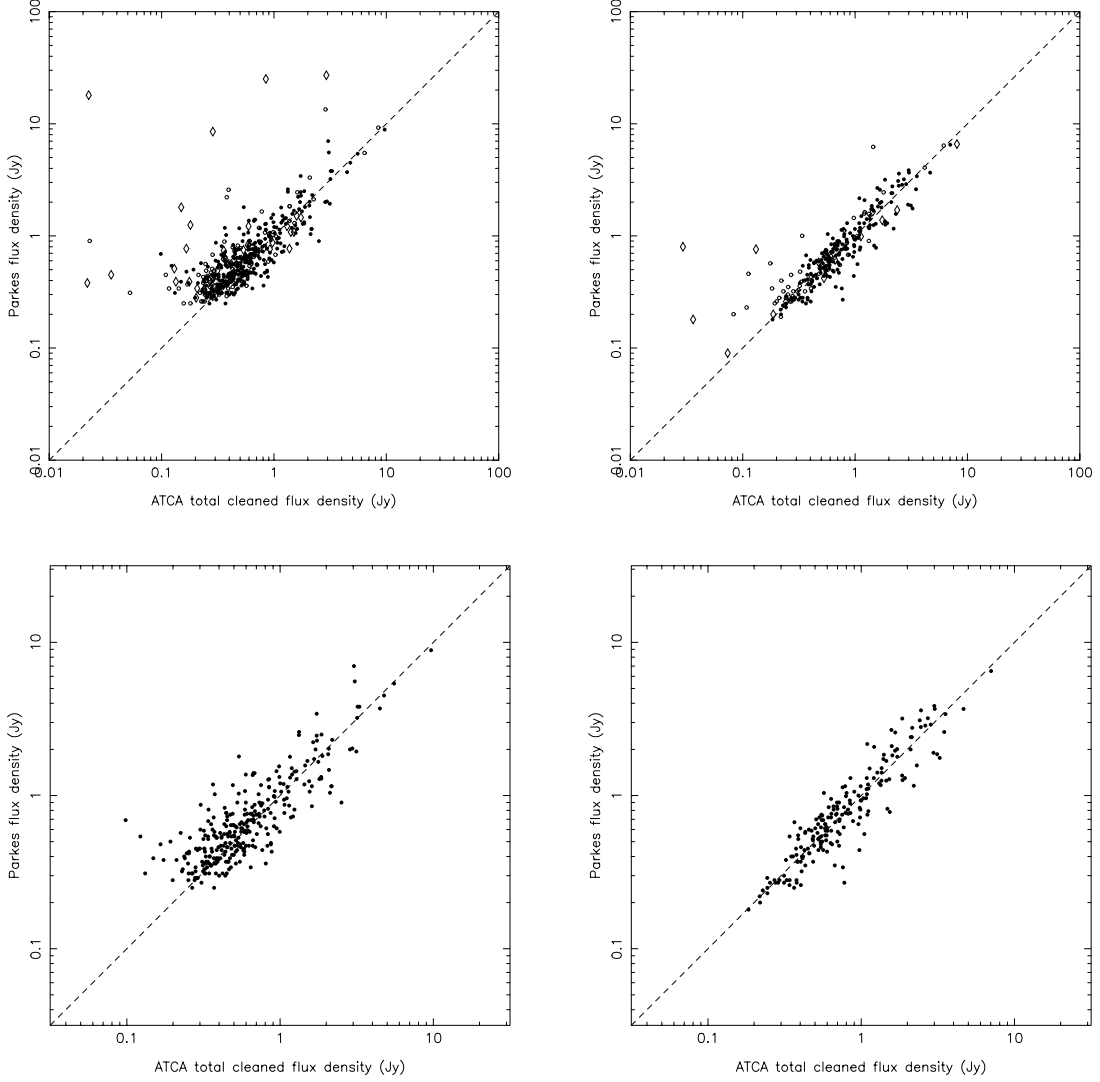


Figure 4.7: Parkes flux densities as a function of ATCA flux densities. The left hand panels show the Parkes 5.0 GHz flux densities against the ATCA 4.8 GHz flux densities while the right hand panels show the Parkes 8.4 GHz flux densities against the ATCA 8.6 GHz flux densities. The top panels show all sources in the sample while the lower panels show only the point sources. Symbols: \bullet = point sources (*i.e.* core to total flux density ratio ≥ 0.95), \circ, \diamond = non-point sources where \diamond represents sources with galactic or Magellanic Cloud positions.

therefore be no “missing” flux density. Figure 4.7 (lower panels) shows that both point source flux density distributions lie along the line of equal intensity and, to first-order, there appear to be no systematic differences between the Parkes and ATCA flux density measurements. The width of the distribution of point source flux densities along the lines would appear to be constant at each frequency, indicating no dependence of fractional variability on flux density. The overall extent of scattering of points around the line of equal intensity in the figure is greater at 4.8 GHz than at 8.6 GHz. This may be because the 8.4 GHz Parkes flux densities were measured more recently than the 5.0 GHz flux densities and hence the 5.0 GHz flux densities have had more time to vary and long timescale variations are more likely to be detected.

4.4.5 Optical Identifications

The COSMOS/UKST Southern Sky Catalogue (Yentis *et al.*, 1992) was used to identify all survey sources with optical counterparts brighter than $M_J = 22.5$ within 2 arcmin of each of the derived radio positions and a list of the closest optical component in each case was tabulated. The distribution of offsets between the radio and nearest optical positions resulted in what appeared to be a Gaussian distribution with an rms of ~ 1 arcsec. All survey sources with no optical counterpart within 4 arcsec of the radio position (*i.e.* about 4σ) were then investigated further. The Digitised Sky Survey was used for this follow up work. Of the 66 objects with a difference greater than 4 arcsec between radio and optical counterpart position, a majority (49) were found to be “empty fields”, whilst the remaining 17 survey sources had optical counterparts, but these were not correctly classified in the COSMOS database.

For 56 of the survey sources, it was not possible to make an identification from the COSMOS database because it does not currently cover regions near the Galactic plane or near the Magellanic Clouds. The Digitised Sky Survey was again used to make a qualitative identification of these objects.

After the above, the position offset distribution was re-determined for the positive COSMOS identifications. This is shown in Figure 4.8 and as histograms of offset in RA and Dec in Figure 4.9. The mean offsets in RA and Dec (Table 4.3) are significantly removed from zero.

Table 4.3: Mean offset between radio and optical positions (radio – optical) for the 339 radio sources with COSMOS identifications.

Direction	Mean (arcsec)	rms (arcsec)
RA	0.58	1.1
Dec	0.28	1.0

A similar analysis had been carried out by Drinkwater *et al.* (1995) who obtained COSMOS identifications for 134 flat-spectrum radio sources using radio-determined positions. They also detected systematic offsets in RA and Dec of

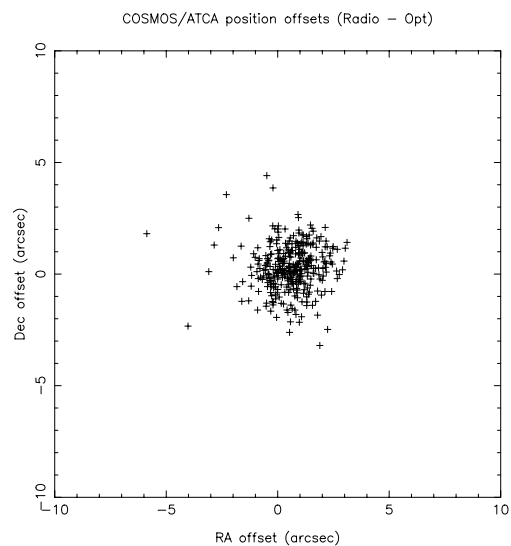


Figure 4.8: Offsets between ATCA and COSMOS catalogue positions.

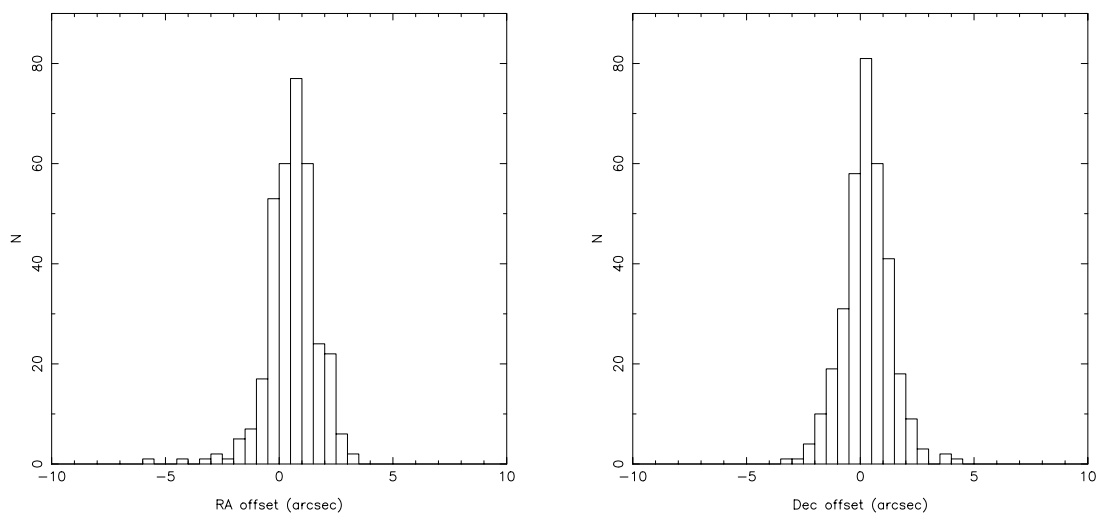


Figure 4.9: Histograms of offsets between ATCA and COSMOS catalogue positions (radio – optical). The left panel shows offsets in Right Ascension and the right panel shows offsets in Declination.

similar sign and magnitude. Drinkwater *et al.* then compared the COSMOS catalogue positions for these sources with those listed in the more accurate Positions and Proper Motions (PPM) optical catalogue (Röser *et al.*, 1994) and found an offset which varied from field to field. The mean offsets between the PPM and COSMOS fields were 0.386 arcsec in RA and -0.054 arcsec in Dec (PPM – COSMOS). These offsets are consistent with the known intrinsic difference between FK4 (COSMOS) and FK5 (PPM) reference frames. After applying these corrections, Drinkwater *et al.* detected an overall improvement in positional coincidence between their optical and radio positions but with a residual offset (radio – optical) of ~ 0.28 arcsec in both RA and Dec. Application of a similar correction to the present sample is not currently possible as the position differences between the COSMOS and PPM catalogues are incomplete. Nevertheless, application of the mean offsets derived by Drinkwater *et al.* provides an estimate of the corrected offsets, shown in Table 4.4, and a similar improvement is seen.

Table 4.4: Mean offset between radio and optical positions (radio – optical) for the 339 radio sources with COSMOS identifications after an estimated correction for the systematic position errors in the COSMOS database as derived by Drinkwater *et al.* (1995).

Direction	Mean (arcsec)
RA	0.19
Dec	0.33

The residual systematic position offsets are most likely due to second-order errors in the COSMOS database (Drinkwater *et al.*, 1996). Mis-alignment between the radio and optical reference frames is unlikely to be the cause of this systematic offset as the frame mis-alignment changes with Right Ascension and Declination. An improvement in the radio-optical frame tie would however decrease the rms of the distributions shown in Figures 4.8 and 4.9.

There is a small probability that an optical identification is actually unrelated to the radio source and that they lie within 4 arcsec of each other by chance. Following Jauncey *et al.* (1982), the search area (which extends to $\pm 4\sigma$) is defined as having an area of $4^2\pi\sigma_\alpha\sigma_\delta$ square arcseconds, where σ_α and σ_δ are the observed rms differences between radio and optical positions in Right Ascension and Declination respectively. The background densities of stellar objects, ρ_s , and galaxies, ρ_g in the UKST plates for a limiting magnitude of $M_J = 22.5$ have been measured by Griffiths *et al.* (1983). Their results show that ρ_s and ρ_g are 2.1 and 1.2 objects per square arcminute respectively. The chance identification rates are thus $4^2\pi\sigma_\alpha\sigma_\delta\rho_s$ for stellar objects and $4^2\pi\sigma_\alpha\sigma_\delta\rho_g$ for galaxies. For this sample the number of chance identifications is 16 stellar objects and 9 galaxies. An rms of ~ 1 arcsec for the position offsets indicates that the scatter seen in Figure 4.8 is dominated by COSMOS position errors rather than ATCA position errors which are less than 0.5 arcsec. Therefore, an improvement in the accuracy of the COSMOS (and not radio) positions and the radio-optical frame tie is required to decrease the number of chance identifications.

Redshift measurements and optical classifications for several of the sources in the sample were found by means of a search conducted via the NASA/IPAC Extragalactic Database. These data are drawn from a wide range publications and are given in Table 4.5.

4.4.6 Overlap with Other Catalogues

This sample contains 114 sources in common with the Parkes Half-Jansky Flat-spectrum Sample (Drinkwater *et al.*, 1996), hereafter PHFS, which has been selected with the same spectral index cutoff but covers a more northerly declination range ($-45^\circ < \delta_{\text{B1950}} < +10^\circ$) and has a higher flux density cutoff ($S_{2.7} > 0.5$ Jy). Accurate radio positions (some of them obtained in the present survey) have allowed optical counterparts to be identified for nearly all of the PHFS sources and a large majority now have redshift measurements. In the process of identifying optical counterparts for their sample, Drinkwater *et al.* have found that a significant number ($\sim 8\%$) of the sources have no optical counterparts down to a limiting detection magnitude of $M_J \sim 22.5$ for the COSMOS database. However, a significant number of them are detected at near-infrared wavelengths and it has been suggested that this reddening is due to dust that may in some cases be found in an intervening lensing galaxy, thus biasing optically selected samples away from possible gravitational lenses (Webster *et al.*, 1996).

4.5 Summary

All of the sample sources have been imaged in a consistent fashion using an automatic processing procedure in **Difmap** and every source has been classified by radio morphology. A measurement of point to total flux density ratio has been made and used to identify possible new calibration sources for the ATCA. Approximately 30% of survey sources have at least 99% of their total flux density contained in an unresolved component. Ten sources were discovered to be accompanied by a second bright source more than 45 arcsec away. Of these, eight are likely to have unrelated companions but two, PKS 0130–447 and PKS 0619–468, appear to be very large core-jet sources. Intra-day variability was detected in PKS 1144–379 and PKS 1415–349. The former is a known intra-day variable source (Kedziora-Chudczer *et al.*, 1996) but the latter is a new detection. The flux densities for the survey sources contained in the Parkes Catalogue and those measured in this survey at 4.8 and 8.6 GHz have been compared. A systematic offset between Parkes and ATCA flux densities of ~ 70 mJy at 4.8 GHz has been detected. A small number of steep-spectrum sources were included in the sample because of inaccurate Parkes flux density measurements. Sub-arcsecond radio positions have been determined for all sample sources with compact structure. Of these, 339 have been identified with optical counterparts from the COSMOS/UKST Catalogue (Yentis *et al.*, 1992). The majority of the remaining sources are outside the coverage of the current COSMOS database or have no catalogued optical counterpart. The number of chance identifications is 16 stellar objects and 9 galaxies brighter than $M_J = 22.5$.

Table 4.5: Flux density and structural information obtained from the ATCA survey and optical identifications from the COSMOS/UKST Southern Sky Catalogue. The columns in the table are labelled as follows: (i) B1950 Parkes Catalogue source name, (ii) Epoch of the observation in years since 1900, (iii) 4.8 GHz total cleaned flux density, (iv) 8.6 GHz total cleaned flux density, (v) 4.8 to 8.6 GHz spectral index, (vi) Fraction of 4.8 GHz flux density confined to a point source, (vii) Fraction of 8.6 GHz flux density confined to a point source, (viii) classification of the object based on an inspection of the radio morphology (P = point source, PW = point source with one or more weak secondary, PX = point surrounded by indistinct, extended structure, R = just resolved but component separation is too small to determine structure, J = core-jet, JW = core-jet where the jet is faint, C = core-dominated classical double, L = steep spectrum lobe-dominated classical double, X = extended with no apparent compact core, ND = non-detection, M = confusing sources also in the field, ? = classification in doubt due to survey limitations), (ix) and (x): RA and Dec (J2000.0) of ATCA derived radio position, (xi) apparent M_J magnitude of the optical counterpart, (xii), (xiii) and (xiv): $\Delta\alpha$, $\Delta\delta$, Δr : RA, Dec and total offsets respectively between optical and radio positions (radio – optical) in arcseconds, (xv) COSMOS catalogue classification (S = star, G = galaxy, T = too faint, J = junk, V = bright galaxy, X = field not in COSMOS database), (xvi) Classification of the object based on an inspection of the Digitised Sky Survey plates for absent or doubtful COSMOS identifications (EF = empty field, ST = stellar, MG = two or more objects merged, CL = appears cloud-like (*e.g.* HII region), CF = crowded field, BG = possible stellar object behind a cloud, EX = extended, WK = weak or faint, OK = COSMOS identification is correct). (xvii), (xviii) Optical Identification (G = galaxy, Q = quasar) and redshift found by means of a search conducted via the NASA/IPAC Extragalactic Database (NED). (xix) Annotations: additional comments and/or images contained elsewhere (* = comments contained in Table 4.6, † = images are presented in Figure 4.10, ‡ = this source is discussed in Chapter 3).

Source	Epoch	$S_{4.8}$	$S_{8.6}$	$\alpha_{8.6}^{4.8}$	$F_{4.8}$	$F_{8.6}$	Type	R.A.	Dec.	B_J	$\Delta\alpha$	$\Delta\delta$	Δr	Class	DSS	ID	z	Annot
0002-478	94.746	0.370	0.388	0.08	0.98	0.97	JW	00:04:35.65	-47:36:19.7	17.1	0.16	-0.48	0.51	S				
0003-833	93.533	0.608	0.220	-1.73	0.17	0.16	X	00:06:09.48	-83:05:43.8	22.3	7.45	13.00	14.98	T	EF			
0005-239	93.867	0.535	0.378	-0.59	0.99	0.99	P	00:08:00.37	-23:39:18.4	16.6	0.69	-0.40	0.79	S		Q	1.41	
0005-262	93.867	0.469	0.340	-0.54	1.00	1.00	P	00:08:26.25	-25:59:11.5	21.8	12.05	3.50	12.55	G	EF			
0008-222	93.867	0.384	0.360	-0.11	1.00	1.00	P	00:10:53.65	-21:57:04.5	22.5	-1.57	-0.34	1.61	T				
0008-264	93.870	0.342	0.379	0.18	0.99	0.99	P	00:11:01.25	-26:12:33.4	19.5	-0.32	-0.83	0.89	S		Q	1.096	
0017-307	94.746	0.464	0.368	-0.39	0.99	0.98	PW	00:19:42.67	-30:31:19.3	19.8	1.47	0.60	1.59	S				
0027-426	94.746	0.883	0.843	-0.08	0.98	0.98	JW	00:30:17.49	-42:24:46.4	17.7	0.07	-1.03	1.03	S		Q	1.66	
0036-216	93.867	0.362	0.218	-0.87	1.00	0.99	P	00:38:29.95	-21:20:04.2	21.0	0.52	0.95	1.08	G				
0038-326	94.746	0.098	0.100	0.03	1.00	0.96	P	00:40:30.65	-32:25:20.5	22.6	1.00	0.20	1.02	S				
0044-846	93.530	0.582	0.486	-0.31	0.99	0.97	PW	00:44:26.60	-84:22:39.8	19.5	-0.35	-0.19	0.40	S				
0045-757	94.743	0.339	0.291	-0.26	0.99	1.00	P	00:47:40.81	-75:30:11.3					X	ST			
0047-579	94.746	1.328	1.355	0.04	0.98	0.98	R	00:49:59.46	-57:38:27.3	17.0	-1.61	-1.22	2.02	S		Q	1.797	
0048-427	94.746	0.995	1.097	0.17	1.00	0.99	P	00:51:09.50	-42:26:33.4	20.0	0.42	-1.61	1.66	S		Q	1.749	
0054-451	94.746	0.402	0.350	-0.23	0.94	0.94	J?	00:56:45.84	-44:51:02.3	19.6	0.82	0.30	0.87	S				
0055-328	94.746	0.277	0.255	-0.14	0.74	0.80	P M	00:58:02.23	-32:34:20.6	20.6	0.95	1.27	1.59	S				*†
0056-572	94.746	0.590	0.508	-0.25	0.97	1.00	P	00:58:46.58	-56:59:11.4	17.3	0.82	1.47	1.68	S		Q	0.018	
0059-287	93.867	0.328	0.213	-0.73	1.00	1.00	P	01:01:52.39	-28:31:20.4	22.8	0.64	-0.44	0.78	T				
0100-760	94.743	0.324	0.403	0.37	1.00	1.00	P	01:02:18.69	-75:46:51.6					X	ST	Q	1.015	

continued on next page

continued from previous page

Source	Epoch	S _{8.6}	S _{8.6}	$\alpha_{8.6}^{\pm}$	F _{4.8}	F _{8.6}	Type	R.A.	Dec.	B _I	$\Delta\alpha$	$\Delta\delta$	Δr	Class	DSS	ID	z	Annot
0101-802	94.743	0.285	0.182	-0.76	0.49	0.39	L?	01:02:49.20	-79:56:05.5	16.9	1.30	-1.41	1.91	G		G	0.057	*,†
0104-408	93.870	1.610	2.456	0.72	0.98	0.97	P	01:06:45.11	-40:34:19.9	18.9	3.11	1.42	3.42	S		Q	0.584	
0110-668	94.743	0.422	0.387	-0.15	0.97	0.97	J	01:12:18.91	-66:34:45.2	17.3	1.28	1.34	1.85	S				
0113-285	93.867	0.243	0.130	-1.07	0.51	0.52	L	01:15:39.56	-28:17:09.2	20.3	45.41	2.20	45.46	S	EF			
0113-310	93.870	0.308	0.248	-0.37	0.89	0.93	J	01:15:46.50	-30:49:19.1	20.3	0.54	0.78	0.95	S				*
0116-219	93.867	0.516	0.534	0.06	0.98	1.00	P	01:18:57.26	-21:41:30.1	19.6	2.47	1.16	2.73	S		Q	1.161	
0118-272	93.867	0.736	0.635	-0.25	0.95	0.99	J	01:20:31.66	-27:01:24.0	17.5	1.14	0.55	1.26	S		Q	0.559	
0122-514	93.870	0.289	0.271	-0.11	0.98	0.99	J	01:24:57.39	-51:13:15.9	19.4	0.88	1.39	1.64	S		Q	0.72	
0123-226	93.867	0.251	0.176	-0.61	0.73	0.76	C	01:26:14.99	-22:22:33.5	19.9	0.71	-0.66	0.97	S		Q	0.72	
0130-447	93.161	0.295	0.219	-0.50	0.77	0.87	C?	01:33:00.90	-44:30:42.2	22.4	1.61	-22.00	22.06	T	EF			*,†
0131-522	93.161	0.365	0.519	0.60	1.00	1.00	P	01:33:05.76	-52:00:03.9	18.0	0.03	2.16	2.16	S		Q	0.02	
0133-204	93.164	0.912	0.884	-0.05	0.99	1.00	P	01:35:37.56	-20:08:46.8	18.2	2.67	-0.20	2.68	S		Q	1.141	
0135-247	93.164	0.778	0.797	0.04	0.86	0.97	C	01:37:38.39	-24:30:54.5	18.9	1.30	-1.02	1.65	S		Q	0.831	
0142-278	93.164	0.732	0.684	-0.12	0.99	1.00	P	01:45:03.44	-27:33:35.2	17.5	1.89	-3.20	3.72	S		Q	1.153	
0144-522	93.870	0.236	0.195	-0.32	0.80	0.86	J	01:46:48.59	-52:02:33.4	13.6	0.91	2.67	2.82	S		Q	0.61	*,†
0150-334	93.873	1.146	0.994	-0.24	0.98	1.00	P M	01:53:10.12	-33:10:25.0	17.4	1.08	1.44	1.80	S				
0153-410	93.161	1.063	0.718	-0.67	1.00	1.00	P	01:55:37.06	-40:48:42.4	19.4	-1.83	-0.56	1.91	G				
0153-663	94.743	0.252	0.167	-0.71	0.91	0.82	J	01:54:31.39	-66:04:15.7	18.0	1.87	1.48	2.39	S				
0155-549	93.870	0.507	0.402	-0.40	0.98	0.99	P	01:56:49.71	-54:39:48.3	20.7	3.54	-22.72	22.99	G	EF			
0158-404	93.873	0.286	0.244	-0.27	0.99	0.96	JW	02:00:11.84	-40:10:57.9	20.5	3.03	1.16	3.24	S				
0202-337	93.873	0.327	0.304	-0.12	0.96	0.95	C	02:04:28.66	-33:28:50.1	16.1	29.44	-5.84	30.01	S	EF	Q	1.003	
0208-512	93.873	3.180	2.998	-0.10	0.96	0.97	PW	02:10:46.72	-51:01:01.9	16.9	-0.47	0.50	0.69	S				
0214-522	93.161	0.500	0.327	-0.72	1.00	1.00	P	02:16:03.16	-52:00:12.3	23.7	-3.09	0.11	3.09	J				
0219-637	93.161	0.396	0.349	-0.21	0.99	1.00	P	02:20:54.17	-63:30:19.4	18.5	-0.29	-0.56	0.63	S				
0220-349	93.161	0.812	0.750	-0.13	0.98	1.00	P	02:22:56.39	-34:41:28.3	21.5	1.47	1.30	1.97	T				
0226-559	93.870	0.481	0.584	0.33	0.99	1.00	PW	02:28:21.60	-55:46:03.0	18.5	1.07	0.98	1.45	S				
0229-398	93.161	0.340	0.342	0.01	0.98	0.97	P	02:31:51.79	-39:35:47.2	21.7	-3.89	16.34	16.80	T	EF			
0230-790	93.530	0.447	0.448	0.01	0.98	1.00	P	02:29:34.86	-78:47:45.4	18.4	1.28	0.44	1.35	S		Q	1.07	
0233-478	93.873	0.329	0.234	-0.58	0.99	0.98	P	02:35:06.43	-47:37:10.1	17.3	0.08	0.34	0.35	S				
0234-301	93.870	0.258	0.192	-0.51	0.96	0.98	JW	02:36:31.17	-29:53:54.9	18.0	1.04	1.36	1.71	S		Q	2.102	
0235-618	93.161	0.588	0.598	0.03	0.97	0.98	PW	02:36:53.25	-61:36:15.0	19.5	-0.38	1.58	1.62	G				
0240-217	93.164	0.834	0.586	-0.60	1.00	0.99	P	02:42:35.94	-21:32:24.6	19.0	1.59	1.92	2.50	G		G	0.314	
0241-513	93.873	0.627	0.336	-1.06	0.35	0.28	L	02:43:13.79	-51:05:18.3	20.6	-0.02	-0.84	0.84	G				
0244-297	93.870	0.281	0.214	-0.46	0.99	1.00	P	02:46:21.47	-29:35:05.1	23.4	-0.05	1.36	1.36	J				
0244-470	93.161	0.888	0.864	-0.05	0.93	0.90	J	02:46:00.09	-46:51:17.3	19.0	0.46	1.36	1.44	S				
0250-225	93.870	0.402	0.389	-0.05	0.95	0.99	PX	02:52:47.96	-22:19:25.3	20.9	0.77	-0.98	1.25	S				

continued on next page

continued from previous page

Source	Epoch	S _{4.8}	S _{8.6}	$\alpha_{8.6}^{\pm}$	F _{4.8}	F _{8.6}	Type	R.A.	Dec.	B _I	$\Delta\alpha$	$\Delta\delta$	Δr	Class	DSS	ID	z	Annot
0252-549	93.161	0.787	0.787	0.00	0.96	0.99	C	02:53:29.17	-54:41:51.3	17.3	-0.41	-0.02	0.42	S		Q	0.537	†
0253-754	94.743	0.252	0.223	-0.21	0.99	0.96	J?	02:53:10.90	-75:13:16.8	23.0	0.86	0.44	0.97	T		Q	1.915	†
0254-334	93.873	0.251	0.273	0.14	1.00	0.99	P	02:56:42.60	-33:15:21.0	18.9	0.23	0.66	0.70	S		Q		
0257-510	93.873	0.539	0.505	-0.11	0.94	0.95	P	02:58:38.75	-50:52:04.4	24.2	1.04	0.72	1.26	S				
0258-344	93.873	0.281	0.188	-0.68	0.93	0.82	C	03:00:36.18	-34:14:05.1	18.0	1.90	-0.22	1.91	S				
0259-316	93.873	0.309	0.342	0.17	0.93	0.99	JW	03:01:16.24	-31:26:15.5	19.7	0.95	1.84	2.07	G				
0301-243	93.164	0.370	0.252	-0.66	0.69	0.90	PW	03:03:26.54	-24:07:10.2	16.4	0.40	1.18	1.25	S				*
0301-721	94.743	0.457	0.407	-0.19	0.92	0.95	J	03:01:38.44	-71:56:34.4	20.3	-0.04	1.53	1.53	S				
0302-623	94.743	2.086	1.849	-0.21	1.00	1.00	P	03:03:50.63	-62:11:25.5	18.9	-0.33	1.45	1.49	S				
0308-611	93.161	0.989	1.206	0.34	0.98	0.99	J	03:09:56.08	-60:58:39.1	18.3	-0.36	0.38	0.68	S				
0312-770	94.743	0.620	0.704	0.22	0.99	0.98	PW	03:11:55.24	-76:51:50.8	16.3	0.02	1.88	1.88	S		Q	0.223	
0315-282	93.870	0.286	0.238	-0.31	0.92	0.97	JW	03:17:33.70	-28:03:18.1	19.9	-0.06	0.04	0.08	S				
0318-388	93.873	0.132	0.116	-0.21	1.00	1.00	P	03:20:46.40	-38:37:28.3	13.3	-5.46	-5.48	7.74	S	EF	Q	2.22	
0325-222	93.870	0.583	0.536	-0.14	1.00	1.00	P	03:27:59.93	-22:02:05.2	18.6	1.94	1.68	2.57	S		Q	0.895	
0327-241	93.164	0.705	0.722	0.04	0.88	0.92	C	03:29:54.07	-23:57:08.2	19.4	2.18	0.09	2.18	S		Q	2.689	
0329-255	93.870	0.211	0.176	-0.31	0.97	0.98	J	03:31:08.92	-25:24:43.0	17.8	2.36	0.94	2.53	S				*
0329-404	93.873	0.806	0.684	-0.28	0.97	0.98	C?	03:30:51.11	-40:14:16.4	22.2	0.76	0.30	0.82	T				†
0331-654	94.743	0.399	0.201	-1.17	0.56	0.58	L	03:31:45.95	-65:17:55.9	21.1	10.32	10.41	14.66	S	EF	Q	1.445	
0332-403	93.161	1.330	1.525	0.23	1.00	0.98	P M	03:34:13.65	-40:08:25.5	16.8	0.41	0.25	0.48	S				
0333-729	94.743	0.354	0.387	0.15	1.00	1.00	P	03:32:43.00	-72:49:04.5	20.1	-0.50	-1.30	1.39	S				
0334-546	93.161	0.511	0.383	-0.49	1.00	0.99	P	03:35:53.92	-54:30:25.0	21.5	2.76	-0.02	2.76	S		Q	1.537	
0335-364	93.873	0.453	0.600	0.48	0.99	0.97	P	03:36:54.02	-36:16:05.9	19.3	0.56	1.62	1.71	S		Q	0.048	*
0338-214	93.164	0.834	0.803	-0.07	0.99	0.99	P	03:40:35.62	-21:19:30.1	16.0	0.27	0.70	0.75	S				
0341-256	93.870	0.367	0.411	0.19	0.95	0.92	J?	03:43:19.52	-25:30:17.2	18.4	0.74	0.22	0.77	S				
0342-528	93.873	0.344	0.232	-0.67	0.99	0.99	PW	03:43:49.33	-52:41:16.7	21.8	-16.41	5.38	17.27	T	EF	Q	0.988	*
0346-279	93.164	1.106	1.537	0.56	0.99	0.99	PW	03:48:38.15	-27:49:13.2	20.5	-0.21	-1.38	1.40	S				
0347-211	93.870	0.339	0.281	-0.32	1.00	0.98	P	03:49:57.84	-21:02:46.5	20.7	1.31	1.58	2.05	S				
0349-278	93.164	0.380	0.176	-1.31	0.52	0.32	X	03:51:45.11	-27:43:10.9	20.7	12.93	-3.88	13.50	G	EF			
0350-518	93.873	0.386	0.332	-0.26	0.87	0.93	P	03:51:28.22	-51:42:55.3	20.6	1.41	1.75	2.25	S				
0355-483	93.161	0.469	0.375	-0.38	1.00	1.00	P	03:57:21.92	-48:12:15.2	16.5	0.88	-1.06	1.38	S		Q	1.005	
0355-669	94.743	0.520	0.457	-0.22	0.98	0.99	PW	03:55:47.89	-66:45:33.6	18.6	-0.27	1.53	1.56	S				
0357-264	93.164	0.428	0.314	-0.53	0.97	0.98	PW	03:59:33.68	-26:15:30.6	21.8	0.80	0.90	1.20	S				
0400-319	93.873	0.537	0.455	-0.28	0.99	1.00	P	04:02:21.27	-31:47:25.7	20.2	0.93	1.28	1.59	S				
0402-362	93.161	1.857	2.410	0.44	0.99	1.00	PW	04:03:53.74	-36:05:02.1	17.0	0.52	0.48	0.71	S		Q	1.417	
0402-477	93.161	0.412	0.277	-0.67	0.88	0.85	J	04:03:47.10	-47:38:46.7	21.3	-0.21	3.86	3.86	S				
0405-331	93.873	0.610	0.594	-0.05	1.00	0.99	P	04:07:33.92	-33:03:46.0	19.4	-0.04	0.06	0.07	S				

continued on next page

continued from previous page

Source	Epoch	S _{8.6}	α _{8.6}	F _{4.8}	F _{8.6}	Type	R.A.	Dec.	B _I	Δα	Δδ	Δr	Class	DSS	ID	z	Annot
0405-385	93.161	1.557	1.932	1.00	1.00	P	04:06:59.02	-38:26:28.3	19.8	0.77	-1.61	1.78	G		Q	1.285	
0406-311	93.161	0.328	0.083	0.10	0.22	X	04:08:25.96	-31:00:34.4	21.8	-3.98	1.46	4.24	S	EF	G	0.115	*
0410-519	93.873	0.318	0.306	0.98	1.00	PW	04:11:37.15	-51:49:23.3	17.3	-1.01	0.75	1.26	S				
0411-462	93.873	0.232	0.167	1.00	0.98	P	04:12:50.29	-46:04:49.5	18.9	0.99	1.11	1.48	S				
0413-210	94.757	1.369	1.322	0.75	0.73	C?	04:16:04.36	-20:56:27.6	18.6	0.57	0.02	0.58	S		Q	0.808	*,†
0414-467	93.873	0.345	0.293	0.98	0.98	P	04:15:58.69	-46:37:49.1	22.8	-2.65	2.08	3.36	S				
0422-380	93.873	1.239	1.623	0.46	0.98	P	04:24:42.25	-37:56:20.4	17.6	-0.43	0.03	0.43	S		Q	0.782	
0422-389	93.873	0.284	0.219	0.92	0.94	J	04:24:33.72	-38:48:41.4	17.8	0.02	0.14	0.14	S				
0426-380	93.161	1.117	1.094	0.98	0.99	PW	04:28:40.43	-37:56:19.5	18.4	-0.39	-0.02	0.39	S		Q	1.03	
0431-512	93.161	0.457	0.358	0.90	0.90	J	04:32:21.18	-51:09:25.5	17.4	0.96	-0.31	1.01	S		Q	0.557	
0432-606	94.743	0.408	0.408	1.00	1.00	P	04:33:34.11	-60:30:13.4	15.6	-3.59	-2.34	4.29	S	MG			
0435-283	93.867	0.283	0.190	1.00	0.97	P	04:37:48.23	-28:13:39.4	18.9	-0.18	-0.42	0.46	S				
0436-203	93.867	0.327	0.291	0.93	0.96	J	04:38:50.49	-20:12:26.4	21.9	26.20	26.90	37.55	T	EF			
0437-454	93.161	0.597	0.571	0.97	1.00	P	04:39:00.85	-45:22:23.1	20.8	1.46	-0.50	1.54	S				
0438-436	93.161	3.034	2.449	0.98	0.98	P	04:40:17.18	-43:33:08.7	19.1	1.19	-0.70	1.38	S		Q	2.852	
0439-299	93.867	0.283	0.212	0.97	0.83	J	04:41:19.51	-29:52:36.3	20.4	0.53	0.08	0.54	S				
0440-285	93.867	0.357	0.402	0.97	0.97	J?	04:42:37.66	-28:25:30.9	17.8	-0.26	-0.30	0.39	S		Q	1.952	*
0448-392	93.161	0.767	0.582	0.98	1.00	P	04:49:42.26	-39:11:10.0	16.8	0.41	-0.58	0.71	S		Q	1.288	
0450-469	93.161	0.508	0.425	0.99	1.00	P	04:51:53.34	-46:53:20.3	19.8	0.26	-1.34	1.37	G				
0451-282	93.867	1.861	1.596	0.99	0.99	PW	04:53:14.65	-28:07:37.5	17.8	-0.10	-0.57	0.58	S		Q	2.559	†
0452-670	94.743	0.022				X	04:52:09.15	-66:55:23.1					X	CL			
0454-234	93.867	1.705	1.580	0.98	1.00	P	04:57:03.18	-23:24:51.8	18.2	0.83	-0.24	0.87	S		Q	1.009	
0454-463	93.161	1.377	1.208	0.79	0.85	C	04:55:50.77	-46:15:59.0	17.3	2.03	0.25	2.04	S		Q	0.858	
0454-692	94.743	0.036	0.032	0.73	0.55	PX?	04:54:26.08	-69:11:01.2					X	CL			*
0454-810	93.530	1.280	1.481	0.25	0.99	PW	04:50:05.30	-81:01:02.2	18.4	-0.32	0.88	0.93	S		Q	0.444	
0503-608	93.530	0.358	0.409	0.23	0.94	J	05:04:01.62	-60:49:52.4	19.2	-0.49	-0.17	0.52	S				
0506-612	95.855	1.738	1.745	0.01	0.87	C	05:06:43.98	-61:09:41.0	17.0	-0.11	-0.45	0.47	S		Q	1.093	
0508-220	93.867	0.356	0.112	1.96	0.62	L	05:11:00.50	-22:01:55.3	21.9	-10.65	2.70	10.98	T	ST			
0510-689	93.530	0.166	0.131	0.23	0.34	PX	05:09:50.45	-68:53:05.1					X	CF			
0511-220	93.867	0.836	0.977	0.26	0.98	P	05:13:49.12	-21:59:15.9	20.2	2.12	0.57	2.19	G		Q	1.296	
0516-621	94.743	0.765	0.736	0.98	0.99	P	05:16:44.92	-62:07:05.4	21.3	-0.18	-0.62	0.65	S				
0521-365	93.161	8.494	6.131	0.55	0.35	PX	05:22:57.98	-36:27:30.9	16.7	0.02	-0.08	0.08	G		G	0.0553	*,†
0522-611	93.530	0.674	0.820	0.33	0.99	PW	05:22:34.32	-61:07:56.7	17.9	0.62	1.06	1.23	S		Q	1.40	
0524-460	93.161	1.049	0.901	0.92	0.96	PW	05:25:31.40	-45:57:55.2	16.5	1.85	-0.03	1.85	S		Q	1.479	
0524-485	93.873	0.548	0.615	0.20	1.00	P	05:26:16.66	-48:30:36.8	19.9	1.16	-0.86	1.45	S				
0525-574	93.873	0.279	0.192	1.00	1.00	P	05:25:58.57	-57:25:07.9	22.4	-6.99	-10.59	12.69	T	EF			

continued on next page

continued from previous page

Source	Epoch	S _{4.8}	S _{8.6}	$\alpha_{4.8}^{\pm}$	F _{4.8}	F _{8.6}	Type	R.A.	Dec.	B _I	$\Delta\alpha$	$\Delta\delta$	Δr	Class	DSS	ID	z	Annot
0528-250	93.867	0.848	0.604	-0.58	1.00	1.00	P	05:30:07.96	-25:03:29.8	17.7	0.80	0.35	0.87	S		Q	2.779	
0528-454	93.873	0.334	0.247	-0.51	1.00	0.99	P	05:30:24.71	-45:24:28.8	22.8	0.23	-11.75	11.75	T	EF			*
0529-305	93.873	0.299	0.193	-0.74	0.88	0.77	L? M	05:31:15.52	-30:32:14.3	23.4	-0.15	0.30	0.34	T	EF			
0530-727	94.743	0.303	0.305	0.01	0.99	0.99	P	05:29:30.03	-72:45:28.5					X	CF			
0531-418	93.873	0.255	0.158	-0.82	0.67	0.81	C	05:33:31.68	-41:49:18.1	20.7	1.75	1.62	2.39	G				*;†
0532-378	93.161	0.550	0.526	-0.08	0.95	0.97	C	05:34:17.50	-37:47:25.3	21.4	1.18	-0.41	1.25	S				
0534-340	93.873	0.735	0.817	0.18	1.00	1.00	P	05:36:28.43	-34:01:11.3	18.3	0.51	0.14	0.53	S				
0534-611	94.743	0.827	0.767	-0.13	0.98	0.99	P	05:34:35.76	-61:06:07.1	19.8	0.25	0.08	0.27	G	CL			
0535-676	93.530	0.181	0.029	-3.09	0.12	0.47	X	05:35:23.45	-67:35:08.4					X				
0537-286	93.867	0.915	0.696	-0.47	1.00	0.99	P	05:39:54.28	-28:39:55.8	19.3	0.93	-0.36	0.99	S		Q	3.104	
0537-441	93.873	3.291	4.656	0.59	0.98	0.99	PW	05:38:50.35	-44:05:08.9	15.4	0.21	-0.16	0.26	S		Q	0.894	*;†
0538-402	93.873	0.267	0.196	-0.53	0.99	0.98	P	05:40:29.08	-40:15:56.1	24.0	1.99	0.97	2.21	J				
0539-530	93.530	0.531	0.432	-0.35	0.98	0.95	J?	05:40:25.18	-53:03:46.9	20.8	-0.86	-0.78	1.16	S				*
0539-691	93.530	0.847					X	05:38:47.60	-69:04:40.3					X	BG			
0540-693	93.530	0.130	0.036	-2.17	0.24	0.43	X	05:40:10.97	-69:19:54.3					X	EF			
0542-735	93.530	0.808	0.663	-0.34	0.79	0.87	C	05:41:50.69	-73:32:15.4					X	CR			
0549-575	93.873	0.432	0.601	0.56	1.00	0.97	P	05:50:09.58	-57:32:24.5	20.0	-0.90	-1.61	1.84	S				
0558-396	93.873	0.400	0.374	-0.11	0.98	0.96	JW	06:00:31.42	-39:37:02.4	18.6	1.38	0.52	1.47	S				
0601-705	94.743	0.282	0.205	-0.54	0.80	0.99	P M	06:01:11.26	-70:36:08.9					X	CR			
0602-424	93.873	0.658	0.711	0.13	1.00	0.98	P	06:04:25.17	-42:25:30.2	20.4	1.47	2.20	2.65	S				
0606-223	93.867	0.663	0.645	-0.05	1.00	1.00	P	06:08:59.69	-22:20:21.0	19.3	1.22	0.36	1.27	S		Q	1.926	
0607-605	94.743	0.581	0.470	-0.36	0.99	0.98	R?	06:07:55.08	-60:31:52.0	18.5	0.46	-0.14	0.48	S				
0610-316	93.873	0.427	0.370	-0.24	0.84	0.87	J	06:12:29.67	-31:38:57.9	17.8	1.02	0.22	1.05	S				
0610-436	93.873	0.498	0.366	-0.52	1.00	1.00	P	06:12:28.59	-43:37:48.3	17.8	0.21	0.25	0.33	S				
0611-727	94.743	0.310	0.202	-0.73	0.99	0.95	P	06:10:11.64	-72:48:13.4	20.9	1.91	-4.66	5.03	S	EF			*;†
0618-252	93.867	1.214	1.048	-0.25	0.96	0.97	J?	06:20:32.12	-25:15:17.5	18.2	0.53	0.30	0.61	S		Q	1.90	*;†
0619-468	93.873	0.246	0.161	-0.72	0.71	0.78	M	06:21:19.44	-46:49:58.4	19.3	1.18	0.94	1.51	S				*;†
0622-441	93.161	0.363	0.282	-0.43	0.85	0.84	C	06:23:31.77	-44:13:02.6	18.6	1.62	0.03	1.62	G		Q	0.688	
0628-627	94.743	0.525	0.492	-0.11	0.97	0.98	P	06:28:57.49	-62:48:44.8	23.4	0.16	-1.31	1.32	S				
0629-418	93.530	0.671	0.698	0.07	0.98	0.97	JW	06:31:12.00	-41:54:27.0	18.1	1.55	1.34	2.05	S		Q	1.416	
0630-261	93.867	0.255	0.210	-0.33	0.88	0.88	PX	06:32:06.50	-26:14:13.9	20.7	0.81	0.41	0.91	S				
0637-337	93.530	0.669	0.542	-0.36	1.00	1.00	P	06:39:20.90	-33:46:00.0	22.9	1.22	-13.32	13.38	T	EF			*;†
0637-752	93.530	6.378	7.038	0.17	0.89	0.97	C?	06:35:46.38	-75:16:16.8	15.9	-0.34	0.34	0.49	S		Q	2.165	
0642-349	93.530	0.911	0.772	-0.28	1.00	0.99	P M	06:44:25.28	-34:59:41.8	17.2	1.37	0.55	1.48	S		Q	0.455	
0646-306	93.873	1.135	1.115	-0.03	0.98	0.98	P	06:44:14.10	-30:44:19.6	19.9	1.61	0.26	1.63	S				
0647-410	93.873	0.289	0.189	-0.72	0.98	0.93	P	06:49:14.11	-41:08:53.0	19.9	2.45	0.45	2.49	S				

continued on next page

continued from previous page

Source	Epoch	S _{4.8}	S _{8.6}	$\alpha_{4.8}^{\pm}$	F _{4.8}	F _{8.6}	Type	R.A.	Dec.	B _I	$\Delta\alpha$	$\Delta\delta$	Δr	Class	DSS	ID	z	Annot
0656-615	94.743	0.313	0.222	-0.59	0.98	0.99	P	06:57:02.77	-61:39:25.7	22.8	-13.41	3.80	13.93	S	EF			
0658-656	93.530	0.476	0.183	-1.63	0.23	0.24	L	06:58:14.62	-65:44:50.5	14.5	11.07	-0.64	11.09	S	EF			
0700-465	93.530	0.493	0.581	0.28	1.00	1.00	P	07:01:34.55	-46:34:36.6	19.7	0.89	-0.03	0.89	S				
0701-784	94.743	0.180	0.066	-1.72	0.19	0.29	L	06:59:16.51	-78:28:58.1	21.6	2.30	-8.03	8.35	G	EF			
0715-663	94.743	0.251	0.150	-0.87	1.00	0.99	P	07:15:12.99	-66:27:52.0	23.3	8.02	5.78	9.89	J	EF			
0718-633	94.743	0.314	0.197	-0.80	1.00	0.99	P	07:19:07.36	-63:26:59.1	22.3	3.05	3.77	4.85	T	EF			
0722-333	93.873	0.203	0.114	-0.99	0.81	0.71	L	07:23:55.21	-33:28:54.6	23.5	4.72	3.01	5.59	J	EF			
0725-444	93.873	0.356	0.234	-0.71	0.99	0.97	P	07:26:57.55	-44:35:19.1	19.7	-4.07	-5.08	6.51	S	EF			*;†
0726-476	93.873	0.440	0.440	0.00	0.97	0.98	P M	07:28:23.51	-47:45:17.0	22.3	0.87	-8.28	8.33	T	EF			
0728-320	93.530	0.316	0.218	-0.63	0.99	1.00	P M	07:30:38.30	-32:08:20.9					X	CR			
0731-465	93.530	0.491	0.359	-0.53	0.98	0.98	P	07:32:44.31	-46:40:18.2	22.0	0.44	-0.20	0.49	S				
0738-674	94.743	0.452	0.482	0.11	0.98	0.99	PW	07:38:56.50	-67:35:50.8	18.2	1.54	2.05	2.56	S		Q	1.663	
0744-691	94.743	0.254	0.246	-0.05	0.97	0.98	J	07:44:20.39	-69:19:07.0	22.5	0.65	-0.33	0.73	T				
0745-330	93.530	0.700	0.756	0.13	0.98	0.99	PW	07:47:19.70	-33:10:47.8					X	EF			
0802-276	93.867	0.753	0.637	-0.28	0.99	1.00	P	08:04:51.46	-37:49:11.4					X	EF			
0804-267	93.867	0.561	0.523	-0.12	0.94	0.96	C	08:06:12.72	-26:52:33.4					X	ST			*;†
0806-710	94.743	0.284	0.181	-0.77	0.30	0.43	C	08:06:34.10	-71:12:15.7	18.9	-0.46	0.69	0.83	S				
0809-493	93.530	0.535	0.529	-0.02	0.89	0.91	PX	08:11:08.89	-49:29:45.6	22.5	0.97	-2.16	2.36	T				
0813-741	94.743	0.235	0.148	-0.78	0.70	0.55	J	08:12:30.84	-74:20:15.2	21.0	5.57	-0.31	5.58	G	EF			
0823-223	93.867	0.594	0.550	-0.13	0.80	0.94	C	08:26:01.58	-22:30:27.3	16.0	-0.11	0.20	0.23	S		Q	0.91	
0834-201	93.867	1.731	1.863	0.12	0.99	0.99	P	08:36:39.22	-20:16:59.0	18.9	2.39	0.54	2.45	S		Q	2.752	
0834-223	93.867	0.274	0.235	-0.26	0.90	0.92	J	08:36:50.78	-22:33:10.1	18.0	0.57	0.98	1.14	G				
0839-314	93.870	0.173	0.174	0.01	0.98	0.98	P	08:41:32.61	-31:36:35.4					X	EF			
0847-572	93.530	0.267	0.073	-2.19	0.23	0.28	X	08:48:03.86	-57:27:14.3					X	CR			
0858-771	94.743	0.309	0.193	-0.80	0.62	0.53	L	08:57:42.63	-77:19:31.8	17.7	-0.40	0.62	0.74	S		Q	0.49	
0902-256	93.867	0.598	0.716	0.31	1.00	1.00	P	09:04:52.19	-25:52:51.7	17.8	1.16	0.59	1.30	S		Q	1.635	
0903-573	93.530	1.309	1.127	-0.25	0.57	0.52	J	09:04:53.36	-57:35:07.6					X	EX	Q	0.695	
0912-330	93.870	0.385	0.288	-0.50	1.00	1.00	P	09:14:36.72	-33:14:52.1					X	ST			
0915-213	93.867	0.605	0.583	-0.06	0.94	0.95	J	09:17:27.03	-21:31:34.3	18.9	1.36	1.38	1.94	G		Q	0.847	
0919-260	93.867	1.805	1.665	-0.14	1.00	1.00	P	09:21:29.36	-26:18:43.2	18.2	0.63	-0.14	0.65	S		Q	2.30	
0920-397	93.870	1.593	1.438	-0.17	0.81	0.89	C	09:22:46.42	-39:59:34.9					X	ST	Q	0.591	
0921-213	93.867	0.402	0.365	-0.16	0.82	0.98	PW	09:23:38.90	-21:35:47.3	16.4	1.31	0.34	1.35	G		G	0.053	
0925-203	93.867	0.709	0.732	0.05	0.82	0.93	C	09:27:51.83	-20:34:50.7	16.4	1.10	0.98	1.47	S		Q	0.348	
0928-787	93.530	0.450	0.254	-0.97	0.97	0.97	P	09:27:49.62	-79:00:53.4	17.0	9.87	-13.19	16.47	S	EF			
0930-338	93.870	0.381	0.342	-0.18	1.00	0.99	P	09:32:36.50	-34:05:58.3	19.5	1.31	0.24	1.33	S				
0936-853	93.530	0.562	0.548	-0.04	0.92	0.95	J	09:30:32.61	-85:33:59.8	20.3	0.99	-0.25	1.02	G				

continued on next page

continued from previous page

Source	Epoch	S _{4.8}	S _{8.6}	$\alpha_{8.6}^{\circ}$	F _{4.8}	F _{8.6}	Type	R.A.	Dec.	B _I	$\Delta\alpha$	$\Delta\delta$	Δr	Class	DSS	ID	z	Annot
0945-321	93.870	0.434	0.342	-0.41	0.98	0.98	JW	09:48:09.51	-32:23:47.2	17.1	-1.29	2.50	2.81	S		Q	2.14	
0958-314	93.870	0.283	0.309	0.15	0.76	0.76	C	10:00:40.84	-31:39:52.1	12.3	2.24	-2.48	3.34	G		G	0.008	
0959-307	93.870	0.249	0.193	-0.44	0.65	0.78	J	10:01:38.96	-30:58:36.3	18.9	1.51	0.38	1.55	S				
0959-443	93.530	0.585	0.474	-0.36	0.63	0.87	C	10:02:00.02	-44:38:01.4					X	EX	Q	0.837	
1005-739	94.743	0.166	0.141	-0.28	0.99	1.00	P	10:06:04.19	-74:09:44.2	20.6	-0.46	-0.56	0.73	S				
1010-427	93.870	0.235	0.171	-0.54	0.93	0.92	J	10:12:36.96	-42:59:05.6					X	EF			
1016-311	93.870	0.432	0.367	-0.28	1.00	1.00	P	10:18:28.75	-31:23:53.5	17.6	0.95	0.86	1.28	S				
1021-323	93.870	0.460	0.483	0.08	1.00	0.99	P	10:24:00.43	-32:34:16.0	18.2	0.35	1.38	1.43	S				
1029-222	93.867	0.306	0.231	-0.48	1.00	1.00	P	10:31:52.31	-22:28:24.3	15.3	-11.59	17.87	21.30	S	EF			
1029-331	93.870	0.232	0.123	-1.08	0.70	0.63	C	10:33:07.65	-33:23:05.3	22.9	1.03	-0.08	1.03	T				
1030-357	93.870	0.391	0.262	-0.68	0.69	0.73	J	10:37:16.08	-36:01:56.3	18.5	1.14	1.41	1.81	S		Q	1.455	*;†
1034-293	93.867	1.190	1.406	0.28	1.00	1.00	P	10:37:16.08	-29:34:02.8	15.9	1.33	-0.62	1.47	S		Q	0.312	*;†
1034-374	93.870	0.575	0.760	0.47	0.96	0.99	P M	10:36:53.43	-37:44:14.4	17.8	0.93	2.53	2.70	S		Q	1.821	*;†
1035-281	93.867	0.277	0.239	-0.25	0.96	0.98	R	10:37:42.46	-28:23:04.3	18.5	0.82	-1.81	1.99	S				
1035-728	94.743	0.272	0.148	-1.03	0.43	0.42	L	10:37:12.80	-73:05:31.0	18.3	-0.49	4.41	4.43	S	OK			
1036-431	93.870	0.239	0.196	-0.33	0.98	0.98	P	10:38:14.70	-43:25:46.1	18.5	0.85	-0.66	1.07	S				
1046-409	93.870	0.898	0.610	-0.66	0.55	0.65	C	10:48:38.27	-41:13:59.9	16.9	0.71	1.72	1.86	S		Q	0.62	
1048-313	93.870	0.790	0.691	-0.23	0.98	0.99	P	10:51:04.78	-31:38:14.1	18.5	0.70	0.42	0.82	S				
1049-650	94.743	0.347	0.312	-0.18	0.98	0.98	JW	10:51:23.55	-65:18:08.6					X	EF			
1055-243	93.166	0.566	0.403	-0.58	0.99	0.99	P	10:57:55.41	-24:33:48.2	19.9	0.59	0.76	0.96	S				
1055-301	93.867	0.360	0.307	-0.27	1.00	1.00	P	10:58:00.42	-30:24:54.9	19.0	2.02	0.77	2.16	S				
1057-797	93.530	1.455	1.574	0.13	1.00	0.99	P	10:58:43.35	-80:03:54.3	18.7	-1.21	0.31	1.25	S				
1101-325	93.870	0.445	0.404	-0.16	0.72	0.90	C	11:03:31.52	-32:51:16.5	16.5	0.98	-0.18	1.00	S		G	0.3554	*;†
1101-536	93.870	0.971	1.084	0.19	0.95	0.99	PX	11:03:52.23	-53:57:00.7					X	ST			*
1102-242	93.166	0.602	0.776	0.43	0.99	0.99	P	11:04:46.18	-24:31:24.9	20.6	0.05	0.91	0.92	S		Q	1.66	
1104-445	93.870	2.960	2.842	-0.07	0.99	0.98	P M	11:07:08.70	-44:49:07.6	16.9	1.00	0.14	1.01	S		Q	1.598	
1105-680	93.164	1.198	1.034	-0.25	0.99	0.97	P M	11:07:12.69	-68:20:50.7					X	ST	Q	0.588	
1110-217	93.166	0.728	0.493	-0.66	1.00	1.00	P	11:12:49.84	-21:58:28.5	23.0	-0.22	2.16	2.17	J				
1116-462	93.870	1.523	1.216	-0.38	0.81	0.88	J	11:18:26.96	-46:34:14.9	16.6	0.00	1.06	1.06	S		Q	0.713	*;†
1117-270	93.867	0.643	0.673	0.08	0.97	1.00	P M	11:20:16.19	-27:19:06.2	18.8	0.47	1.08	1.18	S				*;†
1121-664	93.164	0.372	0.243	-0.73	0.23	0.14	X	11:24:02.14	-66:45:24.2					X	EF			
1126-506	93.870	0.348	0.236	-0.66	1.00	0.99	P	11:28:52.35	-50:55:42.8	17.6	-8.83	3.22	9.39	S	EF			
1133-681	94.743	0.473	0.388	-0.34	0.99	0.99	P	11:36:02.10	-68:27:05.8	21.6	1.83	0.28	1.85	X				
1133-739	93.164	0.617	0.578	-0.11	0.75	0.74	J	11:36:09.68	-74:15:45.4					S				
1142-225	93.166	0.746	0.639	-0.26	1.00	1.00	P	11:45:22.05	-22:50:31.1	19.0	0.70	4.98	5.03	S	EF			
1143-245	93.166	1.441	1.002	-0.62	0.98	1.00	P M	11:46:08.10	-24:47:33.0	17.7	0.48	-0.48	0.68	S		Q	1.95	

continued on next page

continued from previous page

Source	Epoch	$S_{4.8}$	$S_{8.6}$	$\alpha_{8.6}^{\pm}$	$F_{4.8}$	$F_{8.6}$	Type	R.A.	Dec.	B_I	$\Delta\alpha$	$\Delta\delta$	Δr	Class	DSS	ID	z	Annot
1143-287	93.867	0.302	0.291	-0.06	0.99	0.99	P	11:46:26.20	-28:59:18.5	19.5	1.79	-0.76	1.95	S		Q	0.45	
1143-696	94.743	0.554	0.666	0.31	1.00	0.98	P	11:45:53.65	-69:54:01.8					X	WK			
1144-379	93.870	2.512	2.963	0.28	0.98	1.00	P	11:47:01.37	-38:12:10.7	18.4	-0.32	-0.48	0.58	S		Q	1.048	*
1145-676	93.164	1.375	1.213	-0.21	0.90	0.97	J	11:47:33.40	-67:53:41.7					X	EF			*,†
1148-671	93.164	1.641	1.108	-0.67	0.99	0.99	P	11:51:13.46	-67:28:11.0					X	EF			
1150-723	93.164	0.448	0.243	-1.04	0.38	0.29	L	11:52:56.83	-72:39:24.3					X	EF			
1156-221	93.166	0.501	0.323	-0.75	0.90	0.85	R	11:59:11.29	-22:28:36.1	18.6	1.73	1.20	2.10	S		Q	0.565	
1156-663	94.743	0.289	0.262	-0.16	0.98	0.99	PW	11:59:18.33	-66:35:39.5					X	EF			
1157-215	93.867	0.724	0.524	-0.55	0.98	1.00	P	11:59:51.91	-21:48:53.9	17.5	0.98	-0.12	0.99	S		Q	0.927	
1202-262	93.166	0.927	0.843	-0.16	0.64	0.76	L?	12:05:33.22	-26:34:04.3	19.8	0.79	0.16	0.80	S		Q	0.789	*,†
1206-202	93.867	0.582	0.595	0.04	0.99	1.00	P	12:09:14.61	-20:32:38.5	22.3	1.59	0.04	1.59	T				
1206-238	93.867	0.921	0.955	0.06	1.00	1.00	P	12:09:02.45	-24:06:21.3	19.1	0.32	-0.82	0.88	S				
1206-399	93.870	0.385	0.293	-0.47	0.99	0.98	P	12:09:35.24	-40:16:13.1	17.2	0.98	0.59	1.15	S		Q	0.966	
1221-829	93.530	0.618	0.534	-0.25	0.97	0.98	PW	12:24:54.43	-83:13:10.2	21.9	5.19	4.31	6.75	T	EF			*,†
1228-700	94.743	0.237	0.150	-0.78	0.49	0.41	L	12:31:30.85	-70:20:42.3					X	MG			†
1236-684	93.164	0.597	0.501	-0.30	0.98	0.97	PW	12:39:46.66	-68:45:30.8					X	ST			
1244-255	95.847	0.984	1.322	0.50	0.96	0.93	J	12:46:46.80	-25:47:49.5	16.2	1.06	0.20	1.07	S		Q	0.638	
1248-350	93.870	0.281	0.322	0.23	0.99	0.99	P	12:51:39.22	-35:18:39.5	21.2	0.29	0.58	0.65	S				
1250-330	93.870	0.441	0.474	0.13	0.99	1.00	P	12:52:58.39	-33:19:59.9	21.4	-0.44	-0.38	0.58	S				
1250-655	93.164	0.313	0.187	-0.88	0.47	0.38	L	12:53:46.07	-65:48:17.0					X	ST			
1251-713	93.164	1.507	1.359	-0.18	0.95	0.98	PW	12:54:59.91	-71:38:18.3					X	EF			
1254-333	93.870	0.475	0.211	-1.38	0.29	0.33	L	12:57:21.51	-33:34:35.7	17.0	8.93	8.91	12.61	S	ST	Q	0.19	*
1255-316	94.571	1.507	1.458	-0.06	0.99	0.98	P	12:57:59.06	-31:55:16.8	18.5	0.10	1.09	1.09	S		Q	1.924	
1255-670	94.743	0.177	0.206	0.26	0.94	0.96	P	12:58:28.59	-67:19:42.6					X	EF			
1256-220	93.166	0.685	0.614	-0.19	0.97	0.99	J	12:58:54.48	-22:19:31.1	19.6	0.27	0.92	0.96	S		Q	1.306	
1256-229	93.166	0.482	0.482	0.00	0.98	0.99	JW	12:59:08.47	-23:10:38.7	16.7	-1.19	-0.54	1.30	S				
1256-243	94.571	0.372	0.292	-0.41	0.96	0.95	JW	12:59:12.62	-24:36:05.5	17.6	-0.69	-0.24	0.73	S		Q	2.263	
1258-321	93.870	0.428	0.269	-0.79	0.33	0.44	C?	13:01:00.79	-32:26:29.0	13.1	0.05	1.64	1.64	G		G	0.017	*,†
1302-208	94.571	0.309	0.228	-0.51	0.75	0.73	J	13:04:59.07	-21:06:42.4	21.8	0.00	0.18	0.18	T				
1303-827	93.530	0.481	0.321	-0.69	0.46	0.56	C?	13:08:38.28	-82:59:35.0	17.0	1.79	-1.84	2.57	S		G		*,†
1304-215	94.571	0.142	0.114	-0.37	0.71	0.83	J	13:06:42.05	-21:47:51.1	18.8	-0.16	-0.14	0.22	G				
1305-668	94.743	0.386	0.339	-0.22	0.97	0.97	R	13:08:17.39	-67:07:05.2					X	EF			*
1306-678	94.743	0.241	0.140	-0.93	0.63	0.49	L	13:09:39.59	-68:08:51.3					X	EF			
1313-333	94.571	1.854	2.202	-0.29	0.98	0.98	PW	13:16:07.98	-33:38:59.2	16.8	-0.34	-0.29	0.45	S		Q	1.21	
1318-263	94.571	0.477	0.403	-0.29	0.99	0.98	PW	13:21:14.03	-26:36:10.4	20.4	-0.10	0.44	0.45	S				
1327-206	93.166	0.305	0.218	-0.57	0.80	0.84	C	13:30:07.70	-20:56:16.5	16.4	4.10	-2.12	4.62	S	ST	Q	1.169	*

continued on next page

continued from previous page

Source	Epoch	S _{4.8}	S _{8.6}	$\alpha_{8.6}^{\pm}$	F _{4.8}	F _{8.6}	Type	R.A.	Dec.	B _I	$\Delta\alpha$	$\Delta\delta$	Δr	Class	DSS	ID	z	Annot
1327-311	93.870	0.705	0.590	-0.30	1.00	1.00	P	13:30:19.09	-31:22:59.3	18.5	0.15	0.62	0.64	S		Q	1.335	
1328-263	94.571	0.170	0.167	-0.02	0.95	0.99	L	13:31:11.69	-26:39:09.7	17.2	0.94	0.91	1.31	S		Q	0.883	
1330-657	94.743						ND											
1334-649	93.164	0.920	1.089	0.29	0.90	0.96	C	13:37:52.45	-65:09:25.0					X	WK			
1336-237	94.571	0.500	0.565	0.21	0.99	0.98	PW	13:39:01.74	-24:01:13.8	17.4	0.32	-0.09	0.33	S				
1336-260	94.571	0.867	0.792	-0.15	1.00	1.00	P	13:39:19.88	-26:20:30.4	20.1	0.05	0.56	0.56	S				
1337-875	93.533	0.320	0.242	-0.48	0.95	0.93	J?	13:53:02.07	-87:51:07.9	0.0	18.37	5.62	19.21	S	EF		*	
1339-287	94.571	0.414	0.377	-0.16	0.98	0.99	PW	13:42:15.34	-29:00:41.9	18.8	1.38	-0.90	1.65	S			* _{,†}	
1343-601	94.743	2.925	2.368	-0.36	0.80	0.83	J	13:46:49.06	-60:24:29.4					X	EF			
1344-685	94.743	0.134	0.047	-1.77	0.18	0.49	PX	13:47:48.85	-68:44:56.4					X	EF			
1348-289	94.571	0.237	0.205	-0.24	0.96	0.95	J?	13:51:46.84	-29:12:17.5	19.3	0.46	-0.30	0.55	S				
1349-439	93.164	0.608	0.724	0.30	0.99	0.98	PW	13:52:56.54	-44:12:40.4	17.4	2.18	0.47	2.23	S				
1350-662	94.743	0.441	0.412	-0.12	0.39	0.27	C	13:53:57.02	-66:30:50.5					X	EX			
1353-341	93.870	0.605	0.719	0.30	0.95	0.98	C	13:56:05.39	-34:21:10.6	18.6	-0.77	-0.14	0.79	G				
1355-215	94.571	0.261	0.167	-0.76	0.77	0.78	C	13:58:38.23	-21:48:54.9	19.9	1.14	1.27	1.70	S				
1359-281	94.571	0.649	0.478	-0.52	0.88	0.83	C	14:02:02.40	-28:22:25.2	18.7	1.70	-1.22	2.09	S				
1401-688	94.743	0.415	0.347	-0.31	0.90	0.93	C	14:05:28.39	-69:04:02.1					X	WK			
1404-267	94.571	0.420	0.333	-0.40	0.85	0.91	C	14:07:29.75	-27:01:04.4	13.6	-0.89	1.18	1.48	G				
1404-342	94.743	0.370	0.254	-0.64	0.83	0.87	J	14:07:54.93	-34:31:28.0	17.7	0.24	0.48	0.53	S				
1405-287	94.571	0.380	0.350	-0.14	0.89	0.90	J	14:08:49.61	-29:00:23.6	16.9	1.02	-0.34	1.08	S			* _{,†}	
1406-230	94.571	0.354	0.241	-0.65	0.99	1.00	PW	14:09:11.97	-23:15:49.5	17.7	1.56	-1.40	2.10	G			* _{,†}	
1406-267	94.571	0.525	0.700	0.49	1.00	0.99	PW	14:09:50.16	-26:57:37.0	21.8	1.10	1.76	2.07	S				
1412-368	94.743	0.832	0.818	-0.03	1.00	0.98	P	14:15:26.03	-37:05:26.8	22.7	0.33	2.02	2.04	T				
1414-408	94.743	0.241	0.136	-0.97	0.83	0.74	J	14:18:03.16	-41:04:13.6	22.2	-4.68	-10.23	11.25	S	EF			
1415-349	94.743	0.574	0.530	-0.14	0.99	1.00	P	14:18:58.92	-35:09:42.4	18.6	1.44	0.72	1.61	S				
1417-782	95.847	0.225	0.209	-0.13	0.93	0.96	P M	14:23:43.53	-78:29:34.8	18.2	0.46	-1.72	1.78	S			*	
1420-679	93.164	0.870	0.987	0.21	0.97	1.00	P	14:24:55.56	-68:07:58.1					X	EF			
1420-724	94.743	0.371	0.324	-0.23	0.97	0.98	C	14:24:52.27	-72:41:17.0					X	CR			
1421-490	93.164	5.538	4.165	-0.48	0.95	0.93	J	14:24:32.23	-49:13:50.0					X	EF			
1424-418	93.164	2.251	1.795	-0.39	0.95	0.94	J?	14:27:56.29	-42:06:19.6	17.6	0.04	0.72	0.72	S				
1427-448	94.743	0.391	0.276	-0.59	0.82	0.95	R M	14:31:07.17	-45:01:17.4	22.1	-4.02	-2.33	4.64	T	OK			
1427-742	94.743	0.116	0.063	-1.06	0.62	0.71	J	14:32:19.78	-74:27:40.0	13.2	-5.87	1.81	6.14	S	OK			
1435-218	94.571	0.590	0.549	-0.12	0.98	0.99	PW	14:38:09.47	-22:04:54.6	17.4	0.81	1.20	1.45	S				
1438-347	94.743	0.300	0.228	-0.47	1.00	1.00	P	14:41:23.96	-34:56:45.7	17.6	2.64	0.14	2.65	S				
1442-699	94.743	0.207	0.115	-1.01	0.46	0.41	C	14:47:05.25	-70:08:16.5					X	EF			
1448-232	94.571	0.268	0.170	-0.77	0.99	1.00	PW	14:51:02.50	-23:29:30.7	18.8	0.11	0.68	0.69	G				

continued on next page

continued from previous page

Source	Epoch	S _{4.8}	S _{8.6}	$\alpha_{8.6}^{\pm}$	F _{4.8}	F _{8.6}	Type	R.A.	Dec.	B _J	$\Delta\alpha$	$\Delta\delta$	Δr	Class	DSS	ID	z	Annot
1448-648	94.743	0.407	0.330	-0.35	0.98	0.99	P	14:52:39.69	-65:02:03.4	19.6	-5.29	0.56	5.32	X	EF			
1450-338	94.743	0.504	0.323	-0.76	1.00	1.00	P	14:54:02.47	-34:00:57.0	16.4	-1.99	0.73	2.12	G	CR	Q	0.314	
1451-375	93.164	1.382	1.358	-0.03	0.90	0.97	C	14:54:27.43	-37:47:32.8	16.7	-4.12	0.50	4.15	S	MG	Q	1.81	
1451-400	93.164	0.950	0.850	-0.19	0.99	0.99	P	14:54:32.93	-40:12:32.4	21.6	11.38	-13.67	17.79	G				*
1452-367	93.164	0.352	0.230	-0.72	0.54	0.75	J	14:55:09.65	-36:55:07.2	18.3	0.29	0.49	0.57	S				
1454-354	94.743	0.625	0.582	-0.12	0.96	0.95	J	14:57:26.70	-35:39:09.9	13.3	2.91	0.19	2.92	S				
1455-399	93.164	0.431	0.272	-0.78	0.89	0.72	J	14:58:36.36	-40:08:07.8	20.1	-2.30	3.56	4.24	S	OK	Q	1.105	
1456-367	93.164	0.633	0.405	-0.76	0.97	0.97	PW	14:59:15.78	-36:55:47.6	17.6	0.49	-0.82	0.96	S				
1508-325	94.743	0.477	0.404	-0.28	0.98	0.97	J	15:11:50.39	-32:42:57.7					X	CR			
1508-649	94.743	0.229	0.139	-0.85	1.00	1.00	P	15:12:33.37	-65:06:56.3					X	CR			
1508-656	94.743	0.224	0.204	-0.16	0.99	0.99	P	15:12:51.56	-65:53:02.3	21.9	-0.27	0.90	0.94	S				
1511-210	94.571	0.444	0.566	0.41	0.99	1.00	P	15:13:56.97	-21:14:57.2	16.4	1.33	-0.09	1.34	G		G	0.042	
1514-241	94.571	3.144	3.249	0.06	0.97	0.99	PW M	15:17:41.81	-24:22:19.3	18.0	0.52	1.48	1.57	S				
1519-273	94.571	1.743	1.722	-0.02	0.99	1.00	P	15:22:37.68	-27:30:10.6	18.6	4.33	12.16	12.91	S	EF			
1519-294	94.571	0.282	0.234	-0.32	0.97	0.98	PW	15:22:25.48	-29:36:25.0	21.2	12.10	-0.52	12.11	S	EF			
1528-274	94.571	0.253	0.185	-0.53	0.81	0.75	PX	15:31:24.20	-27:35:31.1	20.3	-0.05	-1.94	1.94	G				
1540-828	93.164	0.682	0.565	-0.32	1.00	1.00	PW	15:50:59.14	-82:58:06.8					X	EF			
1548-560	93.870	0.022					X	15:52:38.62	-56:11:10.9	19.4	1.31	-1.25	1.81	G		G	0.15	
1549-790	93.164	4.764	3.483	-0.53	0.99	1.00	P	15:56:58.95	-79:14:04.2	19.4	0.10	0.22	0.24	S		Q	2.145	
1550-269	94.571	0.847	0.723	-0.27	0.96	0.97	PW	15:54:02.47	-27:04:40.2	17.8	2.08	0.54	2.14	S		Q	2.813	
1556-245	94.571	0.380	0.276	-0.54	1.00	1.00	P	15:59:41.41	-24:42:38.6	21.0	1.08	3.48	3.65	S	EF			
1601-222	94.571	0.415	0.244	-0.90	1.00	1.00	P	16:04:01.47	-22:23:40.7	16.2	2.17	1.48	2.63	S				
1602-633	93.164	0.149					X	16:07:07.75	-63:31:36.8	19.3	0.68	0.04	0.69	S				
1604-333	93.870	0.368	0.311	-0.28	0.93	1.00	P M	16:07:34.76	-33:31:09.1	19.7	0.76	0.12	0.77	G		Q	1.71	
1610-771	93.164	3.073	2.719	-0.21	0.98	0.98	PW	16:17:49.29	-77:17:18.4	21.6	1.21	0.95	1.54	S				
1611-710	94.743	0.513	0.466	-0.16	1.00	1.00	P	16:16:30.67	-71:08:31.3	17.2	0.35	0.80	0.87	S		Q	1.36	
1619-680	93.164	1.889	1.396	-0.51	1.00	1.00	P	16:24:18.43	-68:09:12.3	21.0	8.94	3.48	9.59	G	EF	G	0.786	
1622-253	94.571	2.083	2.622	0.39	0.95	0.98	PW	16:25:46.89	-25:27:38.4	18.5	0.56	-0.24	0.61	S		Q	0.815	
1622-297	94.571	2.060	2.098	0.03	0.98	0.99	P	16:26:06.02	-29:51:26.8	16.3	-1.64	1.25	2.06	G		G	0.0427	
1637-771	93.164	0.393	0.338	-0.26	0.51	0.79	PW	16:44:16.12	-77:15:48.8	14.1	-0.38	-5.00	5.01	S	MG			
1643-223	94.571	0.598	0.313	-1.10	0.60	0.51	L	16:46:04.82	-22:28:04.1	21.3	1.13	5.25	5.37	G	WK	G	0.0944	* [†]
1649-788	93.533	0.246	0.129	-1.10	0.45	0.41	L	16:57:34.51	-78:58:48.4	14.2	-0.31	-1.66	1.69	S				
1655-776	93.164	0.988	0.660	-0.69	0.43	0.35	L	17:02:41.01	-77:41:57.5	16.9	2.42	-0.78	2.54	S		G	0.0142	
1657-261	94.571	2.116	2.149	0.03	0.99	0.99	P	17:00:53.15	-26:10:51.6	9.5	2.67	1.11	2.89	S				
1718-649	93.164	4.481	3.542	-0.40	0.99	0.98	PW M	17:23:41.03	-65:00:36.5	17.5	0.87	-0.72	1.13	S				
1719-729	93.164	0.557	0.545	-0.04	1.00	0.99	P	17:26:01.09	-72:59:59.9									

continued on next page

continued from previous page

Source	Epoch	S _{4.8}	S _{8.6}	$\alpha_{4.8}^{\pm}$	F _{4.8}	F _{8.6}	Type	R.A.	Dec.	B _I	$\Delta\alpha$	$\Delta\delta$	Δr	Class	DSS	ID	z	Annot
1725-795	93.533	0.368	0.508	0.55	1.00	1.00	P	17:33:40.70	-79:35:55.8	17.7	2.00	-0.28	2.02	S				
1727-214	94.571	0.286					X	17:30:43.55	-21:32:02.0					X	EF			
1732-598	93.533	0.444	0.493	0.18	1.00	0.99	P	17:36:30.80	-59:51:58.7	21.5	-0.06	0.03	0.07	S				
1733-565	93.533	2.085	0.971	-1.30	0.24	0.35	C	17:37:35.74	-56:34:03.2	17.2	0.10	0.36	0.37	G	EF	G	0.098	
1756-686	93.164	0.411	0.271	-0.71	0.89	0.95	C	18:01:34.71	-68:39:57.8	20.3	0.51	-13.84	13.85	S				
1758-494	93.533	0.525	0.394	-0.49	0.90	0.93	J	18:02:09.87	-49:25:11.3	18.6	0.57	-2.14	2.22	G				
1758-651	93.164	0.642	0.660	0.05	1.00	1.00	PW	18:03:23.50	-65:07:36.8	15.2	3.45	-3.27	4.75	S	MG			
1800-660	93.533	0.212	0.162	-0.46	0.94	0.96	PX	18:05:53.10	-66:00:16.9	17.2	1.22	0.22	1.23	S				†
1800-709	93.164	0.506	0.406	-0.38	0.78	0.83	C	18:06:23.68	-70:58:28.7	21.7	0.59	0.31	0.67	T				
1814-766	93.533	0.338	0.253	-0.49	1.00	0.98	P	18:21:24.73	-76:35:00.2	14.3	0.54	0.12	0.56	V		G	0.0185	
1815-553	93.533	1.163	1.112	-0.08	0.99	0.99	P	18:19:45.38	-55:21:20.6	13.3	0.13	0.19	0.23	S				
1823-455	93.533	0.662	0.672	0.02	0.98	0.98	J	18:27:10.24	-45:33:09.8	18.1	-0.49	0.41	0.64	S			*	
1830-211	94.571	9.661	8.060	-0.31	0.97	0.93		18:33:40.02	-21:03:40.2					X	CR		†	
1831-711	93.164	2.161	2.106	-0.04	0.99	0.99	PW	18:37:28.72	-71:08:43.5	17.8	-0.80	0.25	0.83	S		Q	1.356	
1833-772	93.164	0.432	0.305	-0.59	0.61	0.51		18:40:38.58	-77:09:28.3	14.3	-0.13	2.03	2.04	V			†	
1853-534	93.870	0.532	0.411	-0.44	1.00	1.00	PW	18:57:00.45	-53:25:00.2	21.8	-0.63	-0.08	0.63	S				
1903-802	93.530	1.159	1.077	-0.12	0.99	0.99	P	19:12:40.14	-80:10:05.8	19.6	1.70	0.25	1.72	S		Q	0.50	
1907-872	94.743	0.459	0.429	-0.11	1.00	1.00	P	19:34:25.87	-87:11:59.7	0.0	7.32	-16.31	17.88	S	EF			
1910-466	93.533	0.506	0.401	-0.40	0.90	0.99	P M	19:14:13.83	-46:31:32.0	16.9	0.48	0.98	1.10	S				
1915-458	93.533	0.570	0.494	-0.24	0.92	0.95	J	19:19:16.71	-45:43:38.7	17.2	0.49	0.34	0.60	S				
1918-634	93.533	0.109	0.041	-1.66	0.33	0.42	L	19:22:28.11	-63:16:17.7	18.4	-0.26	7.20	7.21	S	EF			
1922-341	94.743	0.415	0.384	-0.14	0.96	0.99	PW	19:25:17.02	-34:01:01.3	14.5	0.00	0.05	0.05	S			* , †	
1925-610	93.533	0.937	0.960	0.04	0.99	0.99	P M	19:30:06.16	-60:56:09.2	18.5	-0.17	-0.09	0.19	S				
1928-698	93.533	0.328	0.265	-0.36	0.96	0.96	PW	19:33:31.16	-69:42:58.6	18.9	1.34	0.33	1.38	S				
1929-457	93.164	1.029	0.982	-0.08	0.86	0.94	P M	19:32:44.90	-45:36:38.0	15.8	1.15	1.75	2.09	S		Q	0.652	
1933-400	94.743	0.948	0.849	-0.19	0.98	0.98	PW	19:37:16.22	-39:58:01.5	17.7	0.00	0.69	0.69	S		Q	0.966	
1935-452	93.533	0.266	0.217	-0.34	0.93	0.91	PX	19:39:30.11	-45:10:01.2	18.9	0.66	1.05	1.24	S			*	
1936-623	93.533	0.831	0.570	-0.64	0.87	0.92	C	19:41:21.76	-62:11:21.1	22.4	-0.93	0.11	0.94	T				
1941-554	93.533	0.749	0.675	-0.18	0.98	1.00	PW	19:45:24.21	-55:20:48.7	13.3	2.13	2.09	2.99	V		G	0.0147	
1953-325	94.743	0.445	0.545	0.34	0.97	0.99	PW	19:56:59.45	-32:25:45.8	19.9	-0.20	-1.28	1.30	S		Q	1.242	
1953-879	93.533	0.052					X	20:20:25.00	-87:46:11.3	22.8	-10.56	-2.44	10.84	T	EF			
1954-388	94.743	2.856	3.131	0.16	0.98	0.99	PW	19:57:59.82	-38:45:06.1	17.8	0.82	-0.33	0.89	S		Q	0.63	
1955-470	93.533	0.158	0.055	-1.80	0.22	0.34	L	19:58:56.90	-46:57:38.0	22.9	0.64	1.36	1.50	T				
2000-330	93.164	1.003	0.846	-0.29	1.00	1.00	P	20:03:24.12	-32:51:45.4	19.6	0.59	-1.39	1.51	G		Q	3.773	
2002-375	94.743	0.504	0.461	-0.15	0.99	0.98	PW	20:05:55.07	-37:23:41.2	21.9	-6.89	-6.81	9.69	T	EF			
2004-447	93.533	0.546	0.413	-0.47	1.00	0.99	P	20:07:55.20	-44:34:44.3	18.1	1.42	-0.81	1.64	S		Q	0.238	

continued on next page

continued from previous page

Source	Epoch	S _{4.8}	S _{8.6}	$\alpha_{8.6}^{\pm}$	F _{4.8}	F _{8.6}	Type	R.A.	Dec.	B _I	$\Delta\alpha$	$\Delta\delta$	Δr	Class	DSS	ID	z	Annot
2005-489	93.533	1.052	0.991	-0.10	0.99	0.99	PW	20:09:25.40	-48:49:53.6	15.9	-0.62	0.17	0.64	G		Q	0.071	
2012-349	94.743	0.393	0.246	-0.80	0.99	1.00	P	20:15:25.28	-34:45:29.7	22.2	-8.86	15.50	17.85	T	EF			
2013-307	94.743	0.344	0.209	-0.85	0.77	0.72	J	20:16:29.95	-30:35:18.2	19.9	2.22	1.22	2.53	S		Q	0.978	*,†
2013-454	93.533	0.284	0.108	-1.64	0.32	0.30	L?	20:17:13.04	-45:16:47.2	17.6	15.09	5.38	16.02	S	EF			
2014-380	94.743	0.199	0.167	-0.30	0.98	0.99	P	20:17:28.57	-37:53:45.8	19.8	0.55	-0.70	0.90	S				
2016-615	93.533	0.472	0.314	-0.69	1.00	1.00	P	20:21:01.35	-61:24:49.1	20.5	-0.84	0.61	1.04	G				
2020-370	94.743	0.394	0.345	-0.23	0.99	0.99	PW	20:23:46.20	-36:55:20.7	17.0	0.00	2.02	2.02	S		Q	1.048	
2021-330	94.743	0.607	0.565	-0.12	0.87	0.93	C	20:24:35.58	-32:53:35.7	17.6	1.08	0.02	1.08	S		Q	1.47	
2025-538	93.533	0.296	0.243	-0.33	1.00	1.00	P	20:29:35.07	-53:39:07.3	15.7	-2.85	1.30	3.13	S				
2030-689	93.533	0.479	0.472	-0.02	0.94	0.99	PX	20:35:48.87	-68:46:33.6	14.4	2.04	-0.09	2.04	S				
2031-816	94.743	0.253	0.188	-0.50	1.00	1.00	P	20:39:17.70	-81:28:03.2	23.3	1.46	0.66	1.60	T				
2036-577	93.533	0.555	0.460	-0.32	0.94	0.96	PX	20:40:01.08	-57:35:09.7	22.6	1.07	-1.91	2.18	T				
2037-253	93.867	0.492	0.432	-0.22	1.00	0.98	PW	20:40:08.76	-25:07:46.5	17.8	0.21	0.47	0.51	S		Q	1.574	
2047-655	93.533	0.382	0.341	-0.19	0.99	0.97	PW	20:52:06.72	-65:23:11.1	17.0	-1.17	-0.06	1.17	S		Q	2.32	
2052-474	94.743	1.614	1.458	-0.17	0.95	0.96	J	20:56:16.37	-47:14:47.3	17.9	0.95	1.97	2.19	S		Q	1.489	
2053-323	94.743	0.123	0.127	0.05	1.00	0.97	P	20:56:25.06	-32:08:47.9	16.6	1.29	1.68	2.12	S				
2054-377	94.743	0.486	0.574	0.28	0.99	0.99	P	20:57:41.60	-37:34:03.0	18.2	-1.30	-1.20	1.77	S				
2054-581	94.743	0.269	0.094	-1.79	0.27	0.60	PX	20:58:37.59	-57:56:35.8	15.4	-0.87	-0.20	0.89	V				
2056-369	94.743	0.369	0.244	-0.70	0.99	1.00	P	20:59:41.60	-36:45:54.7	21.9	7.79	-1.00	7.86	T	EF			
2058-297	93.867	0.681	0.609	-0.19	1.00	0.98	P	21:01:01.65	-29:33:28.3	16.2	0.92	-0.45	1.02	S		Q	0.698	
2059-334	94.743	0.321	0.229	-0.58	1.00	0.99	P	21:02:45.88	-33:13:16.3	22.1	10.20	5.48	11.57	J	EF			
2059-786	93.530	0.659	0.632	-0.07	0.92	0.96	J	21:05:45.07	-78:25:34.1	22.7	0.16	0.06	0.18	S				
2101-490	94.743	0.708	0.580	-0.34	0.74	0.88	C	21:05:01.15	-48:48:46.5	17.0	0.31	0.02	0.31	S				
2106-413	94.743	2.190	2.305	0.09	0.98	0.99	P	21:09:33.19	-41:10:20.5	19.5	1.59	1.39	2.11	S		Q	1.055	*,†
2109-811	93.530	0.588	0.596	0.02	0.99	0.98	PW	21:16:30.93	-80:53:54.9	18.9	-2.15	3.47	4.08	G	MG			
2123-463	94.743	0.621	0.491	-0.40	0.88	0.90	C	21:26:30.70	-46:05:47.9	18.3	1.38	0.69	1.54	S		Q	1.67	
2130-425	94.743	0.353	0.246	-0.62	0.98	1.00	P	21:34:01.17	-42:18:43.2	18.8	0.26	-11.98	11.99	G	EF			
2135-248	93.867	0.451	0.378	-0.30	1.00	1.00	P	21:38:37.19	-24:39:54.2	17.3	0.32	0.16	0.36	S		Q	0.821	
2138-377	94.743	0.428	0.390	-0.16	0.95	0.96	C	21:41:52.45	-37:29:12.9	17.6	-0.09	-1.11	1.11	S		Q	0.425	
2142-758	93.530	0.848	0.661	-0.43	0.97	0.96	C	21:47:12.75	-75:36:12.9	13.1	1.28	0.62	1.43	S		Q	1.139	
2142-765	93.533	0.379	0.270	-0.58	0.86	0.91	J	21:47:53.19	-76:21:29.4	13.0	1.49	0.81	1.70	S				
2146-783	93.530	1.067	0.769	-0.56	0.98	0.99	P M	21:52:03.19	-78:07:06.4	0.0	2.12	-0.78	2.26	S		Q	2.345	
2149-307	94.743	1.612	1.338	-0.32	0.99	0.99	J	21:51:55.51	-30:27:53.7	17.7	1.11	0.92	1.44	S		G	0.0283	
2152-699	95.847	2.870	1.450	-1.16	0.31	0.73	L	21:57:05.98	-69:41:23.5	14.1	0.53	-2.61	2.66	V				
2153-760	93.533	0.432	0.397	-0.14	1.00	1.00	P	21:57:59.24	-75:49:53.6	12.9	0.92	0.47	1.03	S		Q	0.116	
2155-304	94.743	0.449	0.457	0.03	0.97	0.98	PW	21:58:52.06	-30:13:32.2	13.4	-0.41	0.59	0.72	S				

continued on next page

continued from previous page

Source	Epoch	S _{4.8}	S _{8.6}	$\alpha_{8.6}^{\pm}$	F _{4.8}	F _{8.6}	Type	R.A.	Dec.	B _I	$\Delta\alpha$	$\Delta\delta$	Δr	Class	DSS	ID	z	Annot
2200-238	93.867	0.688	0.822	0.30	1.00	1.00	P	22:02:56.00	-23:35:10.2	17.7	0.75	0.09	0.76	S		Q	2.118	
2204-573	94.746	0.320	0.230	-0.56	0.99	0.99	PW	22:07:54.01	-57:07:36.7	16.8	-0.83	0.69	1.08	S		Q	2.725	
2206-237	93.867	0.921	0.581	-0.78	1.00	0.98	R	22:09:20.18	-23:31:54.1	17.6	-0.54	0.20	0.57	G		G	0.087	
2210-257	93.867	0.724	0.636	-0.22	0.97	0.98	PW	22:13:02.50	-25:29:30.2	17.9	2.33	0.82	2.47	S		Q	1.833	‡
2212-299	93.867	0.386	0.287	-0.50	1.00	1.00	P	22:15:16.01	-29:44:23.4	17.2	0.71	-0.04	0.71	S		Q	2.703	
2220-351	94.743	0.515	0.434	-0.29	0.98	0.98	PW	22:23:05.93	-34:55:47.2	18.5	1.73	0.64	1.84	G		Q	0.298	
2226-211	93.867	0.023					X	22:29:57.88	-20:54:29.3	20.9	1.20	15.66	15.71	S	CL			
2227-399	94.743	0.375	0.524	0.57	1.00	1.00	P	22:30:40.28	-39:42:52.1	17.4	0.90	0.42	1.00	S		Q	0.323	
2232-488	94.746	1.069	1.134	0.10	0.97	0.99	P	22:35:13.23	-48:35:58.7	17.6	0.00	-0.22	0.22	S		Q	0.51	
2236-364	94.743	0.334	0.195	-0.92	0.21	0.25	PX	22:39:31.12	-36:09:12.4	11.7	0.85	0.16	0.87	S				*,†
2236-572	94.746	0.870	1.055	0.33	0.99	0.99	P	22:39:12.08	-57:01:00.8	20.0	10.46	1.80	10.62	S	EF			
2239-631	94.743	0.193	0.208	0.13	0.98	0.99	P	22:43:07.86	-62:50:57.3	17.5	-0.27	-0.97	1.00	S				*,†
2240-260	93.867	0.909	0.800	-0.22	0.92	0.94	J?	22:43:26.42	-25:44:30.6	17.9	0.95	0.92	1.32	S		Q	0.774	
2243-563	94.746	0.523	0.588	0.20	0.94	0.97	PW	22:46:16.80	-56:07:46.0	19.8	-0.33	-0.30	0.44	S				
2245-328	94.746	0.539	0.546	0.02	0.99	0.99	P	22:48:38.69	-32:35:52.1	18.2	1.09	-1.24	1.65	S		Q	2.268	
2253-278	93.867	0.254	0.279	0.16	1.00	0.96	P	22:56:00.15	-27:35:56.1	17.5	-0.52	-1.44	1.53	S				
2254-204	93.867	0.440	0.450	0.04	0.99	1.00	P	22:56:41.19	-20:11:40.5	17.8	2.97	0.58	3.03	S				
2254-367	94.746	1.176	0.960	-0.35	1.00	0.99	P	22:57:10.60	-36:27:43.9	11.4	1.23	-0.44	1.30	G		G	0.0056	
2255-282	93.867	1.669	1.852	0.18	0.96	0.99	PW	22:58:05.95	-27:58:21.0	16.6	-0.10	-0.93	0.94	S		Q	0.926	
2257-270	93.867	0.390	0.312	-0.38	0.98	0.98	JW	23:00:25.50	-26:44:22.4	18.3	0.94	0.96	1.35	S		Q	1.481	
2258-817	93.533	0.323	0.226	-0.61	0.99	0.99	P M	23:03:00.82	-81:26:04.6	0.0	-1.08	0.91	1.41	S				
2300-683	94.743	0.308	0.359	0.26	0.84	0.93	C	23:03:43.56	-68:07:37.4	15.9	1.96	-0.94	2.18	S		Q	0.512	
2303-656	94.743	0.322	0.220	-0.65	1.00	1.00	P	23:06:59.45	-65:21:32.4	22.7	-6.55	10.34	12.24	T	EF			
2304-230	93.867	0.665	0.557	-0.30	0.99	1.00	P	23:07:38.66	-22:47:53.3	22.6	17.18	14.54	22.50	T	EF			
2306-312	94.746	0.458	0.412	-0.18	0.97	0.98	J	23:09:14.33	-30:59:12.6	18.3	1.41	0.59	1.52	S				
2311-452	94.746	1.241	0.842	-0.66	1.00	0.99	P	23:14:09.38	-44:55:49.1	19.1	1.49	-0.22	1.51	S				
2312-319	94.746	0.558	0.431	-0.44	1.00	0.99	PW	23:14:48.49	-31:38:39.6	17.6	2.49	1.23	2.78	S		Q	2.884	
2313-438	94.746	0.644	0.485	-0.48	0.99	0.99	P	23:16:21.10	-43:37:46.7	19.0	0.85	-0.64	1.06	S		Q	0.284	
2314-340	94.746	0.630	0.289	-1.32	0.94	0.95	P M	23:16:43.38	-33:49:12.3	18.0	1.36	0.08	1.37	S		Q	1.847	*,†
2314-409	94.746	0.246	0.184	-0.49	0.99	1.00	P	23:16:46.92	-40:41:21.0	18.2	2.13	1.22	2.46	S		Q	2.448	
2321-375	94.746	0.545	0.599	0.16	0.96	0.98	J	23:24:07.11	-37:14:22.5	18.3	0.65	-1.55	1.68	S		Q	0.37	‡
2326-477	94.746	1.731	1.715	-0.02	0.97	0.97	J	23:29:17.70	-47:30:19.0	15.6	-0.24	-1.23	1.26	S		Q	1.299	
2326-502	94.746	0.452	0.487	0.13	1.00	1.00	P	23:29:20.89	-49:55:40.5	17.3	0.30	-0.02	0.30	S		Q	0.518	
2329-384	94.746	0.560	0.401	-0.57	1.00	0.99	P	23:31:59.48	-38:11:47.6	17.1	0.00	-0.69	0.69	S		Q	1.195	
2329-415	94.746	0.411	0.385	-0.11	1.00	0.99	PW	23:32:19.06	-41:18:37.6	18.2	-0.35	1.23	1.28	S		Q	0.97	
2331-240	93.867	1.017	0.982	-0.06	1.00	1.00	P	23:33:55.22	-23:43:40.4	16.5	0.21	0.20	0.30	G		G	0.0477	

continued on next page

continued from previous page

Source	Epoch	$S_{4.8}$	$S_{8.6}$	$\alpha_{4.8}^{\pm}$	$F_{4.8}$	$F_{8.6}$	Type	R.A.	Dec.	B_I	$\Delta\alpha$	$\Delta\delta$	Δr	Class	DSS	ID	z	Annot
2332–293	93.867	0.149	0.231	0.75	0.99	0.98	PW	23:35:18.70	–29:07:16.3	18.5	–0.20	0.20	0.29	S		Q	2.14	
2333–415	94.746	0.584	0.557	–0.08	0.99	0.99	R	23:36:33.99	–41:15:21.8	20.3	–0.53	0.83	0.98	S				* , †
2333–528	94.746	1.545	1.310	–0.28	0.99	0.99	P	23:36:12.14	–52:36:21.9	18.8	–1.28	–8.86	8.95	S	EF			
2334–525	94.746	0.471	0.363	–0.44	0.99	0.99	PW	23:37:23.16	–52:16:20.0	18.8	0.86	–0.84	1.21	S				
2337–334	94.746	0.751	0.558	–0.51	0.95	0.96	J	23:39:54.53	–33:10:16.7	21.5	26.19	–5.04	26.67	G	EF			
2344–514	94.746	0.373	0.342	–0.15	0.98	0.99	P	23:47:19.86	–51:10:36.0	17.4	–0.88	0.45	0.99	S				
2351–309	94.746	0.320	0.303	–0.10	0.99	0.99	P	23:53:47.46	–30:37:48.5	16.8	1.01	–0.12	1.02	S				
2352–342	94.746	0.353	0.163	–1.32	0.55	0.98	P M	23:55:25.80	–33:57:55.2	16.6	2.14	0.30	2.16	S		Q	0.706	* , †
2353–686	94.743	0.923	0.974	0.09	1.00	0.99	P	23:56:00.67	–68:20:03.5					X	ST	Q	1.716	
2355–534	94.746	1.773	1.663	–0.11	0.99	0.99	PW	23:57:53.26	–53:11:13.8					X	ST	Q	1.006	

Table 4.6: Additional notes on selected survey sources. Where appropriate, the separation or extent, r (in units of arcsec), and position angle θ of secondary component(s) have been included. In some cases there is an accompanying image in Figure 4.10 and this is indicated by the presence of a * in the second column.

Source	Image	Comments
0055–328	*	Strong, steep spectrum confusing source (~ 50 mJy at 4.8 GHz, ~ 27 mJy at 8.6 GHz). $r = 231$, $\theta = 128.7$.
0101–802	*	Two steep spectrum lobes, each with \sim east-west extension. Some evidence for a faint flat spectrum core at 8.6 GHz. $r = 4.5$, $\theta = -2$.
0113–310		Source is 85 arcsec from phase centre, position angle is 93.5° .
0130–447	*	North component has flat spectrum, south component has steep spectrum. $r = 93$, $\theta = 157$.
0144–522	*	Jet is 26 arcsec long, $\theta = 99.9$.
0301–243		Very diffuse extension, point dominates.
0329–404	*	Core-jet ($r = 2.4$, $\theta = -77$) with weak steep spectrum component to east ($r = 13.5$, $\theta = 97$), not seen at 8.6 GHz.
0341–256		Core with close secondary. $r = 1.2$, $\theta = -148$.
0346–279		Inverted core, steep secondary. $r = 2.2$, $\theta = 119$.
0406–311		NED classification is a pair of galaxies, $z = 0.115$ and 0.05 .
0413–210	*	Flat spectrum core with steep extension at position angles -83° and 147° .
0440–285		Inverted core, weak secondary (~ 6 mJy), difficult to separate at 4.8 GHz. Probably a core-jet. $r = 1.4$, $\theta = -33$.
0454–692		Weak. 100 arcsec from phase centre at position angle 87° .
0521–365	*	Dominated by extended structure. $r = 8.5$, $\theta = 123$.
0529–305		Looks like core-jet but both cpts steep $r \approx 4.5$, $\theta \approx -1$. Confusing source at 4.8 GHz, $r = 165$, $\theta = -152$.
0532–378	*	Core dominated, 2 lobes and a jet. Jet: $r \approx 2$, $\theta \approx 150$, brightest lobe: $r \approx 4.5$, $\theta = -156$.
0537–441	*	Two weak, steep spectrum components in NW and SW at 4.8 GHz. Weak extension at 8.6 GHz? $r = 4.0, 4.5$, $\theta = -50, -109$ respectively.
0539–530		Not well separated, separation at 4.8 GHz is ~ 0.7 arcsec, sep'n at 8.6 GHz is ~ 0.4 arcsec. $\theta \approx -34$.
0618–252	*	Extended emission from a flat spectrum core, need greater resolution to classify properly. $r \approx 1.8$, $\theta \approx -44$ and 136 .
0619–468	*	Two confusing sources, nothing near phase centre. Brightest object is a flat-spectrum point source ~ 138 arcsec from phase centre with position angle 29.8° . The other source is extended and steep-spectrum at $r = 326$, $\theta = -138$ with respect to the flat-spectrum component.
0637–752	*	Bent core-jet ($r \approx 14$, $\theta = -84$) with steep spectrum component to east ($r = 10.3$, $\theta = 90$).
0726–476	*	Quite strong confusing source (~ 13 mJy), $r = 80.3$, $\theta = 21$.
0806–710	*	Core-dominated classical double with broad lobes. $r \leq 14$, $\theta = 56, -83$ to -115 .
1029–331	*	Extension is S-shaped. $r \geq 4.2$, $\theta = -17$ to 47 and -133 to 163 .
1030–357	*	Core-jet. $r \approx 16$, $\theta = -148$.
1034–374	*	~ 19 mJy confusing source. $r = 48$, $\theta = -6$.
1101–325	*	Large extent. $r \approx 39$, $\theta \approx -13$ and $r \approx 27$, $\theta \approx -173$.
1101–536		Core-halo, halo has steep spectrum. $r = 2.0$.
1116–462	*	Jet appears compact. $r = 2.2$, $\theta = -83$.
1117–270	*	Weak confusing source (~ 9 mJy). $r = 95$, $\theta = -144$.
1144–379		Shows variability, known to be an intra-day variable. See Section 4.4.3.
1145–676	*	Core-jet, $r = 37$, $\theta = 70$.
1202–262	*	One flat spectrum core and several steep cpts. Brightest lobe $r = 10$, $\theta = -156$.
1228–700	*	Classical double, extended structure dominates. $r = 2.8$, $\theta = 18$ and $r = 1.8$, $\theta = -120$.
1254–333		COSMOS identification is correct. The optical counterpart lies along an extended radio component joining two steep-spectrum lobes.
1258–321	*	Linear structure, flat spectrum core. $r \geq 18$, $\theta = 119, -61$.

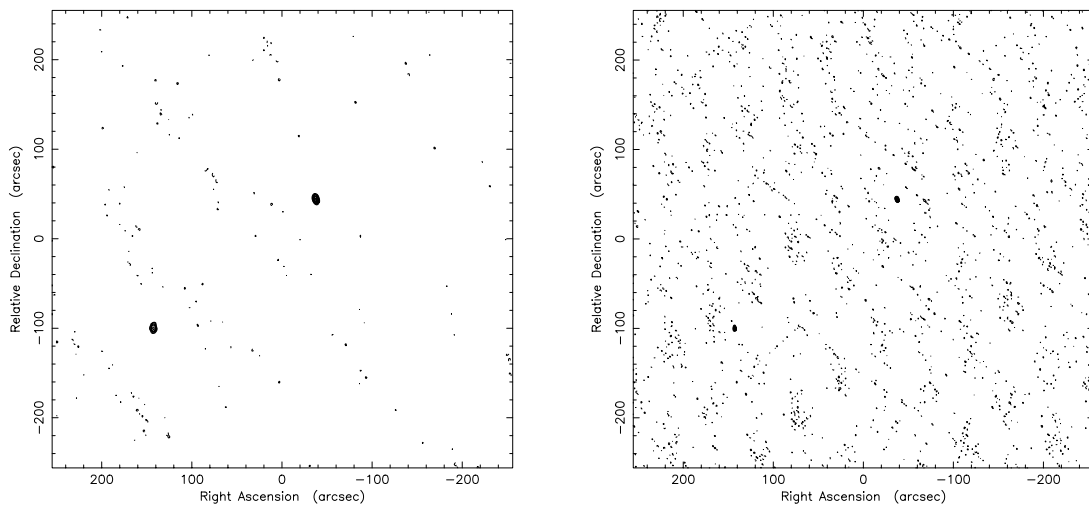
continued on next page

continued from previous page

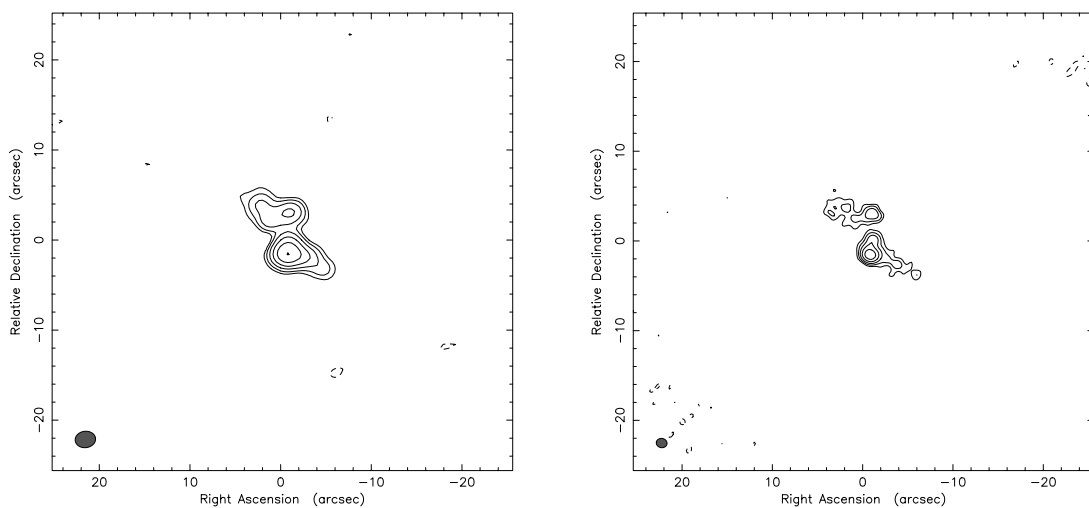
Source	Image	Comments
1303–827	*	Triple. Central cpt has flat spectrum, the others steep. $r = 6.6, 14.8$ $\theta = 142, -21$.
1305–668		Weak, steep spectrum secondary, core just resolved. $r = 2.5$, $\theta = -172$.
1327–206		COSMOS catalogue position is incorrect due to the influence of a bright, nearby galaxy.
1337–875		Close double, probably one steep spectrum, one flat. Difficult to estimate flux densities. $r \approx 0.3$, $\theta = 149$.
1339–287	*	10 mJy secondary at 4.8 GHz, just detected at 8.6 GHz? $r = 3.4$, $\theta = 129$.
1350–662	*	Ring-like. Planetary nebula. $r = 1.3$.
1404–342	*	Core-jet ($r = 4.1$, $\theta = -143$) with a steep spectrum component 49 arcsec from core with position angle 49° .
1405–287	*	Jet has a curved “tail”. $r = 5.3$, $\theta = -64$.
1415–349		Shows variability, may be an intra-day variable. See Section 4.4.3.
1424–418		Probably a close core-jet. $r = 0.9$, $\theta = -115$.
1452–367		COSMOS catalogue position is incorrect. The radio source is coincident with a bright galaxy.
1655–776	*	Weak core, dominant lobes. Strong component at $r = 11.7$, $\theta = 76$.
1823–455		Close core-jet. $r = 0.9$, $\theta = -61$.
1922–341	*	Steep spectrum secondary is ~ 16 mJy at 4.8 GHz. $r = 130$, $\theta = 147$.
1935–452		Core-halo, difficult to compare 4.8 GHz and 8.6 GHz as extension is weaker at 8.6 GHz. $r \approx 2$.
2013–307	*	Core-jet plus and surrounding steep spectrum extension. $r = 2.8$, $\theta = -102$.
2101–490	*	Core-dominated classical double, “bridge” joining E lobe to core. $r = 12$, $\theta = 105$ and $r = 15$, $\theta = -108$.
2236–364	*	Very extended. Possible ~ 35 mJy core.
2240–260	*	Core-jet or core-halo?. A flat spectrum core surrounded by several steep spectrum components.
2314–340	*	Confusing source is 31 mJy at 4.8 GHz and 8 mJy at 8.6 GHz. $r = 235$, $\theta = -118$.
2333–415	*	Very close double? Weak (~ 4 mJy) secondary 53 arcsec away, position angle is -155° , not seen at 8.6 GHz. $r = 0.8$, $\theta = 38$.
2352–342	*	~ 70 mJy confusing source at 4.8 GHz, not seen at 8.6 GHz. $r = 366$, $\theta = 26$.

Figure 4.10: Images of selected ATCA survey sources at 4.8 GHz (left) and 8.6 GHz (right). All contours are multiples ($-1, 1, 2, 4, 8, 16, 32, 64, 128, 256, 512$) of the bottom contour level which is three times the rms noise level in the map.

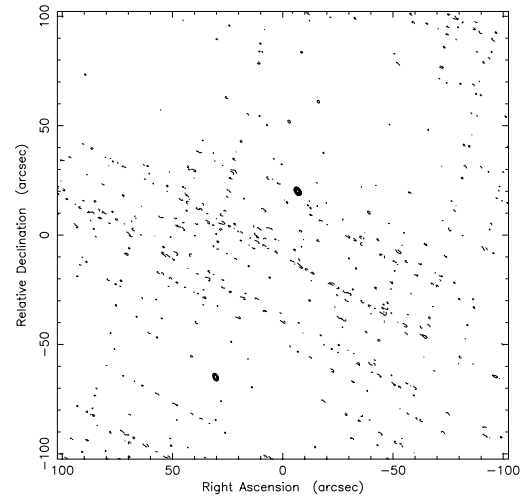
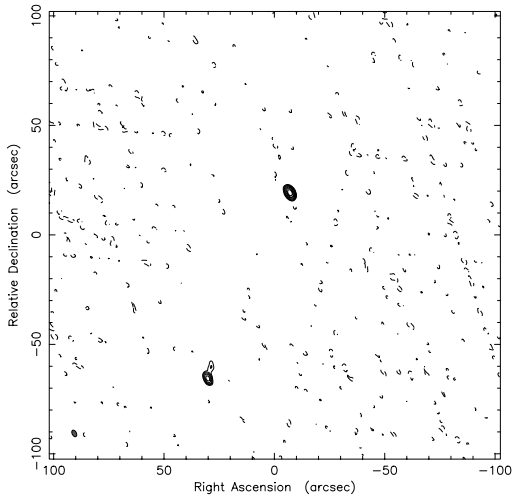
0055–328



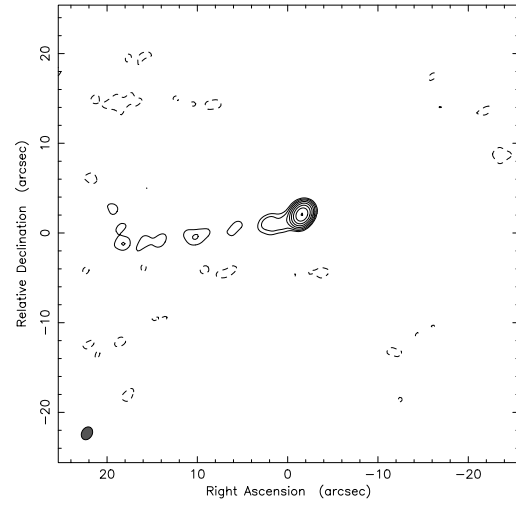
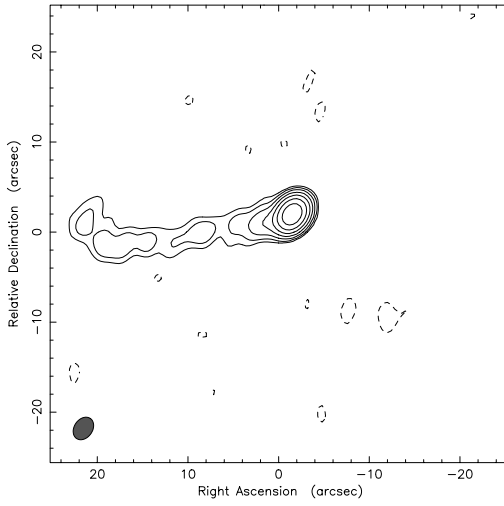
0101–802



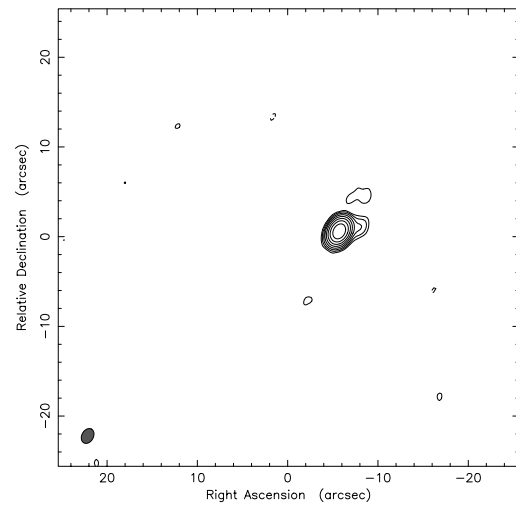
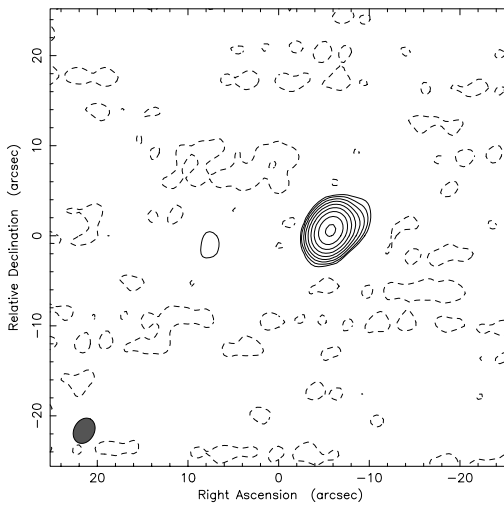
0130–447



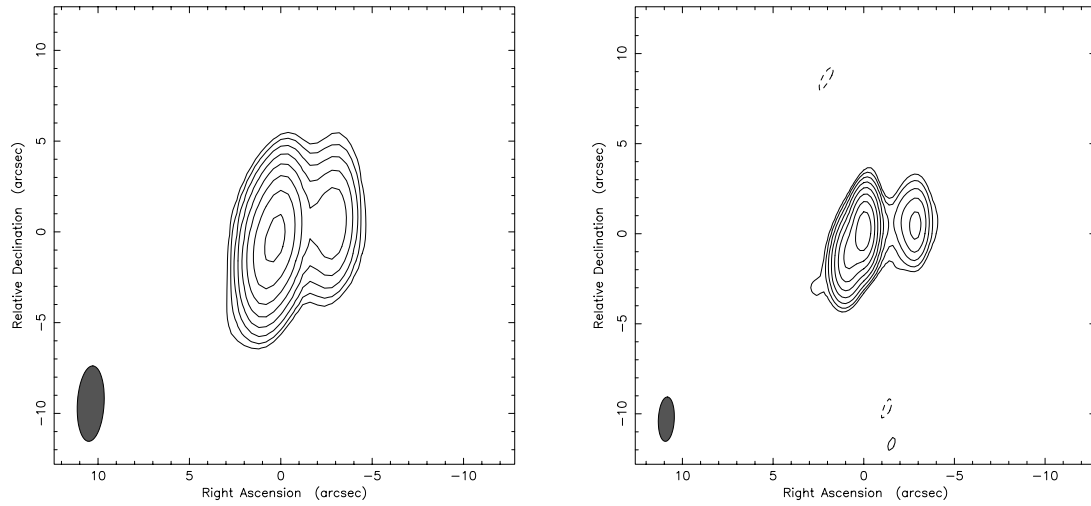
0144–522



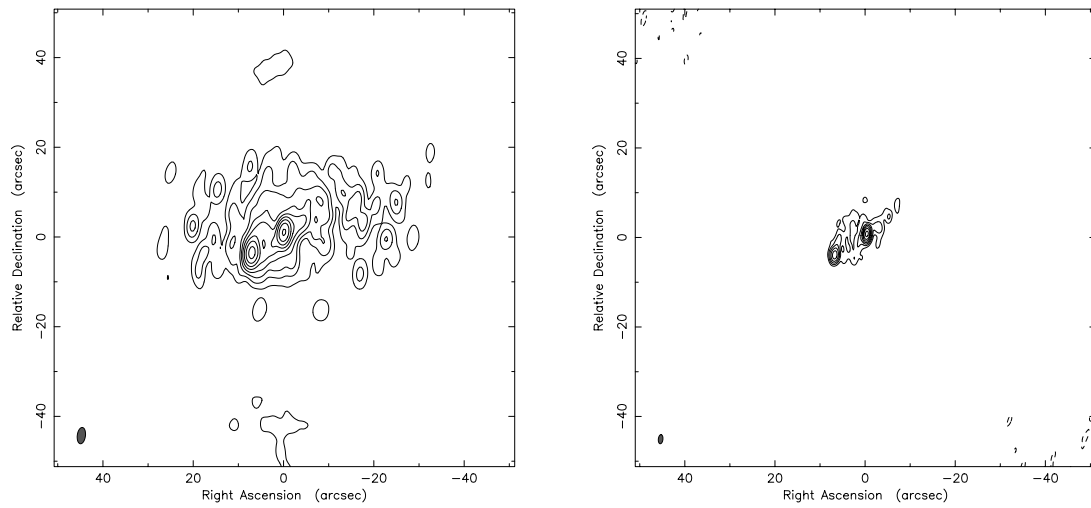
0329–404



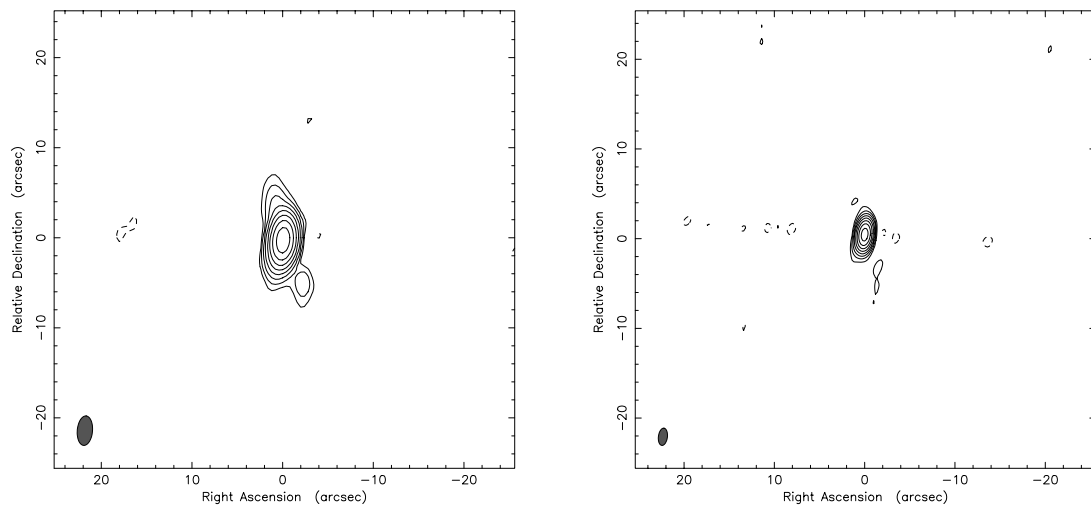
0413–210



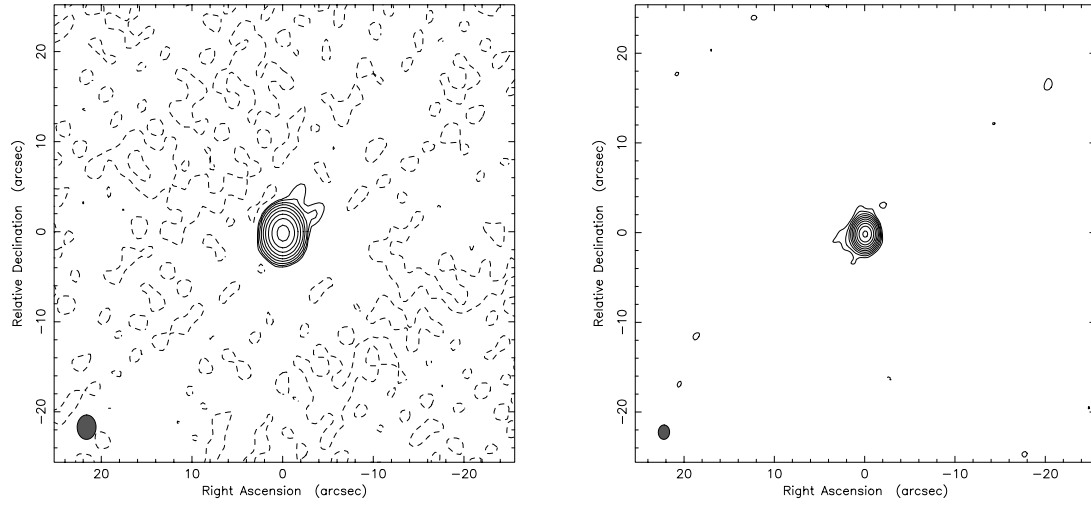
0521–365



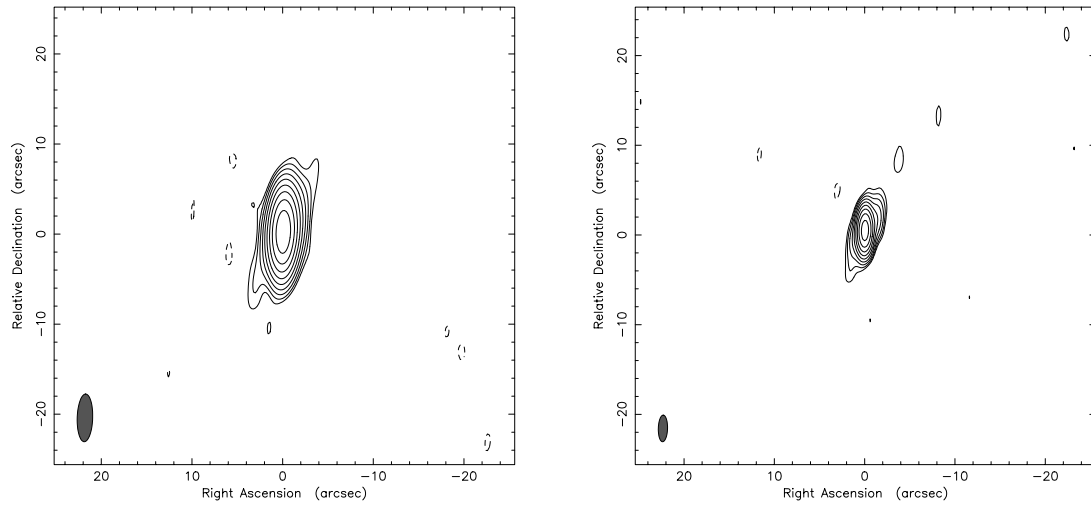
0532–378



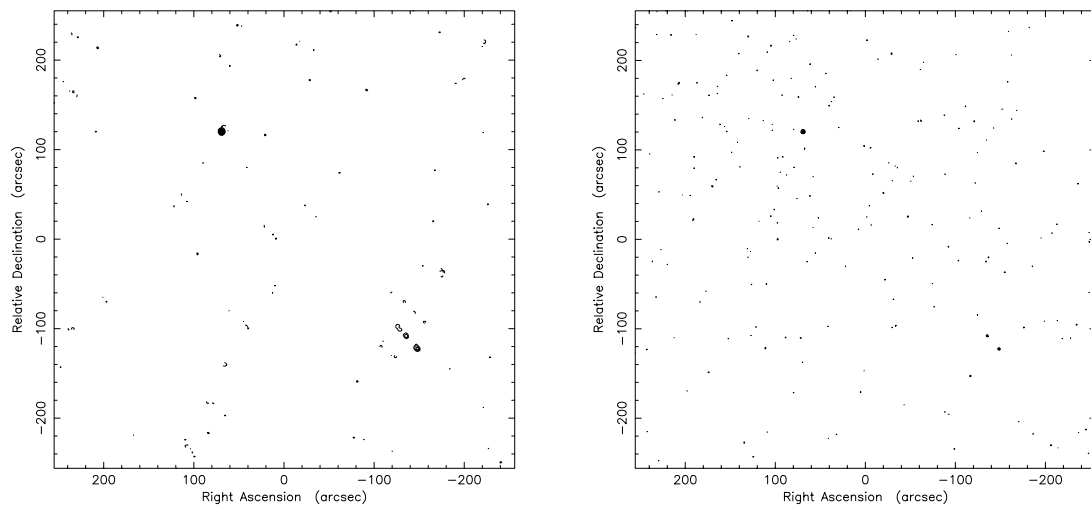
0537–441



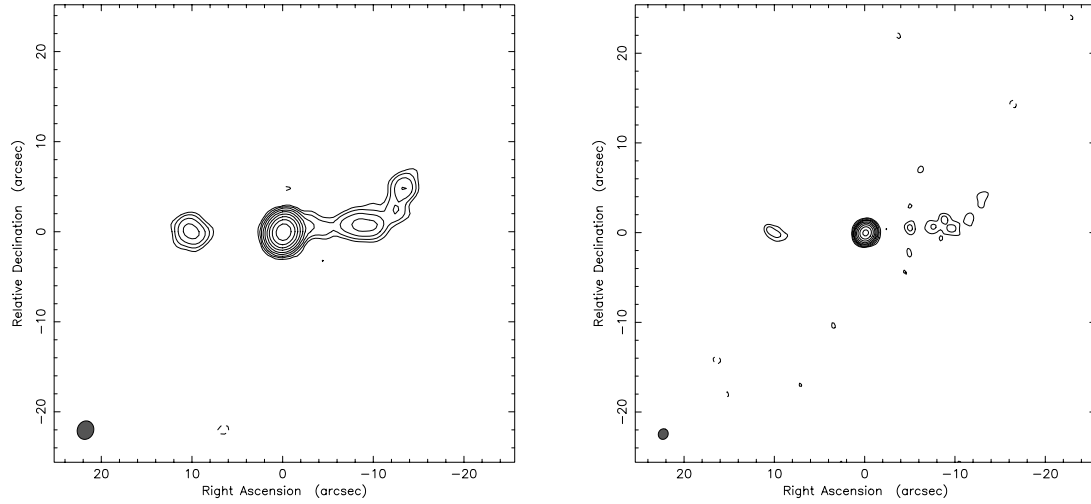
0618–252



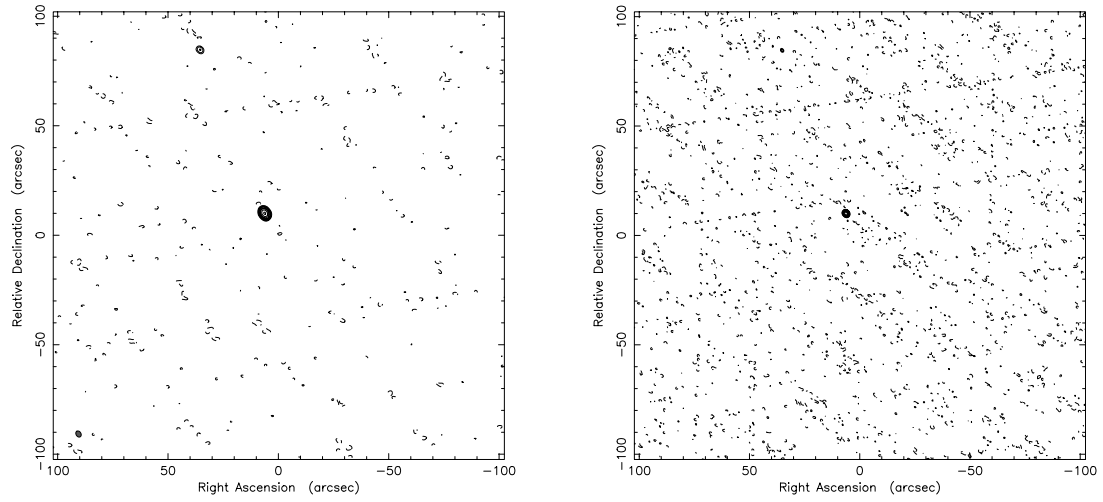
0619–468



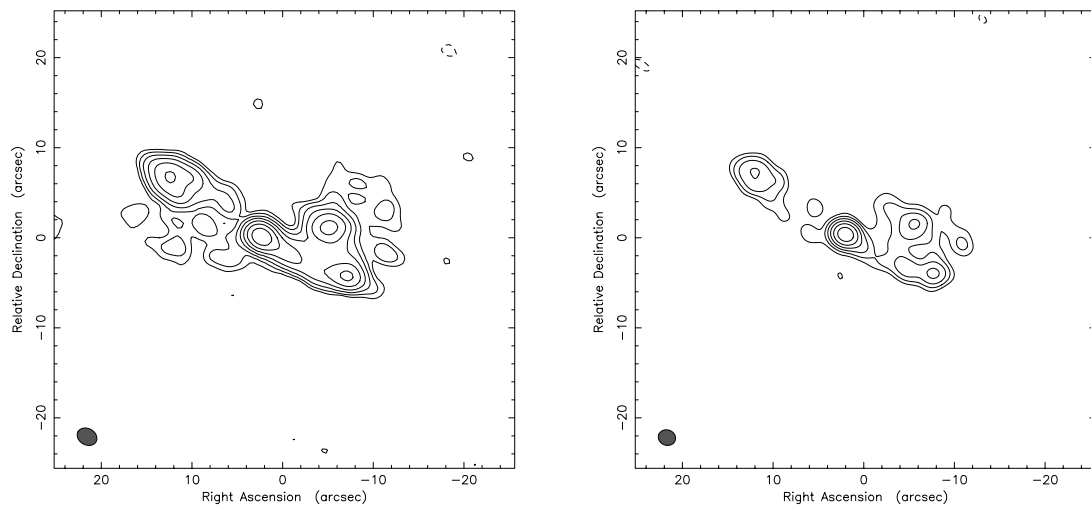
0637–752



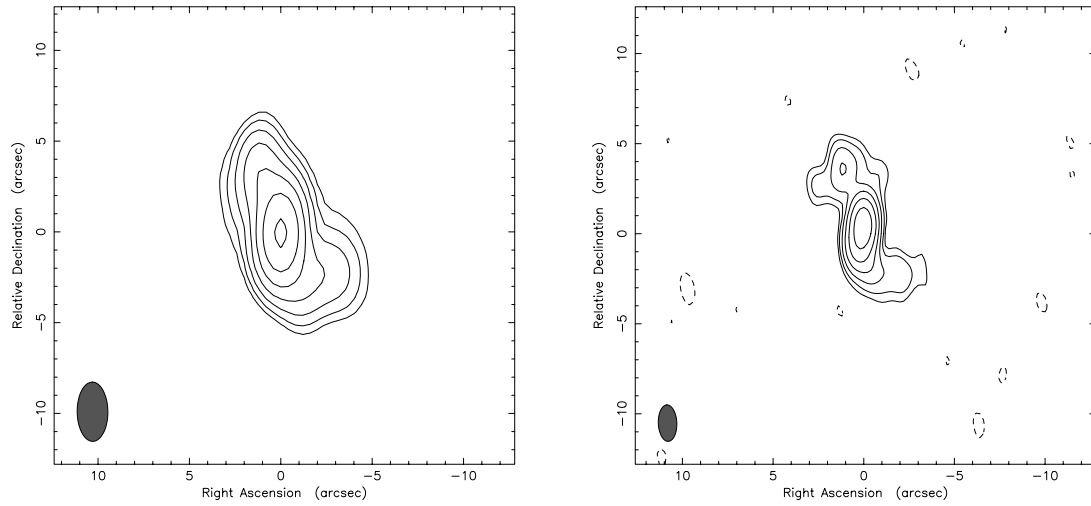
0726–476



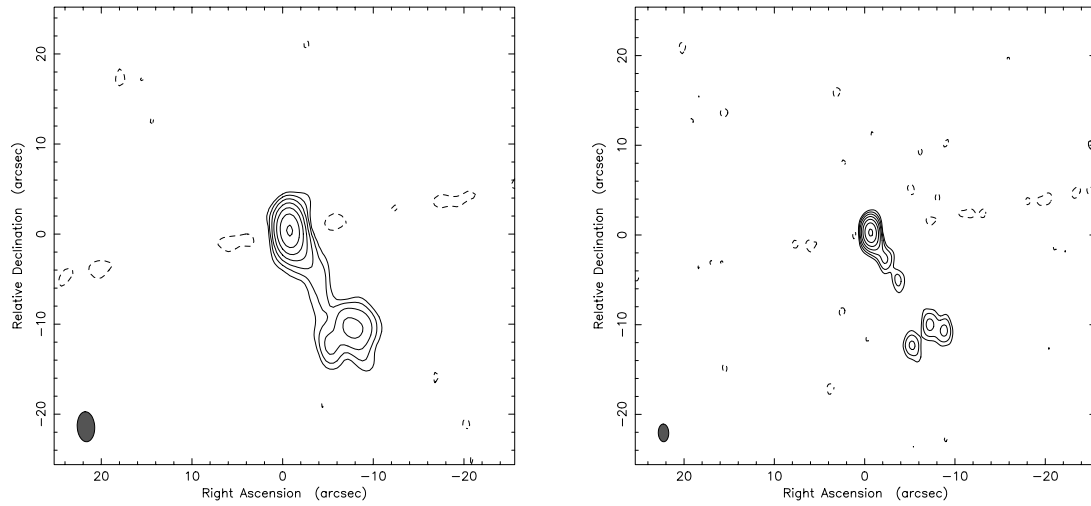
0806–710



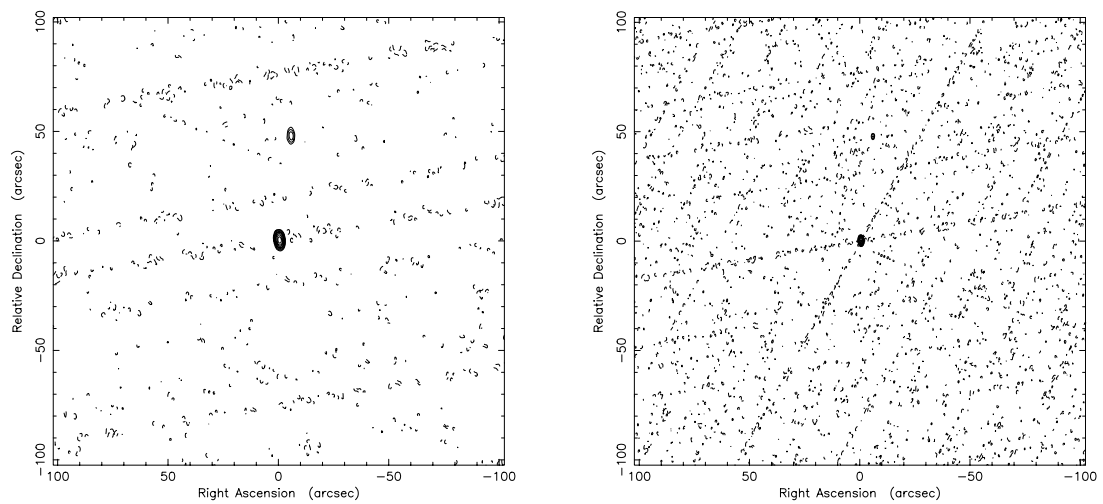
1029–331



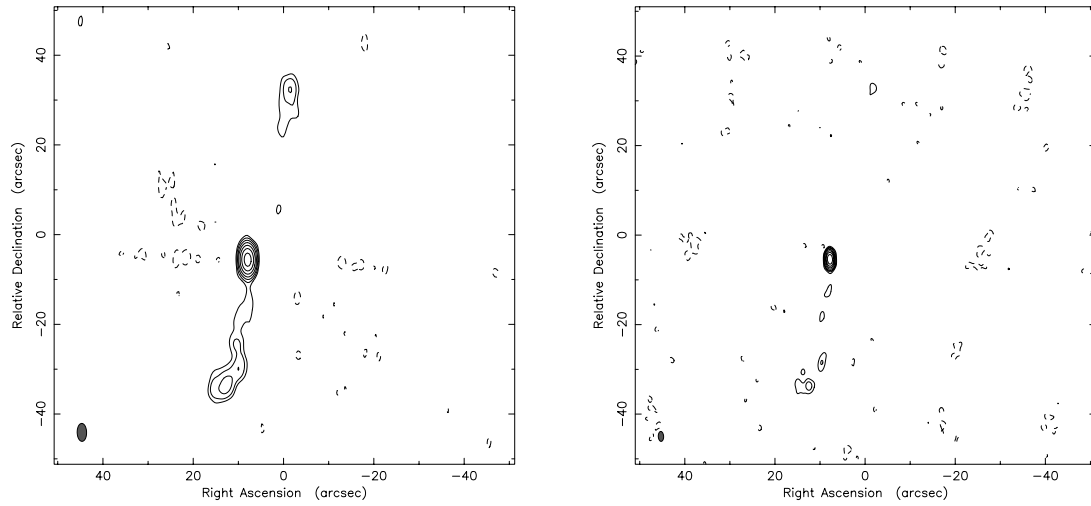
1030–357



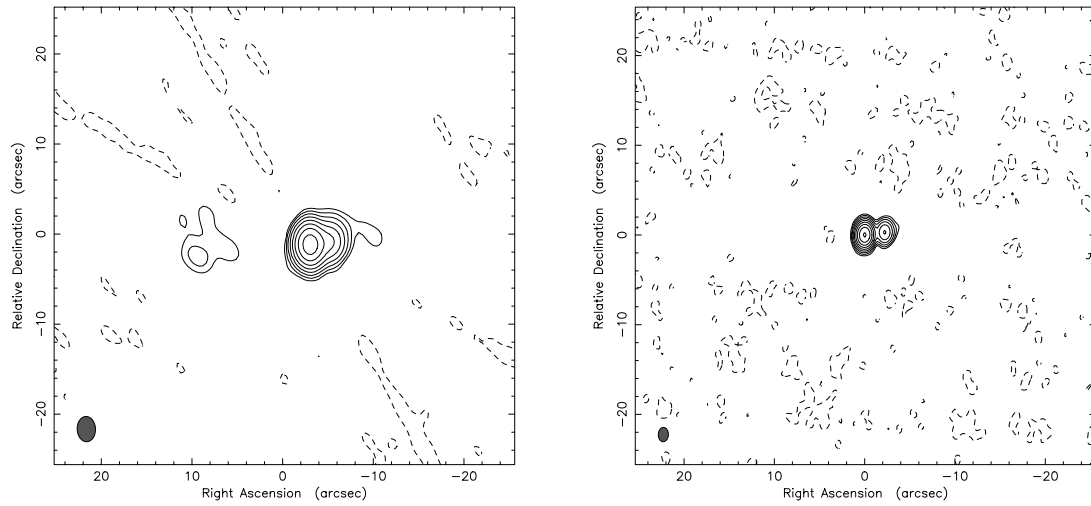
1034–374



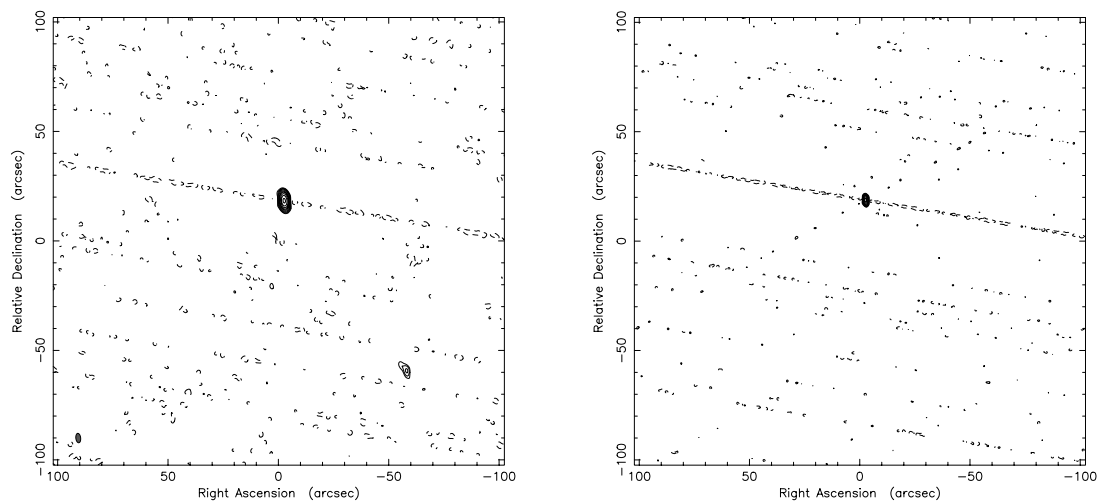
1101–325



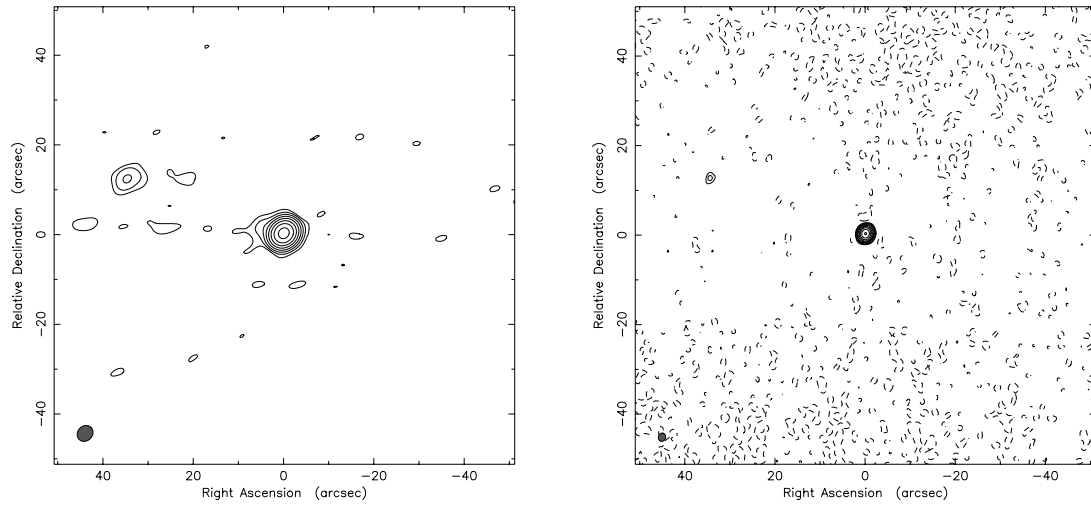
1116–462



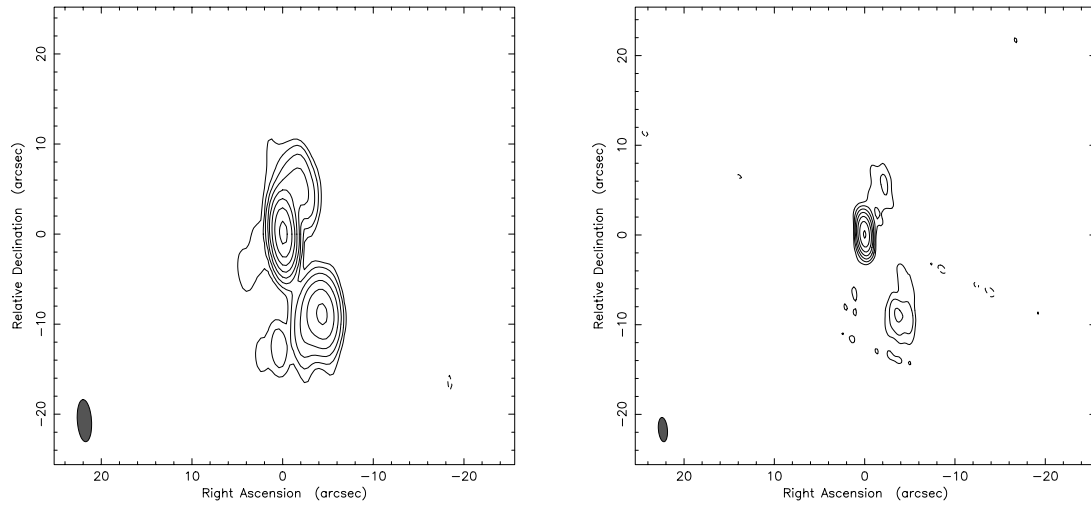
1117–270



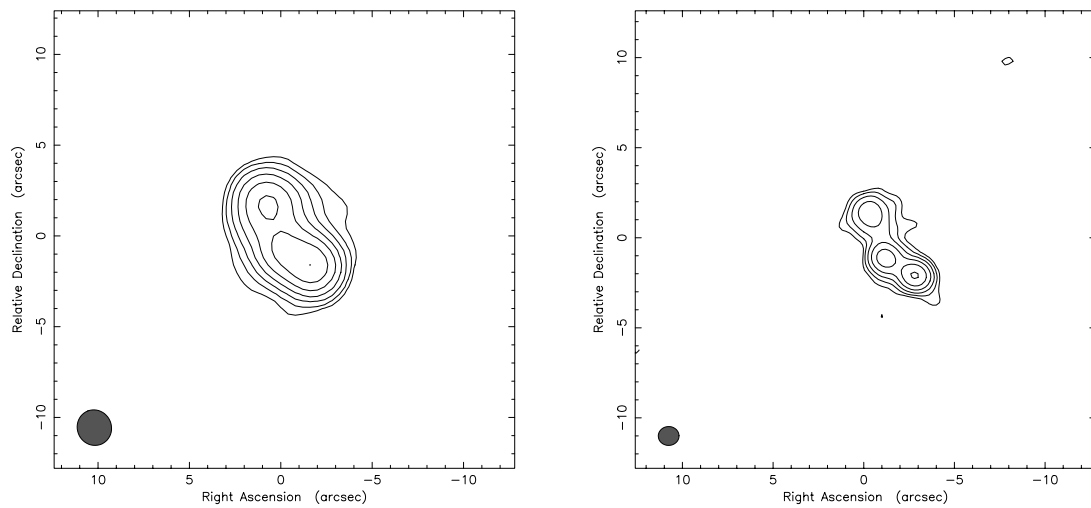
1145–676



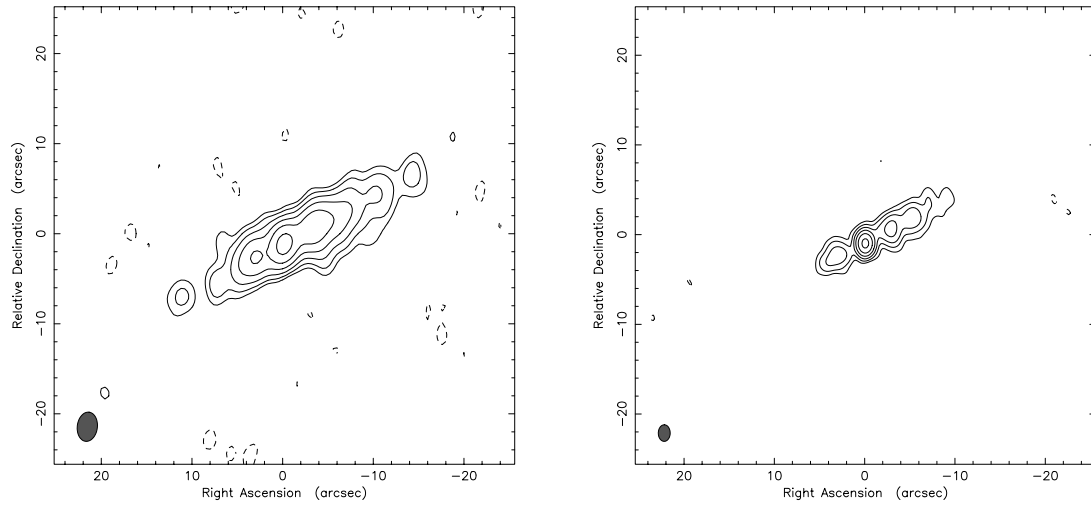
1202–262



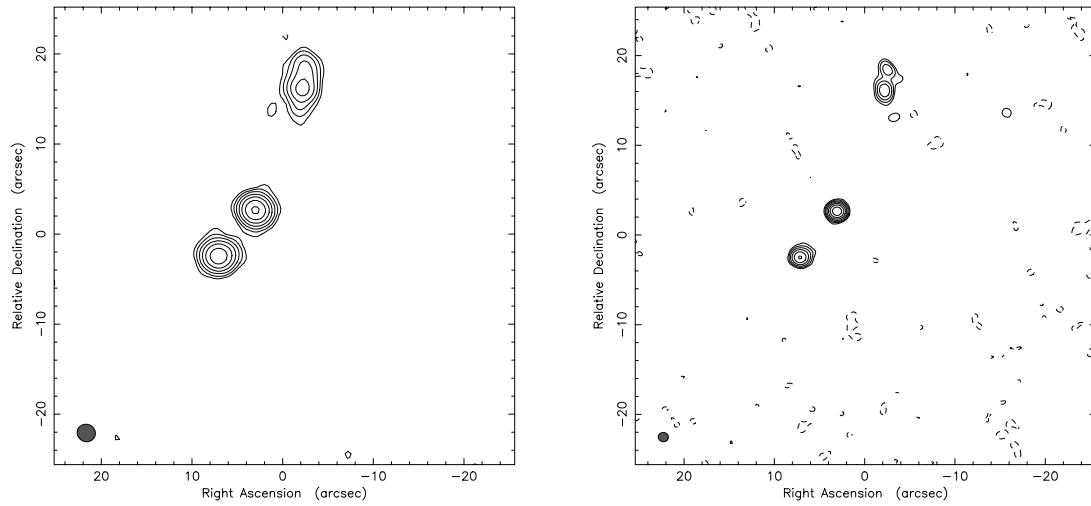
1228–700



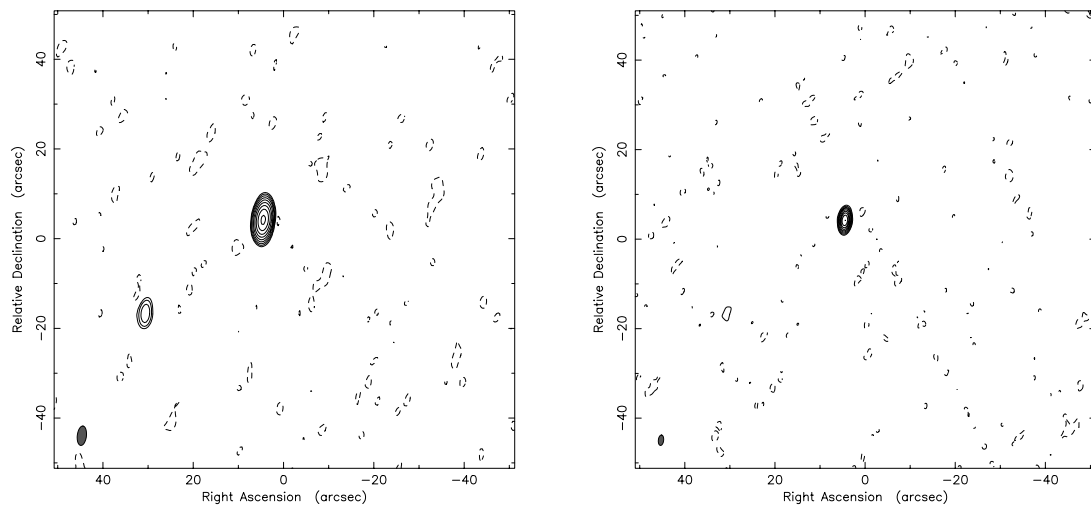
1258–321



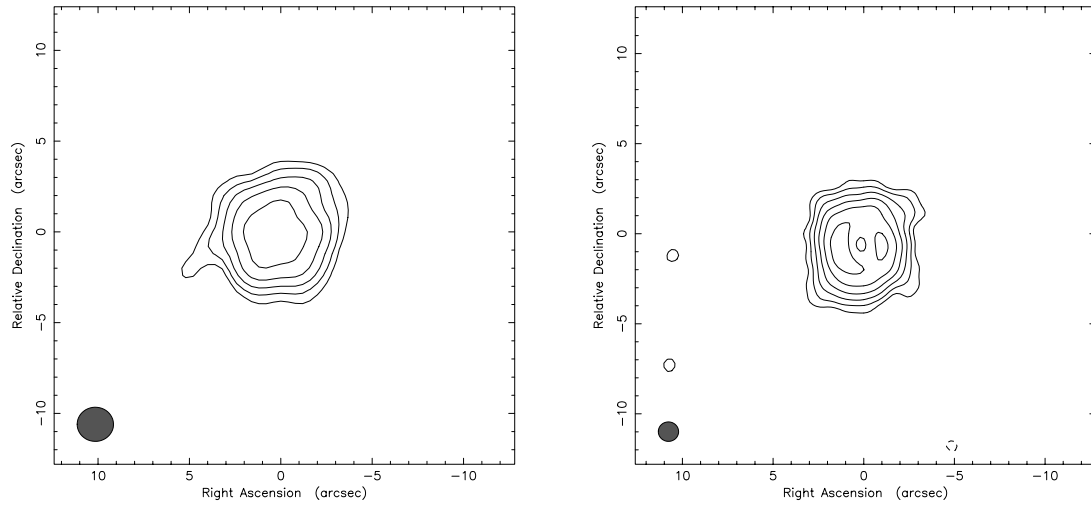
1303–827



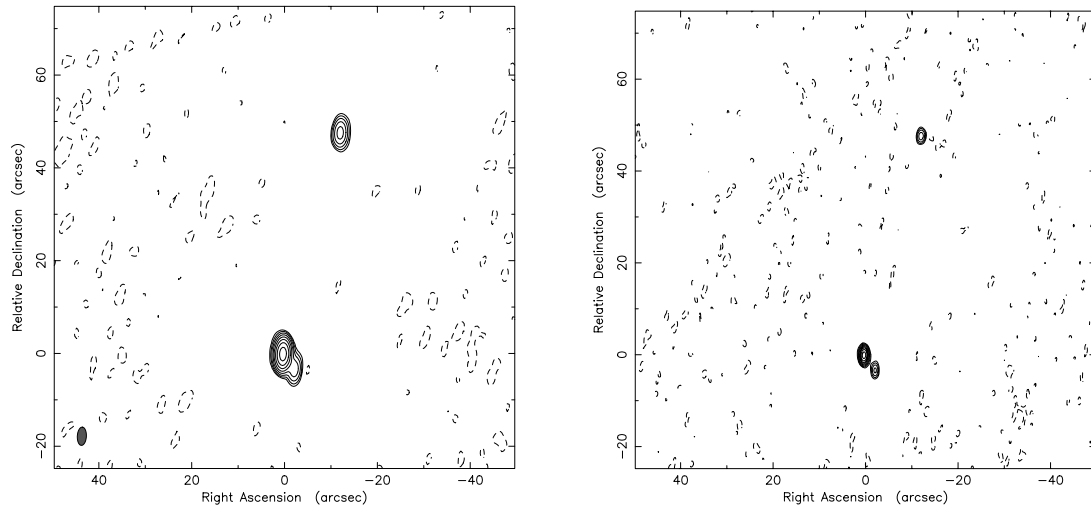
1339–287



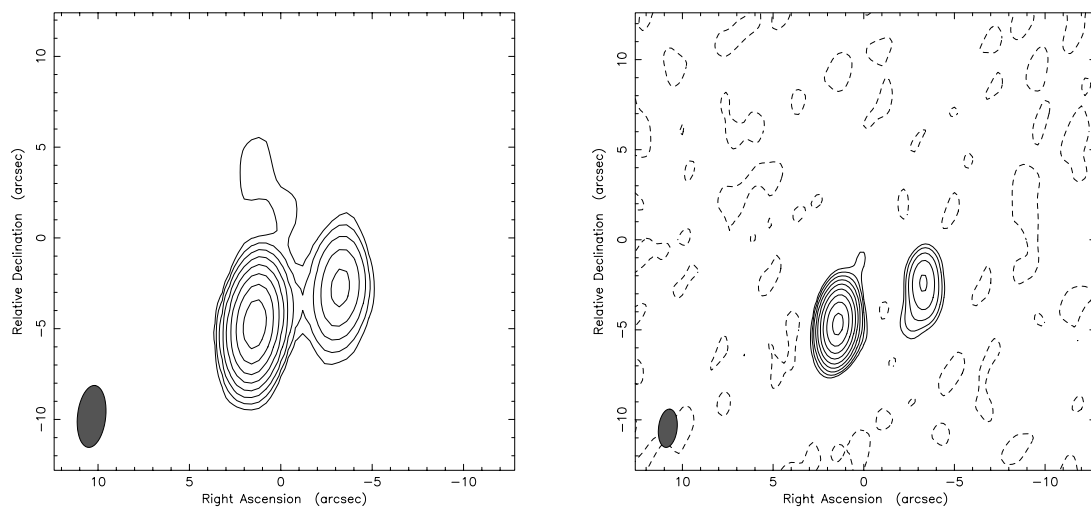
1350–662



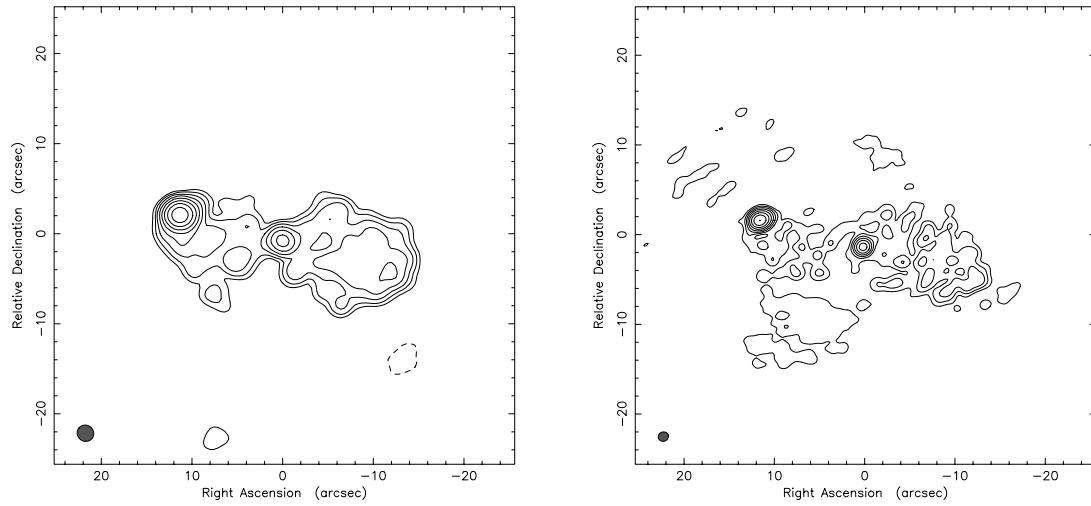
1404–342



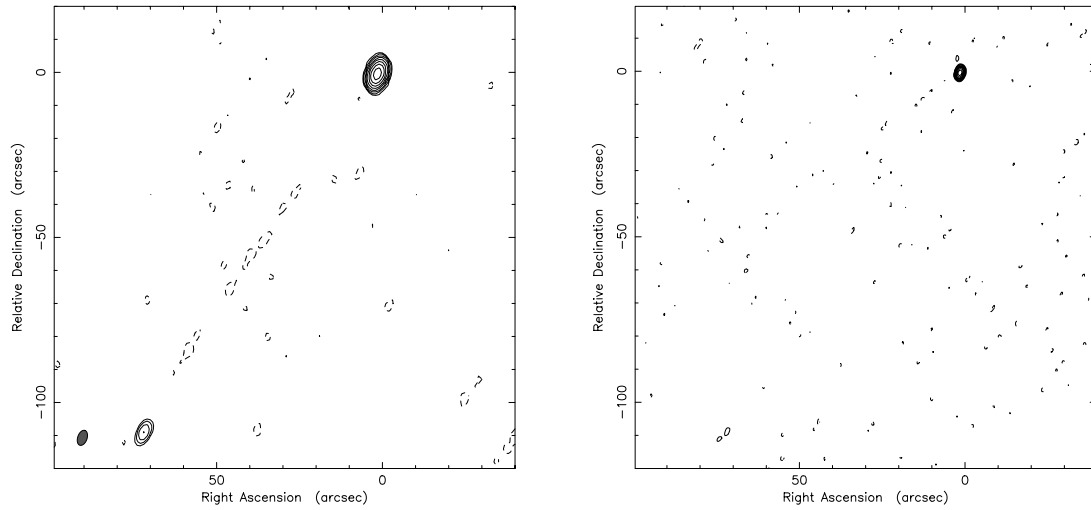
1405–287



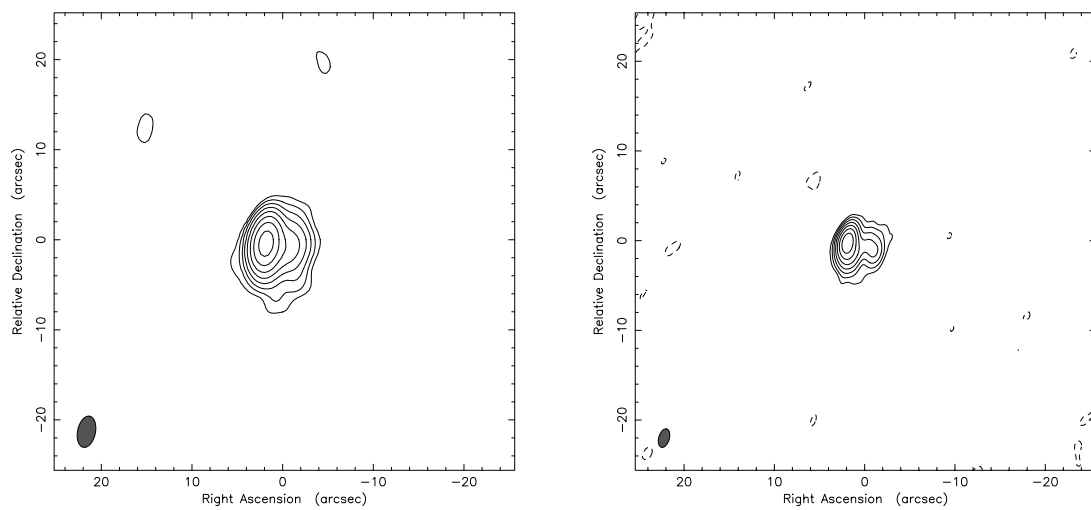
1655–776



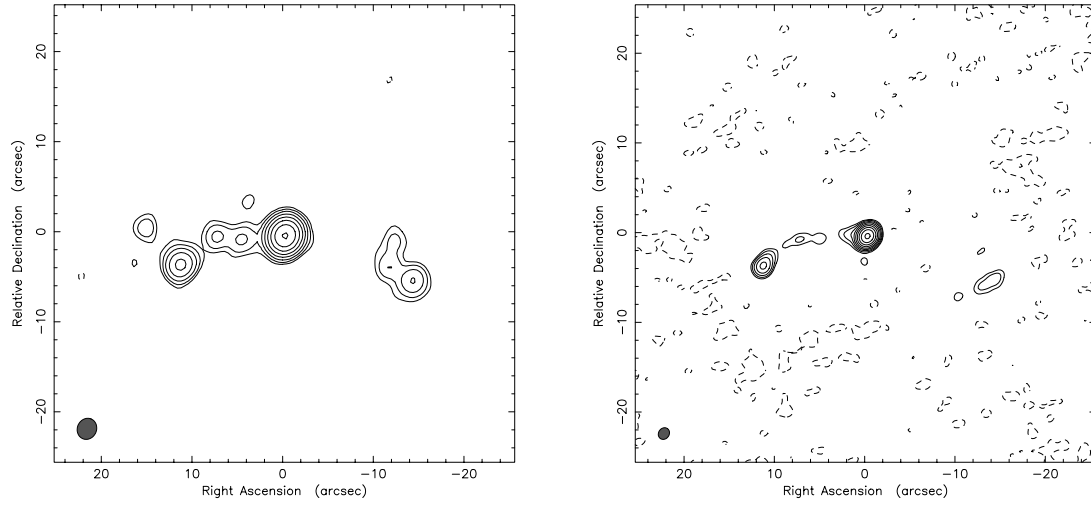
1922–341



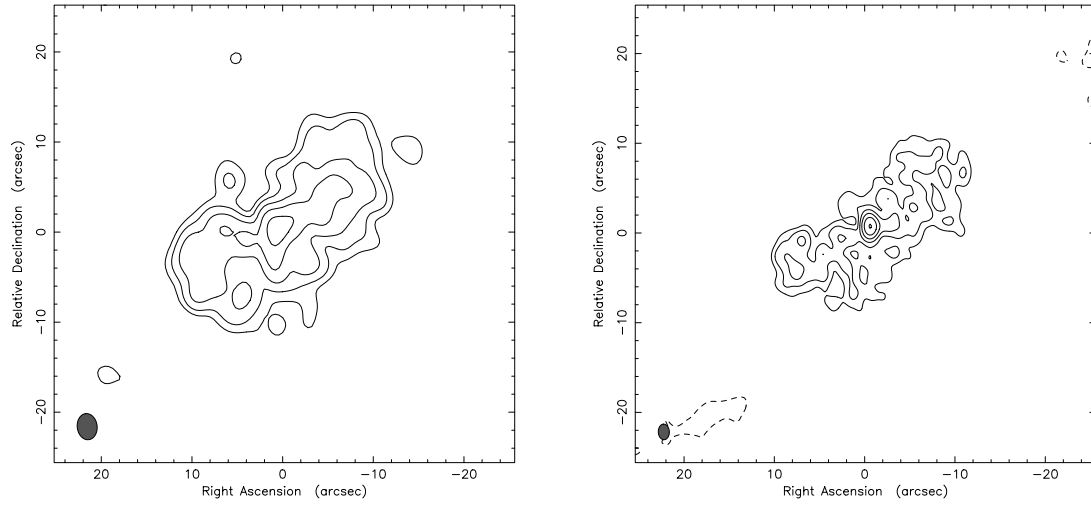
2013–307



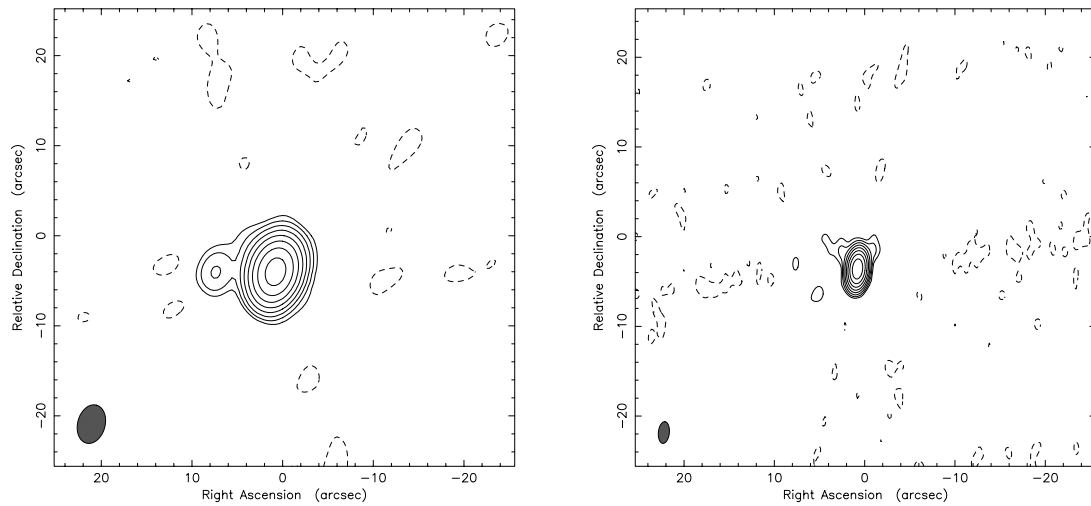
2101–490



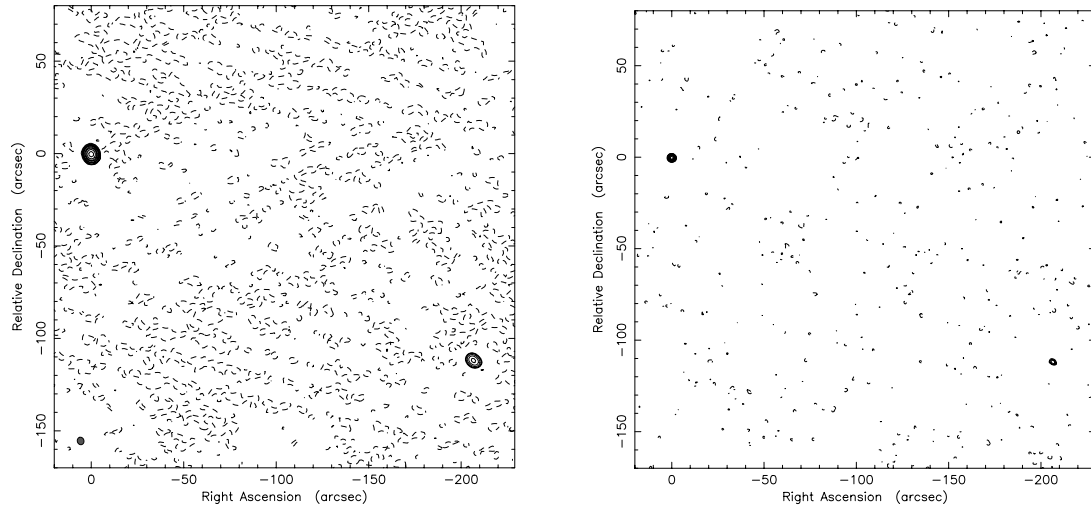
2236–364



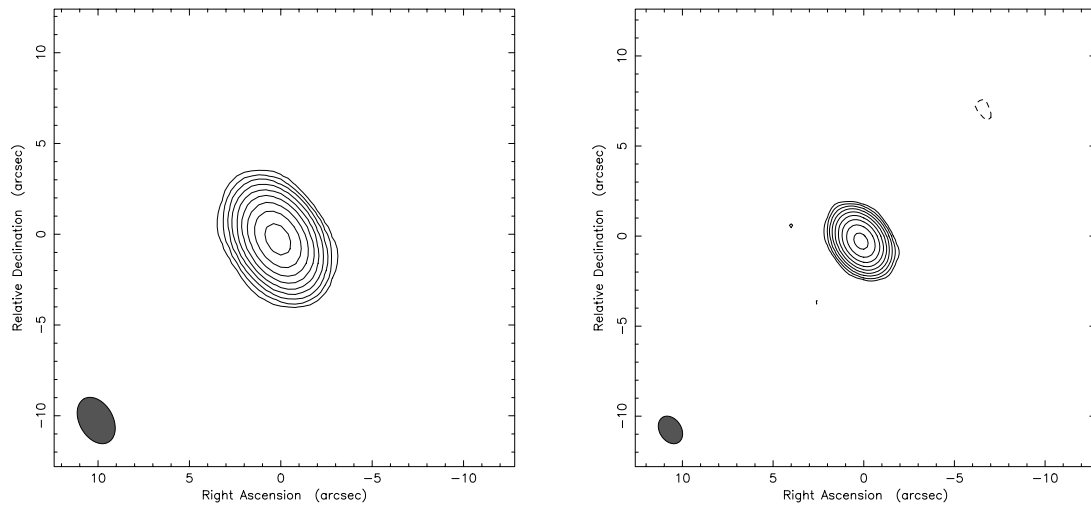
2240–260



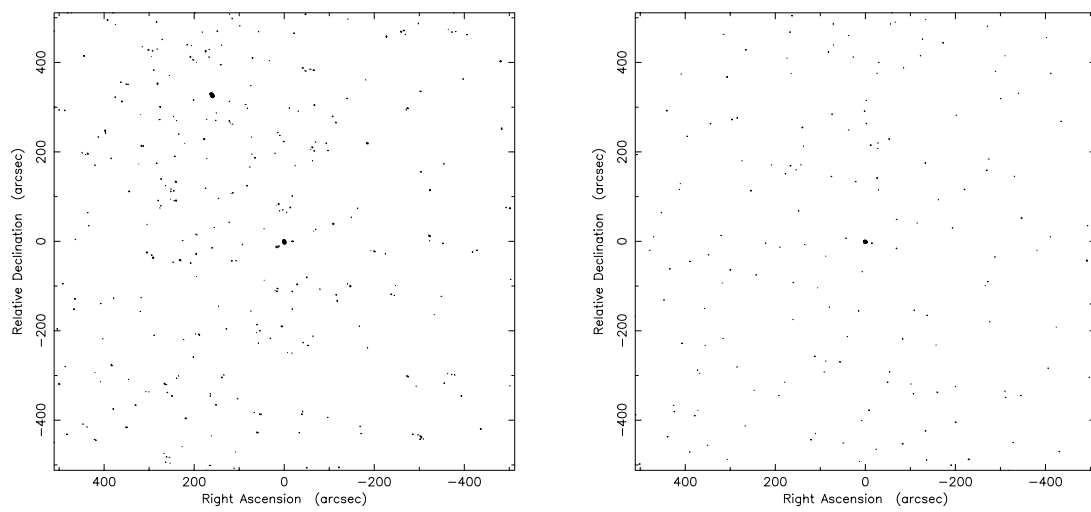
2314–340



2333–415



2352–342



Chapter 5

PKS 1830–211: Radio Structure

5.1 Introduction

Following earlier suggestions that it may be a gravitational lens (Rao and Subrahmanyan, 1988; Subrahmanyan *et al.*, 1990), the strong, ~ 10 Jy, flat-spectrum radio source PKS 1830–211 was found in 1991 to be an Einstein ring/gravitational lens (Jauncey *et al.*, 1991) and remains the brightest such object found in the radio sky by almost two orders of magnitude. Because PKS 1830–211 is such a strong and variable radio source, sensitive observations can be made of its properties, observations that would be difficult, or impossible, for weaker radio lenses. The second part of this thesis is directed at some measurements of its properties.

The symmetric morphology of the source, comprising two compact, flat-spectrum components of similar brightness located on opposite sides of a 1 arcsec ring, immediately suggests a close alignment of a background source behind a lensing mass. Moreover, there is evidence of unusually high rotation measures in some parts of the source which argues that the lensing galaxy is probably a gas-rich spiral (Nair *et al.*, 1993). VLBI images of the two compact components show significant morphological differences that are difficult to interpret.

While the interpretation of the source as a gravitational lens beyond the Galaxy (Subrahmanyan *et al.*, 1992) is secure, it lies in a crowded and heavily obscured field close to the Galactic Centre and so far all efforts to identify optical or infra-red counterparts either for the lensing galaxy or the lensed source have been unsuccessful (Djorgovski *et al.*, 1992; Jauncey *et al.*, 1993). In particular, the failure of optical measurements to furnish any redshifts has driven the search for these critical parameters into the radio spectrum. A radio search for molecular absorption toward PKS 1830–211 is described in Chapter 6.

Total flux density monitoring of PKS 1830–211 over more than six years have revealed large variations on timescales of months (Lovell *et al.*, 1996). Such short timescale changes suggest the presence of compact, milliarcsecond scale structure, and VLBI observations of the two compact cores in PKS 1830–211 have shown significant structural differences between the two cores that are difficult to understand (Garrett *et al.*, 1996). The flux density variations have been demonstrated to be confined to the compact structure (King, 1994). Therefore regular monitoring observations that measure the flux densities of the two compact components

have the potential to provide a lensing time delay (van Ommen *et al.*, 1995). Flux density monitoring observations of PKS 1830–211 are described and analysed in Chapter 7. This chapter describes the radio structure of PKS 1830–211.

In Sections 5.2 and 5.3 data from 5 GHz MERLIN and EVN observations of PKS 1830–211 are presented. The observations were made in September 1991 as a result of a successful proposal submitted on behalf of the Southern Hemisphere VLBI Experiment (SHEVE) collaboration (Preston *et al.*, 1989; Jauncey *et al.*, 1994). The author has analysed the calibrated data and the results of this analysis, which included imaging and model-fitting of the EVN data and model-fitting the MERLIN data, are presented. The MERLIN image presented in Section 5.2 was provided by Dr. T. Muxlow (Muxlow, 1996) from the data collected under this proposal.

5.2 Low Resolution Radio Structure

Figure 5.1 shows a VLA snapshot image of PKS 1830–211 at 15 GHz from the dataset of van Ommen *et al.* (1995; van Ommen, 1996) which clearly shows the unusual double structure with an inversion symmetry. Some of the major features of the source are labelled in the figure. The image displays the two compact cores, A and B, and their associated jets with components C and D indicating the knots in the jets. The two cores have a separation of ~ 1 arcsec at a position angle of $\sim 42^\circ$. Object E has been interpreted by some as the third lensed image of the core of the background source.

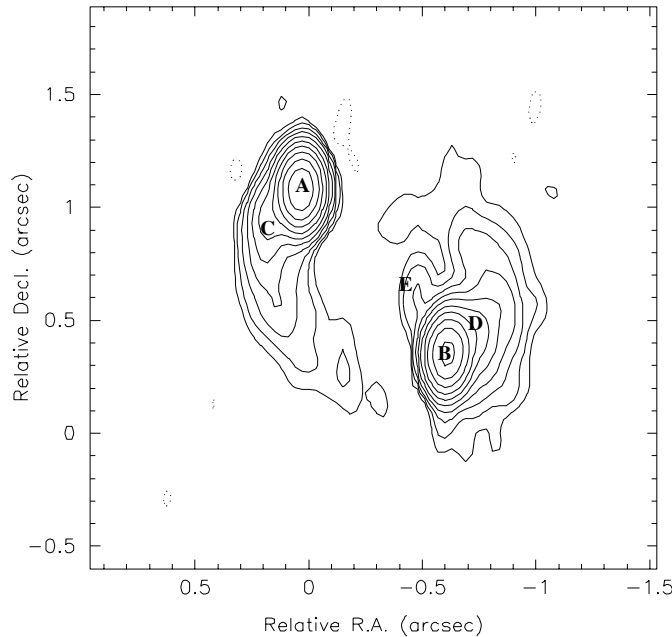


Figure 5.1: A 14.94 GHz VLA snapshot image of PKS 1830–211 at 0.1 arcsec resolution (van Ommen *et al.*, 1995) with various sub-components of the source labelled. Contours are $-0.1, 0.1, 0.2, 0.4, 0.8, 1.6, 3.2, 6.4, 12.8, 25.6$, and 51.2 % of the peak flux density, which is 3.405 Jy/beam. The beam size is 180 by 98 mas at a position angle of -0.3° .

A moderately higher resolution image from data obtained with the MERLIN array at 5 GHz (Figure 5.2) is similar to the 15 GHz VLA image but also accentuates some differences in the two components. The jet emanating from the NE compact component is narrower in cross-section than the SW jet which appears to be blended with other extended emission. The Einstein ring is clearly visible at this frequency and shows a distinct elliptical shape. Object E is also detected, approximately 0.3 arcsec to the NE of the SW component.

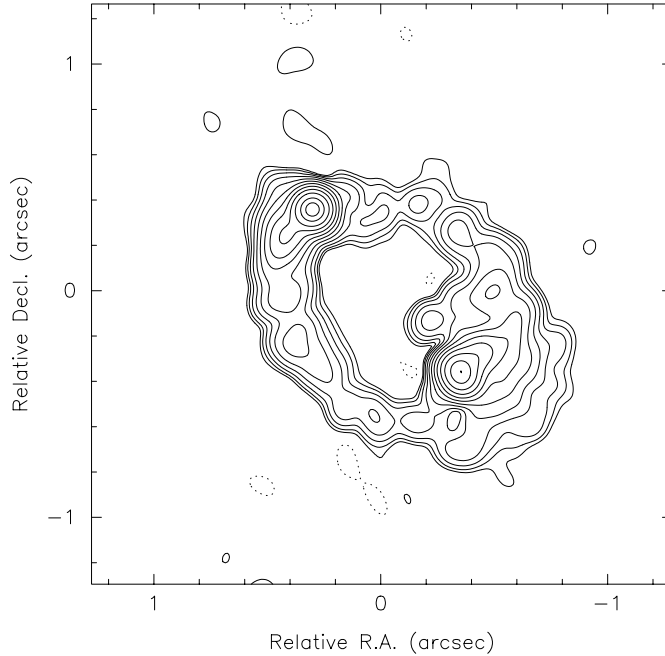


Figure 5.2: PKS 1830–211 at 4.993 GHz, imaged with the MERLIN array in September 1991 (courtesy T. Muxlow). Contours are -0.05 , 0.05 , 0.1 , 0.2 , 0.4 , 0.8 , 1.6 , 3.2 , 6.4 , 12.8 , 25.6 , 51.2 and 80 % of the peak flux density, which is 2.12 Jy. The map has been restored with a circular beam of FWHM 100 mas.

There also appears to be an asymmetry in the polarisation properties of the two components. VLA observations by Subrahmanyam *et al.* (1990) at 15 and 22 GHz showed a difference in polarisation angle in the NE compact component, corresponding to a rotation measure of 1300 rad m^{-2} . Nair *et al.* (1993) argue that such a large rotation measure cannot be ascribed to our galaxy but must be due to an intervening galaxy, probably the lensing galaxy. The absence of a similar change in polarisation angle in the SW component indicates that the obscuring galaxy is situated closer on the sky to the NE component.

5.2.1 Modelling the Lens

Physical measurements that are important in any lensing model include: the lensing galaxy position with respect to the lensed image, its orientation, mass, ellipticity and redshift; the magnification ratio of the lensed components; the redshift of the background source and its position with respect to the lensed image, and the lensing time delay.

In the case of PKS 1830–211, the lensing galaxy is yet to be identified and so its physical parameters remain unknown (except redshift, see Chapter 6). These parameters must therefore be inferred from the lensed image. The magnification ratio of the two flat-spectrum components has been measured at many wavelengths at many epochs. However, several authors have reported a change in ratio with wavelength which Rao and Subrahmanyan (1988) cited as evidence against PKS 1830–211 being a gravitational lens. The measurement of this parameter will be discussed again in Section 5.4. The position of the background source is not directly measurable and must be determined indirectly by modelling the lens. Lastly, the time delay may be measured through regular monitoring of the flux densities of the two compact components and new constraints on the time delay from recent observations are discussed in Chapter 7.

Three attempts to model PKS 1830–211 have been published; Subrahmanyan et al. (1990; SNRS), Kochanek & Narayan (1992; KN), and Nair, Narasimha & Rao (1993; NNR). A comparison of these by NNR (from their own perspective) appears in Appendix A to their paper. Briefly, the first and third of the above apply schematic modelling of an interactive “cut-and-try” flavour to fit the radio images, while KS use an iterative formal inversion method of minimised χ^2 dubbed “LensClean”. The work of NNR may be thought of as a logical development of the early attempts of SNRS, since similar techniques were employed in both, but the great wealth of additional data (principally in the form of new radio images) available to NNR allow the analysis to be carried much further, essentially superseding that of SNRS. Therefore, only the KN and NNR models will be discussed.

Both models were made using relatively low resolution images from the VLA and MERLIN as little high resolution data were available at the time. For example, the images used by KN did not show component E, nor did they fully reveal the radial extension of the ring near the SW core (as seen in Figures 5.1 and 5.2). While both KS and NNR model the (unlensed) source as a core-jet, and obtain reasonable fits to the lensed images, their respective models are striking more for their differences than their similarities. Qualitatively, both models comprise a “core-jet” background source, with the (unlensed) “core” lying close (~ 0.1 arcsec) to the NE of the lens, and producing the two bright lensed components. Beyond this, however, there is little similarity between the models. The inferred structure of the jet for example is quite different in each case: in the KN picture it extends westward through the tangential caustic (producing the complete ring), but in NNR the source is extended in the opposite direction, beginning as a “knot”, and continuing as a jet which then bends back through the south by almost 180 degrees in order to pass through the tangential caustic.

The models are also quite different quantitatively: the derived lensing potential of NNR is highly elliptical ($e = 0.63$) with a core radius of $\theta_c = 0.34$ arcsec, while KN infer an almost circular potential $e = 0.05$ with a core radius of $\theta_c = 0.51$ arcsec. A significant influence on the modelled lensing potential is the magnification ratio of the two images of the lensed core:

Magnification Ratio

The NNR model was based on the 8.4 GHz VLA image of Jauncey *et al.* (1991) and the 15 GHz VLA image of SNRS. NNR estimate the compact core magnification ratio using VLA data taken at two epochs by measuring the ratio of the change in amplitude in the two components. This provided an estimate of 1.79 ± 0.06 for the magnification ratio.

Two images were used by KN to fit a model with the LensClean technique: the 8.4 GHz VLA and 1.7 GHz MERLIN images of Jauncey *et al.* (1991). This technique produced conflicting results. The best fit to the VLA map resulted in a different source position to the best fit of the MERLIN map, although the secondary minimum in the MERLIN fit was coincident with the best fit to the VLA data. The compact component magnification ratio is assumed in LensClean to be that measured directly from the map, *i.e.* there is no attempt to account for the non-variable steep-spectrum structure that contributes to the peak flux densities at low resolution. KN suggest that this may be the reason for the conflicting solutions and conclude that the best fit to the VLA data represents the true solution for the inversion and that the magnification ratio is likely to be closer to that of the VLA map (1.42) than the MERLIN map (0.95).

Time Delay

The estimated time delay between the two principal lensed images is also quite different in the two models. Unfortunately, KN not only omit to give this rather crucial lens parameter in their paper, but present insufficient details to allow it to be readily extracted by the reader. However, by hand-measuring the Figures for the positions of the the unlensed and lensed images of the “core” relative to the lens it is possible to deduce the time delay for the first of their eight models (V1a).

Following KN, the standard lens equation can be cast in the form

$$\mathbf{s} = \mathbf{x} - \nabla\phi(\mathbf{x})$$

where \mathbf{s} is the source plane coordinate, \mathbf{x} the lens (image) plane coordinate, and ϕ is the scaled (dimensionless) two-dimensional gravitational potential. The excess time delay $t(\mathbf{x})$ of an imaged component at \mathbf{x} , relative to the unlensed delay, is then given by

$$t(\mathbf{x}) = (1 + z_L) \frac{D_{OL}D_{OS}}{cD_{LS}} [|\mathbf{s} - \mathbf{x}|^2/2 - \phi(\mathbf{x})]$$

(cf. equations 2–4 of Blandford et al., 1989) where z_L is the redshift of the lens, D_{OL} , D_{OS} , D_{LS} are the angular-diameter distances, respectively, observer-lens, observer-source, lens-source, and c is the speed of light. Substituting model parameters for KN’s model V1a from their Table 1 into their equation 3.2a, and using hand measurements of their Figures 3a and 7, gives

$$t(\mathbf{x}_{NE}) - t(\mathbf{x}_{SW}) = (0.43_{\text{geom}} - 2.85_{\text{potl}}) (1 + z_L) [(D_{OL}D_{OS}/D_{LS})/\text{Gpc}] \text{ days}$$

keeping the geometric and gravitational potential terms, referred to by the “geom” and “potl” subscripts respectively, separate to conform with NNR’s notation in their Table 3. The uncertainty in the above total delay is estimated to be about 5%, comprising the formal errors in the lens parameters and the limited precision extractable from the figures. Thus while the SW component is delayed relative to the NE in both models, the actual delay in the KN model is only about half that of NNR.

Conclusions

The two models described above have relied on different core magnification ratio estimates, resulting in quite different solutions (even using the same technique, as KN found with the conflicting solutions from different datasets). Therefore, it is important to measure the true compact component flux density ratio to provide a better constraint on the models. Such a measurement is attempted in Section 5.4 and again in Chapter 7 using ATCA flux density monitoring observations. The following section describes the VLBI structure of PKS 1830–211.

That these two careful pieces of work should produce such disparate models of the brightest known radio lens is rather surprising, particularly given the high quality of the radio images available, and suggests that one or both approaches is neglecting some important property of the lens. One obvious possibility, suggested by the presence of a second significant mass along the line of sight (Chapter 6), is that the effective lensing potential is more complex in form than has been allowed thus far. Indeed, NNR attribute the key differences between their model and those of KN to the different form assumed for the lensing potential in each case, and that the simple SIS (singular isothermal sphere) form, adopted by KN for computational convenience, may be inadequate to represent high-magnification ring structures of the kind evident in PKS 1830–211. [In view of this, it is worth noting that NNR are themselves obliged to invoke a singular “nuclear” potential, superimposed on their larger oblate spheroidal lensing mass, in order to demagnify the third image of the bright component to a level consistent with its non-detection]. Significantly, in modelling the lens MG1131 + 0456, Chen, Kochanek and Hewitt (1995) find that an “isothermal” (singular) mass distribution is inconsistent with the structure of the extended ring in that system (confirming the central component as a lensed image), but conclude that some additional lensing mass of uncertain origin is imposing an external shear to their model potential. It is tempting to speculate that the confirmed presence of a second galaxy-scale mass along the line of sight to PKS 1830–211 is likewise placing serious limitations on the success of any model based on a single, simple form for the distribution of the lensing mass.

5.3 High Resolution Radio Structure

It was not until PKS 1830–211 was imaged at very high resolution that a remarkable dis-similarity between the two flat spectrum components A and B was

revealed. Shown in Figure 5.3 are high resolution images made from data obtained with the European VLBI Network (EVN) array in September 1991 (various sub-components are labelled here). The data were calibrated within AIPS and imaged with Difmap. The NE component possesses at least three sub-components (labelled in order of brightness A1, A2 and A3), while the SW component appears to possess a compact core (B1) and an extension in the direction of the gravitationally-distorted jet (B2).

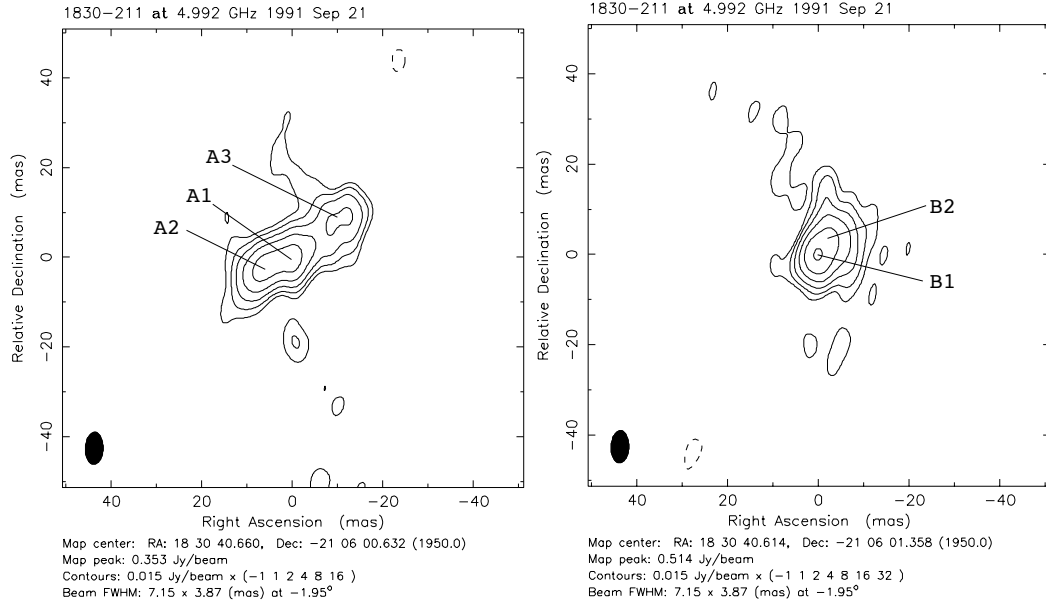


Figure 5.3: The NE (left) and SW (right) compact components of PKS 1830–211 at 4.992 GHz. Various sub-components have been labelled in order of brightness. This dataset is from our EVN observation made in September 1991.

Whilst it seems likely that sub-component B1 is an image of the compact core of the lensed object, it is not clear which is its counterpart in the NE component. There are at least two methods available to determine the nature of the sub-components. First, the sub-component brightness temperatures can be estimated by fitting Gaussian components to them. Second, a comparison with VLBI images at other frequencies might allow the spectral indices of the various sub-components to be determined. The two images of the compact core should both possess similar brightness temperatures and spectral indices at milliarcsecond resolution as gravitational lensing preserves brightness temperature and is achromatic (see also Section 5.4. These two methods have been applied to the data and are described in Sections 5.3.1 and 5.3.2.

5.3.1 Brightness Temperature Estimates

PKS 1830–211 is known to suffer inter-stellar scattering (Jones *et al.*, 1996a) which has the effect of broadening a given image component by a factor proportional to the square of the wavelength. Any brightness temperature measurement will be less than the true value due to the broadening effect. Nevertheless, if one assumes

that both NE and SW VLBI compact components are scattered to the same degree, the inferred brightness temperatures will be comparable and thus useful in this analysis.

The AIPS task JMFIT was used to fit elliptical Gaussian components to the cleaned 5 GHz EVN image. Three Gaussian components, corresponding to sub-components A1, A2 and A3 were fitted to the NE image and similarly, two Gaussian components were fitted to the sub-components in the SW component. Brightness temperatures, which are proportional to flux density and inversely proportional to the subtended solid angle, were thus calculated for each sub-component. These values are shown in Table 5.1

Table 5.1: Elliptical Gaussian sub-components fitted to the NE and SW images in the 5 GHz VLBI image of PKS 1830–211 and their associated brightness temperatures.

Component	Peak flux density (Jy beam ⁻¹)	Maj (mas)	Min (mas)	PA (°)	T _B (K)
A1	0.287	3.8	2.1	104	1.8×10^9
A2	0.358	8.5	2.9	123	7.1×10^8
A3	0.149	12.3	6.8	120	8.8×10^7
B1	0.493	4.6	3.4	131	1.6×10^9
B2	0.220	10.7	5.8	21	1.7×10^8

The sub-components with the highest brightness temperatures in the NE and SW images are A1 and B1 respectively and they are very similar in magnitude. All other sub-components appear to possess brightness temperatures significantly less than A1 or B1. No other simple connection can be made between sub-components based on brightness temperature, therefore this analysis shows that A1 and B1 are lensed images of the same component in the background object.

5.3.2 Spectral Index Analysis

The second method of identifying the lensed core in the NE component is carried out by a super-position of the VLBI images of PKS 1830–211 at two or more frequencies and then estimating the spectral indices of the sub-components.

Shown in Figure 5.4 are super-positions of the 5.0 GHz EVN image of the NE component of PKS 1830–211 with VLBI images made at 2.3 (King, 1994) and 22.0 GHz (Jones *et al.*, 1996a). The images were registered based on the assumption that the compact SW sub-component (B1) occupies the same location with respect to the compact NE sub-component at all frequencies (this is the expected behaviour for a gravitational lens). It was also assumed that the peak in the brightness distribution of the SW component at 2.3 and 5.0 GHz is coincident with the unresolved SW core at 22 GHz, where little or no extended structure is apparent.

There is a significant displacement (~ 4 mas) between the bright core in the NE image at 22 GHz and A1, the nearest sub-component in the 5 GHz image.

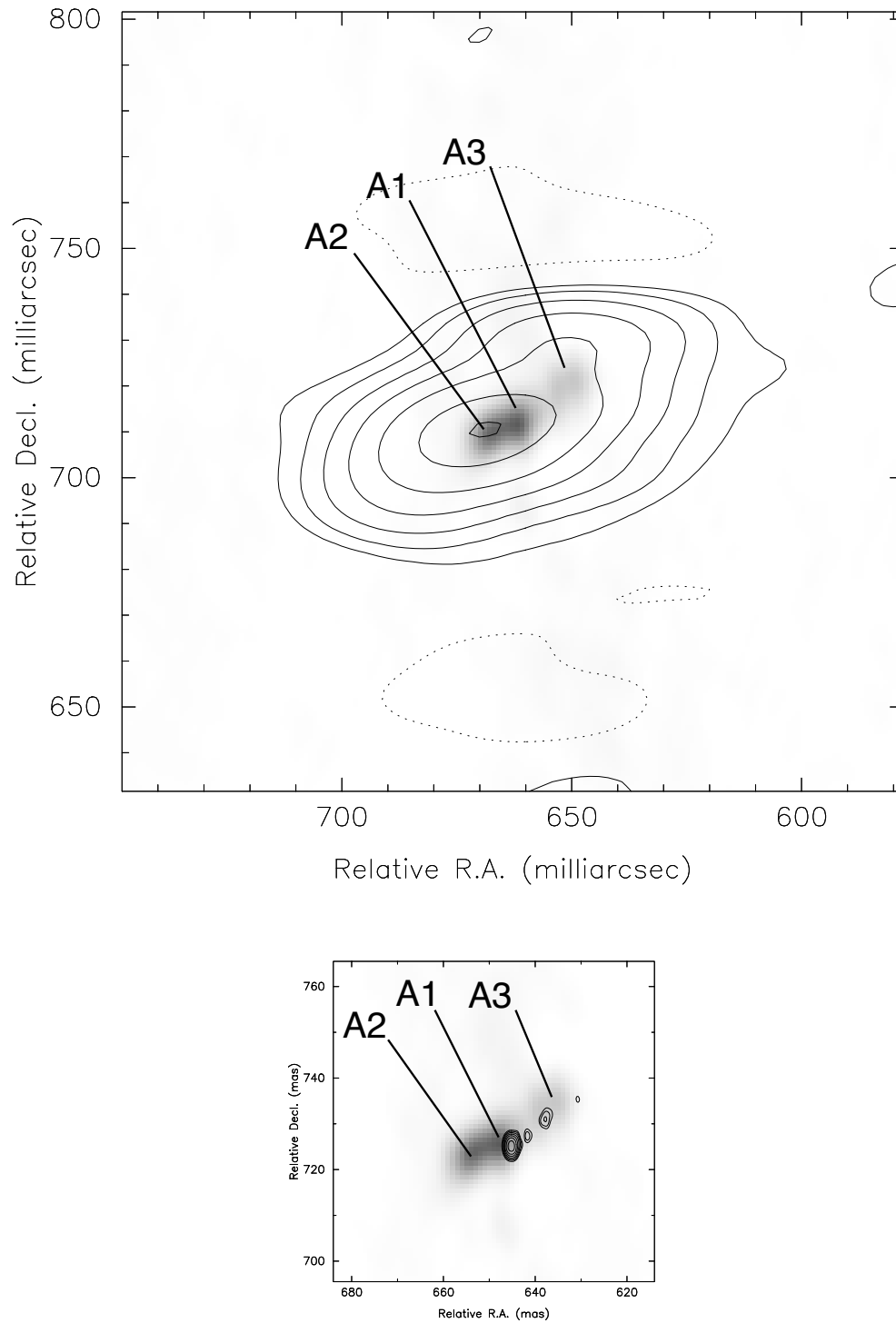


Figure 5.4: Superimposed images of the NE component of PKS 1830–211. The upper and lower frames are presented at the same scale and in both cases the greyscale image is from EVN data (see Figure 5.3). The contoured image in the top panel is a May 1991, 2.3 GHz SHEVE image (King, 1994), while the contoured image in the lower panel is a May 1994, 22 GHz VLBA image (Jones *et al.*, 1996a).

However, they are likely to be associated as there are two possible reasons for the ~ 4 mas mis-alignment: first, the 22 GHz data were imaged after correlating the raw data at two phase centres (one for each of the NE and SW components) and as a result, the NE component at 22 GHz was registered from a poorly imaged SW component which had been affected by bandwidth smearing; second, the image of the SW component at 5 GHz (Figure 5.3, right hand panel) contains an extended component to the NE, thus the alignment with the 22 GHz image based on the peak in the brightness distribution of the 5 GHz SW image may have shifted the 22 GHz component a little toward the NW.

Alternatively, it may be argued that the brightest sub-component in the 22 GHz image of the NE component is coincident with sub-component A2 in the 5 GHz image. If this were the case, the alignment between the compact sub-component in the SW at 22 GHz and the corresponding 5 GHz sub-component would be very poor, the difference in position would be ~ 9 mas with the 22 GHz image lying at a position angle of approximately 109° with respect to the SW component in the 5 GHz image. Furthermore, the position angle and separation of the brightest and second-brightest sub-components in the NE component at 22 GHz are approximately -52° and 9.4 mas respectively whereas the position angle and separation of A2 with respect to A1 at 5 GHz are about -72° and 5.7 mas respectively.

No attempt has been made to quantitatively measure and compare the spectral indices of the various sub-components as all of these observations were made at different epochs and it is well established that the compact structure of PKS 1830–211 is highly variable. Also, each of these images were made at very different resolutions and so are sensitive to different scale structure. Nevertheless, it might be possible to make some qualitative statements on the relative spectral indices of the sub-components.

The top panel of Figure 5.4 presents the superposition of the EVN image of the NE component (greyscale) and the contoured 2.3 GHz SHEVE image (King, 1994). Although these observations were made at different resolutions, it would appear that both images show very similar structure. Component A2 in the 5.0 GHz image would appear to coincide with the peak in the brightness distribution at 2.3 GHz, indicating that this component dominates at the lower frequency, whereas components A1 and A2 possess similar brightness at 5.0 GHz. Therefore, one can deduce that component A2 possesses a steeper spectral index than A1, and this is borne out when comparing the 5.0 and 22 GHz data (the lower panel in Figure 5.4). The 22 GHz VLBA image (Jones *et al.*, 1996a) shows no evidence of component A2, but does show a “jet” at a position angle coincident with that seen at 5.0 GHz (component A3). Similarly, the 15 GHz VLBA image of Garrett *et al.* (1996) shows a ~ 15 mas jet at a position angle of $\sim -50^\circ$ and no evidence of component A2. The separations and position angles of the three sub-components for all VLBI observations that clearly resolve them are listed in Table 5.2. These data suggest that the jet in this object possesses a significantly flatter spectral index than component A2, although it is much steeper than A1 (the ratio of peak brightness in A2 compared to A3 is $\sim 2.5:1$ at 5.0 GHz and $\sim 8:1$ at 22 GHz). It is also important to note that the position angle of A1 with respect to A2 is not the same as that of A3 with respect to A1. Such an alignment might be expected

if either A2 or A3 was a counter-jet.

Table 5.2: Position angle and separation estimates for sub-components of the NE VLBI image of PKS 1830–211 at three frequencies.

Freq (GHz)	Position angle (°)		Separation (mas)	
	A2 w.r.t A1	A3 w.r.t. A1	A1 to A2	A1 to A3
5.0	108	–51	5.7	~ 14
15	–	–50 [†]	–	15
22	–	–52	–	9.4

[†] This value was estimated from the published image (Garrett *et al.*, 1996)

5.3.3 Conclusion

The milliarcsecond-scale EVN images clearly demonstrate the dramatic differences between the two compact components in PKS 1830–211. Two methods have been employed to identify the compact flat-spectrum core in the two components and both methods identify A1 and B1 as lensed images of the same compact component in the background source.

5.4 Continuum Spectra of the Components of PKS 1830–211

If the background source in PKS 1830–211 consisted solely of a compact core, then the resultant lensed image would consist primarily of two bright images of the core, magnified by different factors. As gravitational lensing is achromatic, the two components in the image would possess the same brightness ratio irrespective of frequency, provided the core does not intersect a caustic in source space. This is unlikely, and none of the existing models of PKS 1830–211 predict such behaviour.

The background source, however is more complex than an isolated core. Instead, it is believed to possess a high brightness temperature ($\sim 10^8$ to 10^9 K) flat-spectrum core and a low brightness temperature ($\sim 10^6$ K) steep-spectrum jet that has been lensed into a ring and NNR argue that it is this steep-spectrum component that causes the apparent increase in flux ratio with frequency in the low resolution images (*i.e.* as frequency increases, the contribution from the steep-spectrum component in the NE and SW components decreases).

Radio telescope arrays act as brightness temperature “filters” where the range of brightness temperatures an array is sensitive to increases with baseline length. Therefore, high-resolution radio imaging of PKS 1830–211 will be sensitive only to the high brightness temperature, compact structure and not the low brightness temperature Einstein ring. An examination at high resolution of the flux densities of the compact components in PKS 1830–211 at different frequencies will show if the change in flux density ratio with frequency observed at lower resolutions

is caused by the low brightness temperature steep-spectrum component. Such measurements are also important in modelling the total flux density variations in the source, as they provide an estimate of the spectra of the variable compact components and the non-variable Einstein ring.

5.4.1 Measuring the Compact Component Flux Densities

The measurement of the compact component flux densities in PKS 1830–211 to obtain a continuum spectrum of each component and to obtain flux density ratios is difficult for several reasons:

First, PKS 1830–211 is highly variable and, as will be discussed in Chapter 7, this variability is frequency dependant. For example, a flux density measured when PKS 1830–211 is flaring at one frequency will not necessarily be comparable with a measurement made at the same time at a different frequency. To avoid this problem, measurements must be taken when PKS 1830–211 is in a quiescent state.

Second, it is difficult to separate core flux density from extended, steep-spectrum flux density, especially in VLA and MERLIN data. This is less of a problem with VLBI observations which are sensitive only to compact structure. For example, the method employed by van Ommen *et al.* (1995) to measure component flux densities from VLA images by fitting Gaussian components, is likely to provide artificially high values. This is because there will be a contribution from the ring (as discussed in Section 5.2.1, above) which is not clearly separated from the compact core at that resolution. The resulting component ratios are likely to be depressed. This effect will be resolution dependant, as can be seen in the 8.4 GHz data of van Ommen *et al.*: the differences between total flux density and the sum of the NE and SW component flux densities (*i.e.* the Einstein ring flux density) are consistently larger in the higher resolution images (with the VLA in A configuration) than in the low resolution images (with the VLA in B and BnA configuration). A similar effect is seen in the 15 GHz measurements of van Ommen *et al.* To avoid this problem, all measurements must be made at a similar high resolution.

Third, PKS 1830–211 is known to suffer inter-stellar scattering (Jones *et al.*, 1996b). This means that any measurements of core flux density, especially at low frequencies, is likely to contain a contribution from the jet that is impossible to remove. To avoid this problem, observations made at frequencies ≥ 2.3 GHz will be used, where the scattering size is less than ~ 15 mas, the size of the NW “jet” in the NE component (Figure 5.3).

Each of the data-sets chosen for this analysis are described below in order of frequency. The results are presented in Table 5.3.

2.3 GHz

Observations of PKS 1830–211 were made at 2.3 GHz with the SHEVE array in May 1991 (King, 1994). Figure 7.1 shows that at this time (day 388), PKS 1830–211 was in a quiescent phase, thus making the data suitable for this

Table 5.3: Estimated compact component flux densities and flux density ratios.

Array	Freq. (GHz)	Flux densities (Jy)				Ratio S _{NE} /S _{SW}
		Total	NE	SW	Ring	
SHEVE	2.3	9.1	1.68 ± 0.17	0.99 ± 0.10	6.4 ± 0.20	1.70 ± 0.14
EVN	5.0	6.5	1.86 ± 0.04	1.52 ± 0.04	3.1 ± 0.06	1.22 ± 0.03
MERLIN	5.0	6.5	2.14 ± 0.04	1.92 ± 0.04	2.4 ± 0.06	$1.11 \pm 0.03^\dagger$
MERLIN	5.0	6.5	1.66 ± 0.08	1.41 ± 0.08	3.4 ± 0.11	$1.18 \pm 0.07^\ddagger$
VLA	15	3.14	1.50 ± 0.06	1.00 ± 0.06	0.6 ± 0.08	1.50 ± 0.07
SEST	100	2.1	1.33 ± 0.1	0.76 ± 0.1	0.0	1.75 ± 0.15

[†] Component flux densities calculated from the map peaks.

[‡] Component flux densities calculated from fitting a simple model to the longest baselines.

analysis. A “compact flux density” measurement for each component was made by calculating the total integrated flux density in the NE and SW components. This is a reasonable assumption, as will be shown in the discussion of the 5.0 GHz data below.

5.0 GHz

No total flux density measurements were made near the date of the 5 GHz EVN and MERLIN observations (September 1991, day 520 in Figure 7.1) so it is difficult to tell if the source was quiescent or not at the time. The total flux density during these observations was 6.5 Jy which is at least 1 Jy less than any other 5 GHz measurement in the figure. Also, these observations were made nearly 200 days before the peak of the 8.4 GHz outburst, and since the outburst appears to propagate to lower frequencies at later times, it seems likely that PKS 1830–211 was not particularly active at 5 GHz at this time.

As the ENV and MERLIN observations were made at the same time, the data provides an opportunity to compare methods of measuring the compact component flux densities. Three measurements were made and the results are presented in Table 5.3. First, the total integrated flux density was measured in the NE and SW EVN images to provide an estimate of the compact flux density in each component. Second, the peak flux densities in the 100 mas resolution MERLIN image (Figure 5.2) were measured in the NE and SW components. Third, the MERLIN *u-v* data were edited so that only the longest baselines (2.8 to 3.6 M λ) were left thus providing a dataset that was sensitive to the most compact structure. A simple model, consisting of two point sources, was then fitted to the data to estimate the flux densities of the two compact components.

Of the two methods applied to the MERLIN data, the second provides a better estimate of the compact flux density as derived from the EVN data and the flux density ratios are consistent in these two cases. These measurements suggest that an integration of the total flux density in VLBI images and estimating flux density through fitting a simple model to long-baseline data in images from smaller arrays produce consistent flux density ratio estimates. The component flux densities and

flux density ratios derived from both the EVN and long baseline MERLIN data will be used in the following analysis.

15 GHz

The calibrated 15 GHz data of van Ommen *et al.* (1995) was re-analysed by the author for this measurement (van Ommen, 1996). An observation that was made in July 1990 (day 78 in Figure 7.1) was used, as that appears to be a time when PKS 1830–211 was quiescent. As with the MERLIN data, only the long-baseline u - v data (620 to 870 k λ) were used to obtain flux density estimates for the NE and SW compact components and hence a flux density ratio. No 8.4 GHz component measurements were made because of the low-resolution VLA configuration during the quiescent period when van Ommen *et al.* made their observations.

100 GHz

PKS 1830–211 has recently been observed at 100 GHz using SEST (Wiklind and Combes, 1996a). The flux density of the steep-spectrum structure is extremely weak at this frequency and so there is little contribution from the Einstein ring. Although no flux density monitoring data is available at the time of the observations (which would indicate if PKS 1830–211 was quiescent or not at the time), the total flux density during the SEST observations was measured as 2.1 Jy. This value is similar to those measured at the Nobeyama Millimetre Array (Kamenô, 1995) when PKS 1830–211 appeared to be quiescent so it is assumed that PKS 1830–211 was quiescent during the SEST observations as well. Therefore, these measurements provide a good estimate of the flux density ratio at 100 GHz when the source was probably in a quiescent state. Wiklind and Combes infer a magnification ratio of 1.75 ± 0.15 from the depth of the absorption features in their observations.

5.4.2 Results

Figure 5.5 shows the estimated quiescent spectra of the two compact components along with a total flux density spectrum. Figure 5.6 again shows the quiescent total flux density spectrum, the sum of the compact component spectra (*i.e.* the contribution from the variable component) and the remaining, non-variable steep-spectrum Einstein ring flux density. Extra data points were available for the Einstein ring flux density spectra because the points may be determined when PKS 1830–211 is undergoing an outburst. Additional points at 8.4 and 15.0 GHz were determined from the VLA data of van Ommen *et al.* (1995) taken during the high spatial resolution observations. As the Einstein ring flux density must remain constant, the scatter in these points provides an estimate of the error in the compact component flux density measurements displayed in Figure 5.5. The rms scatter in these points has been adopted as the errors in that figure for the 5 and 15 GHz points. It is therefore likely that formal error estimates at other frequencies are an underestimate of the true errors and so any detections of trends in the data must be considered with some caution. A simple power-law has been

fitted to the Einstein ring flux density measurements using a least-squares method, giving a spectral index of -1.0 ± 0.1 ($S \propto \nu^\alpha$).

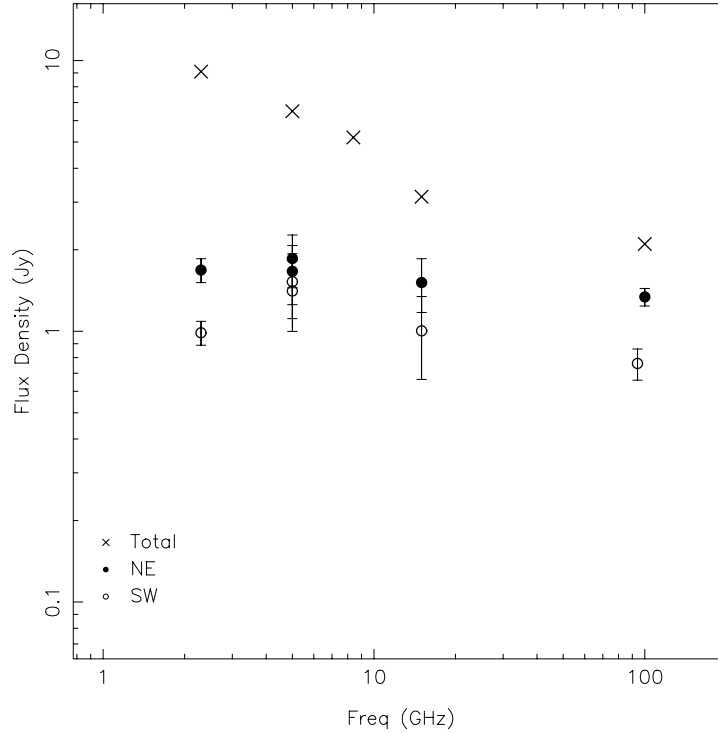


Figure 5.5: Quiescent flux density continuum spectra of PKS 1830–211 and its compact components.

The inferred compact component flux density ratios are presented in Figure 5.7. A least squares fit of the function $R = m \log \nu + c$ to the data was made, where R is flux density ratio and ν is frequency in GHz. The gradient, m , is 0.13 ± 0.12 . Therefore, the figure shows no clear trend for an increase or decrease in ratio with frequency, especially considering the likely underestimate of errors. The mean flux density ratio is 1.54 ± 0.25 .

5.5 Summary

An analysis of the flux densities compact, high brightness temperature structure in PKS 1830–211 has shown no clear trend for an increase or decrease in flux density ratio of the two compact components with frequency. Therefore there is no evidence that the two images of the core of the background source have different continuum spectra over nearly 2 magnitudes of frequency. An examination, over several epochs of the scatter in the measured flux densities of the (non-variable) Einstein ring shows that the formal errors in the compact component flux density measurements are an underestimate of the true errors, thus strengthening the argument against a detectable difference in the spectra of the two compact components.

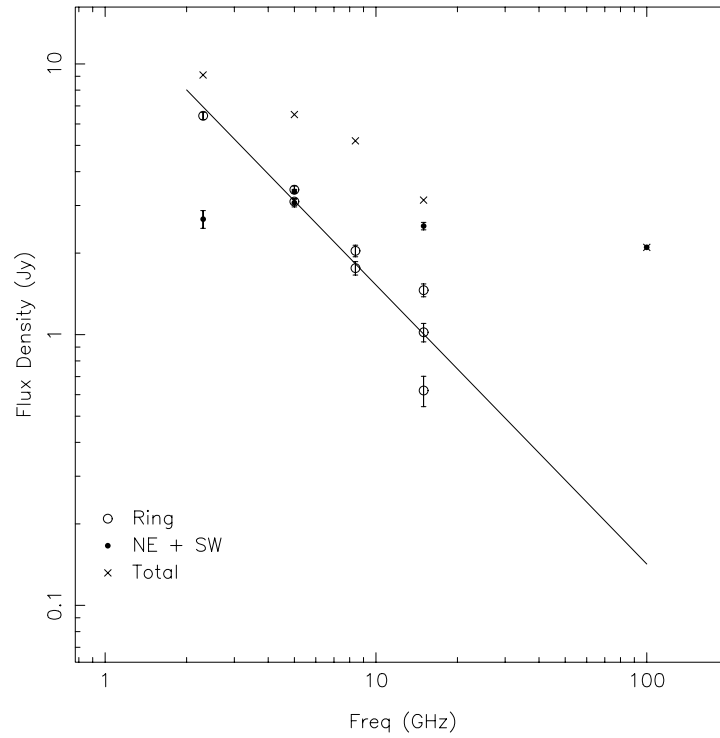


Figure 5.6: Quiescent flux density continuum spectra of PKS 1830–211 and its variable and non-variable components. A power-law spectrum has been fit to the Einstein ring data (solid line).

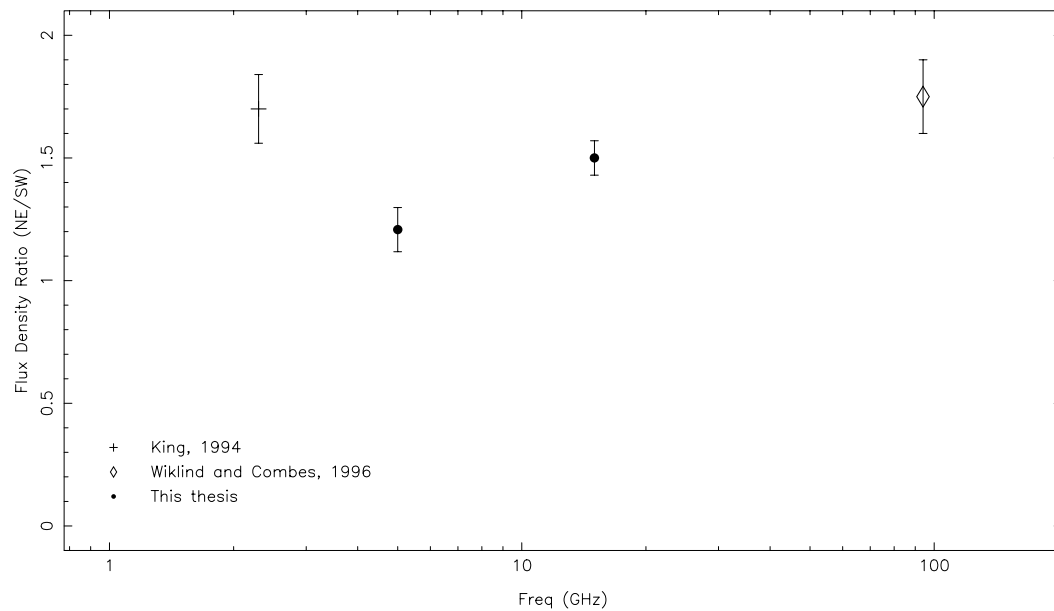


Figure 5.7: Quiescent compact component flux density ratios of PKS 1830–211. The mean flux density ratio at 5.0 GHz (derived from the EVN data and the long baseline MERLIN data) is shown.

The mean flux density ratios of the compact components is 1.54 ± 0.25 , a value consistent with the models of Kochanek and Narayan (Kochanek and Narayan, 1992), who suggest a ratio near 1.42, and Nair *et al.* (1993) who estimate a ratio of 1.79 ± 0.06 . Therefore, neither model can be ruled out based on the available flux density ratio measurements.

VLBI images of PKS 1830–211 show that the NE and SW components possess a compact core (labelled A1 and B1 respectively in Figure 5.3) and an extension in the direction of the gravitationally-distorted jets (labelled A2 and B2) which form the Einstein ring seen in lower resolution images (*e.g.* Figure 5.2). The NE component also contains a ~ 15 mas “jet” (labelled A3) directed at a position angle of $\sim -51^\circ$, almost diametrically opposed to the direction of the lensed jet. This striking difference has persisted over at least three years (Jones *et al.*, 1993; Garrett *et al.*, 1996) and so seems unlikely to be due to lensing time delay effects. The alternative explanation that scattering by a high gas concentration in front of the NE component is causing the additional linear structure is ruled out as there is no λ^2 dependence on the length of this feature in the 5 and 15 GHz images.

This unexplained additional feature in the NE component of PKS 1830–211 may indicate that a simple lensing model may not be appropriate in this case. Clearly, further observations are required in order to determine the parameters of the system such as the redshifts of the lensing galaxy and the background source as well as the lensing time delay. The next chapter describes a radio search for molecular absorption towards PKS 1830–211 that can provide redshift information for this system.

Chapter 6

PKS 1830–211: A Search for Absorption

6.1 Introduction

In order to model a gravitational lens and obtain an estimate of the Hubble constant (H_0), it is essential that the redshifts of the lensing object and the background source be determined. Redshift measurements are typically made by searching for absorption or emission features in the optical spectrum of the source in question. Unfortunately PKS 1830–211 lies at a low galactic latitude and longitude and so all attempts to date to obtain an optical identification have been thwarted by a very crowded field with a large amount of extinction. Observations (Djorgovski *et al.*, 1992; Jauncey *et al.*, 1993) revealed a foreground M star nearly coincident with the NE radio component. Such conditions are likely to make spectroscopy of any optical identification, which must be weak compared to the confusing foreground objects, very difficult. It seems likely then that any successful redshift measurement must be made at wavelengths that are not as severely affected by foreground stars and extinction. This has driven redshift searches to radio and millimetre wavelengths and in this chapter, a survey for redshifted H_i and OH absorption towards PKS 1830–211 and subsequent follow-up observations are discussed.

6.2 Single Dish Observations

Detection of molecular absorption in a source of unknown redshift is technically challenging, requiring wide receiver bandwidths and being subject to severe man-made radio interference. The observations described here were made as part of a series of cooperative observations at the Parkes Observatory with the Project Phoenix group (Tarter, 1996) on June 10 and 11, 1995 at the end of a 5 month period of SETI observations. The Project Phoenix receiver and signal processing equipment were used to cover a frequency range of 995 to 1675 MHz, nicely complementing a previous absorption search over the frequency range 400–1000 MHz at Green Bank, which yielded a null result (McMahon *et al.*, 1993). The Phoenix

system at Parkes provided spectral resolution of 643 Hz with an effective instantaneous bandwidth of 20 MHz in two circular polarisations and a system temperature of approximately 20~25 K over the surveyed band. Spectra were collected through the SETI Multi-Channel Spectrum Analyser which allows simultaneous collection of two 10 MHz bandwidth, dual-polarisation spectra. Each spectral band was observed with an integration time of 138 seconds on at least 4 occasions over a wide range of hour angles. Reference spectra were taken in the same manner in a direction 1 degree further away from the galactic plane. They were used to calibrate the system bandpass.

The Project Phoenix equipment has been designed to collect spectra in a topocentric reference frame in order to easily recognise ground-based signals. Corrections for Earth rotation, orbital motion and heliocentric motion have been made so that the data presented here are relative to the solar system barycentre. The spectra have been binned into 7.7 kHz channels and the amplitude scale is based on an estimated system equivalent flux density of 37 Jy at 1.2 GHz. An rms error of 27 mJy is achieved with four 138 sec “on/off” scan pairs.

The observations covered the entire frequency range mentioned, bar the two intervals 1535–1635 MHz and 1165–1175 MHz which were both omitted because of excessive interference. Although interference of both terrestrial and satellite origin was profuse over most of the remaining band, it was generally of very narrow bandwidth and easily recognisable, and did not greatly impede the search.

A single absorption system was detected with two main sub-components of similar amplitude, centred at 1191.1 MHz with a line width of approximately 50 km s^{-1} (Figure 6.1a). The absorption feature was detected with comparable strength on two consecutive days. On the second day, observations of PKS 1830–211 were bracketed with those of PKS 1921–293, a nearby source of similar flux density. No evidence of the absorption feature was seen in this comparison source.

Estimates of the frequencies and widths (at FWHM) of the two spectral sub-components have been made by fitting two Gaussian functions to the absorption profile shown in Figure 6.1b. The fitted Gaussians for the low and high-velocity components have widths of $16 \pm 2 \text{ km s}^{-1}$ and $25 \pm 2 \text{ km s}^{-1}$ respectively.

The observed width and profile of the absorption suggest two alternatives. If only one compact component of the image is suffering absorption, then the observed line width presumably represents a number of superposed clouds of cold gas through an intervening galaxy seen close to edge-on (as the width is similar to lines of sight through our own Galactic disk). If, on the other hand, both compact components are being absorbed, the galaxy must be close to face-on to avoid a much larger width from differential rotation within the galaxy. High-resolution imaging with VLBI is required to answer this question.

6.3 VLBI Observations

VLBI observations were made on 18 September 1995 with four telescopes of the Australian Long Baseline Array (LBA) (Preston *et al.*, 1993; Jauncey *et al.*, 1994): Hobart; Coonabarabran; Parkes and the five antennas of the Australia Telescope

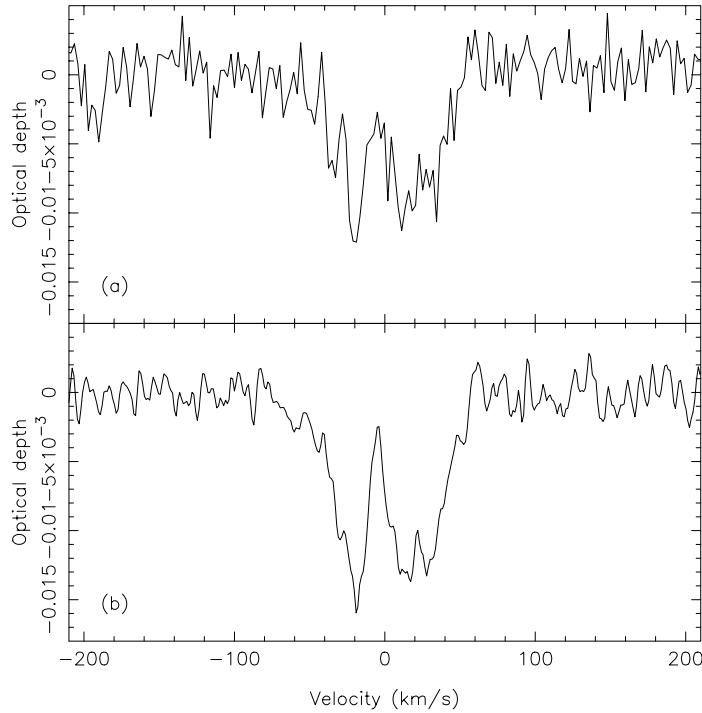


Figure 6.1: Discovery spectrum taken at Parkes with the Project Phoenix SETI Receiver (top) and a confirmation spectrum taken at the ATCA during the VLBI observations (bottom).

Compact Array (ATCA) acting as a phased array. S2 recorders (Wietfeldt *et al.*, 1991) were used, operating in dual polarisation (LCP and RCP) with 4 MHz bandwidth centred on 1191.0 MHz. Correlated visibilities between all six antennas of the ATCA were also recorded to produce an improved total-power spectrum (Figure 6.1b).

The VLBI observations demanded an observing frequency not normally used in radio astronomy. As a consequence, there were several technical problems in performing this experiment and only four observatories were able to participate. Parkes was able to observe as it still had the SETI receiver available at the time. Both Coonabarrabran and the ATCA possess very similar receivers which are nominally capable of covering a frequency range of 1.25 to 1.78 GHz in the 20 cm band, but after some adjustment were able to tune to the desired frequency, although with increased system temperatures. Hobart was able to participate in the experiment with a modified room-temperature 20 cm receiver.

PKS 1830–211 was observed over an 8 hour period interleaved with PKS 1921–293, a bandpass calibrator. The VLBI data were correlated at the ATNF VLBI correlator (Wilson *et al.*, 1996) with 3 correlator blocks in operation. This meant that two passes of the data through the correlator were required in order to obtain visibilities on all baselines. Editing and calibration of the data was carried out in AIPS whilst imaging and model-fitting was done within Difmap (Shepherd, 1994). Phase self-calibration was only applied after a model was obtained that provided a satisfactory fit to the amplitude visibilities and closure phase. No correlated flux was detected on the long ($> 4 M\lambda$) baselines to

Hobart owing to interstellar scattering in the source at this low frequency. Once a cleaned and phase self-calibrated continuum map had been obtained, the spectra at the positions of the two compact components were obtained within AIPS using the ISPEC task. The final continuum image and associated spectra are shown in Figure 6.2.

The continuum VLBI image shown is similar to an earlier 2.3 GHz VLBI image (Jauncey *et al.*, 1991) and shows the two compact components of PKS 1830–211, but little of the low brightness ring which is heavily resolved at this resolution. Figure 6.2 also shows the absorption spectrum of each component, clearly demonstrating that the two velocity components of the absorption system obscure different parts of the source. The low velocity component is also heavily resolved and therefore must be obscuring only the extended ring while the high velocity component is resolved only partially and covers the NE component but is weak or absent in the SW component. This, together with a comparison of the relative optical depths in Figures 6.1 and 6.2, also allows us to infer that the angular size of the absorbing features must be greater than a few tenths of an arcsecond.

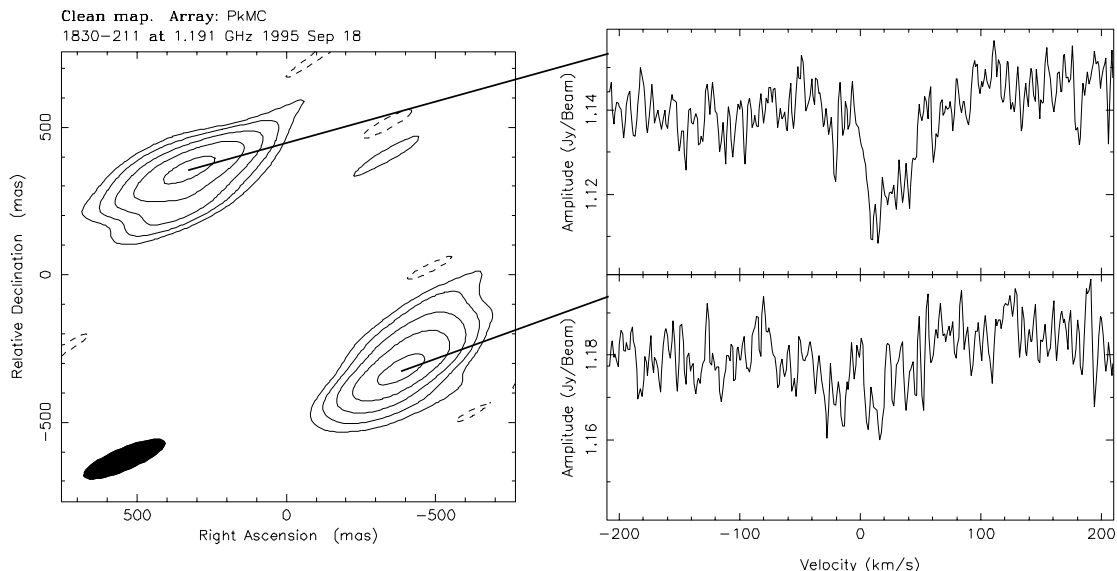


Figure 6.2: 1.19 GHz VLBI continuum map of PKS 1830–211 (left). The restoring beam is 294 by 75.2 mas and the contours are at $-5, 5, 10, 20, 40$ and 80% of the map peak which is 1.27 Jy per beam. Also shown here are the spectra of the two continuum components (right).

A molecular absorption system at a redshift of 0.88582 ± 0.00001 has also been found in this source (Wiklind and Combes, 1996a), and is argued to arise in an intervening galaxy rather than in the lensed object. This has been confirmed by observations with the BIMA array which have spatially resolved the $z = 0.89$ absorption (Frye *et al.*, 1996). It is likely that the 1191 MHz detection constitutes a second absorption system in PKS 1830–211 and is probably HI absorption in an intervening galaxy at a redshift of 0.1926 ± 0.0001 . In support of this it is noted that there are no catalogued lines near 2246 MHz, the rest frequency of the observed absorption if it belongs to the $z = 0.89$ system. Further, observations of the bright Galactic sources Sgr B2, Ori KL and IRC 10216 with the 26 m telescope

at Hobart to search for a possible unlisted transition at this frequency, detected nothing above an rms noise level of $\sim 0.1\%$ of the continuum. Moreover, the detection appears to lie mainly in front of the NE component whilst the $z = 0.89$ absorption is confined to the SW component (Wiklind and Combes, 1996a; Frye *et al.*, 1996). This absorption feature also displays velocity structure not seen in the $z = 0.89$ absorption profiles.

The interpretation of the feature in Figure 6.1 as OH is unlikely for two reasons. First, the spectra show none of the ‘satellite’ profiles typical of OH absorption and second, there was no evidence of absorption at 1016 MHz corresponding to HI at the same redshift, which should have been clearly visible. Neither can this be a hydrogen recombination line as there should have been many such lines across the band and there were not.

Wiklind and Combes (1996b) report no evidence of molecular absorption in PKS 1830–211 at $z = 0.19$ in their SEST observations. However this is not totally unexpected as the total solid angle subtended by the source at these high frequencies is small ($\sim 1 \text{ mas}^2$) and hence the probability of intersecting a dense molecular cloud along the line of sight is presumably small.

The absorption feature seen in Figure 6.1 is very similar in both width and column density to that found in the lens system 0218+357 (Carilli *et al.*, 1993), which is convincingly argued to arise from HI absorption in the lensing galaxy, probably a spiral galaxy seen nearly edge-on. A similar interpretation is likely for the absorption in PKS 1830–211, with the line of sight intercepting several HI clouds in a gas-rich galaxy at $z = 0.19$. The two features seen in the absorption profile may well correspond to two spiral arms of $\sim \text{kpc}$ scale seen nearly superposed, both of which partially obscure the ring and one of which obscures the NE compact component. Such a picture is entirely consistent with the properties of HI clouds and galaxy dynamics observed within our own Galaxy.

Independent evidence for a considerable amount of material along the line of sight is suggested by the unusually high rotation measure seen in the NE component (Nair *et al.*, 1993; Subrahmanyan *et al.*, 1990). Furthermore, the observed downturn in total flux density of PKS 1830–211 below 1 GHz (Rao and Subrahmanyan, 1988) implies significant free-free absorbing material obscuring the non-compact structure, which has a steep spectrum and cannot be synchrotron self-absorbed.

6.4 A Compound Gravitational Lens?

While the HI absorption toward PKS 1830–211 indicates the presence of a galaxy at $z = 0.19$, this does not infallibly imply *a priori* that gravitational lensing is taking place at this redshift, any more than it does for the $z = 0.89$ system. That lensing of some kind is taking place is beyond dispute given, for example, the near-simultaneous variation seen in the flux density variations of the two compact components (van Ommen *et al.*, 1995), apparently separated by more than $\sim 10 \text{ kpc}$, is a most improbable effect in any non-lensed interpretation. It seems almost certain therefore, that at least one of the two redshift systems at $z = 0.19$

and $z = 0.89$ is partaking in the lensing and there is further evidence that both systems may be involved.

Firstly, the lens evinces a quite paradoxical appearance at high resolution as has been noted in Chapter 5. VLBI images made over a 3 year period (Jones *et al.*, 1993; Garrett *et al.*, 1996) show the SW component to be unresolved at \sim milliarcsecond resolution while the NE component shows a well resolved linear structure. This difference in morphology of the two components is too long-lived to be due to the difference in propagation times to the two components, estimated to be no more than a few tens of days (Nair *et al.*, 1993; van Ommen *et al.*, 1995; Chapter 7). The results presented here suggest that the second absorption system at $z = 0.19$ may be responsible for this striking disparity in the two images by causing additional lensing distortion of the NE image, thus forming a compound gravitational lens. Secondly, attempts to model PKS 1830–211 with a single, simple gravitational potential have achieved only modest success, and have produced markedly different models (see Chapter 5, Section 5.2.1).

The presence of a second lensing galaxy in this system adds an extra layer of complexity to any lensing model. This galaxy is likely to influence the light travel time through the NE component and so must be considered before H_0 can be determined from the time delay. It is important therefore to estimate the mass and position of the $z = 0.19$ system. It is not possible to obtain this information from the VLBI data. However polarisation images of PKS 1830–211 at two or more frequencies to map rotation measure would help to delineate changes in the electron density along various lines of sight to the lens. Such observations may help to locate the $z = 0.19$ galaxy with respect to the lensing system.

6.5 Summary

This chapter has described the detection of a new absorption feature towards PKS 1830–211, most likely due to neutral hydrogen in a redshift system at $z = 0.19$. Follow-up VLBI observations have spatially resolved the absorption and reveal it to cover the NE compact component and part of the lower surface brightness ring. A second galaxy has been discovered by Wiklind and Combes (1996a) at $z = 0.89$ which appears to cover the SW component only (Frye *et al.*, 1996). This information, together with the unusual compact structure seen in VLBI observations (Chapter 5) indicates that both galaxies may be distorting the image of the background source, making PKS 1830–211 a compound gravitational lens.

Chapter 7

Flux Density Monitoring of PKS 1830–211

7.1 Total Flux Density Measurements

Gravitational lens observations offer the potential to measure the Hubble constant, H_0 . The parameters derived from lensing models, such as the magnifications and positions in a lensing system, are dimensionless and so provide no overall scale. It is by measuring the time delay that the scale of the lensing system and hence H_0 is determined.

The time delay, $\Delta\tau$, between two light paths in a lensing system is given by:

$$\Delta\tau = \tau_{\text{geom}} + \tau_{\text{grav}} \quad (7.1)$$

where τ_{geom} is the contribution to the time delay caused by the geometrical difference in path lengths of the two light rays and τ_{grav} is the time delay due to the gravitational potential of the lensing galaxy, the relativistic time delay. Both of these contributing factors scale as H_0^{-1} , so a lensing model that can reproduce the geometry of a system also provides the scaled time delay $H_0\Delta\tau$. Consequently, the measurement of the time delay in a well modelled lensing system will provide an estimate for H_0 (Refsdal, 1964; Refsdal, 1966; Narayan and Bartelmann, 1996).

PKS 1830–211 is an especially good candidate for time delay measurements because it is strong and highly variable. Monitoring the flux densities of the two compact components in PKS 1830–211 is thus a very good method for determining the time delay, provided that measurements are made on a timescale shorter than the total flux density variations. Compact component monitoring observations have been made and are continuing (Section 7.2), but the determination of the variability timescale and an understanding of the propagation delay of flux density outbursts from one observing frequency to the next is most efficiently carried out through total flux density measurements.

The total flux density of PKS 1830–211 has been monitored on a regular basis at 2.3 and 8.4 GHz with the University of Tasmania’s Mount Pleasant 26 m radiotelescope since late 1990 by King (1994; King *et al.*, 1996), by the author and King between May 1991 and mid 1993, and since mid 1993 solely by the author. These data form a major part of the light curve measurements collected

for PKS 1830–211 thus far are presented in Figure 7.1 which shows this source to be highly variable.

The 2.3 GHz flux density decreased from 10 Jy in November 1990 to a minimum of 9 Jy during 1992, then increased to ~ 10 Jy and has since shown little sign of variability, although the recent sampling is poor. Over the same interval, the flux density at 8.4 GHz has exhibited greater variability, more than doubling from an initial value of 5 Jy in late 1990 to a peak of ~ 11 Jy early in 1992, before decreasing to ~ 7.5 Jy. VLA observations by van Ommen *et al.* (1995) show that the 15 GHz total flux density increased before the 8.4 GHz brightening seen at Mount Pleasant. Although the 15 GHz time series is not well sampled, it is clear from these data that the 15 GHz outburst precedes the 8.4 GHz feature by as much as ~ 200 days. A limited amount of total flux density data are also available at millimetre wavelengths (Kamenó, 1995) and this reveals a decrease in flux density over ~ 150 days starting early in 1992 and presumably a peak in flux density sometime before then. This decrease in flux density began before the peak at 8.4 GHz, however it is unclear when it occurred with respect to the 15 GHz peak.

Many variable radio sources display this sort of general behaviour in that flux density changes are first seen at short wavelengths and then propagate to long wavelengths (*e.g.* Kellermann and Pauliny-Toth, 1968). This behaviour provides the opportunity to predict the time of an outburst at centimeter wavelengths by monitoring the total flux density at millimetre wavelengths. Such information can then be used mount a centimeter wavelength VLBI campaign to monitor the compact structure of the lensed images for the duration of an outburst.

In 1966, van der Laan proposed a model to explain the observed flux density outbursts in synchrotron sources. The model involves an expanding cloud of relativistic particles, initially optically thick, which becomes optically thin, at first only to short wavelength radiation, but gradually to longer wavelengths as the expansion continues. Such a scenario results in a strong outburst in flux density being seen first at short wavelengths and later propagating to longer wavelengths with a reduced amplitude. However, the behaviour specifically predicted by the van der Laan model is not common (Kellermann and Owen, 1988). Nevertheless, PKS 1830–211 shows the general behaviour predicted by this model and therefore it is useful to test if the model is consistent with the data in this case. The van der Laan model may be used in this particular lensing system because the two variable components have similar spectra and a small time delay compared to the timescale of the outburst. If a van der Laan-type model is applicable in this case, it may be useful to predict the time of an outburst.

If the synchrotron radiation originates in a cloud of relativistic electrons moving in a magnetic field and the energy distribution of the electrons is a power law

$$N(E)dE = KE^{-\gamma}dE, \quad (7.2)$$

then the radiation also follows a power law of the form

$$S \propto \nu^\alpha \quad (7.3)$$

where $\alpha = (1 - \gamma)/2$. The model given by van der Laan (1966) expresses flux

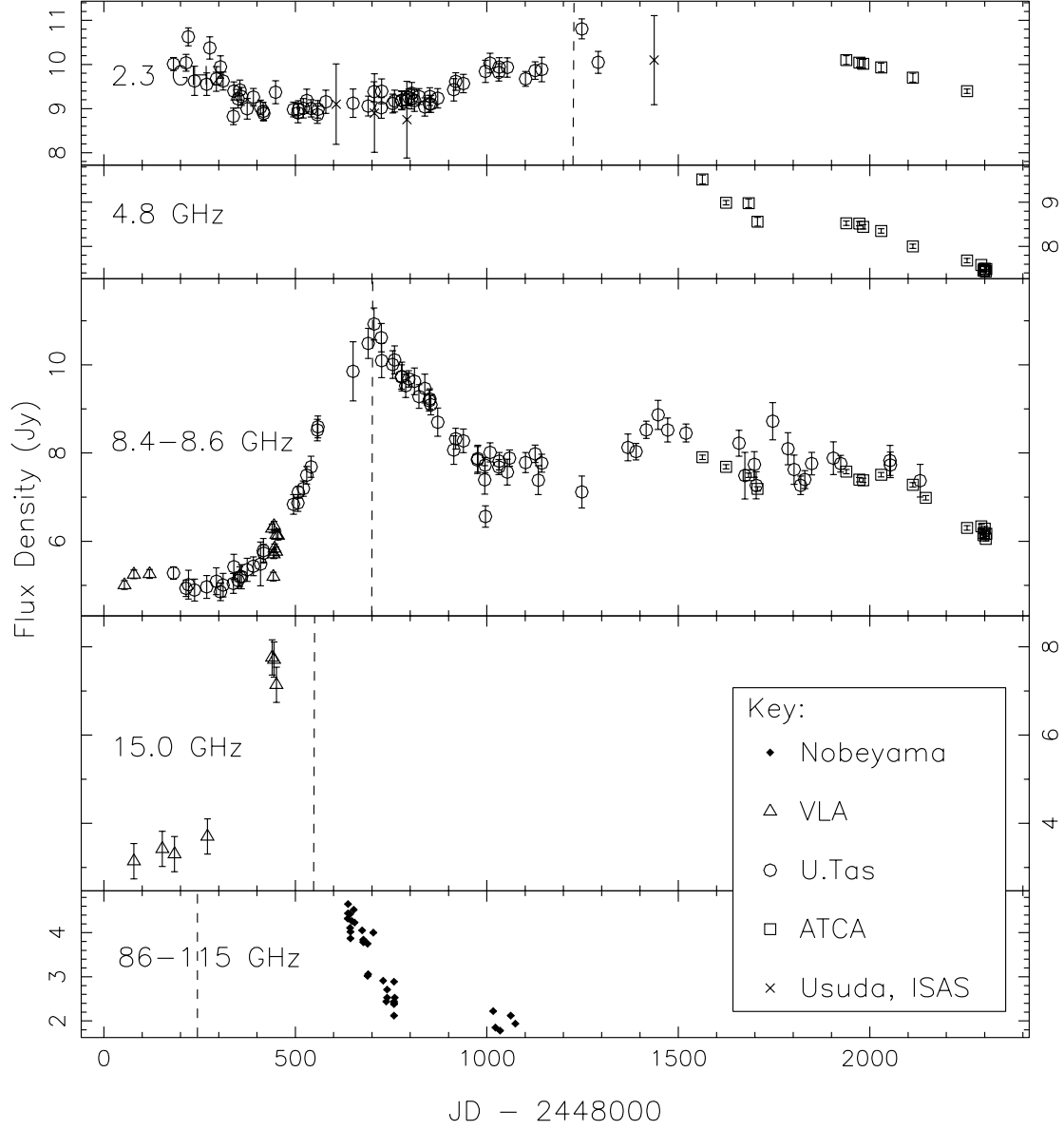


Figure 7.1: Total flux density light curve for PKS 1830–211. The vertical dashed lines indicate the time of the outburst peak for $\gamma = 2$ as shown in Table 7.1

density as a function of time for an expanding cloud as follows

$$S(\nu, t) = S_{m1} \left(\frac{\nu}{\nu_{m1}} \right)^{\frac{5}{2}} \left(\frac{t}{t_1} \right)^3 \frac{\left[1 - \exp \left\{ -\tau_m \left(\frac{\nu}{\nu_{m1}} \right)^{-\left(\frac{\gamma+4}{2}\right)} \left(\frac{t}{t_1} \right)^{-(2\gamma+3)} \right\} \right]}{1 - \exp(-\tau_m)} \quad (7.4)$$

where S_{m1} is the maximum flux density reached *in the variable component of the source* at frequency ν_{m1} at time t_1 and τ_m is the optical depth at the frequency at which the flux density is a maximum. Whilst the source is opaque at a given frequency ($\tau \gg 1$), flux density increases as $S_2/S_1 = (t_2/t_1)^3$ and when it becomes transparent ($\tau \ll 1$), flux density decreases with time as $S_2/S_1 = (t_2/t_1)^{-2\gamma}$. The peak flux density at a given frequency is related to the peak at a second frequency by the relationship

$$\frac{S_{m2}}{S_{m1}} = \left(\frac{t_2}{t_1} \right)^{-(7\gamma+3)/(\gamma+4)} = \left(\frac{\nu_{m2}}{\nu_{m1}} \right)^{(7\gamma+3)/(4\gamma+6)} \quad (7.5)$$

where S_{m2} is the peak flux density reached at time t_2 and frequency ν_{m2} .

As the flux density monitoring data for PKS 1830–211 show only one well sampled, strong peak it is not possible at this stage to estimate a value for γ . Instead the predicted times and flux densities for peaks at the observed wavelengths for several reasonable values of γ are examined, to determine if the model is consistent with the observed outbursts.

Table 7.1 shows the estimated peak flux density amplitudes and times for the outburst at all of the observed frequencies. All calculations used the position, amplitude and time of the 8.4 GHz peak to estimate ν_{m1} , S_{m1} and t_1 . S_{m1} , the amplitude of the outburst, was estimated to be 5.8 Jy by subtracting an assumed quiescent flux density of 5 Jy (measured from the pre-outburst data). The predicted outburst times are all consistent with the available data, although the absence of high frequency flux density measurements near their peak means that these parameters are not well constrained. Predicted outburst times for $\gamma = 2$ are shown in Figure 7.1 and a plot showing the measured outburst times against wavelength (after Kellermann and Pauliny-Toth, 1968) which demonstrates the need for further constraints is presented in Figure 7.2. The predicted outburst amplitudes above quiescent levels are also consistent with those measured at 2.3 GHz (assuming a pre-outburst quiescent flux density of ~ 9 Jy) but would appear to be larger than the data would suggest for 15 and 86–115 GHz (assuming a pre-outburst quiescent flux density of ~ 3.5 and ~ 2.0 Jy respectively).

The total flux density monitoring program has shown that a van der Laan-like model is consistent with the observations of the large outburst. Regular high frequency (≥ 15 GHz) monitoring during a future outburst will help to constrain the model parameters further, but even with the current dataset it is possible to predict the time of an outburst at longer wavelengths to within a month or so, provided the peak is seen first at the high frequency. A predicted outburst time at a given frequency through regular monitoring at a high radio frequency is essential if high-resolution VLBI imaging of the compact structure in PKS 1830–211 from the beginning of an outburst is to be achieved. It would then be possible to

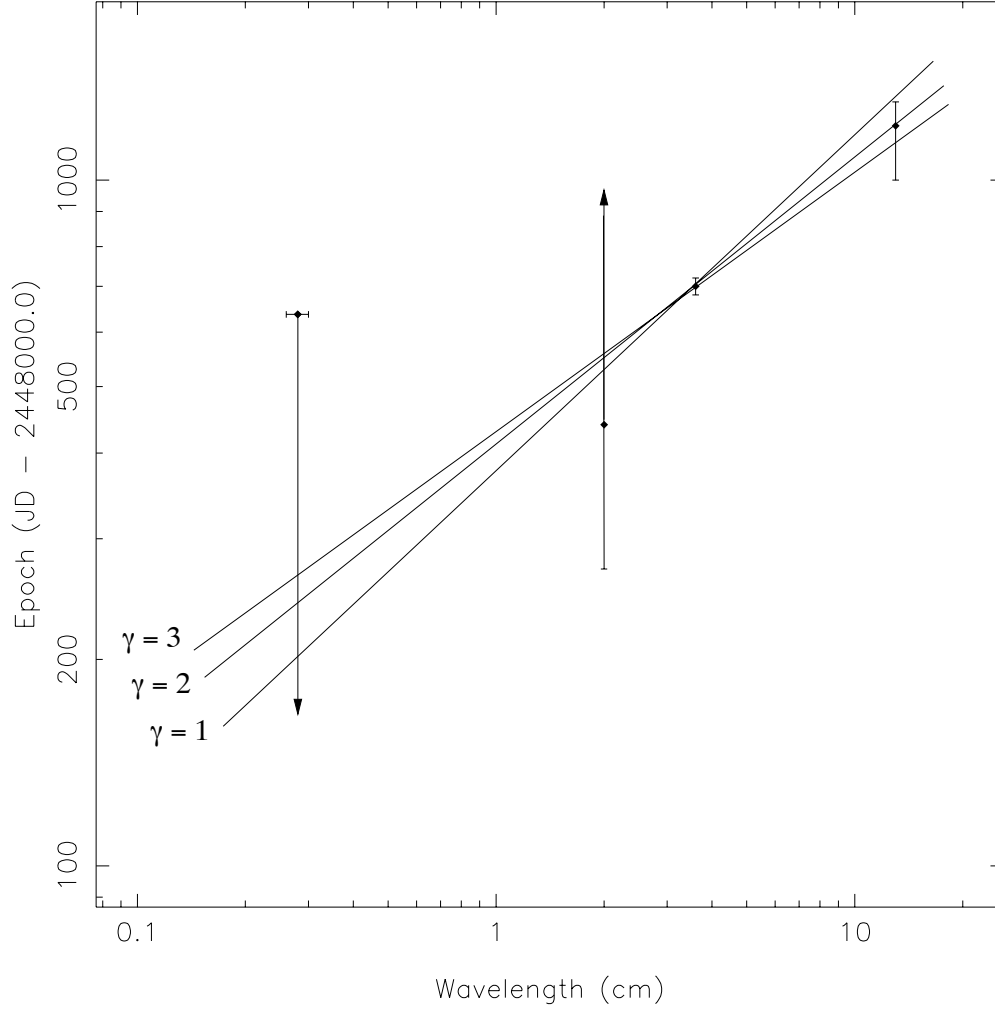


Figure 7.2: The time at which flux density reached a maximum as a function of wavelength. The model is also presented for several values of γ . Although the data does not provide a well constrained value of γ , it is clear that a peak at 100 GHz occurs several hundred days before a peak at 8.6 GHz.

Table 7.1: Predicted peak outburst times and flux densities from Equation 7.5 for various reasonable values of γ . The 8.4 GHz data were used to obtain $S_{m1} = 5.8$ Jy and $t_1 = 700$ days. Predicted outburst times for $\gamma = 2$ are shown in Figure 7.1.

ν_{m2} (GHz)	t_2 (JD - 2448000.0)			S_{m2} (Jy)		
	$\gamma = 1$	$\gamma = 2$	$\gamma = 3$	$\gamma = 1$	$\gamma = 2$	$\gamma = 3$
2.3	1338	1220	1158	1.6	1.2	1.0
15	524	546	559	10.4	11.7	12.6
86–115	204 ± 15	243 ± 15	268 ± 15	69 ± 10	119 ± 20	159 ± 30

examine the relationship between flux density and structural changes. Moreover, relatively high frequency VLBI observations of PKS 1830–211 would be required in such observations so that the effects of inter-stellar scattering are reduced (Jones *et al.*, 1996b). Therefore, total flux density monitoring is best undertaken at the highest frequency practically available. Such observations would provide the earliest possible warning of an outburst. A program is underway at Hobart to prepare for 22 GHz flux density monitoring of PKS 1830–211 that should provide at least 200 days warning of an outburst at 8.6 GHz.

7.2 ATCA Flux Density Monitoring Observations

The total flux density monitoring observations at Mt. Pleasant have shown only relatively long timescale fluctuations, of the order of several months. The presence of a single peak in the 8 GHz total flux density light curve (Figure 7.1) indicates that the lensing time delay is less than a few months (a time delay that was much longer would result in a broader or double-peaked light curve). Consequently, in order to sufficiently time resolve these variations in the compact components it is necessary to measure the flux densities of the two components separately on timescales shorter than the total flux density variations, at least as frequently as one observation per month. ATCA observations allow the compact components of PKS 1830–211 to be resolved and therefore the flux density of both components can be monitored.

As was found in Chapter 3, the ATCA is capable of clearly separating the two components of PKS 1830–211 at 8.6 GHz when the array is configured with a 6 km baseline. There are many benefits to ATCA observations. Once the morphology of an ATCA 8.6 GHz image has been determined from a cuts observation (such as that made in the ATCA gravitational lens survey, see Section 3.1) in the form of a simple two component model, only a single ATCA cut that clearly separates the two components is required to measure their separate flux densities. Some of the flux density in the Einstein ring will also be measured as part of the compact components. However the flux density of the ring has been shown to be constant (King, 1994), as expected from its size and radio spectrum, and therefore does not present a problem in determining a time delay. The established model can be used to estimate the component flux densities because, if we assume that the model positions and sizes do not change between observations, then there are only two variables to be fitted to the data: the flux densities of the two model components. The wavelength agility of the ATCA allows for total flux densities of PKS 1830–211 to be made quickly at 8.6, 4.8, 2.3 and 1.2 GHz, adding to our knowledge of the flux density variations for this source. Also, the data are easily processed, allowing for a quick analysis and any time-critical follow-up observations to be made. Lastly, with the introduction of time set aside for “Service Observations” at the ATCA, it has finally become possible to make such observations on a regular basis.

PKS 1830–211 was observed during the ATCA gravitational lens survey cuts

observations (Chapter 2) in July 1994. A simple model consisting of two circular Gaussian functions was fitted to the calibrated 8.6 GHz data in `Difmap` using the `modelfit` command with self-calibration applied. The rms of the fit between the observed and model visibilities was 63 mJy ($\sim 1.5\%$ of the component flux densities) showing that the data are well described by this model. The parameters of the fitted model components are shown in Table 7.2, and show a separation and position angle between the two components to be 948 ± 90 mas and $46 \pm 5^\circ$ respectively, consistent with values measured with VLBI where the components are more clearly separated, but as part of the ring is seen in the ATCA observations, it is preferable to use them instead of those obtained from VLBI. For example, the separation and position angle of the compact components in the 8.4 GHz VLBI data of King (1994) are 971 mas and 41.6° respectively. This confirms that the two compact components of PKS 1830–211 are resolved and can be monitored with the ATCA by fitting a simple two component model.

7.2.1 Simulations

To verify that a single cut was sufficient to reliably measure the compact component flux densities, the raw data from the observation described above were edited to a single cut at a LST when the two components are resolved. The model established from the complete dataset (shown in Table 7.2) was then used as a starting point with both model component flux densities increased by 0.5 Jy to simulate a change in flux density. Phase self-calibration was then applied and the new model fitted to the data with only the flux densities allowed to change. The resulting flux densities tended to be slightly larger in each component (up to ~ 70 mJy greater), the extended structure having a greater influence on the final model in the case of a single cut. The component flux densities from a single cut observation must then be considered to be an overestimate when compared to a multiple cuts observation, but systematically so. This extra short-baseline flux density is also likely to be a contribution from the (constant) Einstein ring.

Table 7.2: The template model derived from a cuts observation at 8.6 GHz of PKS 1830–211 in July 1994 and used for component flux density estimates from single cut ATCA service observations. The model was restricted to two circular Gaussian components. The second and third columns show the distance and position of the components from the phase centre whilst the fourth column lists the FWHM of the circular Gaussian.

Flux Density (Jy)	Radius (mas)	Theta (deg)	FWHM (mas)
4.52	0	0	170
3.44	948	-134	160

To check that this method of measuring component flux densities is reliable, some simulated datasets were created and then analysed using the same methods as described above. The simulated datasets were created using the program `Fake`, part of the Caltech VLBI Software package (Pearson, 1991), for a PKS 1830–211-like source at a declination of -21° . The source model that was used consisted

of a 1.1 Jy ring with a 4.0 Jy point source on the ring at a position angle of 45° with respect to the centre of the ring and a 3.0 Jy point source, also on the ring and directly opposite the 4.0 Jy component. A cuts observation was simulated and two circular Gaussians fitted to the data. The total flux density in this model accounted for 99.8% of the total flux density, both Gaussian components receiving a similar contribution from the ring flux density.

The resulting source model was used as the template for fitting further simulated data which consisted of a single cut only and with compact component flux densities changed in the model by as much as 1 Jy. For all the simulated data that was analysed, the change in flux density that was measured was the same as that simulated to within 1%. This clearly demonstrates that a single cut observation is sufficient to reliably detect flux density changes in excess of 1% in each of the compact components of PKS 1830–211.

7.2.2 The Observations

ATCA service observations began on 9 August 1995 and are continuing. A schedule was prepared to observe PKS 1830–211 first simultaneously at 4.8 and 8.6 GHz for a 20 min integration followed by a similar integration at 1.2 and 2.3 GHz. Each integration was bracketed by 5 min observations of PKS 1921–293, a phase and bandpass calibrator. Total flux density calibration was achieved by observing the primary ATCA calibrator PKS 1934–638 for 10 min. In addition, a series of similar but more closely spaced observations was made over a two week period between 26 July and 8 August 1996 at 4.8 and 8.6 GHz only.

Figure 7.3 shows the total flux density measurements made at the ATCA as part of the service observations. Also shown are other ATCA flux densities, some of which were measured during the gravitational lens survey and some provided by other observers. Variability has clearly been detected at all frequencies except 1.2 GHz. As a comparison, the 8.6 GHz flux density measurements made at Mt. Pleasant are displayed along with the ATCA 8.6 GHz flux densities in Figure 7.3. It is encouraging to note the good agreement between the ATCA and Hobart flux density measurements as this shows the reliability of the single dish measurements in revealing the smaller flux density variations.

7.2.3 Analysis

Each 8.6 GHz cut was fit with the template model as described above. Following Tzioumis *et al.* (1989), flux density errors were estimated by fixing one of the components with a small offset to the flux density and allowing the flux density of the other component to vary. The fit of the new model to the visibilities was then examined to see if a significant difference could be seen. If there was no detectable difference then the offset was increased until there was. This process was repeated for both components and with both positive and negative offsets, the final values of which were used to estimate the error in flux density. In each case the uncertainty in flux density was less than 0.05 Jy.

The NE and SW component flux density light curves obtained from the 8.6 GHz

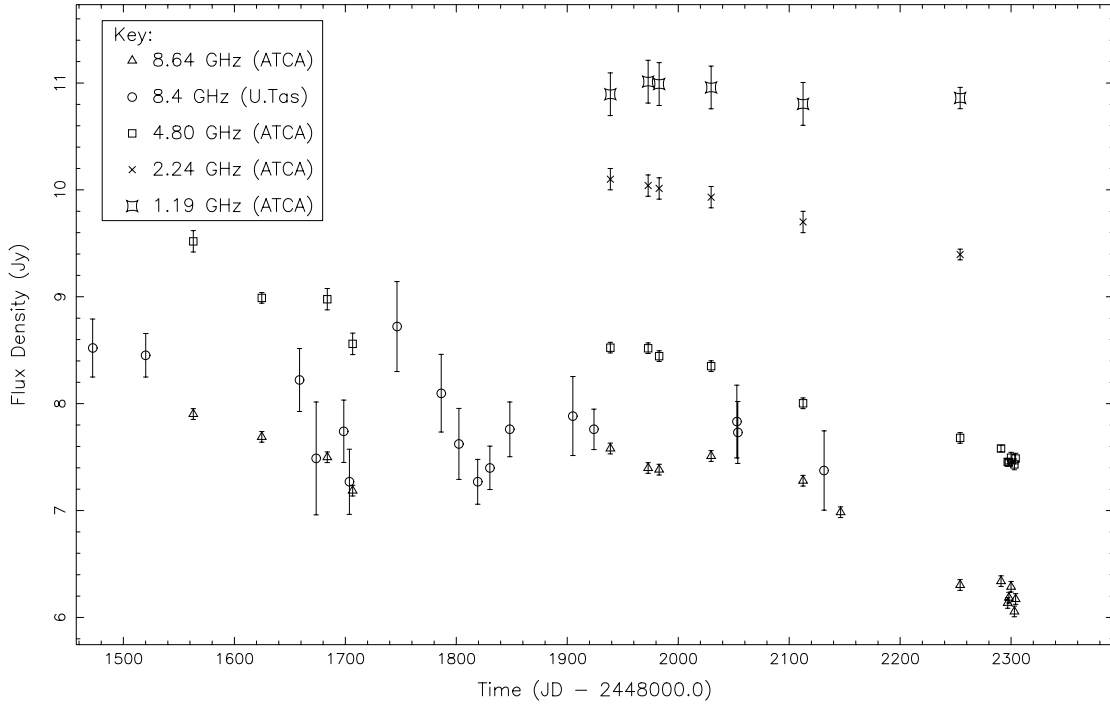


Figure 7.3: Total flux density light curve for PKS 1830–211 from ATCA service and gravitational lens survey observations. Also shown are 8.4 GHz data from Mt. Pleasant.

ATCA data, shown in Figure 7.4, clearly display very similar profiles, indicative of a short time delay. A closer inspection of the two light-curves does reveal some small differences that are due to the lensing time delay. This is most easily seen in the rapidly sampled region near day 2300 where the NE component light curve appears to be declining while the SW light curve appears relatively constant. Another significant difference between the two light curves can be seen in the four observations between days 1900 and 2060 where the NE component light curve appears to reach a local minimum before the SW component light curve. A visual inspection of the data in these two time periods would suggest a time delay between 10 and 20 days with the NE component leading. A formal estimation of the time delay will be described below.

Also of note is the apparent change in the variability behaviour of PKS 1830–211 at 8.6 GHz. The early part of the complete light-curve (Figure 7.1) appears to be smooth with no short term flux density fluctuations and only the large timescale outburst. This light curve would appear to have changed character over the past ~ 2 years and now shows many rapid short-term fluctuations. Alternatively, these rapid and relatively small amplitude variations may be persistent but were not as apparent during the large, dominant outburst around day 700.

To estimate the time delay, it is important to consider how the variability of the lensed source is detected by the observer. In the following analysis, the subscripts 1 and 2 refer to the NE and SW components of PKS 1830–211 respectively. It is convenient to describe the light curve of the NE compact component of the lensed image in the following way:

$$S_1(t) = S_v(t) + S_c \quad (7.6)$$

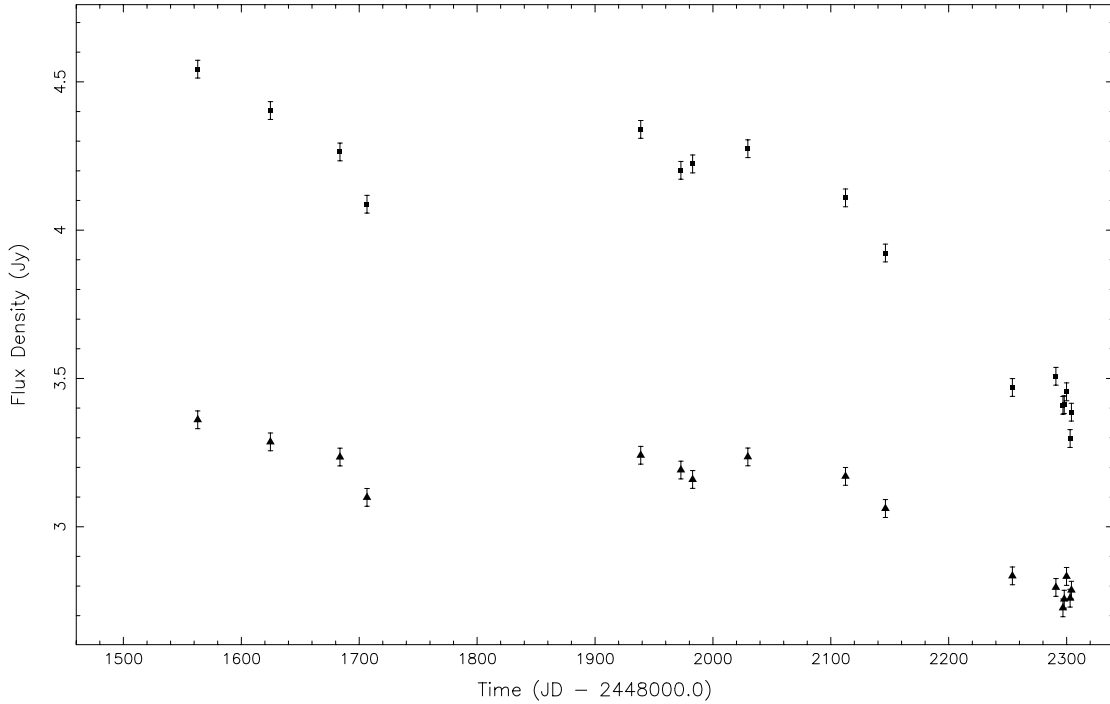


Figure 7.4: The 8.6 GHz light curve data for both components PKS 1830–211 from the ATCA. The measured NE component flux densities are represented by the square symbols and the measured SW component flux densities are represented by the triangular symbols.

such that the variations of the compact core are composed of a constant flux density, S_c , and a variable component, $S_v(t)$, whose time average is zero, *i.e.* $\langle S_v(t) \rangle_t = 0$. This light curve is detectable along a second path, magnified by a different amount and with a time delay, $\Delta\tau$

$$S_2(t) = \frac{1}{\mu} S_1(t + \Delta\tau) \quad (7.7)$$

where μ is the relative magnification ratio. Also lensed is an extended component that forms the Einstein ring. Observations by King (1994) have shown that the variability in PKS 1830–211 is confined to the compact components, and consequently the Einstein ring contributes a constant flux density S_{ring} . The total observed flux density can therefore be described as

$$S_m(t) = S_1(t) + S_2(t) + S_{\text{ring}} \quad (7.8)$$

The work of van Ommen *et al.* (1995), where VLA snapshot observations were used to separate the compact components of PKS 1830–211 from most of the extended structure, has shown that the Einstein ring contributes at least 0.5 Jy to the total flux density at 8.6 GHz. Therefore, because the combined component flux densities derived here at 8.6 GHz are equal to the total flux density, the effect of the ring flux density must be considered before attempting to determine a lensing time delay.

In the ATCA observations, neither $S_1(t)$ nor $S_2(t)$ are measured directly, instead the measured quantities are

$$S_{m1}(t) = S_1(t) + S_{c1} \quad (7.9)$$

and

$$S_{m2}(t) = S_2(t) + S_{c2} \quad (7.10)$$

where the quantities $S_{c1,2}$ are constant but unknown and $S_{\text{ring}} = S_{c1} + S_{c2}$. On applying equations 7.6 and 7.7, the measured quantities become

$$S_{m1}(t) = S_v(t) + S_c + S_{c1} \quad (7.11)$$

and

$$S_{m2}(t) = \frac{1}{\mu} S_v(t + \Delta\tau) + \frac{1}{\mu} S_c + S_{c2} \quad (7.12)$$

Subtracting the time average in each of these expressions leaves only the variable component in each light curve; $S_v(t)$ and $\frac{1}{\mu} S_v(t + \Delta\tau)$ whose time averages are zero. These two variable components can now be compared for different values of μ and $\Delta\tau$ so that a solution for the relative magnification ratio and the time delay can be obtained.

Dispersion Analysis

A correlation of the two light curves was attempted using the dispersion analysis method introduced by Pelt *et al.* (1994; 1996) to analyse the component light curves of the gravitational lens 0957+561. This method was chosen because it avoids any interpolation between data points. Methods that are based on interpolation are likely to lead to erroneous results as they put equal weight on assumed and measured data.

Following Pelt *et al.*, for every test value of μ and $\Delta\tau$, two light-curve datasets a_i and b_i ($i = 1, \dots, N$) are obtained. Together they form a combined light-curve where a_i contains the NE variable component data and b_i contains the SW component data moved in flux density and time by the test values for μ and $\Delta\tau$ respectively. The dispersion, D^2 , of this combined light curve is calculated from the weighted sum of squared differences between nearby a_i, b_i pairs over the entire curve and is described as

$$D^2(\Delta\tau, \mu) = \frac{\sum_{ij} W_{ij} V_{ij} (a_i - b_j)^2}{2 \sum_{ij} W_{ij} V_{ij}} \quad (7.13)$$

where

$$V_{ij} = \frac{1}{1 + \left(\frac{|t_i - t_j|}{\delta} \right)^2} \quad (7.14)$$

$$W_{ij} = \frac{W_i W_j}{W_i + W_j} \quad (7.15)$$

and $W_i = 1/e_i^2$ where e_i is the standard error in data point i . The weighting factor V_{ij} ensures that data pairs are only given significant weighting if they are less than $\sim \delta$ days apart. A value for δ must thus be chosen so that it is significantly less than the timescale of flux density variations. The values of $\Delta\tau$ and μ for which D^2 is a minimum are thus the best estimate of the time delay and magnification ratio.

The dispersion method has been shown to be successful for 0957+561 where the time delay is large (417 ± 3 days (Kundić *et al.*, 1996)) and there is a large dataset. The individual component flux density dataset for PKS 1830–211 is much smaller however and the time delay is also believed to be small, no more than 44 ± 9 days according to van Ommen *et al.* (1995). This has some important consequences when applying the above correlation method. Firstly, the weighting function V_{ij} is biased toward a time delay of zero days as maximum weight is given to data point pairs with zero difference in time. This problem is not encountered for 0957+561 as the time delay is well removed from zero. Secondly, as the test time delay value becomes large compared to δ the number of strongly weighted data point pairs from which D^2 is determined decreases rapidly. This latter problem is a direct result of the small number of PKS 1830–211 data points and can only be overcome by continued monitoring, which has been scheduled on the ATCA. However the first problem can be addressed by a modification to V_{ij} .

To avoid the strong weighting on data point pairs with near-zero time separation, V_{ij} was modified to the following form:

$$V_{ij} = \begin{cases} 1 & \text{if } |t_i - t_j| \leq \delta, \\ \frac{1}{1 + \left(\frac{\delta - |t_i - t_j|}{\delta}\right)^2} & \text{if } |t_i - t_j| > \delta. \end{cases} \quad (7.16)$$

This applies a constant weighting for points with separations less than δ and a function similar to V_{ij} as described in equation 7.14 that decreases with increasing time difference for point separations larger than δ .

The component light curves in Figure 7.4 show the flux density to be decreasing for most of the entire period of the observations. This makes a well constrained estimate of the time delay difficult *as there are no well sampled changes in gradient from which the two curves can be registered*. Instead, with the available data there is a significant range of combinations of time delay and component flux density ratio that can be applied and still provide a satisfactory correlation. Nevertheless, this data has a change in gradient sufficient to provide some limitations on $\Delta\tau$ and μ .

Before a correlation of the light curves can be made, an estimate of δ , essentially the timescale of variability, must be determined. An inspection of the light curves in Figure 7.4, especially the last 7 epochs, shows significant changes in flux density on timescales of a few tens of days. Time delay and amplification values were determined using the dispersion analysis technique for values of δ in the range 10 to 40 days and the fitted values of $\Delta\tau$ and μ are shown in Table 7.3. *This analysis clearly shows that the fitted value for μ does not depend heavily on δ whilst $\Delta\tau$ does.*

In their analysis of the $z = 0.89$ absorption spectra towards PKS 1830–211, Wiklind and Combes (Wiklind and Combes, 1996a) predict a point-image magnification ratio of 1.75 ± 0.15 , provided the $z = 0.89$ galaxy covers the SW component only (which has been proved by Frye *et al.* (1996)). The fitted values for μ in the present analysis range from 1.75 to 1.89 and are therefore consistent with the

Table 7.3: Estimated values for time delay and component magnification from a correlation of the 8.6 GHz light curves.

δ (days)	$\Delta\tau$ (days)	μ
10	−0.5	1.89
15	−8.7	1.87
20	−14.3	1.85
25	−12.2	1.83
30	−5.2	1.81
35	−2.6	1.79
40	−1.7	1.75

measurement of Wiklind and Combes. These measurements of μ were made independently but are entirely consistent with each other. Furthermore, this new measurements of μ is consistent with that used in the lensing model of Nair *et al.* (1993). In their model, Kochanek and Narayan (1992) suggest that a magnification ratio near 1.4 is correct. However, when the dispersion analysis of the ATCA data is applied with $\mu = 1.4$, a very poor correlation is achieved. This result suggests that the Kochanek and Narayan model might not be correct.

$|\Delta\tau|$ decreases as δ approaches zero, probably because the weighting function becomes similar to the original (equation 7.14) for small δ . Figure 7.5 shows contours of D^2 for $\delta = 15$ and $\delta = 20$ along with the combined light curve for the best fit values of $\Delta\tau$ and μ in each case. The maximum time delay occurs when $\delta \sim 20$ d and then approaches zero as δ increases. Although $\Delta\tau$ is not well constrained by the data, *it is clear that it is negative, i.e.* that the flux density changes occur first in the NE component, and that the curves follow each other within ~ 14 days.

Obtaining a well constrained time delay in a gravitational lens has, in general, proved more difficult than first imagined. For example, an accurate determination of the time delay in 0957+561 has only recently been determined (Kundić *et al.*, 1996) despite ~ 17 years of monitoring observations. This measurement was only possible after a well defined, sharp and high signal-to-noise change was seen in the light curves of both lensed components.

It would seem that most of the weight on a non-zero time delay in PKS 1830–211 comes from the intensive period of observations around day 2300. Without these points included in the analysis it is difficult to detect a significant time difference between the two light curves, and this is most likely the result of under-sampling the light curve. Also, any sharp changes that may have occurred in the light curve during these observations would not have been sampled at a sufficient rate to allow for an accurate registration. Clearly more regular monitoring observations are required, at the rate of one per week, over a period of time sufficient to see a significant change in gradient of the light curves. An ATCA proposal to do this has been accepted and observations will begin in early 1997.

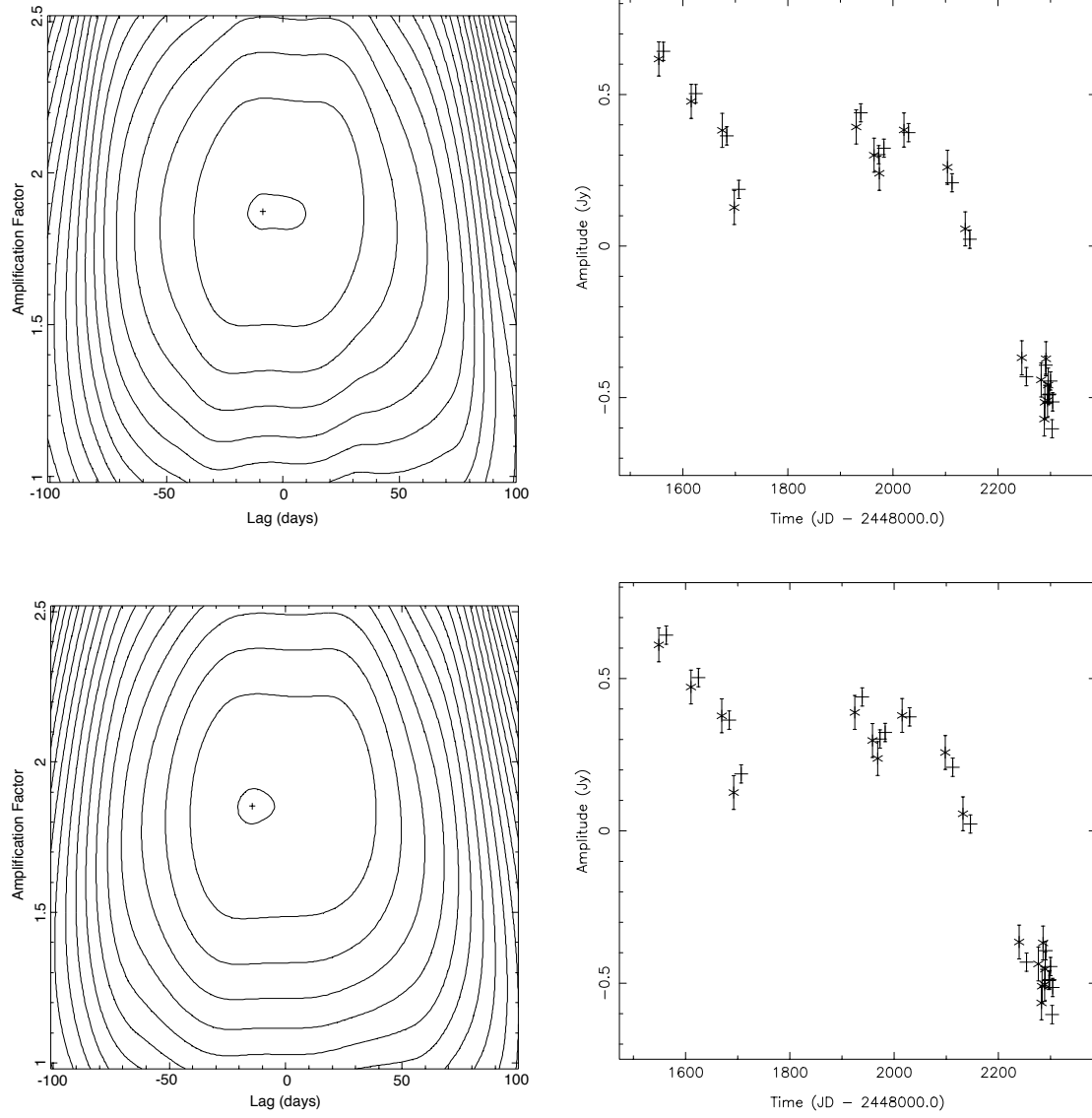


Figure 7.5: Contours of D^2 (left) and combined light-curves (right) for PKS 1830–211 when $\delta = 15$ (top) and $\delta = 20$ (bottom). Contours in the top left panel start at $D^2 = 0.00669$ and all are separated by 0.00373. Contours in the lower left panel start at $D^2 = 0.00848$ and all are separated by 0.00364. In the right-hand panels, NE component data points are plotted with a ‘+’ symbol and the shifted and amplified SW component points are plotted with a ‘*’ symbol.

To estimate an error in the time delay measurement, the correlation analysis was carried out again with a data set reduced by one point in each light curve measured at the same epoch. In other words, for the light-curve datasets a_i and b_i ($i = 1, \dots, N$), the data points a_j and b_j were removed and a correlation analysis made repeatedly for all $j = 1, \dots, N$. This was done for $\delta = 20$ and $\nu = 1.85$: the values that provided the maximum time delay. The range of solutions for $\Delta\tau$ should provide some indication of the error in the time delay measured from the entire dataset and should also provide an indication on the dependance of the solution on a single epoch.

When the dispersion analysis was made as described above, very little change was detected in the solution, with the time delay changing by no more than ~ 1 day except for the case when the point measured at day 2254 was removed. The removal of that point resulted in a time delay of +12.6 days. This suggests that the day 2254 data represent a point of inflection in the light curve that is necessary for a correct registration. This dependence on a single point can only be removed through more regular monitoring of the compact component flux densities.

Without a significant, well sampled inflection in the light curve it is not possible to obtain a reliable time delay measurement. The dispersion analysis indicates a maximum time delay of $\sim -14 \pm 1$ days, but this is dependant on a point measured on day 2254. Without that epoch, the dispersion analysis solution is in complete disagreement with a visual inspection of the better-sampled regions of the data which suggest a delay of up to ~ -20 days. Therefore a conservative estimate of the lensing time delay of -14 ± 7 days must be made based on the available data.

7.3 Implications on Source Redshift and H_0

The time delay estimate described above allows for some restrictions to be placed on the redshift of the background source and the Hubble constant. The lensing model proposed by Nair *et al.* (1993) predicts a time delay between the NE and SW compact components of:

$$\Delta\tau = (0.95_{\text{geom}} - 5.26_{\text{potl}}) (1 + z_L) \left[\left(\frac{D_{OL}D_{OS}}{D_{LS}} \right) / \text{Gpc} \right] \text{ days} \quad (7.17)$$

and the inferred lensing time delay from the model of Kochanek and Narayan (1992), as derived in Chapter 5, Section 5.2.1 is:

$$\Delta\tau = (0.43_{\text{geom}} - 2.85_{\text{potl}}) (1 + z_L) \left[\left(\frac{D_{OL}D_{OS}}{D_{LS}} \right) / \text{Gpc} \right] \text{ days} \quad (7.18)$$

where D_{OL} , D_{OS} and D_{LS} are the angular diameter distances between the observer and the lens, the observer and the background source and the lens and the background source respectively and z_L is the redshift of the lensing galaxy. Angular diameter distance is given by

$$D = \frac{c}{H_0 q_0^2 (1 + z)^2} \left(q_0 z + (q_0 - 1) \left[(1 + 2q_0 z)^{1/2} - 1 \right] \right)$$

and if a standard cold dark matter cosmology is assumed (*i.e.* $q_0 = 1/2$):

$$D = \frac{2c}{H_0(1+z)^2} \left(1+z - (1+z)^{1/2} \right)$$

Two lens redshifts must be considered: $z = 0.89$ and $z = 0.19$. It should be noted that the models includes only one lensing galaxy, therefore in discussing a lens at one of these redshifts, the other galaxy is assumed not to influence the system. In the following discussion, reasonable values of H_0 are assumed to be between 50 and 100 $\text{kms}^{-1} \text{Mpc}^{-1}$.

$z = 0.19$

If the lens is assumed to possess a redshift of 0.19, then $D_{OL} = 4.20 \times 10^4 H_0^{-1} \text{Mpc}$. In this case, the source redshift must be greater than 0.89 as the galaxy at this redshift is known not to be the background source (Wiklind and Combes, 1996a) and must therefore be closer.

Figure 7.6 shows a plot of H_0 against background source redshift for time delays of -7 , -14 , -21 and -44 days for both models using Equations 7.17 and 7.18. The graphs shows that none of these time delays provide a background source redshift greater than 0.89 and a Hubble constant greater than 50 $\text{kms}^{-1} \text{Mpc}^{-1}$. Therefore, there are no acceptable background source redshifts if the lensing galaxy is at $z = 0.19$, unless the Hubble constant is much lower than is generally accepted.

$z = 0.89$

If the lens is assumed to possess a redshift of 0.89, then $D_{OL} = 8.65 \times 10^4 H_0^{-1} \text{Mpc}$.

Figure 7.7 shows a plot of H_0 against background source redshift for a range of time delays for both models using Equations 7.17 and 7.18. The Figure shows that for the Nair *et al.* model a time delay longer than ~ 14 days is needed for acceptable ranges of source redshift and H_0 . If an error of 7 days is placed on the above estimate of $\Delta\tau$, then the Nair *et al.* model favours source redshifts greater than $z \sim 2.0$ and a Hubble constant larger than $\sim 60 \text{kms}^{-1} \text{Mpc}^{-1}$. The Figure also shows that for the Kochanek and Narayan model a time delay of 14 ± 7 days places a lower limit on source redshift of ~ 1.3 .

In contrast to this, a time delay of -44 days as suggested by van Ommen *et al.* (1995) would favour a background source redshift approximately in the range $1.2 < z < 2.0$ using the Nair *et al.* model or approximately $1.0 < z < 1.2$ using the Kochanek and Narayan model for reasonable values of H_0 .

7.4 Summary

Monitoring observations of PKS 1830–211 over the past ~ 6 years have revealed dramatic changes in total flux density over a wide range of frequencies. A large total flux density outburst has been detected at several frequencies, most clearly at 8.4 GHz with the Mt. Pleasant radiotelescope. Outbursts occur first at high

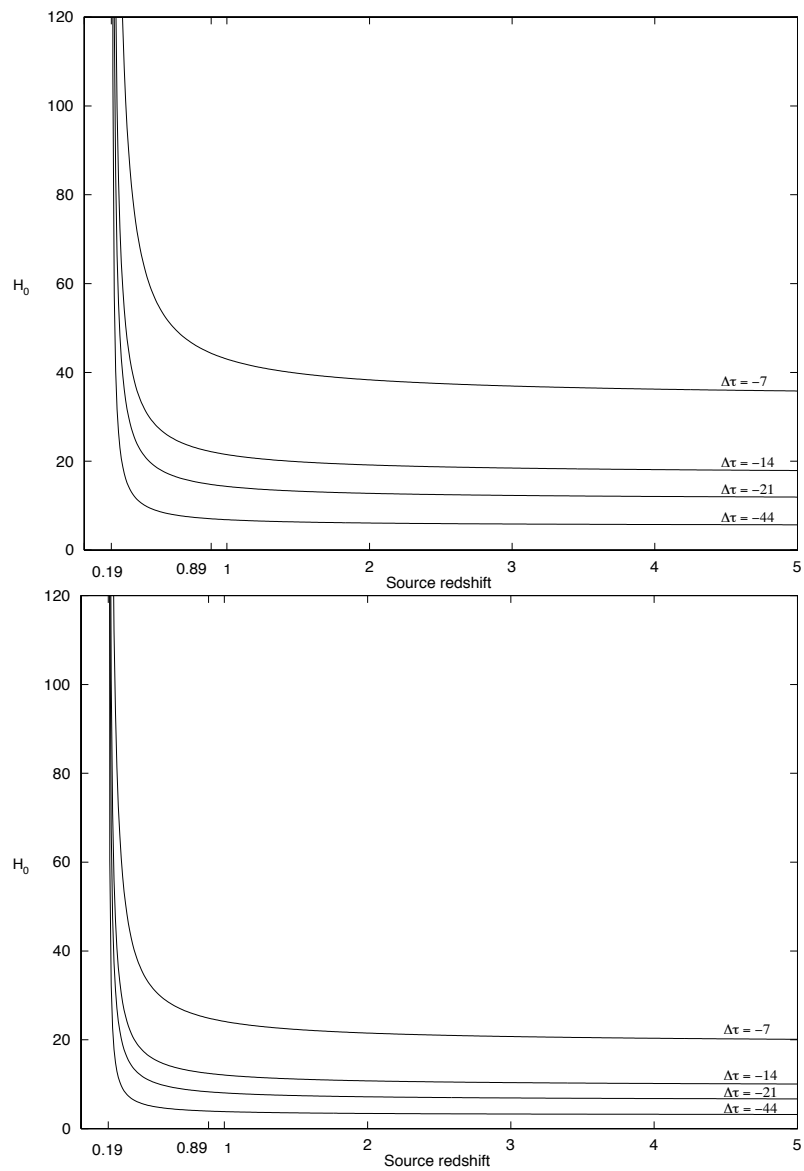


Figure 7.6: H_0 plotted against source redshift for several time delay values for a $z = 0.19$ lens using the lensing model proposed by Nair *et al.*, (1993) (top) and that proposed by Kochanek and Narayan, (1992) (bottom).

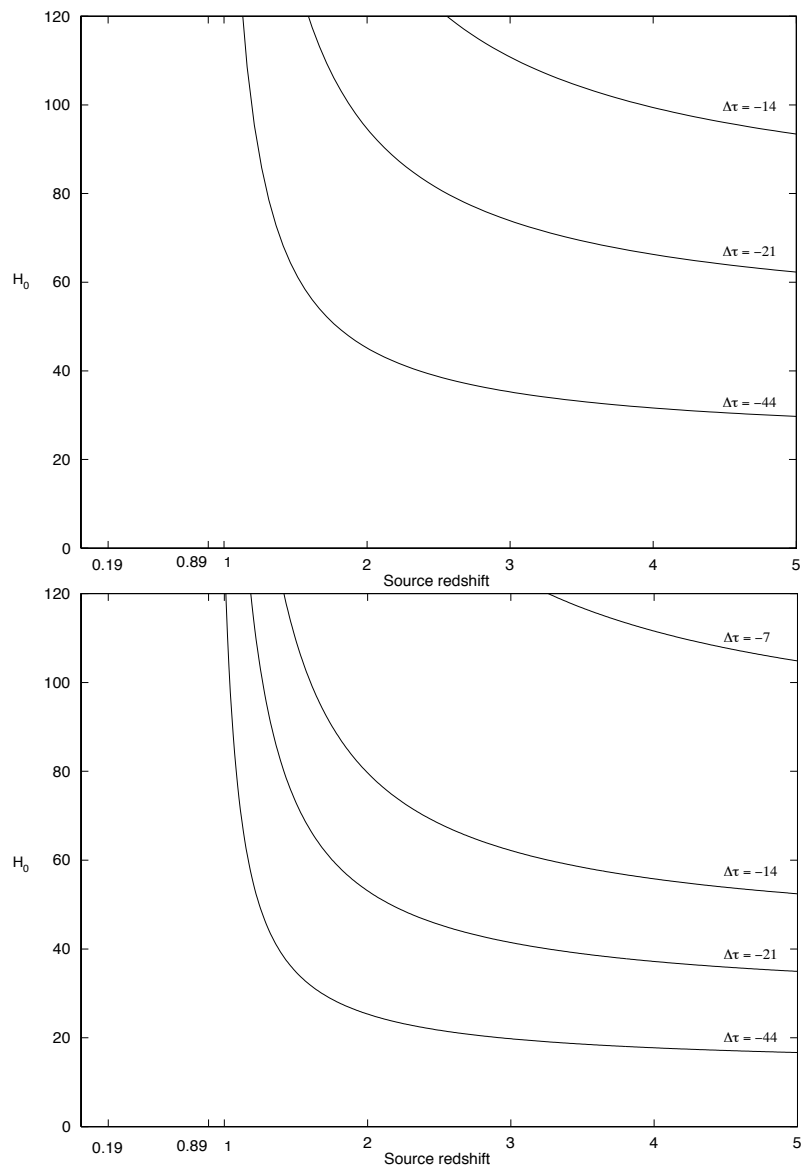


Figure 7.7: H_0 plotted against source redshift for several time delay values for a $z = 0.89$ lens using the lensing model proposed by Nair *et al.*, (1993) (top) and that proposed by Kochanek and Narayan, (1992) (bottom).

frequencies, propagating to lower frequencies at later times, therefore high frequency monitoring of PKS 1830–211 can be used to predict outbursts at centimeter wavelengths which can be monitored with VLBI. Outburst times, based on the 8.4 GHz data, were predicted for other frequencies by applying a van der Laan-like (1966) model and found to be consistent. Regular flux density monitoring of PKS 1830–211 at a high frequency would allow for an outburst to be predicted at a lower frequency and observed at high resolution through the entire event. For example, the 22 GHz monitoring program underway at Hobart should provide at least 200 days warning of an outburst at 8.6 GHz.

Total flux density monitoring observations have been made with the ATCA since July 1994 and in particular, the compact components have been monitored at 8.6 GHz. These observations have shown the lensing time delay to be 14 ± 7 days, significantly shorter than predicted by van Ommen *et al.* (1995), and have measured the magnification ratio to be $1.82 \pm \sim 0.07$ which is consistent with the flux density ratio obtained by Wiklind and Combes (1996a) at 100 GHz.

If the lensing galaxy is at $z = 0.19$, neither the Nair *et al.* model nor the Kochanek and Narayan model provide acceptable background source redshifts for the derived time delay, thus ruling the $z = 0.19$ galaxy out as the main lensing galaxy.

If the lensing galaxy has a redshift of 0.89, a time delay measurement of 14 ± 7 days requires a Hubble constant greater than $\sim 60 \text{ kms}^{-1} \text{ Mpc}^{-1}$ and a source redshift greater than ~ 2.0 for the lensing model of Nair *et al.*, while the Kochanek and Narayan model predicts a source redshift greater than ~ 1.3 .

Chapter 8

Conclusions

8.1 The Gravitational Lens Survey

A radio survey for southern hemisphere gravitational lenses has been completed for the 461 strongest flat-spectrum Parkes Catalogue radio sources with the ATCA. Simulations have shown that the survey was capable of resolving and determining spectral indices for all compact double sources with separations between 1.5 and 20 arcsec, individual component flux densities greater than 6 mJy and flux density ratios of less than ~ 30 . The survey is therefore complete for such sources. Further, all compact double sources were resolvable at 8.6 GHz if their separations were greater than 0.82 arcsec. Large Einstein ring-like structures would also have been detected and identified, as was shown for the detection of the Planetary Nebula PKS 1350–662.

Three gravitational lens candidates were detected in the sample: PKS 1830–211, PKS 0252–549 and PKS 2321–375. Of these, PKS 1830–211 is a previously detected and confirmed gravitational lens while PKS 0252–549 and PKS 2321–375 are candidate gravitational lenses. No new strong, gravitational lenses with multiply imaged cored were found in the sample as all new candidates show weak companions implying large magnification ratios. Further radio observations are required to confirm these two new detections and observations at optical wavelengths are needed to measure the redshifts of these systems and to detect weak optical counterparts. Sensitive VLBI observations of PKS 0252–549 would also be of value to confirm that the weak southern flat spectrum component is compact.

All survey sources have been imaged in a consistent fashion and classified according to radio morphology, and optical identifications have been made for 339 sources on the basis of radio/optical position coincidence. The number of chance identifications is 16 stellar objects and 9 galaxies brighter than $M_J = 22.5$. The number of coincidences can be reduced by removing systematic errors in the COSMOS positions. As was expected for a flat-spectrum sample, a majority of the sources were dominated by unresolved, compact radio structure. More than 60% of survey sources have $\geq 95\%$ of their total flux density contained in an unresolved component.

Intra-day variability was detected in two sources. PKS 1144–379 is an intra-day variable source that has already been found by Kedziora-Chudczer *et al.* (1996). However, PKS 1415–349 is a new detection. The redshift of this object is currently unknown, but is probably a quasar, based on a positive stellar COSMOS identification. Its radio flux density variability is equally strong at 4.8 and 8.6 GHz, and the two light curves are correlated. This behaviour is similar to that of PKS 0405–385 (Kedziora-Chudczer *et al.*, 1996). PKS 0405–385 was observed in this survey but not found to vary, confirmation of the episodic nature of its variability. This source is also the subject of a successful VSOP proposal. PKS 1415–379 is an exciting new intra-day variable candidate and will be the subject of further monitoring over a wide range of frequencies.

Two possible very large separation sources were detected: PKS 0130–447 and PKS 0619–468. The former is identified with a faint infra-red object and the latter with a $M_J = 19.3$ stellar object, probably a quasar. Redshifts are not available for either of these objects, however their implied sizes, given a nominal redshift of 1, are 1.8 and 6.3 Mpc respectively. By comparison, the largest radio galaxies are up to ~ 1 Mpc in extent. It would therefore seem that these two objects are either unusually large or much closer to the observer than expected. In either case, they certainly warrant further investigation to measure their redshifts and to image their extended radio structure.

This survey, whilst complete to a low flux density for compact double sources with separations greater than 1.5 arcsec, was not complete for smaller compact component separations. To detect lenses with component separations less than 1.5 arcsec in the south requires the use of VLBI observations. Such a program has already been started by the author and collaborators.

Any new southern hemisphere radio gravitational lens search will continue to rely on the ATCA for observations in the foreseeable future. To maintain completeness over a similar dynamic range will require longer integration times on program sources as the flux density limit must be reduced. For example, increasing the flat-spectrum sample to 2000 sources would require a flux density cutoff of $S_{5.0} \approx 100$ mJy for similar declination limits but would require an increase in integration time to approximately 4 min per cut. Such a survey would require ~ 40 days of ATCA observing time. A more appropriate catalogue from which to draw sources for such a survey is the PMN survey (Wright *et al.*, 1996 and references therein). For these sources, limited ATCA observations have been made that provide coeval flux density and hence spectral index measurements so that a flat spectrum sample can be drawn.

8.2 PKS 1830–211

As described in Chapter 6, a new absorption system toward PKS 1830–211 has been detected and is most likely due to H I at $z = 0.19$. The absorbing galaxy covers the NE component and part of the Einstein ring while the absorption system discovered by Wiklind and Combes (1996a) covers the SW component only (Frye *et al.*, 1996). The paradoxical appearance of this lens at high resolution,

as described in Chapter 5, remains unexplained. However, if both of the galaxies along the line of sight are involved in lensing the background source, this striking disparity may be explained.

Total flux density monitoring observations of PKS 1830–211 have revealed it to be highly variable. A large flux density outburst has been detected at 8.4 GHz, which reached a maximum on JD ~ 2448700 . Large flux density changes were also detected at other frequencies and outburst time predictions from applying a van der Laan-like model (van der Laan, 1966) are consistent with the data. Total flux density monitoring of PKS 1830–211 at high frequencies may prove useful in predicting large outbursts at lower frequencies which could then be followed in detail with VLBI observations at high resolution.

NE and SW component flux densities have been monitored with the ATCA over the past 2 years. It has been demonstrated that the data are capable of providing a time delay measurement provided observations are made at a rate of approximately one per week. A correlation analysis of the NE and SW light curves has provided good constraints on the relative component magnification ratio which is 1.82 ± 0.07 . This value is consistent with the ratio of 1.75 ± 0.15 measured by Wiklind and Combes from their millimetre wave observations of the $z = 0.89$ absorption system. The time delay although not well constrained by this correlation analysis, is of the order of 2 weeks. It is proposed to continue the ATCA monitoring program at sampling rate of one observation per week to more stringently constrain the time delay and relative magnification ratio measurements.

The PKS 1830–211 Einstein ring/gravitational lens system is much more complex than initially expected. None of the published lensing models fully explain the structure of this source, however several new constraints on the lensing system have recently come to light. They include the redshifts of two intervening lensing galaxies, the relative magnification ratio of the two compact components and a time delay. An optical counterpart for PKS 1830–211 is yet to be detected. However the recent commissioning of large optical telescopes and advances in instrumentation may allow for an identification to be made, especially in the red end of the spectrum. An HST proposal has been submitted to image the field in the near infra-red to search for the optical counterparts and to determine a redshift for the lensed object. A space VLBI proposal has been approved to use existing ground-based radio telescopes and the VSOP spacecraft to image PKS 1830–211 at 22 GHz. The very high resolution images from such an observation will provide more valuable information on the small-scale structure of this enigmatic object.

References

- Blandford, R., Kochanek, C., Kovner, I., and Narayan, R.: 1989, *Science* **245**, 824–830
- Bolton, J., Savage, A., and Wright, A.: 1979, *Aust. J. Phys. Astrophys. Suppl.* **46**, 1
- Burke, B.: 1989, in Mellier, Fort, and Soucail (eds.), *Gravitational Lensing, Toulouse Workshop*, pp 127–135
- Carilli, C., Rupen, M., and Yanny, B.: 1993, *Astrophys. J.* **412**, L59–L62
- Chen, G., Kochanek, C., and Hewitt, J.: 1995, *Astrophys. J.* **447**, 62–81
- Djorgovski, S., Meylan, G., Klemola, A., Thompson, D., Weir, W., Swarup, G., Rao, A., Subrahmanyan, R., and Smette, A.: 1992, *Mon. Not. R. Astron. Soc.* **257**, 240–244
- Drinkwater, M., Barnes, D., and Ellison, S.: 1995, *Publ. Astron. Soc. Aust.* **12**, 248–257
- Drinkwater, M., Savage, A., Webster, R., Condon, J., Ellison, S., Francis, P., Jauncey, D., Lovell, J., and Peterson, B.: 1996, *Mon. Not. R. Astron. Soc.*, accepted
- Fomalont, E. and Wright, M.: 1974, *Galactic And Extragalactic Radio Astronomy*, pp 256–290, Springer-Verlag
- Frye, B., Welch, W., and Broadhurst, T.: 1996, *Astrophys. J., Lett.*, submitted
- Garrett, M., Nair, S., Porcas, R., and Patnaik, A.: 1996, in C. Kochanek and J. Hewitt (eds.), *IAU 173: Astrophysical Applications of Gravitational Lensing*, pp 189–190, Kluwer Academic Publisher
- Griffiths, R. E., Murray, S. S., Giacconi, R., Bechtold, J., Murdin, P., Smith, M., Macgillivray, H. T., Ward, M., Danziger, J., and Lub, J.: 1983, *Astrophys. J.* **269**, 375–386
- Heeschen, D., Krichbaum, T., Schalinski, C., and Witzel, A.: 1987, *Astron. J.* **94(6)**, 1493–1507
- Högbom, J.: 1974, *Astron. Astrophys. Suppl. Ser.* **15**, 417–426
- Jauncey, D., Batty, M., Gulkis, S., and Savage, A.: 1982, *Astron. J.* **87(5)**, 763–773
- Jauncey, D., Preston, R., Reynolds, J., King, E., Meier, D., Tzioumis, A., Jones, D., Murphy, D., Nicolson, G., Ferris, R., Costa, M., Gough, R., Hoard, D., Amy, S., Blair, D., Campbell-Wilson, D., Clay, R., Edwards, P., Gwinn, C., Hamilton, P., Johnson, B., Jones, P., Kembell, A., Lobdell, E., Lovell, J., McAdam, W., McCulloch, P., Norris, R., Perlman, E., Sinclair, M., St. John, M., Skjerve, L., Wark, R., and White, G.: 1993, in R. Davis and R. Booth (eds.), *Sub-Arcsecond Radio Astronomy*, pp 134–136, Cambridge University

Press

- Jauncey, D., Reynolds, J., Tzioumis, A., Ferris, R., Norris, R., Sinclair, M., Migenes, V., Gough, R., Wark, R., Preston, R., Meier, D., Murphy, D., Jones, D., Hoard, D., St. John, M., Skjerve, L., King, E., McCulloch, P., Lovell, J., Hamilton, P., Costa, M., Blair, D., Edwards, P., Clay, R., Campbell-Wilson, D., Amy, S., McAdam, W., White, G., Jones, P., and Nicolson, G.: 1994, in J. Robertson and W. Tango (eds.), *Very High Angular Resolution Imaging*, pp 131–133, Kluwer, Dordrecht
- Jauncey, D., Reynolds, J., Tzioumis, A., Muxlow, T., Perley, R., Murphy, D., Preston, R., King, E., Patnaik, A., Jones, D., Meier, D., Bird, D., Blair, D., Bunton, J., Clay, R., Costa, M., Duncan, R., Ferris, R., Gough, R., Hamilton, P., Hoard, D., Kemball, A., Kesteven, M., Lobdell, E., Luiten, A., McCulloch, P., Murray, J., Nicolson, G., Rao, A., Savage, A., Sinclair, M., Skjerve, L., Taaffe, L., Wark, R., and White, G.: 1991, *Nature* **352**, 132–134
- Jauncey, D., Wright, A., Peterson, B., and Condon, J.: 1978, *Astrophys. J.* **219**, L1–L5
- Johnston, K., Fey, A., Zacharias, N., Russell, J., Ma, C., de Vegt, C., Reynolds, J., Jauncey, D., Archinal, B., Carter, M., Corbin, T., Eubanks, T., Florkowski, D., Hall, D., McCarthy, D., McCulloch, P., King, E., Nicolson, G., and Shaffer, D.: 1995, *Astron. J.* **110**(2), 880–915
- Jones, D., Jauncey, D., Preston, R., Reynolds, J., King, E., Meier, D., Tzioumis, A., Murphy, D., Nicolson, G., Ferris, R., Costa, M., Gough, R., Hoard, D., Amy, S., Blair, D., Campbell-Wilson, D., Clay, R., Edwards, P., Gwinn, C., Hamilton, P., Johnson, B., Jones, P., Kemball, A., Lobdell, E., Lovell, J., McAdam, W., McCulloch, P., Norris, R., Perlman, E., Sinclair, M., St. John, M., Skjerve, L., Wark, R., and White, G.: 1993, in R. Davis and R. Booth (eds.), *Sub-Arcsecond Radio Astronomy*, pp 150–151, Cambridge University Press
- Jones, D., Preston, R., Murphy, D., Jauncey, D., Reynolds, J., Tzioumis, A., King, E., McCulloch, P., Lovell, J., van Ommen, T., Costa, M., and Nicolson, G.: 1996a, *Astrophys. J., Lett.*, accepted
- Jones, D., Preston, R., Murphy, D., Meier, D., Jauncey, D., Reynolds, J., and Tzioumis, A.: 1996b, in C. Kochanek and J. Hewitt (eds.), *IAU 173: Astrophysical Applications of Gravitational Lensing*, pp 345–346, Kluwer Academic Publisher
- Kamenno, S.: 1995, *Flux Density Measurements of PKS 1830–211 from the Nobeyama Millimeter Array.*, private communication
- Kedziora-Chudczer, L.: 1996, in preparation
- Kedziora-Chudczer, L., Walker, M., and Jauncey, D.: 1996, *Astrophys. J., Lett.*, submitted
- Keeton, C. and Kochanek, C.: 1996, in C. Kochanek and J. Hewitt (eds.), *IAU 173: Astrophysical Applications of Gravitational Lensing*, pp 419–439, Kluwer Academic Publisher
- Kellermann, K. and Owen, F.: 1988, in *Galactic and Extragalactic Radio Astronomy*, Astronomy and Astrophysics Library, Chapt. 13, Springer-Verlag, Berlin, Second Edition, G.L. Verschuur and K.I. Kellermann (eds.)

- Kellermann, K. and Pauliny-Toth, I.: 1968, *Ann. Rev. Astron. Astrophys.* **6**, 417–448
- King, E.: 1994, *Ph.D. Thesis*, Physics Department, University of Tasmania
- King, E., Lovell, J., McCulloch, P., and Jauncey, D.: 1996, *Astron. J.*, in preparation
- King, L. and Browne, W.: 1996, *Mon. Not. R. Astron. Soc.* **282**, 67–76
- Kochanek, C.: 1993a, *Mon. Not. R. Astron. Soc.* pp 453–463
- Kochanek, C.: 1993b, in R. Davis and R. Booth (eds.), *Sub-Arcsecond Radio Astronomy*, pp 117–122, Cambridge University Press
- Kochanek, C.: 1996, *Astrophys. J.* **473**, 595
- Kochanek, C. and Narayan, R.: 1992, *Astrophys. J.* **401**, 461–473
- Kundić, T., Turner, E. L., Colley, W. N., Gott, J. R., Rhoads, J. E., Wang, Y., Bergeron, L. E., Gloria, K. A., Long, D. C., Malhotra, S., and Wambsganss, J.: 1996, *Princeton Observatory Preprint 687*, submitted
- Langston, G., Schneider, D., Conner, S., Carilli, C., Lehar, J., Burke, B., Turner, E., Gunn, J., Hewitt, J., and Schmidt, M.: 1989, *Astron. J.* **97**(5), 1283–1290
- Lovell, J., McCulloch, P., King, E., and Jauncey, D.: 1996, in C. Kochanek and J. Hewitt (eds.), *IAU 173: Astrophysical Applications of Gravitational Lensing*, pp 347–348, Kluwer Academic Publisher
- Maoz, D., Bahcall, J., Doxsey, R., Schneider, D., Bahcall, N., Lahav, O., and Yanny, B.: 1992, *Astrophys. J.* **394**, 51–60
- Maoz, D., Bahcall, J., Schneider, D., Bahcall, N., Djorgovski, S., Doxsey, R., Gould, A., Kirhakos, S., Meylan, G., and Yanny, B.: 1993, *Astrophys. J.* **409**, 28–41
- McMahon, P., Moore, C., Hewitt, J., Rupen, M., and Carilli, C.: 1993, *Bull. Am. Astron. Soc.* **25**, 1307
- Muxlow, T.: 1996, *Imaging of 5 GHz MERLIN observations of PKS 1830–211*, private communication
- Myers, S., Fasnacht, C., Djorgovski, S., Blandford, R., Matthews, K., Neugebauer, G., Pearson, T., Readhead, A., Smith, J., Thompson, D., Womble, D., Browne, I., Wilkinson, P., Nair, S., Jackson, N., Snellen, I., Miley, G., de Bruyn, A., and Schilizzi, R.: 1995, *Astrophys. J.* **447**, L5–L8
- Nair, S., Narasimha, D., and Rao, A.: 1993, *Astrophys. J.* **407**, 46–59
- Narayan, R. and Bartelmann, M.: 1996, *Lectures on Gravitational Lensing*, Postscript file including figures at this URL: <http://www.mpa-garching.mpg.de/Lenses/Preprints/JeruLect.ps.gz>, Lectures held at the 1995 Jerusalem Winter School
- Osmer, P. and Smith, M.: 1980, *Astrophys. J., Suppl. Ser.* **42**, 333–349
- Patnaik, A. R., Browne, W. A., Wilkinson, P. N., and Wrobel, J. N.: 1992, *Mon. Not. R. Astron. Soc.* **254**, 655–676
- Pearson, T.: 1991, *Bull. Am. Astron. Soc.* **23**, 991–992
- Pelt, J., Hoff, W., Kayser, R., Refsdal, S., and Schramm, T.: 1994, *Astron. Astrophys.* **286**, 775–785
- Pelt, J., Kayser, R., Refsdal, S., and Schramm, T.: 1996, *Astron. Astrophys.* **305**, 97–106
- Perley, R.: 1981, *Astron. J.* **87**, 859–880

- Preston, R., Jauncey, D., Meier, D., Tzioumis, A., Ables, J., Batchelor, R., Faulkner, J., Gates, J., Greene, B., Hamilton, P., Harvey, B., Haynes, R., Johnson, B., Lambeck, K., Louie, A., McCulloch, P., Moorey, G., Morabito, D., Nicolson, G., Niell, A., Robertson, J., Royle, G., Skjerve, L., Slade, M., Slee, O., Stolz, A., Watkinson, A., Wehrle, A., and Wright, A.: 1989, *Astron. J.* **98**, 1–26
- Preston, R., Jauncey, D., Reynolds, J., King, E., Meier, D., Tzioumis, A., Jones, D., Nicolson, G., Ferris, R., Costa, M., Gough, R., Hoard, D., Amy, S., Blair, D., Campbell-Wilson, D., Clay, R., Edwards, P., Gwinn, C., Hamilton, P., Johnson, B., Jones, P., Kembell, A., Lobdell, E., Lovell, J., McAdam, W., McCulloch, P., Norris, R., Perlman, E., Sinclair, M., St. John, M., Skjerve, L., Wark, R., and White, G.: 1993, in R. Davis and R. Booth (eds.), *Sub-Arcsecond Radio Astronomy*, pp 428–429, Cambridge University Press
- Qian, S., Witzel, A., Krauf, A., Krichbaum, T., and Britzen, S.: 1996, in P. Hardee, A. Bridle, and J. Zensus (eds.), *Energy Transport in Radio Galaxies and Quasars*, p. 55, ASP conf. series, vol 100
- Rao, A. and Subrahmanyan, R.: 1988, *Mon. Not. R. Astron. Soc.* **231**, 229–236
- Refsdal, S.: 1964, *Mon. Not. R. Astron. Soc.* **128**, 308–310
- Refsdal, S.: 1966, *Mon. Not. R. Astron. Soc.* **132**, 101–111
- Reynolds, J.: 1990, *A Revised Flux Scale for the AT Compact Array*, AT Technical Note AT/39.3/040, ATNF
- Reynolds, J., Jauncey, D., Russell, J., King, E., McCulloch, P., Fey, A., and Johnston, K.: 1994, *Astron. J.* **108**(2), 725–730
- Reynolds, J., Jauncey, D., Staveley-Smith, L., Tzioumis, A., de Vegt, C., Zacharias, N., Perryman, M., van Leeuwen, F., King, E., McCulloch, P., Russell, J., Johnston, K., Hindsley, R., Malin, D., Argue, A., Manchester, R., Kesteven, M., White, G., and Jones, P.: 1995, *Astron. Astrophys.* **304**, 116–120
- Röser, S., Bastian, U., and Kuzmin, A.: 1994, *Astron. Astrophys. Suppl. Ser.* **105**, 301–303
- Shepherd, M.: 1994, *Bull. Am. Astron. Soc.* **26**, 987
- Subrahmanyan, R., Kesteven, M., and te Lintel Hekkert, P.: 1992, *Mon. Not. R. Astron. Soc.* **259**, 63–66
- Subrahmanyan, R., Narasimha, D., Pramesh Rao, A., and Swarup, G.: 1990, *Mon. Not. R. Astron. Soc.* **246**, 263
- Surdej, J. and Soucail, G.: 1993, in J. Surdej, D. Fraipont-Caro, E. Gosset, S. Refsdal, and M. Remy (eds.), *Gravitational Lenses in the Universe*, p. 205, Université de Liège
- Tarter, J.: 1996, in *Proceedings of the Society for Photo-Optical Instrumentation Engineers (SPIE), Optical SETI Meeting*, in press
- Tzioumis, A., Jauncey, D., Preston, R., Meier, D., Nicolson, G., Batchelor, R., Gates, J., Hamilton, P., Harvey, B., Haynes, R., Johnson, B., McCulloch, P., Moorey, G., Morabito, D., Niell, A., Robertson, J., Royle, G., Skjerve, L., Slade, M., Slee, O., Watkinson, A., Wehrle, A., and Wright, A.: 1989, *Astron. J.* **98**, 36–43
- Unewisse, A., Hunstead, R., and Piestrzynski, B.: 1993, *Proc. Astron. Soc. Aust.*

- 10(3)**, 229–232
- van der Laan, H.: 1966, *Nature* **211**, 1131–1133
- van Ommen, T.: 1996, *VLA observations of PKS 1830–211*, private communication
- van Ommen, T., Jones, D., Preston, R., and Jauncey, D.: 1995, *Astrophys. J.* **444**, 561–566
- Véron-Cetty, M. and Véron, P.: 1987, *A Catalogue of Quasars and Active Nuclei*, ESO, Munich, 3rd Edition
- Wall, J.: 1994, *Aust. J. Phys.* **47**, 625–655
- Wall, J. and Peacock, J.: 1985, *Mon. Not. R. Astron. Soc.* **216**, 173
- Walsh, W. and McKay, D.: 1996, *Australia Telescope Compact Array User's Guide*, ATNF, 2.01 Edition, W.M. Walsh and D.J. McKay eds.
- Wambsganss, J., Cen, R., Ostriker, J., and Turner, E.: 1996, in C. Kochanek and J. Hewitt (eds.), *IAU 173: Astrophysical Applications of Gravitational Lensing*, pp 65–70, Kluwer Academic Publisher
- Webster, R., Francis, P., Holman, B., Masci, F., Drinkwater, M., and Peterson, B.: 1996, in C. Kochanek and J. Hewitt (eds.), *IAU 173: Astrophysical Applications of Gravitational Lensing*, pp 393–398, Kluwer Academic Publisher
- Wietfeldt, R., Newby, P., Baer, D., Cannon, W., Feil, G., Jakovina, R., Leone, P., and Tan, H.: 1991, in H. Hirabayashi, M. Inoue, and H. Kobayashi (eds.), *Frontiers of VLBI*, pp 177–181, UAP, Tokyo, Japan
- Wiklind, T. and Combes, F.: 1996a, *Nature* **379**, 139–141
- Wiklind, T. and Combes, F.: 1996b, *SEST observations of PKS 1830–211*, private communication
- Wilson, W., Roberts, P., and Davis, E.: 1996, in E. King and D. Jauncey (eds.), *to appear in Proceedings of the 1995 Asia Pacific Telescope Workshop*
- Wright, A., Griffith, M., Hunt, A., Troup, E., Burke, B., and Ekers, R.: 1996, *Astrophys. J., Suppl. Ser.* **103**, 145
- Wright, A. and Otrupcek, R.: 1990, *PKSCAT90: The Southern Radio Source Database*, v1.01 Edition
- WWW: 1996, *The STScI Digitized Sky Survey*, World Wide Web URL: <http://stdatu.stsci.edu/dss/>
- Yentis, D., Cruddace, R., Gursky, H., Stuart, B., Wallin, J., MacGillivray, H., and Collins, C.: 1992, in H. MacGillivray and E. Thomson (eds.), *Digitised Optical Sky Surveys*, p. 67, Kluwer, Dordrecht